INCORPORATING THE INTERFACIAL FRICTION ANGLE CONCEPT INTO THE PDC SINGLE CUTTER AND FULL BIT MODELING

By

AMIN ATASHNEZHAD

Bachelor of Science in Production Engineering
Azad University
Omidiyeh, Iran
2008

Master of Science in Drilling Engineering
Amirkabir University of Technology
Tehran, Iran
2012

Submitted to the Faculty of the
Graduate College of the
Oklahoma State University
in partial fulfillment of
the requirements for
the Degree of
DOCTOR OF PHILOSOPHY
Dec 2019

INCORPORATING THE INTERFACIAL FRICTION ANGLE CONCEPT INTO THE PDC SINGLE CUTTER AND FULL BIT MODELING

Dissertation Approved:

Dissertation Adviser – Dr. Geir Hareland

Dr. Runar Nygaard

Dr. Prem Bikkina

Dr. Jack C. Pashin

ACKNOWLEDGEMENTS

I would like to express my sincere gratitude to my advisor Prof. Geir Hareland for the continuous support of my Ph.D study and research, for his patience, motivation, and immense knowledge. His guidance helped me through all the time of research and writing of this thesis.

I would also like to thank all of my lab members working with me for their additional help throughout my PhD program. In particular, my friend, Dr. Saman Akhtarmanesh, who worked countless hours with me and helped me throughout the entire process. I also greatly appreciate my Eileen Nelson and Seth Sleeper for reviewing this work.

Additionally, I would like to thank my committee members; Dr. Runar Nygaard, Dr. Prem Bikkina, and Dr. Jack C. Pashin, for taking the time to review my thesis, and am very grateful for their valuable input.

Finally, I would like to thank my father REZA, the man to whom I own everything, and my mother SHAHNAZ, the giver of endless love, for their continued support and patience over the years. They supported me through this entire time, and I could not have accomplished this without them. Thank you.

Name: AMIN ATASHNEZHAD

Date of Degree: Dec, 2019

Title of Study: INCORPORATING THE INTERFACIAL FRICTION ANGLE CONCEPT INTO THE PDC SINGLE CUTTER AND FULL BIT MODELING

Major Field: CHEMICAL ENGINEERING

Abstract: Over the past century, oil and gas served an important role in the US energy sector. The oil industry continually has worked to reduce the drilling cost by increasing drilling efficiency. Drilling is a time-consuming and costly operation in which a wellbore is drilled into underground formations to extract the oil and gas from hydrocarbon reservoirs. In well construction, drilling cost is one of the main parts of the total well cost. According to the Energy Information Administration (EIA), the average drilling cost for an onshore well is about 26% of the total well costs (drilling, completion, and facilities), while for an offshore well, the cost rises to about 40% of the total well costs (EIA, 2016). As the energy demand increases in the world markets, oil companies are trying to access resources in more hostile environments, which often increases the time and cost of drilling. The objective of this study is to improve the ROP estimation for PDC bits by introducing a novel ROP model for hard rocks. The effect of cutter geometry and wear flat areas (both PDC and stud) are integrated into the new PDC ROP model. The interfacial friction angle models for single cutter and full bit are presented and used to improve the cutter force and ROP model estimation accuracy. A novel PDC wear model is developed based on the physical work done by the cutter which integrates both the PDC and stud wear coefficients. This research has numerous potential applications in the drilling industry such as: developing or integrating into current drilling optimization software, autonomous drilling decision making, real-time optimization, and problem solver software.

TABLE OF CONTENTS

Chapter Page

LIST OF TABLES

Table Page

Table page

LIST OF FIGURES

Figure Page

Figure Page

Figure Page

Figure Page

Figure Page

Figure Page

Figure Page

NOMENCLATURE

α	shear angle (degree)
σ_c	uniaxial rock strength (psi)
ψ	interfacial friction angle (degree)
τ	shear strength (psi)
μ	the internal friction angle (degree)
β	rake angle of cutting tool (degree)
δ	the cutter depth of cut (inch)
μ_d	drag coefficient (degree)
ΔD	drilling interval length (ft)
ς	the ratio of the vertical to the horizontal force acting on cutting face (-)
ε	intrinsic specific energy (psi)
ω_1	PDC layer wear flat areas efficiency (-)
ω_2	stud wear flat areas efficiency (-)
δ_n	normalized depth of cut (-)
$\psi_{\text{single cutter}}$	single cutter interfacial friction angle (degree)
ψ_{fullbit}	full bit interfacial friction angle (degree)
α_{PDC}	PDC layer wearing coefficient (ft. lb_f/cube-inch)
α_{stud}	stud wearing coefficient (ft. lb_f/cube-inch)
α_{ave}	averaged PDC and stud wearing coefficients (ft. lb_f/cube-inch)
α	wear constant, the amount of work per unit volume of material (ft. lb_f/cube-inch)
$\overline{T}_W$	mean flat area temperature of PDC cutter (Celsius)
f	thermal response function ($C\frac{cm^2}{W}$)
σ_{cr}	critical penetrating stress (psi)
$\mathcal{A}_1$	the theoretically calculated area beneath the cutter (square inch)
$\mathcal{A}_2$	the weighted area beneath the cutter (square inch)

ΔP_{bit}	pressure drop in bit (psi)
ΔD	drilling interval length (ft)
σ_c	uniaxial rock strength (psi)
a_s and b_s	empirical constants for different lithologies (-)
a_1, b_1, c_1	empirical coefficients (-)
a_2, b_2	empirical coefficients (-)
a_4, b_4	empirical coefficients (-)
A_v	cutter front area (square inch)
ABR	formation abrasiveness (-)
A_c, A_{cut}, A_v	area of cut (cutter front area) (square inch)
A_0	cutting area (square inch)
$A_{contact}$	area of cutter face that is in contact with rock (square inch)
A_h	the area beneath the cutter face (square inch)
A_w	total wear flat area (square inch)
A_w'	weighted wear flat area (square inch)
$A_{w,PDC}$	PDC layer wear flat area (square inch)
$A_{w,stud}$	stud wear flat area (square inch)
A_H	the total area beneath the cutter (square inch)
A''_w	projection of cutter wear flat area on X-Y plane (square inch)
A_b	bit area (square inch)
ABR	abrasiveness (-)
b(x)	bit blade effect function (-)
BR	back rake angle (degree)
BHA	bottom hole assembly (-)
BG	bit grade (-)
BSS	Berea sandstone
C_1, C_2	rock type constants (-)
CCS	confined compressive strength (psi)
COR	correction factor (effect of WOB and RPM nonlinearity on ROP) (-)
C	machining constant (-)
C_B	number of blade coefficient (-)
CP	confining pressure (psi)
CCS	confined compressive strength (psi)

d_c, D_c	cutter diameter (inch)
DOC	depth of cut (inch)
DOC_n	normalized depth of cut (-)
DEA	differential evolution algorithm (-)
D_b	bit diameter (inch)
F_t, F_d, F_s^c	cutter tangential (drag) force (lbf)
F_a, F_n, F_n^c	cutter axial (normal) force (lbf)
F	cutter penetrating force (lbf)
G	coefficient determined by bit geometry, cutter size, and cutter design (-)
HSI	hydraulic square inch (HP/sq-inch)
h(x)	hydraulic function (-)
HP	horsepower (-)
HHP	hydraulic horsepower (HP)
IFA	interfacial friction angle (degree)
ID	inner diameter (in)
JSA	junk slot area (square inch)
K_f	cutter-rock friction coefficient (-)
K_{hf}	rock-formation thermal conductivity ($\frac{\frac{w}{cm}}{C}$)
K_{wf}	numerical constant (-)
M	number of nodes representing the rock surface on the vertical plane (-)
MS	Mancos shale
ML	machine learning (-)
MSE	mechanical specific energy (psi)
MW	mud weight (ppg)
N	number of planes (-)
N_c	number of cutters (-)
N_b	number of blades (-)
n1, n2	rock type constants (-)
OD	outer diameter (in)
P_c	confined pressure (psi)
PDC	polycrystalline diamond cutter (-)
Q	flowrate (GPM)
r_i	the element radius (inch)

RPM	revolution per minute (rpm)
ROP	rate of penetration (ft/hr)
RS	rock strength (psi)
R_e	equivalent radius (inch)
R	radial coordinate (-)
S_0	unconfined compressive strength (psi)
S_s	the shear strength of the material being cut (psi)
SR	side rake angle (degree)
S	confined compressive strength (psi)
SPP	standpipe pressure (psi)
SWG	Sierra white granite
t_{PDC}	PDC cutter thickness (inch)
TM	Tennessee marble
TX pink	Texas Pink Granite
UCS	unconfined compressive strength (psi)
UCS_n	normalized unconfined compressive strength (-)
V_n	normalized cutter velocity
V	cutting speed ($\frac{m}{s}$)
V_{worn}	worn volume (cube inch)
$V_{total\ worn}$	total worn-out section (cube-inch)
WOB	weight on bit (lbf)
W_f	bit wear function (-)
W_c	bit wear coefficient (-)
W_1, W_2 and W_T	cutter drag, normal works ($ft.lb_f$)
W_T	cutter total works ($ft.lb_f$)

CHAPTER I

INTRODUCTION

The drilling cost includes rig rental, bits, casing strings, drilling fluids, and service costs. The rig rental cost, which is the larger part of the drilling cost, is a direct function of the drilling time. The drilling time includes the rotating time, connection time, and tripping time. While the connection time is more or less fixed for a specific interval, the rotating time depends on how operational parameters (WOB, RPM, etc.) are applied during drilling a well. Therefore, an optimum drilling plan should be able to reduce the rotating time by increasing the average drilling ROP and decreasing the tripping time (Hareland et al., 2008 b). Furthermore, horizontal wells allow multiple wells to be drilled from the same drilling location. Along with the previously mentioned advantages of horizontal wells, the lateral sections of a horizontal well increase the length of the well considerably. The rotating time and total cost of drilling increase when the wellbore becomes longer, which makes the use of drilling optimization necessary to ensure an economical drilling operation. To reduce the rotating time and total cost of the drilling process, the drilling operation should be translated into a mathematical model. The model consists of expressing the system, entity, or phenomenon using a mathematical language and is the platform for simulation, optimization, and design. Engineers in different industries are continually trying to reduce costs using modeling and optimization.

In the drilling industry, the rate of penetration (ROP) is the speed that the drilling bit penetrates the formation and is expressed in feet or meters per hour. The drilling ROP affects the drilling time and consequently the drilling cost.

At the present time, the application of drilling simulators has become the leading technology in well planning. The ROP models act as the core engine for the drilling simulator and provide an estimation for ROP by taking important drilling parameters as input, including WOB, RPM, bit details, hydraulics, and formation properties. To achieve a precise ROP simulator, having an accurate ROP model is essential.

Several researchers have presented different ROP models based on the type of drilling bits. Maurer (1962) established a model for the roller cone bits at low RPM and WOB, assuming a perfect cleaning condition around the drill bit and annular space. Walker et al. (1986) introduced a ROP model for insert bits by including the bit weight, well depth and laboratory determined rock strength. Warren (1987) proposed a model for the roller cone bits by taking the rock strength, RPM, WOB and bit diameter. Winters et al. (1987 b) developed a ROP model for roller cone bits taking the bit design, operating conditions, and the rock mechanics into account. They found that the rock ductility had a major effect on bit performance. Hareland and Rampersad (1994) developed a ROP model for drag bits including wear which comprised of cutter-rock interaction. This model included mass conservation and assumed an ideal bit cleaning condition. Motahhari et al. (2010) also developed a PDC ROP model based on single cutter rock interaction by assuming perfect bit cleaning. Kerkar et al. (2014) developed another ROP model for PDC bits and incorporated the bit details such as the number of blades, cutter details, and integrated bit wear and hydraulics.

Once the desired parameter (e.g. ROP) is expressed in a mathematical equation, the next step is to find the global minimum or maximum of such equation, known as optimization. Drilling cost optimization has always been one of the major interests of researchers in petroleum engineering.

Speer (1958) introduced the drilling optimization using optimum drilling parameters. Galle and Woods (1963) introduced a graphical method to find the optimum RPM and WOB for roller cone bits. Bourgoyne and Young in 1974 used the minimum cost formula for drilling optimization. They showed that maximizing the ROP could reduce the drilling cost (Eren and Ozbayoglu, 2010). Onyia (1987) and Rampersad et al. (1994) applied a Geological Drilling Log (GDL) to generate input for drilling simulation and optimization. The GDL is calculated by inverting the ROP model for any specific bit (e.g. tricone bits, PDC bits). The GDL is then used in conjunction with ROP models for any specific bit to simulate the bit penetration rate. This research showed how the obtained information during drilling can be utilized for the optimization of future wells in the same oil field.

Hareland et al. (2007) developed a drilling simulator software (Optimizer) which estimates the Apparent Rock Strength Log (ARSL) based on drilling data. Also, the drilling optimizer application in Managed-Pressure Drilling (MPD) was demonstrated (Hareland et al., 2008 a). The software simulates the drilling process for multiple drilling bits, pull depths and operational parameters. The drilling scenario with the minimum cost is chosen as the optimum drilling scenario. A large reduction (more than 30%) in drilling cost was proven just by drilling simulation on conventional wells in Canada using the Optimizer software (Hareland et al., 2008 b).

Most of the systems in engineering are non-linear, multi-dimensional under various complicated constraints (Lummus, 1970). This leads to complicated mathematical equations, which are known as models. The common way to solve mathematical equations is analytical methods. The analytical methods find the exact global minimum/maximum of functions. Although the analytical methods give the explicit answers for models, solving such complex equations with numerous constraints are hard, time-consuming, and in some cases, impossible.

Metaheuristic methods can be applied to solve complicated sets of mathematical equations with a high degree of nonlinearity and complex constraints. Their applications include multi-objective

function optimization (Urade and Patel, 2012), routing (Shen et al., 2009), scheduling (Pandey et al., 2010), partitioning (Erdeljan et al., 2014), pattern recognition (Omran et al., 2006), classification such as decision tree (Chen et al., 2014), random forest (Malik et al., 2011) and K nearest neighbor (Zhang et al., 2010), image processing (Omran et al., 2006), data mining (Grosan et al., 2006) and machine learning (Gaur et al., 2013). Metaheuristic methods are inspired mostly by nature, such as the flight of bird flocks, ant movement strategy, or the flight patterns of bees. These methods generate a sample of feasible solutions and try to improve the overall fitness index in each iteration. Metaheuristic methods do not guarantee that the solution found is the global optimum. These methods tend to go toward the global optimum quickly, and because of that, they can effectively deal with complicated problems. Metaheuristic algorithms are useful in cases in which classical methods become stuck in local minima.

The Differential Evolution Algorithm (DEA) is a powerful, yet simple metaheuristic one. It benefits from a simple arithmetic operation and a novel sampling technique which adaptively changes the step size during population evolution. It perturbs the best solution value into existing population vectors using crossover operation. Price in 1996 tested the performance of DEA on 15 benchmark functions. He found that the DEA was the fastest method for solving eleven of them and was competitive for the remaining four (Price, 1996). Applying metaheuristic methods is easy in comparison to analytical methods and therefore, in this study, the potential application of DEA is used to find the constants of single cutter interfacial friction angle (IFA) model taking the data into account. In this work the DEA was coded in Python and solved along with the PDC ROP model to find the full bit (Internal Friction Angle) IFA model constants.

Studies have already been done in the drilling optimization and simulation domain. Hareland et al. (2008) developed a software (Optimizer) for drilling simulation. The software benefits from comprehensive models for both rollercone and PDC bits. The Optimizer software can be used to generate rock strength, which provides further input for drilling simulation and optimization. The

user can then manually divide a drilling interval into several subsections and apply desired bits, WOB, and RPM to reduce drilling costs. Although the user can reduce the drilling costs by using the simulator, the learning process is time-consuming and relies on the user's background knowledge, experience, and patience. In addition, finding the most cost-effective drilling scenario is almost impossible due to many feasible solutions and multiple local optima. In other words, the Optimizer software is good at drilling simulation, but is lacking an optimization tool.

Self et al. (2017) found the optimum WOB and RPM for a drilling interval and selection between two bits. They used the Kerkar et al. (2014) ROP model in conjunction with the Particle Swarm Optimization (PSO) algorithm for simulation and optimization. However, their work was limited to a selection between two bits. The Kerkar et al. (2014) model does not take the details such as PDC cutter diameter, wear flat areas for stud and PDC, and the interfacial friction between the cutter and rock into account. The Kerkar et al. (2014) model also ignored the above-mentioned parameters effects on cutter wear which affects the ROP consequently and because of that, their optimization results are not very reliable.

The interfacial friction is referred to as frictional force at the contact area between the PDC cutter face and rock (Rahmani, 2013). The interfacial friction concept is included in new single and full PDC bit models to improve the full bit ROP model's accuracy. The goal of this study is to propose a pure theoretical – empirical model for PDC bits which includes the interfacial friction between PDC cutter and rock. It worth to mention that, other than the application in the oil and gas drilling industry, the models developed in this study are applicable to the geothermal wells as well.

The novel features of this thesis which makes it distinct from previous works are as follows:

- The single PDC cutter model analytical equations were developed and used as a base for a PDC full bit ROP model. Incorporating the wear flat area details (PDC and stud) makes the new ROP model distinct from previous works.

- The novel PDC wear model is derived based on the physical definition of work. The unique PDC wear model considers the effects of both stud and PDC wear coefficients. The PDC wear model also includes the concept of interfacial friction. This aspect makes the new wear model unique compared to previously published models.
- The interfacial friction angle (IFA) concept is presented and incorporated in PDC single and full bit models to improve models' estimations.
- A single cutter IFA model was developed based on single cutter data and used along with the single cutter force models to improves models force estimations accuracy.
- The differential evolution algorithm (DEA) was used in cooperation with the new proposed PDC ROP model to develop a new full bit IFA based model.
- The new full bit IFA model along with new PDC ROP model were verified using data from literature.

This thesis consists of five chapters. Chapter one provides an introduction to the modeling and optimization work and proposes the goal of the thesis. Chapter two introduced a review of previous works in PDC ROP modeling, single cutter rock interaction modeling, statistical ROP modeling, and optimization work. This chapter also discusses the IFA concept. Chapter three, expounds the technical approach toward developing a single cutter and full bit models. In chapter three, the cutter contacts area equations for sharp and blunt cutter are proposed. A new single cutter PDC model for sharp and blunt cutters, two IFA models for single cutter and full bit, and the full bit PDC ROP model are proposed. Chapter three presents a novel real-time bit wear model, which incorporates the wear flat areas (PDC and stud) and wear constants of both PDC and stud material. In chapter three also discusses the cutter depth of cut calculation. In chapter four, the developed IFA models (for single cutter and full bit) are presented and verified with data. The full bit ROP model is used cooperatively with the full bit IFA model to estimate the ROP of four and five-bladed PDC bits in SWG and BSS. Appendices A, B, C, D, and E present developed equations for sharp and blunt

cutter contact area, cutter wear flat areas both for PDC and stud, sharp and blunt cutter front area, sharp and blunt cutter beneath areas, cutter worn volume, and the wear flat area width and length. Appendices F present the Python notebook codes which are used in this research for developing two IFA models for single cutter and full bit using a differential evolution algorithm (DEA). Appendix G provides all data used in this dissertation.

CHAPTER II

BACKGROUND AND LITERATURE REVIEW

This chapter reviews the previous studies and expounds the researches on full bit PDC ROP modeling, cutter-rock interaction modeling, IFA concept, and the optimization literature.

The drilling time is a function of multiple general parameters including drilling hydraulic properties, bit details, well geometry, drilling string details, and formation properties (Figure 2.1). These parameters have integrated effects on each other, which make the drilling optimization a complex process (e.g. the mud properties affect the bit hydraulic, the rock confinement and WOB which as consequently influence the ROP). The relationship between the ROP and the above-mentioned parameters has been an important research topic in drilling engineering for decades.

Models are developed to demonstrate the effects of different variables on the desired parameter or parameters. The models are mostly expressed in mathematical forms (e.g., empirical models, analytical models, numerical models, etc.). Nonetheless, they can be expressed in different forms known as Machine Learning Algorithms (ML), such as Artificial Neural Network (i.e. ANN, Deep Net, and Recurrent Net), Decision Tree, Random Forest, K-Nearest Neighbor (KNN), Logistic Regression, Support Vector Machine (SVM), etc. In some cases, it is necessary to use advanced optimization methods to find the optimum solution due to the model complexity.

The rate in which a drill bit penetrates into a formation (ROP) is a critical parameter in drilling engineering and well plan. ROP is a function of different parameters including WOB, RPM, hydraulic design, bit specifications and other parameters (Figure 2.1). Researchers have developed a variety of PDC ROP models (full bit and single cutter), which are provided and discussed in the following sections.

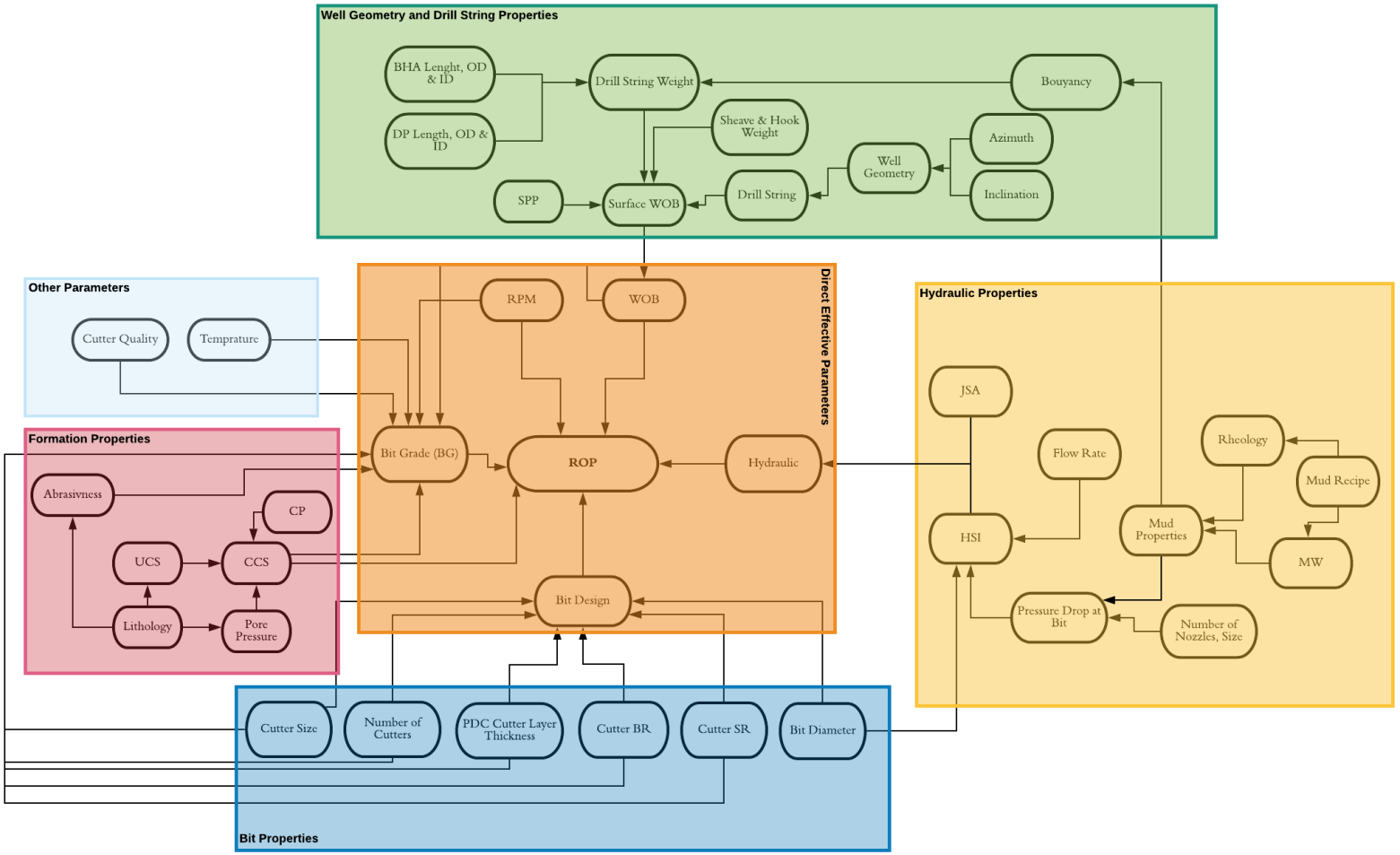

Figure 2.1. Parameters that influence on drilling rate of penetration (ROP)

2.1 Polycrystalline Diamond Compact (PDC) ROP models

2.1.1 Bingham (1965) ROP model

Bingham (Bingham, 1965) developed a basic ROP model applicable to all bit types. The Bingham model is provided in Equation 1.

$$ROP = a \times RPM \times \left(\frac{WOB}{D_b}\right)^b \ldots\ldots \text{Eq. } 2.1$$

The unit of ROP (rate of penetration) is ft/hr, WOB is in klb, RPM is in revolution per minute and D_b is bit diameter in inches. The coefficients a and b are representative of the formation drillability and are determined for each specific lithology. The Bingham model does not include the bit type, bit wear, cutter shape and orientation, drilling hydraulic, and formation details (Soares et al., 2016).

2.1.2 Hareland and Rampersad (1994) ROP model

Hareland and Rampersad modeled the drag bits ROP based on cutter-rock interaction in 1994.

$$ROP = \frac{14.14 \times N_c \times RPM \times A_v}{D_b} \ldots\ldots \text{Eq. } 2.2$$

In Equation 2.2, N_c is the number of cutters and A_v is the area of rock compressed ahead of a cutter in square inch. The A_v is different for different drag bit cutter shapes. For a PDC cutter the $d_c$is cutter diameter. Figure 2.2 provides a schematic of a PDC cutter in 3D. In Figure 2.2, the SR and BR angles are shown using α and θ respectively. The area ahead of a PDC cutter is calculated using Equation 2.3.

$$A_v = \cos(SR) \times \sin(BR)$$

$$\times \left[\left(\frac{d_c}{2}\right)^2 \times \cos^{-1}\left(1 - \frac{4WOB}{\cos(BR)\,\pi {d_c}^2 \sigma_c}\right) \right.$$

$$\left. - \sqrt{\left(\frac{2WOB}{\cos(BR)\,\pi N_c \sigma_c} - \frac{4WOB^2}{\cos(BR)\,\pi N_c {d_c \sigma_c}^2}\right)\left(\frac{WOB}{\cos(BR)\,\pi \sigma_c}\right)} \right] \ldots\ldots \text{Eq. 2.3}$$

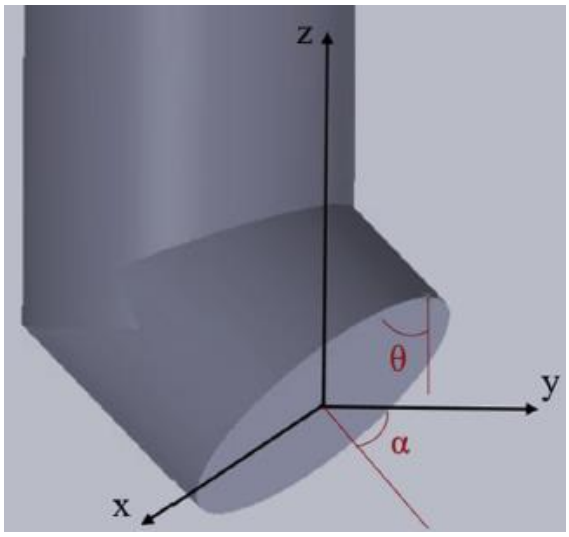

Figure 2.2 A 3D schematic of a PDC cutter (Soares et al., 2016)

It was noticed that ROP does not show a linear relationship with WOB and RPM, therefore, a correction factor (COR) was introduced that is multiplied by the ROP model. The COR Equation is provided in Equation 2.4. In COR Equation, the a is representative of an empirical correction factor for lithology, the b is representative of the bit rotation correction factor and c denotes the mechanical WOB empirical correction factor.

$$COR = \frac{a}{(RPM^b \times WOB^c)} \ldots\ldots \text{Eq. 2.4}$$

The bit wear function, W_f is multiplied into the ROP model to give the Hareland and Rampersad model (1994) a general form (Equation 2.5).

$$ROP = W_f \times \frac{a}{(RPM^b \times WOB^c)} \times \frac{14.14 N_c RPM}{D_B} \times \cos(SR) \times \sin(BR)$$
$$\times \left[\left(\frac{d_c}{2}\right)^2 \times \cos^{-1}\left(1 - \frac{4WOB}{\cos(BR)\,\pi {d_c}^2 \sigma_c}\right) \right.$$
$$\left. - \sqrt{\left(\frac{2WOB}{\cos(BR)\,\pi N_c \sigma_c} - \frac{4WOB^2}{\cos(BR)\,\pi N_c {d_c \sigma_c}^2}\right)\left(\frac{WOB}{\cos(BR)\,\pi \sigma_c}\right)} \right] \ldots\ldots \text{Eq. 2.5}$$

It is important to notice that Hareland and Rampersad used the uniaxial rock strength (σ_c) in their model, which can cause overestimation in ROP calculation.

2.1.3 Motahhari et al. (2010) ROP model

Motahhari et al. (2010) developed a model for PDC bits by assuming 100 percent efficient bit cleaning. The model is provided in Equation 2.6.

$$ROP = W_f \times \left(\frac{G \times RPM^{\gamma} \times WOB^{\alpha}}{D_B \times S}\right) \ldots\ldots \text{Eq. 2.6}$$

The W_f is bit wear function and is calculated using Equation 2.7.

$$W_f = K_{wf} \times \left(\frac{WOB}{N_c}\right)^{\rho} \times \frac{1}{S^{\tau} \times {A_w}^{\rho+1}} \ldots\ldots \text{Eq. 2.7}$$

In the previous equations, γ and α are ROP related exponents, G is a coefficient determined by bit geometry, cutter size, and cutter design. K_{wf} is a numerical constant, N_c is the number of cutters, A_w is wear flat area, S is the confined compressive strength and is a function of unconfined compressive strength (S_0) and confining pressure (P_c) through Equation 2.8 (Rampersad et al., 1994).

$$S = S_0 \times (1 - a_s {P_c}^{b_s}) \ldots\ldots \text{Eq. 2.8}$$

In Equation 2.8, the a_s and b_s are empirical constants for different lithologies. It is important to notice that since the Motahhari model does not take the drilling hydraulics into account, it can cause ROP overestimation in some cases.

2.1.4 Kerkar et al. (2014) Model

The Kerkar et al. (2014) model is provided in the following set of Equations. This model includes drilling hydraulics and bit geometry as well as other parameters to estimate the ROP.

$$\mathrm{ROP} = \left[\frac{\mathrm{K1} \times \mathrm{WOB}^{a1} \times \mathrm{RPM}^{b1} \times \cos(\mathrm{SR})}{\mathrm{CCS}^{c1} \times \mathrm{D_b} \times \tan(\mathrm{BR})}\right] \times \mathrm{W_f} \times \mathrm{h(x)} \times \mathrm{b(x)} \ldots\ldots \mathrm{Eq.\ 2.9}$$

In Equation 2.9, K1 is calibration constant, a_1, b_1, c_1 are empirical coefficients, D_b is bit diameter, CCS is confined compressive strength, W_f is bit wear function, h(x) is hydraulic function and b(x) is bit blades effect function on ROP. The W_f, h(x), and b(x) are defined in the Equations 2.10 through 2.14.

$$\mathrm{W_f} = 1 - a_3 \times \left[\frac{\mathrm{BG}}{8}\right]^{b_3} \ldots\ldots \mathrm{Eq.\ 2.10}$$

BG is the bit dull grade and it can change from 0 for a new bit to 8 for a completely worn out bit. The hydraulic effect is included in the ROP model using Equation 2.11.

$$\mathrm{h(x)} = a_2 . \frac{(\mathrm{HSI} \times \frac{\mathrm{JSA}}{2\mathrm{D_{bit}}})^{b_2}}{\mathrm{ROP}^{c_2}} \ldots\ldots \mathrm{Eq.\ 2.11}$$

In the above equation, the HSI is hydraulic square inch for a bit and is calculated by dividing the hydraulic horsepower (HHP) to the bit area. The HSI model is provided in Equation 2.12. The JSA is the junk slot area and is determined by adding up the surface area between blades in the bit face. The a_2, b_2 are empirical coefficients.

$$\mathrm{HSI} = \frac{\frac{\mathrm{Q} \times \Delta \mathrm{P_{bit}}}{1714}}{\left(\frac{\pi}{4}\right) \mathrm{D_{bit}}^2} \ldots\ldots \mathrm{Eq.\ 2.12}$$

The b(x) incorporates the effect of the number of blades into the ROP model and is calculated by Equation 2.13. In Equation 2.13, the N_b is the number of blades:

$$b(x) = \frac{RPM^{1.02-0.02N_b}}{RPM^{0.92}} \dots\dots \text{Eq. } 2.13$$

The BG is bit grade and is estimated using Equation 2.14. In this Equation, ΔD is drilling interval length, ABR is the abrasiveness of the formation for a drilling interval, a_4 and b_4 are empirical coefficients and W_c is bit wear coefficient:

$$\Delta BG = W_c \times \sum_{i=0}^{n} \Delta D_i \times WOB_i{}^{a_4} \times RPM_i{}^{b_4} \times CCS_i \times ABR_i \dots\dots \text{Eq. } 2.14$$

The Kerkar et al. (2014) wear function does not take the effect of cutter wear flat area into account. Also, the interfacial friction was not included in the Kerkar bit wear model. The interfacial friction between PDC cutter and rock affect not only the depth of cut and ROP, but the cutter forces which consequently influence the bit wear.

None of the above-mentioned models take into account the effect of PDC and stud quality on bit wear. The PDC layer and stud have different wear coefficients, which should be considered for bit wear calculation. The area beneath the bit includes stud and PDC layer wear flat areas. Previous models do not incorporate the stud and PDC layer wear flat areas into account. In addition, stud material has a lower wear coefficient which causes higher wear rate compared to the PDC material. Therefore, lower contact area efficiency is expected for stud. In the new ROP model, the bit stud and PDC layer wear quality and wear flat areas are taken into account to improve estimation for drilling ROP. In addition, a new real-time bit wear estimation model is developed by taking the physical work that is done by the PDC cutter, which provides more realistic values for bit wear. The cutter normal and drag forces are calculated using the single cutter force model developed in this study for both sharp and blunt cutters. The new single cutter force models included the effect of interfacial friction angle into account. The

estimated forces (cutter normal and drag forces) are inserted back into the PDC wear model to achieve the cutter work amount.

2.2 Single Cutter Rock Interaction Models

There are few studies that explain the cutter rock interaction and their basic concepts (Detournay and Defourny, 1992; Glowka, 1987; Gerbaud et al., 2006). The interaction between cutter surface area and the rock results in friction, which affects the normal and tangential forces on the cutter. The friction between cutter surface area and the rock itself is influenced by rock/cutting properties, cutter surface characteristics, cutter BR, cutter velocity, drilling mud properties, and normal force on the cutter (Rahmani, 2013).

2.2.1 Ernst and Merchant (1941) Model

Ernst and Merchant (1941) assumed a single shear plane between an intact rock and the cut always exists during the cutting process. They calculated the tangential and axial force on the cutter by taking the cutter geometry and interfacial friction into account. The tangential and axial forces equations are provided in Equations 2.15 and 2.16.

$$F_t = \frac{\tau \times A_c \times \cos(\psi + \theta)}{\sin\alpha \times \cos(\alpha + \psi + \theta)} \dots\dots \text{Eq. } 2.15$$

$$F_a = F_t \times \tan(\psi + \theta) \dots\dots \text{Eq. } 2.16$$

In Equation 2.15, the τ is shear strength, A_c is the area of the cut, and α is the shear angle which is determined by taking the principal minimum energy into account. Ernst and Merchant assumed low depth of cut for a cutter, and therefore the tangential force, (F_t), is responsible for the entire work that is done by the cutter. A relationship between cutter BR (θ), shear angle (α), and interfacial friction angle (ψ) was achieved by taking partial derivation of Equation 2.15 with respect to the shear angle

(α). They found that Equation 2.17 governs as a constraint between cutter BR (θ), shear angle (α), and interfacial friction angle (ψ).

$$2\alpha + \psi + \theta = \frac{\pi}{2} \ldots\ldots\ldots \text{Eq. 2.17}$$

2.2.2 Merchant (1940) Model

Merchant's model was proposed for metal cutting in 1940. The Merchant expressed the tangential and axial cutter forces on the shear plane through Equations 2.18 and 2.19.

$$F_n = A_0 \times S_s \times \left(\tan\left(\frac{C + \tau - \beta}{2}\right) + \cot\left(\frac{C - \tau + \beta}{2}\right)\right) \ldots\ldots\ldots \text{Eq. 2.18}$$

$$F_t = A_0 \times S_s \times \left(\tan\left(\frac{C + \tau - \beta}{2}\right) + \cot\left(\frac{C - \tau + \beta}{2}\right) - 1\right) \ldots\ldots\ldots \text{Eq. 2.19}$$

In this set of Equations, the F_n and F_t are axial and tangential cutter forces respectively, C is machining constant, and it is related to the rate of change in the shear strength of metal, A_0 is the cutting area, S_s is the shear strength of the material being cut, and β is the rake angle of the cutting tool.

Merchant (1944) also developed a card model for the single cutter and explained that the cuttings are generated due to shear forces on the shear plane (Rahmani, 2013). Merchant also improved the Ernst and Merchant model (1941) by incorporating the internal friction angle (IFA). Equation 2.17 was modified to Equation 2.20 to include an internal friction angle. Rahmani, in 2013, applied both Equations 2.17 and 2.20 to lab data and found that Equation 2.17 provides a better estimation for the shear angle.

$$2\alpha + \psi + \theta = \frac{\pi}{2} - \varphi \ldots\ldots\ldots \text{Eq. 2.20}$$

2.2.3 Glowka (1987) Model

In 1987, Glowka developed a single PDC cutter model for estimating the cutter force, temperature, and wear. The single cutter data was used to measure the rock drillability and to study the theoretical considerations, which account for the interaction between cutters on the bit face. He found that the penetrating force on a worn PDC cutter is proportional to the cutter wear flat area at a given depth of cut. Also, he observed that for a given depth of cut and wear flat area, a larger worn cutter requires no greater penetrating force than a small cutter. The normal force for worn and new cutters is provided at Equations 2.21 and 2.22.

$$F = A_w \times C_1 \times \delta^{n1} \ldots\ldots \text{Eq. } 2.21$$

$$F = C_2 \times \delta^{n2} \ldots\ldots \text{Eq. } 2.22$$

In these equations, F is the cutter penetrating force, A_w is cutter wear flat area, δ is the cutter depth of cut, C_1, C_2, n1 and n2 are rock type constants. The cutter drag force (F_d) is calculated by taking the drag coefficient (μ_d) into account.

$$\mu_d = \frac{F_d}{F} \ldots\ldots \text{Eq. } 2.23$$

$$F_d = \mu_d \times F \ldots\ldots \text{Eq. } 2.24$$

Glowka (1987) found that the waterjet assistance extends the bit life in hard rocks through reducing the bit WOB, torque, and cutter forces. The model was incorporated into a PDC wear computer code to be used for general PDC bit analysis. The results were promising in term of estimating the WOB, drilling torque, and bit life. The Glowka (1987) model showed that the bits with a sharper profile require less WOB than flat profiles. At the same time, the bits with sharper profiles wear faster and require greater WOB as the drilling length increases.

2.2.4 Detournay and Defourny (1992) Model

In 1992, Detournay and Defourny assumed plastic failure of rock at a small depth of cut (0.04 inch) and developed a single cutter model for sedimentary rocks. They developed a sharp cutter model by taking the Ernst and Merchant (1941) cutter geometry into account. They assumed cutter tangential force as a function of intrinsic specific energy (ε) and the area of cut (A_c). The ε is an empirical input defined as the minimum required energy to drill rock. They found that the intrinsic specific energy is equal to the unconfined compressive strength of the rock at atmospheric pressure (Rahmani, 2013). They found also that the intrinsic specific energy is a function of bottom hole pressure, pore pressure, rock-cutter interfacial friction angle (ψ), and cutter BRs angle (Detournay et al., 2008). They concluded that for a blunt cutter, the angle between the forces acting on cutter wear flat area is close to the internal friction angle of rock due to a thin layer of cutting accumulation underneath the cutter wear flat area (Rahmani, 2013).

For a sharp cutter, the cutter tangential and normal force can be calculated as a function of the cross-sectional area of cut using Equations 2.25 and 2.26.

$$F_s^c = \varepsilon \times A_c \ldots\ldots \text{Eq. } 2.25$$

$$F_n^c = \varsigma \times \varepsilon \times A_c \ldots\ldots \text{Eq. } 2.26$$

Where ε is intrinsic specific energy, ς is the ratio of the vertical to the horizontal force acting on cutting face, and A_c is the cutting area. Detournay and Defourny introduced a specific energy and drilling strength by dividing the tangential and axial force to cutting face. The cutter forces can be back-calculated using these two quantities once they are known from laboratory data.

2.2.5 Hanson and Hansen (1995) Model

In 1995, Hanson and Hansen developed a numerical bit dynamics model for PDC drill bit under conditions of a full-scale drilling simulator test. Their model includes the PDC cutter interaction with bottom hole and side wall rock surface, induced vibration of main mechanical components of a full-scale drilling simulator, the bit impact energy loss, and the friction between the bit gage and hole wall. They assumed the N vertical planes emanating from the Z-axis in a spoke-like fashion. The bottom-hole and side-wall rock surface is represented on vertical planes by the ordered set $\{R_i, Z_i, i = 1, M\}$, where R is the radial coordinate and M is the number of nodes representing the rock surface on the vertical plane at that particular time step. They used 9×10^6 nodes on each vertical plane to represent the bottom hole and side wall surfaces.

Hanson and Hansen (1995) established two separate PDC cutter force models using the regression method, which consists of a simple functional relationship between the normal and tangential force to the PDC area of cut, RPM, wellbore pressure, PDC cutter wear flat area, and the cutter BR (Hanson and Hansen, 1995). The first single cutter model is based on the data from the single cutter force tests. The PDC cutter tangential and axial force was measured for different cutter BR, the area of the cut, wellbore pressure, RPM and wear flat areas. The regression analysis was used to fit a physical reasonable functional form on single cutter data for a number of rock types, including MS, Pierre shale, Solenhofen limestone, Hartz greywacke, and Carthage limestone. Hanson and Hansen (1995) developed their second single cutter force model based on full-scale bit simulator experiments in Carthage limestone at atmospheric conditions. For a given bit design, ROP, and RPM, they calculated the area of cut for an individual cutter. They used a priori functional form as a force cutter model and applied the regression analysis to achieve the best fit. Both models have similar accuracy, but the second model gives more accurate estimation in Carthage limestone.

2.2.6 Yan (1997) Model

In 1997, Yan studied the single PDC cutter fragmentation mechanism in hard rocks. He used the Forcht (1941) model to achieve the stresses caused by the concentrated load in a wedge (Forcht, 1941). Yan conducted a two-dimensional analysis of stress fields based on linear elasticity theory to describe the behavior of the rock under cutter force. The analysis showed that the entire region in a rock body can be divided into two compressive and tensile sub-regions. His theoretical analysis and lab tests showed that the cutting process is discontinued process that can be regarded as a repeated cycle. Yan found that the two cracks are imposed on the rock in each cycle. The first one is a straight line which is initiated at cutter tip and propagated into the rock. The second one is curved, which is propagated toward the surface after the first crack has stopped propagation. The straight-line crack is initiated and propagated due to tensile strength, while the curved one is propagated due to shear strength. Due to the crack being caused by tension at the cutter tip, the crack direction can be determined by taking the principal stress at the cutter tip.

The Yan force model fits the laboratory test data for SWG very well, while it does not fit as well for TM and BSS at the high BR and SR angles. The model suggested higher values for vertical cutter forces compared to the horizontal one (estimated cutter vertical force is greater than horizontal one). The Yan model suggests that the horizontal and vertical forces on cutter are not changed with the change in cutter SR. The model prediction for chip size and shape was verified against the lab data and showed good agreement in most cases.

2.2.7 Gerbaud et al. (2006) Model

Gerbaud et al. (2006) observed that there is a built-up edge of cutting on cutter face in the lab which controls the flow of crushed materials. They developed a new single cutter model by taking the buildup edge of failed materials on cutting face. They concluded that due to the energy is transferred between

cutter face and rock through a built-up edge on cutter face, the shear angle should be independent of cutter orientation and friction. Such an assumption is not in accordance with the Smith 1998 observations in the lab for ductile rocks (shale). Smith, in 1998, observed that the thickness of ribbons decreases for polished faced cutters compared to non-polished cutter faces (Figure 2.3). Therefore, the polished cutter has a lower interfacial friction angle (ψ) that increases the shear angle, which consequently reduces the size of ribbons. Gerbaud et al. (2006) included the effect of frictional forces which are introduced by a chamfer in their single cutter model.

Figure.2.3. Shale ribbons for tests with water at 9000 psi CP and 0.011-inch depth of cut for polished (left) and non-polished cutter (right)(Smith, 1998)

They considered two different mechanisms at chamfer with respect to the cutter depth of cut. If the cutter depth of cut is greater than the chamfer, the cutting is trapped between the chamfer and rock surface, which impose additional forces to the cutter. If the depth of cut is lower than the chamfer, the chamfer becomes a cutting force with higher BR angle.

2.2.8 Rahmani (2013) Model

Rahmani (2013) assumed that the behavior of fine-grained rocks like shale under high CP is more like metals. He modified the Ernst and Merchant (1941) model which was for metal cuttings including the cutter balling and bit body effects on cutter forces under CP (Rahmani, 2013). For a sharp cutter, they added the effect of friction force on the shear plane to the Ernst and Merchant model (1941). The friction

angle between the cutting and intact rock at the shear plane was assumed equal to the rock internal friction angle. Rahmani (2013) included the effect of CP on cutter tangential force by taking the shear plane area and bottom hole pressure into account. Detournay and Defourny in 1992 assumed that the total forces on cutter are the product of two uncoupled forces, one on cutter face and another on cutter wear flat area. Rahmani (2013) took the same assumption and developed a model for blunt cutters. Rahmani (2013) hypothesized that the proportion of maximum normal force to the wear flat area should not be greater than rock confined compressive strength. In addition, the contact area friction between wear flat and rock is equal to the rock internal friction angle due to broken rock adherence to the cutter wear flat area. Such an assumption for the wear flat area friction coefficient is valid, based on the Dagrain and Richard (2006) observations for carbonate rocks.

Rahmani (2013) verified his model for three different rocks including Catoosa shale, MS, and Carthage limestone using single test data. The Rahmani single cutter model did not account for the effect of the chamfer on cutter axial and tangential forces explicitly. Rahmani (2013) included the chamfer effect by calculating an average BR angle from the tip of the chamfer to the rock surface.

2.2.9 Carrapatoso et al. (2015) Model

The effect of cutter chamfer geometry, cutter BR, and cutter aggressiveness on a single cutter were studied using numerical modeling (Carrapatoso et al., 2015). They applied discrete element modeling (DEM) and finite element modeling (FEM) to simulate the effect of cutter BR and cutter chamfer on cutting efficiency in Carbonate Rocks. The mechanical specific energy (MSE) was used as a criteria for measuring the cutter efficiency. As defined by Teale in 1965 (Teale, 1965), the MSE is the amount of work that should be carried out to excavate unit volume of rock. The cutter aggressiveness was defined as the slope of a tangential force to axial cutter force components. It was found that decreasing the chamfer size increases the cutter aggressiveness, which correlated to a higher penetration rate. Carrapatoso's simulations also showed that the cutter aggressiveness is not sensitive to cutter BR. They

found that the cutter MSE altered slightly with changing in cutter chamfer size. Therefore, the cutter chamfer should not decrease the cutting efficiency in conducted experiments. The simulation done by Carrapatoso et. al. did not take the effect of cutter vertical velocity on cutter performance into account. They mentioned that the effect of cutter vertical velocity should be studied separately as it happens experimentally.

2.2.10 Cheng et al. (2018) Model

In most of the previous single cutter models, the shape of the failure surface was assumed to be a straight line. Therefore, all the equilibrium force equations are developed based on straight failure surface, which imposes error to the models. In addition, the number of models that take the hydrostatic pressure effect on cutting procedure into account, are limited. The bottom hole hydrostatic pressure affects the cutting force and mechanical specific energy, which consequently reduces the drilling efficiency (Cheng et al., 2018). Cheng et al. (2018) solved the cutting forces by taking the in-situ stress, pore pressure, and hydrostatic pressure into account to develop a new single cutter model. Cheng et al. (2018) found the shear failure surface for different depth of cuts, BR, and cohesion strengths, through connecting the maximum shear stress points predicted by the model. They found that the failure surface is a curved line instead of a straight line, and this was a significant part of their model. The failure surface shape was confirmed using 3D surface topography for granite cuts.

2.3 Statistical Models

The application of statistical models such as Artificial Neural Network (ANN) in drilling ROP simulation and optimization is well established in the literature (Arehart et al., 1989; Mohaghegh et al., 1995; Karri, 1999; Dashevskiy et al., 1999; Fruhwirth et al., 2006; Marana et al., 2010; Ashrafi et al., 2018).

Bilgesu et al. (1997) applied the ANN to their drilling data to find complex patterns such as WOB, RPM, mud flow rate, formation hardness, and the bit type. They used a simulator to generate drilling data to eliminate errors coherent to field measurements. The validity of the trained ANN was demonstrated with data from the existing field as well as from the drilling simulator.

Gidh et al. (2012) applied ANN for real-time drilling optimization. They benefited from the huge drilling record database (DRB) and geographical bit data filters to find pertinent offset wells. The database includes more than 3 million bit runs and was initiated in 1985. The DRB user interface was used to filter the data and to identify the offset wells that had used the same bit. A rock strength software was used to determine the formation's rock strength and abrasiveness, and to identify the bit that possesses the appropriate combination of durability, gauge protection, and hydraulic configuration. Their ANN system learned how the bit drills and wears out in any similar formation. The trained ANN then was applied to offer the best combination of WOB, RPM, and flow rate to reduce the drilling cost. They reported three days saving in an 8 ½ inch hole section using their new system.

Ashrafi et al. (2018) applied a hybrid artificial neural network for ROP estimation. They used 1000 data points collected from mud logging and petrophysical logs and applied four metaheuristic algorithms including Particle Swarm Algorithm (PSO), Genetic Algorithm (GA), biogeography-based optimizer (BBO), and imperialist competitive algorithm (ICA) to find the ANN parameters. The WOB, RPM, pump flow rate, pump pressure, pore pressure, gamma-ray, density log, and shear wave velocity were selected as ANN input parameters.

Hegde and Gray (2018) estimated the ROP using four input parameters including WOB, flow-rate, RPM, and rock strength. Ashrafi et al. (2018) developed their ANN model by taking parameters such as pump pressure, gamma ray, pore pressure, and shear wave velocity as input.

The very first and most common mistake in applying machine learning algorithms (i.e. ANN, Random forest) in the literature is picking up the wrong input parameters for ROP prediction. The machine

learning (ML) algorithms can take any number of arrays of input parameters and map them to one or more than one output no matter what those parameters are. From a drilling engineer's point of view, selecting drilling depth, pump pressure, flow rate, IADC code, drilling torque, plastic viscosity, standpipe pressure, shear wave velocity, and flow-rate are not correct for ROP estimation, although they have may an effect on ROP in some cases (Soares and Gray, 2018; Hegde and Gray, 2018; Elkatatny et al, 2017; Amer et al, 2017; Hegde et al, 2017). The ML algorithms structure (i.e. ANN number of layers and number of inputs) can be expanded to fit any size of data with any accuracy which can be misleading.

Conducting sensitivity analysis is one common step to evaluate the accuracy and performance of models (either analytical, numerical or statistical). The ML algorithms usually fail the sensitivity analysis since they do not comply with solid mathematical equations for their simulation as analytical models do. For instance, the ANN is composed of a 1D or 2D network which is inspired by the biological brain. The function is defined in the nodes and the model constants are found using iterative search algorithms. Depending on the number, type and arrangement of layers, functions that are applied to the network, and the arrangement of layers, different types of networks with different functionalities are obtained (i.e. ANN, RNN, and CNN).

Overfitting the ML algorithm is very common. Overfitting means that although the model error on training data is small, the model error on newly introduced data, unseen during training, is high. Overfitting happens either when the training set contains noisy instances, or the training instances are not a good representative of the instances' space. Both of these situations are common in real-life application (Hindi and Alakhras, 2009).

During the overfitting, the ML parameters and functions are changed in a way to mimic the training data, and therefore the model accuracy for training data would be high. This could be the potential reason that some of the statistical ROP models in the literature reported high accuracy.

The machine learning (ML) algorithms need a huge amount of data and strongly rely on that. A trained network for a ROP estimation is applicable just for that field and is barely applicable for other formations. The ML algorithms rely on data and because of that their accuracy and performance will be affected by feeding bad data (i.e. noise in data).

The independent parameters should be selected and separated and used as input to machine learning algorithms (i.e. ANN, random forest, etc.). This requires the user to have a deep understanding of drilling procedure and details of the mechanism involved underneath the bit.

The ML algorithms have a huge application in other domains such as image recognition (Deep Neural Network), Natural Language Processing (NLP), anomaly detection, autonomous driving vehicles, etc, however, it is not suggested in drilling ROP modeling due to above-mentioned insufficiencies.

2.4 Interfacial friction angle (IFA)

The relative movement between the cutter face and cutting suggests the existence of a friction force at the cutter face, which is known as interfacial friction. The normal element of interfacial friction on the cutter face is upward, which reduces the effective normal force on the cutter, and consequently reduces the cutter depth of cut. Therefore, to achieve an accurate PDC ROP estimation, it is necessary to have an accurate estimation of interfacial friction. The effect of different factors such as cutter size, cutter chamfer, cutter BR, cutter wear flat area, cutter face characteristics, rock properties, cutter normal force, rock saturation, and drilling fluids on cutter forces and interfacial friction angle (ψ or IFA) were investigated by several authors (Smith, 1955; Smith et al., 2002; Kuru and Wojtonowicz, 1992; Smith, 1998; Richard, 1999; Haung, 1999; Rahmani, 2013; Akbari et al. 2014).

Experiments have shown that the interfacial friction angle (ψ) is lower for polished cutters, compared to the standard ones (Smith, 1955; Smith et al., 2002). Polishing the cutter face area reduces the surface roughness, which consequently decreases the coefficient of friction. Smith et al. (2002) conducted a

direct interfacial friction test and found that the interfacial friction angle for Twin Creek Siltstone was higher compared to the Catoosa shale (Rahmani, 2013). Also, they found that the rock saturation and drilling fluid type (oil or water) slightly affected the interfacial friction coefficient. Kuru and Wojtonowicz (1992) investigated the effect of drilling fluidtype on the friction coefficient for Nugget sandstone, MS, and BSS. They found that the friction coefficient is higher for Nugget sandstone and MS in oil-based mud, while for BSS, higher friction coefficient showed up in water-based mud. Hibbs, in 1983, found that the cutter velocity slightly affects the friction coefficient.

The single cutter tests have shown that in Anhydrite, Coal, and sandstone, the bigger the wear flat area is, the greater the friction coefficient and lower normal stress at wear flat (Rahmani, 2013). In contrast, the friction coefficient in carbonates remains independent of wear flat roughness due to materials sticking to the wear flat area. This, however, causes rock grain sliding friction rather than cutter wear flat on the rock (Dagrain and Richard, 2006). Rahmani conducted triaxial compressive strength tests on 20 different rocks and found that the friction angle underneath the cutter is well correlated with the internal friction angle of the rock.

Coudyzer and Richard (2005) studied the influence of BR and SR angles on both the magnitude and orientation of the cutter cutting force. They observed that the cutter cutting force is strongly affected by the BR angle, while the SR angle has almost no effect. They found that force inclination varies strongly with the cutter orientation, indicating that force angle cannot be viewed as a simple interfacial friction angle as commonly accepted in the literature. It is also well documented in the literature that the BR drastically affects the angle between the normal to the cutter face and the force vector (ψ) (Nishimatsu, 1972; Richard, 1999; Akbari et al., 2014; Rostamsowlat et al., 2018). Therefore, ψ is not a measure of interfacial friction angle between the rock and cutter face, as it is often considered in the literature, and a more complex failure mechanism must be considered (Coudyzer and Richard, 2005). Coudyzer and Richard (2005) argued that there is a build-up edge of crushed material on the cutting face that controls the failed materials in such a way that the angle between force and velocity is

unaffected. They observed that ψ, varies rapidly with BR, while ψ + BR is slowly decreased versus depth of cut (DOC). They concluded that the angle between the force vector and normal to the cutter face (ψ) cannot be considered as a measurement of the interfacial friction angle between the rock and cutter face.

Akbari et al. (2014) investigated the effect of cutter size, chamfer geometry, and BR angle on PDC cutter friction for Carthage marble rock. They found that the interfacial friction angle decreases by increasing the cutter BR angle, which is in accordance with previous works (Smith, 1998; Richard, 1999; Haung, 1999). They hypothesized that at low cutter BR angles, the flow of broken rock in front of the cutter face is upward, which introduces an upward tangential frictional force to the cutter surface. Increasing the cutter BR angle results in a backward flow of a portion of broken rock that introduces another tangential frictional force downward on the cutter face, which consequently, reduces the apparent friction force. They concluded that the effect of cutter size on cutter frictional response is insignificant. Akbari et al. (2014) concluded that the chamfer size increases the normal force on the cutter for the same depth of cut, while it does not change the cutter tangential force response.

Rostamsowlat et al. (2018) performed a comprehensive set of cutting experiments on a wide range of rock samples (Limestone and sandstone). They found that the intrinsic energy is in good agreement with rock UCS when the cutter is positioned at BR angle between five to twenty degrees. They observed that the interfacial friction angle is independent of the depth of cut for a given BR angle, which was also reported by other researchers (Richard and Dagrain, 2012; Richard, 1999). It was observed that the decrease in interfacial friction angle versus BR, follows a universal trend and is independent of rock type.

2.5 Optimization works

Once the ROP is expressed through a mathematical Equation, the next step is to find the global minimum or maximum of such equation, so-called optimization. Drilling cost optimization has always been one of the major interests of researchers in petroleum engineering. Researchers have taken different approaches for drilling optimization, which are provided and discussed in the following sections.

2.5.1 Speer (1958)

Speer (1958) developed an optimization method to reduce the drilling cost by finding the best combination of WOB, RPM, and hydraulics. How WOB, RPM, and hydraulics affect the ROP, what the upper limits are for these parameters, the interrelation between these three parameters in different formations, and their combination that results in lower drilling cost, were answered by Speer. Speer (1958) established five empirical models to show the relationship between WOB, RPM, hydraulic horsepower, and ROP. These models combined into a chart to determine the optimum drilling techniques from field data. He found that there is a direct relation between ROP and WOB for a rock if sufficient bottom cleaning is maintained. The optimum WOB has an inverse relation with the formation drillability, the optimum RPM varies inversely with WOB, and the ROP varies in direct proportion with RPM under laboratory tests. The ROP varies inversely with RPM under field operation, in other words, the response of ROP to increase in RPM decreases as rotary speed increases (Speer, 1958). In addition, the optimum RPM which results in the lowest cost varies inversely with the WOB. The optimal combination of drilling scenarios could be determined using charts proposed by Speer.

2.5.2 Graham and Muench (1959)

In 1959, Graham and Muench developed an optimization approach to find the best WOB and RPM to reduce the total drilling cost. Their cost function included the cost of the rig for both drilling and tripping, along with the cost of the bit. Graham and Muench (1959) assumed that the bit life for rollercone is limited by bearing failure and the WOB is not limited by considerations such as hole deviation and hydraulics. Higher WOB or higher RPM improved the ROP and reduced the drilling cost, but they can decrease the bit life and increase the drilling cost by adding the bit and tripping expenses. Therefore, they performed a mathematical analysis to find whether or not a change in WOB or RPM would reduce the drilling costs. It was concluded that for any drilling condition, there is an optimum combination of WOB and RPM which minimizes the total drilling cost. They found that the optimum combination of WOB and RPM that decreases the overall drilling time can be achieved by varying a constant RPM iteratively while calculating the cost at various depths. The optimum combination of WOB and RPM are dependent on rig cost and bit bearing life.

2.5.3 Galle and Woods (1963)

In 1963, Galle and Woods developed a graphical method for drilling optimization. Their procedure can be used for determining the best combination of constant WOB and RPM, the best WOB for any RPM, and the best RPM for any WOB. An optimization approach based on the best combination of WOB and RPM is useful when the rig flexibility permits the use of any WOB and RPM. Optimization based on the best constant WOB for any RPM is useful when the rig limitations or vibration problems dictate the RPM that must be used. Lastly, optimization based on the best constant RPM for any WOB is required when the crooked-hole conditions or a limited number of drill collars dictate the maximum applicable WOB. For each of these three optimization approaches, the limiting effect of teeth, bearings, and drilling rate on bit life was considered separately. Galle and Woods (1963) established mathematical relations to achieve the best WOB and RPM for the lowest drilling cost. They also developed graphs

and procedures to determine the best combination of constant WOB and RPM, the best constant WOB for any RPM, and the best constant RPM for any given WOB. Using their graphs, one can calculate the drilling cost, footages, time, and condition of teeth and bearings of the dull bit. Their graphs and charts were applicable for rolling cutter rock bits and a wide variety of formations. The field tests demonstrated the application of their new optimization method.

2.5.4 Reed et al. (1972)

Reed et al. (1972) used the Monte Carlo vibrational approach to obtain the optimum WOB and RPM. In this method, a random path for a solution is initialized and the cost is calculated. In the next step, an iterative method is introduced by selecting random numbers for every point along the path. The new generated paths are evaluated and are kept if the cost is less than the original; however, if the cost is higher, the point is given a new random number. This process is repeated until either number of an iteration is achieved or a convergence criteria is satisfied. In general, it is difficult to place great confidence in the existing drilling equations which are a base for drilling optimization. If the drilling equations were developed based on field experience, the overwhelming variety of problems that can occur would cause certain doubts. On the other hand, if the equations were established based on the laboratory data, then one can question if the essential field conditions have been modeled or simulated properly. Another inconsistency in optimization analysis comes from the parameters that are fed into the drilling equations. Many tests conducted in the field indicate that formation variability makes it difficult to study the effect of different parameters on drilling rate.

This inconsistency is made greater by the fact that parameters are estimated on one well, whereas drilling is optimized on another one. Reed et al. (1972) concluded that despite above-mentioned inadequacy and imperfections, the results of the optimization method are still valuable.

2.5.5 Bourgoyne and Young (1974)

Bourgoyne and Young (1974) conducted a study to find the optimal drilling parameters. They incorporated the effect of formation properties, compaction, differential pressure, bit diameter, WOB, RPM, bit teeth wear, and bit hydraulics, and established a ROP model for roller-type rock bits. The ROP model coefficients were obtained by conducting multiple regression analysis on detailed drilling data. The optimization was performed on the ROP model by finding the optimum WOB, RPM, and the bit hydraulics. Bourgoyne and Young (1974) expressed the drilling cost as a function of bit cost, hourly rig cost, trip time, connection time, drilling time, and footage drilled. They derived optimization equations from drilling models and used them for the optimization procedure. The risk factors such as hole deviation problems, bit balling, mud type, percent solids, hole washout, and variable pump costs were ignored in their study. Bourgoyne and Young (1974) optimization model in most cases has shown a considerable reduction in drilling cost between a few percent to 30 percent. The optimized WOB and RPM are very sensitive to the regression constants. Therefore, model coefficients should be corrected with newly gained data from the field, to improve the optimization accuracy.

2.5.6 Maidla and Ohara (1991)

Maidla and Ohara (1991) applied dimensional analysis and developed a new ROP model by considering the effect of rock compressive strength, formation strength, compaction, differential pressure, WOB, RPM, tooth wear, and bit hydraulics. The major difference between their model and the Bourgoyne and Young (1974) model was the effect of formation compressive strength. Multiple regression analysis was used to find the coefficients for both models. Both models were checked with the data in two ways. The ROP was calculated using the model with the coefficients found for that well and was then compared with the actual recorded data for the same well. The data from the previous well was used to find the model coefficients for each lithology. These coefficients were averaged considering the distance from each well to the one to be predicted and its respective lithology thickness. Maidla and

Ohara (1991) developed a computer program for simultaneous selection of a roller-cutter bit, bit bearing, WOB, and drill string rotation to minimize the drilling cost. Their computer program uses the drilling cost function to find the best WOB and RPM for a given situation. The computer program can be modified to print out iso-cost and iso-ROP graphs for cost-effective drilling.

2.5.7 Rampersad at al. (1994)

Rampersad et.al. (1994) developed a Geological Drilling Log (GDL) for drilling optimization using the information obtained while drilling an oil or gas well. The drilling models are used to create a GDL for the entire drilling section. The GDL is created by inversion of drilling ROP models specific to the bits used for drilling each interval. The method for optimization is to achieve the GDL using the data from the field. The calculated GDL along with the ROP model are used for drilling simulation and cost analysis. Numerous simulations are conducted to achieve the lowest drilling cost, and the optimum drilling parameters are calculated utilizing the learning curve concept. Rampersad et.al. (1994) used a GDL to select the bits (Tricone or Natural Diamond) and operating conditions properly for a drilling interval. They concluded that the new drilling optimization approach can be used for any pre-planned well or post-analysis of wells to minimize the drilling cost. In addition, the GDL approach provides certain answers to the drilling engineers and provides guidelines and well-founded conclusions.

2.5.8 Rommetveit et al. (2004)

In 2004, Rommetveit et al. (2004) proposed Drilltronics, which was new drilling automation and monitoring system. Drilltronics used all available surface and subsurface data for drilling simulation and optimization. The system is composed of several elements including software modeling with algorithms that reflect the wellbore behavior, real-time drilling data which are logged from at high acquisition rate, real-time diagnosis of drilling problems, and a drilling simulator. The Drilltronics modules include hole cleaning, downhole pressure, tripping, torque and drag, stick-slip prevention, bit

load optimization, integrated drilling simulator, data quality improvement, system monitoring, and control. The bit load optimization module's purpose is to determine the optimum WOB and RPM on a bit. This system modulates the WOB and RPM and observes the changes in ROP. The effect of mud rheology and pore pressure were included by taking the pump rate and standpipe pressure into account. Rommetveit et al. (2004) incorporated the effect of bit wear on ROP by including a bit wear function in the bit load optimization module. It is also possible to use the module in automatic mode for real-time simulation and optimization purposes. They increased the rate of penetration by 15% to 30% by preventing the stick-slip by means of activating a stick-slip prevention module.

2.5.9 Dupriest and Koederitz (2005)

In 2005, Dupriest and Koederitz used the mechanical specific energy (MSE) concept for drilling optimization. The MSE monitoring provides the ability for continuous detection of inefficiency in a drilling system. They used the MSE surveillance to find the founder point which enables the system to optimize the ROP. The MSE quantifies the relationship between the amount of input energy and ROP (Dupriest and Koederitz, 2005). Teal, in 1965, found that the MSE values are numerically equal to rock compressive strength in the lab (Teal, 1965). Therefore, the MSE concept can be used as a reference point for drilling efficiency. The bit is efficient when the MSE values are close to the rock confined compressive strength. Dupriest and Koederitz (2005) were able to improve the drilling efficiency through recognizing the bit and bottom hole assembly (BHA) balling via monitoring the MSE. They also found that recognizing the vibrational founder that reduces drilling efficiency, is far more difficult to address since fundamental redesign in other features is required.

2.5.10 Hareland et al. (2007)

Hareland et al. (2007) applied a simulator for drilling optimization to more than 50 wells in Western Canada. The main objective was to reduce the drilling cost and time and improve drilling efficiency.

The simulator generates the rock strength using the drilling data which is obtained from the optimization of nearby wells. By extending the rock strength to adjacent wells, the optimum drilling scenarios were obtained in terms of WOB, RPM, bit types, and pull-out depths. The simulator results matched well with the actual field ROP data, as well as with drilling time and costs. They achieved an average of 15% to 20% reduction in drilling cost by applying the simulator results.

2.5.11 Eren and Ozbayoglu (2010)

In 2010, Eren and Ozbayoglu applied a multiple regression method for drilling optimization. They adopted the Bourgoyne and Young (1974) ROP model and used multiple regression to obtain a set of coefficients representing the drilling data gathered. They found that the drilling rate of penetration can be modeled in a real-time environment as a function of independent parameters such as WOB, RPM, mud weight, and formation details. In order to conduct real-time optimization, the real-time data was fed to a central computer. The central computer program uses real-time data and calculates the new ROP model constants. They determined the optimum drilling parameters by taking the new model constants into account. The aim was to find the WOB and RPM for a drilling interval in order to reduce the drilling cost per foot. Eren and Ozbayoglu found that the data quality is very important for real-time drilling optimization. Another important point is the wellbore inclination consideration in the analysis. They used the normalized WOB and obtained higher accuracy for ROP prediction, which consequently resulted in more precise optimization designs.

2.5.12 Hamrick (2011)

In 2011, Hamrick used a mechanical specific energy (MSE) approach for drilling optimization. The MSE is the work that is needed for destroying the unit volume of rock. Hamrick analyzed the MSE to obtain the optimal drilling parameters including WOB and RPM. The parameters that are used for calculating the conventional MSE are interdependent. Hamrick (2011) established a mathematical

relationship between parameters and rewrote the MSE equation in terms of one independent parameter (i.e. WOB). The new MSE form, based on a single independent parameter, can be minimized mathematically. Once the optimum WOB was obtained, the other parameters (torque and penetration per revolution) were calculated based on the interdependent relationship. He used the first derivation of the MSE Equation and minimized the MSE to achieve the optimum WOB. Having the optimum WOB, the optimum torque and penetration per revolution could be determined using the developed mathematical relationship.

2.5.13 Hankins et al. (2014)

Hankins et al. (2014) applied the Hareland and Rampersad PDC ROP model (1994) for drilling optimization purposes. They rearranged the ROP model to calculate the rock strength from drilling data. The calculated rock strength was used to simulate the nearby well ROP. Once simulation results were validated, the optimum drilling parameters including WOB, RPM, hydraulics, and bit specification were found.

CHAPTER III

PDC ROP MODELING

In this chapter, the contact area equations for sharp and blunt cutters are presented. The contact area of a cutter is used for calculating the cutter front area, which later is used for ROP estimation. The single cutter interfacial friction angle (ψ) (IFA) model is developed by taking cutter depth of cut, cutter velocity, and rock unconfined compressive strength into account. The single cutter force model is developed by incorporating the cutter contact areas and the IFA model for sharp cutters. The single cutter force model for a blunt cutter includes the effect of cutter wear flat area and interfacial friction angle (IFA). The new PDC blunt single cutter model takes the effects of essential parameters such as BR and SR angles, cutter size, cutter PDC layer thickness, cutter quality and wear flat area of both the stud and PDC layer into account. A full bit IFA model is developed similar to the single cutter IFA model however the constants are found utilizing the full bit data. The full bit IFA model is solved in the new ROP model to incorporate the effect of IFA and improve the accuracy of the ROP model. A new ROP model for PDC bits is introduced in which the volume of cut per revolution is calculated for a single cutter and is extrapolated to the cutting face of the bit, to achieve the total cutting volume that is cut from the formation. Previous PDC ROP models suffer from shortcomings such as deficient wear function model, ignoring the effect of wear flat areas (both stud and PDC wear flat areas), ignoring the effect of IFA, and ignoring the orientation and geometry of the cutter.

3.1 PDC single cutter contact area calculation

The depth that a cutter penetrates into the rock, along its normal direction is known as depth of cut (DOC). The depth of cut is a function of cutter normal force, rock strength, and the area beneath the cutter. For a blunt cutter, the area beneath the cutter includes the area beneath the cutter face (A_h in Figure 3.1) and wear flat area (C-E in Figure 3.2), while for a sharp cutter it is only the area beneath the cutter face (A_h in Figure 3.1). In the following pages, the contact area equations for both sharp and blunt cutters are presented. The cutter front area (A_v) is then calculated by taking the cutter contact area ($A_{contact}$) and cutter BR angle into account.

3.1.1 PDC single cutter model contact area equation for sharp cutter

In general, it is assumed that the cutter penetrates into the rock until the normal stress beneath the cutter face (A_h), satisfies the rock strength. The required area beneath the cutter face (A_h) is calculated by dividing the cutter normal force into the rock strength. The area in front of the cutter (A_v) and the cutter-rock contact area ($A_{contact}$) can be back-calculated by taking the A_h and cutter BR angle into account. It is worth mentioning here that the A_v is known as the area of cut (A_{cut}) in the literature. The $A_{contact}$, which is known as a circle segment area in geometry, is a function of the depth of cut (DOC), and is provided in Equation 3.1. The cutter depth of cut (in Equation 3.1) can be found by taking both $A_{contact}$, D_c, and cutter BR angle into account. A schematic of a sharp (unworn) single PDC cutter is provided in Figure 3.1.

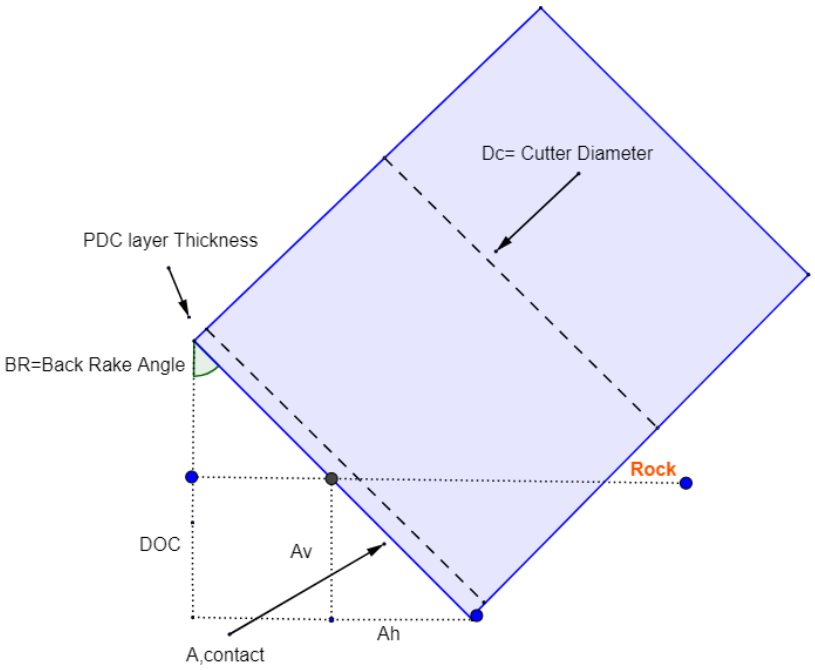

Figure 3.1. A schematic of a sharp PDC cutter and its associated areas

$$A_{contact} = \left(\frac{D_c}{2}\right)^2 \times \cos^{-1}\left(\frac{\frac{D_c}{2} - \frac{DOC}{\cos(BR)}}{\frac{D_c}{2}}\right) - \left(\frac{D_c}{2} - \frac{DOC}{\cos(BR)}\right) \times \sqrt{D_c \times \frac{DOC}{\cos(BR)} - \left(\frac{DOC}{\cos(BR)}\right)^2} \quad \ldots\ldots\ldots \text{Eq. 3.1}$$

The derivation or the equation of $A_{contact}$ are provided in Appendix A.

3.1.2 PDC single cutter contact area equation for blunt cutter

A schematic of a blunt cutter with bit grade equal to BG is seen in Figure 3.2 (see Appendix A section A.1.3) (Winters et al., 1987 a).

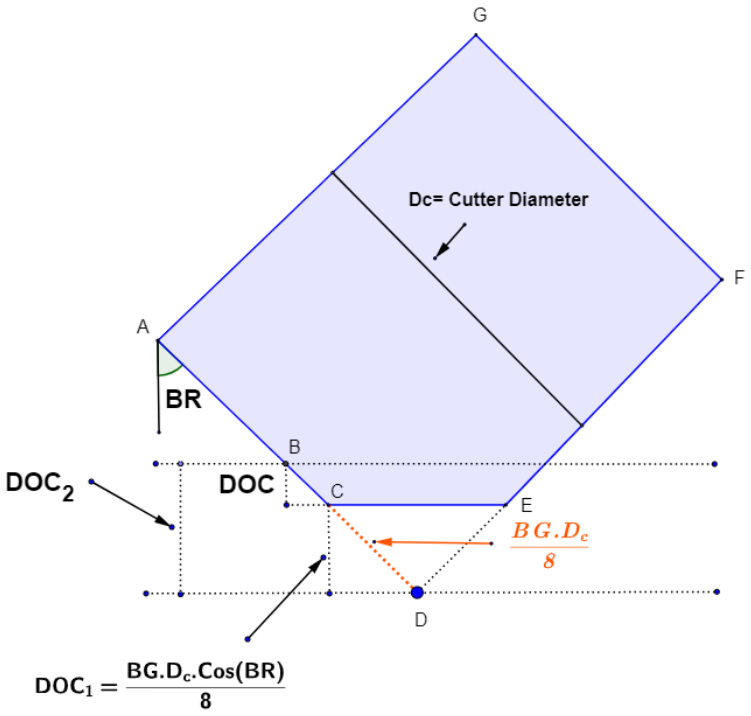

Figure 3.2. A schematic of a blunt cutter and the associated areas

The blunt cutter contact area (BC in Figure 3.2), is achieved by subtracting the area of BD from the area of CD in Figure 3.2. Therefore, the contact area of a sharp cutter in Figure 3.2 (ADFG) with two depth of cuts equal to DOC_2 and DOC_1 respectively, are calculated using Equation 3.1 and subtracted to achieve the blunt cutter contact area. The DOC_2 equation is provided at the following (see Equation A.44 in Appendix A).

$$DOC_2 = DOC + \frac{BG \times D_c \times \cos(BR)}{8} \quad \ldots\ldots\ldots \text{Eq. } 3.2$$

For a blunt cutter, Equation 3.1 is turned into a general form of Equation 3.3 by taking Equation 3.2 into account (see section A.1.3 and A.2.2 for details).

$$A_{contact} = \left[\left(\frac{D_c}{2}\right)^2 . \cos^{-1}\left(\frac{\frac{D_c}{2} - \left(\frac{\left(DOC + \frac{BG \times D_c \times \cos(BR)}{8}\right)}{\cos(BR)} \right)}{\frac{D_c}{2}} \right) - \left(\frac{D_c}{2} - \left(\frac{\left(DOC + \frac{BG \times D_c \times \cos(BR)}{8}\right)}{\cos(BR)} \right) \right) . \sqrt{2.\left(\frac{D_c}{2}\right).\left(\frac{\left(DOC + \frac{BG \times D_c \times \cos(BR)}{8}\right)}{\cos(BR)} \right) - \left(\frac{\left(DOC + \frac{BG \times D_c \times \cos(BR)}{8}\right)}{\cos(BR)} \right)^2} \right] - \left[\left(\frac{D_c}{2}\right)^2 . \cos^{-1}\left(\frac{\frac{D_c}{2} - \left(\frac{BG.D_c}{8}\right)}{\frac{D_c}{2}} \right) - \left(\frac{D_c}{2} - \left(\frac{BG.D_c}{8}\right) \right) . \sqrt{2.\left(\frac{D_c}{2}\right).\left(\frac{BG.D_c}{8}\right) - \left(\frac{BG.D_c}{8}\right)^2} \right] \quad \ldots\ldots\ldots \text{Eq. 3.3}$$

3.2 Depth of cut calculation

Two parameters ($\mathcal{A}_1$ and $\mathcal{A}_2$) are defined as follows and are used to calculate the depth of cut. $\mathcal{A}_1$ is the theoretically calculated area beneath the cutter and is calculated using Equation 3.4. $\mathcal{A}_1$ should be used to achieve force balance between weight on cutter (downward) and the rock reaction (upward) force. In Equation 3.4, the WOB is in lbf, RS is rock strength in psi, and N_c is the number of cutters. The RS can be either unconfined compressive strength or confined compressive strength (CCS) depending on drilling conditions.

$$\frac{\frac{WOB}{N_c}}{RS} = \mathcal{A}_1 \quad \ldots\ldots\ldots \text{Eq. 3.4}$$

The stud material wear coefficient is lower than of the PDC layer, and because of that, it wears faster and causes less contact area. Therefore, 100% ideal contact area between stud and rock is not expected.

Ignoring the efficiency of stud wear flat area may cause error in ROP estimation. The weight on the cutter is turned into the depth of cut by taking the area beneath the cutter into account. Therefore, ignoring the stud wear flat area efficiency causes overestimating of the area beneath the cutter, which results in underestimating the depth of cut. Underestimating the depth of cut resulted in underestimation for ROP. The new model takes the efficiency of stud wear flat area into account to provide a realistic estimation of ROP.

$\mathcal{A}_2$ is the weighted area beneath the cutter and is a summation of the weighted wear flat area (A_w') and area beneath the cutter face (A_h). $\mathcal{A}_2$ is calculated using Equation 3.5 and should attain a sum equal or close to $\mathcal{A}_1$ by adjusting the depth of cut (DOC) value. The DOC is reported as a cutter depth of cut.

$$\mathcal{A}_2 = A_w' + A_h \ldots\ldots \text{Eq. } 3.5$$

A_w' is the weighted wear flat area and is calculated using Equation 3.6. The cutter wear flat area includes the stud and PDC wear flat areas. The stud material has lower wearing resistance compared to the PDC layer, and because of that, it wears faster. Therefore, there is not 100% contact between the stud wear flat area ($A_{w,stud}$) and rock during drilling to compare to the PDC layer wear flat area ($A_{w,PDC}$). ω_1 and ω_2 are PDC layer and stud wear flat areas efficiency. The efficiency of stud wear flat area (ω_2) is determined through lab experiments.

$$A_w' = \omega_1 . A_{w,PDC} + \omega_2 . A_{w,stud} \ldots\ldots \text{Eq. } 3.6$$

The total wear flat area (A_w), PDC layer wear flat area ($A_{w,PDC}$), and the stud wear flat area ($A_{w,stud}$) are calculated using Equation 3.7, 3.8, and 3.9. Note that for a sharp cutter, there is no wear flat area and $\mathcal{A}_2$ in Equation 3.5 and is equal to the area beneath the cutter face (A_h).

$$A_w = \left(\frac{\left(\frac{Dc}{2}\right)^2}{2} \left(\sin^{-1} \left(\frac{\left(\frac{\left(\frac{BG.\,D_c.\,Cos(BR)}{8}\right)}{Sin(90-BR)} \right) - \frac{Dc}{2}}{\left(\frac{Dc}{2}\right)} \right) + \frac{\left(\frac{\left(\frac{BG.\,D_c.\,Cos(BR)}{8}\right)}{Sin(90-BR)} - \frac{Dc}{2} \right) \sqrt{2\left(\frac{Dc}{2}\right)\left(\frac{\left(\frac{BG.\,D_c.\,Cos(BR)}{8}\right)}{Sin(90-BR)} \right) - \left(\frac{\left(\frac{BG.\,D_c.\,Cos(BR)}{8}\right)}{Sin(90-BR)} \right)^2}}{\left(\frac{Dc}{2}\right)^2} \right) \right) \times \frac{2}{Cos(90-BR)} \quad \ldots\ldots\ldots \text{Eq. 3.7}$$

$$A_{w,PDC} = \left(\left(\frac{\left(\frac{Dc}{2}\right)^2}{2} \left(\sin^{-1} \left(\frac{\left(\frac{\left(\frac{BG.\,D_c.\,Cos(BR)}{8}\right)}{Sin(90-BR)} \right) - \frac{Dc}{2}}{\left(\frac{Dc}{2}\right)} \right) + \frac{\left(\frac{\left(\frac{BG.\,D_c.\,Cos(BR)}{8}\right)}{Sin(90-BR)} - \frac{Dc}{2} \right) \sqrt{2\left(\frac{Dc}{2}\right)\left(\frac{\left(\frac{BG.\,D_c.\,Cos(BR)}{8}\right)}{Sin(90-BR)} \right) - \left(\frac{\left(\frac{BG.\,D_c.\,Cos(BR)}{8}\right)}{Sin(90-BR)} \right)^2}}{\left(\frac{Dc}{2}\right)^2} \right) \right) - \left(\frac{\left(\frac{Dc}{2}\right)^2}{2} \left(\sin^{-1} \left(\frac{\left(\frac{\left(\frac{BG.\,D_c.\,Cos(BR)}{8}\right) - t_{PDC}.\,Cos(90-BR)}{Sin\theta} \right) - \frac{Dc}{2}}{\left(\frac{Dc}{2}\right)} \right) + \frac{\left(\frac{\left(\frac{BG.\,D_c.\,Cos(BR)}{8}\right) - t_{PDC}.\,Cos(90-BR)}{Sin(90-BR)} - \frac{Dc}{2} \right) \sqrt{2\left(\frac{Dc}{2}\right)\left(\frac{\left(\frac{BG.\,D_c.\,Cos(BR)}{8}\right) - t_{PDC}.\,Cos(90-BR)}{Sin(90-BR)} \right) - \left(\frac{\left(\frac{BG.\,D_c.\,Cos(BR)}{8}\right) - t_{PDC}.\,Cos(90-BR)}{Sin(90-BR)} \right)^2}}{\left(\frac{Dc}{2}\right)^2} \right) \right) \right) \times \frac{2}{Cos(90-BR)} \quad \ldots\ldots\ldots \text{Eq. 3.8}$$

$$A_{w,Stud} = A_w - A_{w,PDC} \quad \ldots\ldots\ldots \text{Eq. 3.9}$$

The area of the cutter face that is in contact with the rock is the cutter contact area ($A_{contact}$) which is calculated using Equation 3.1 or 3.3 depending on the bit grade.

The cutter contact area ($A_{contact}$) is turned into the area beneath the cutter face (A_h) by taking the cutter BR into account (Equation 3.10).

$$A_h = A_{contact}.\,Sin(BR) \quad \ldots\ldots\ldots \text{Eq. } 3.10$$

Figure 3.3, shows the different areas including stud wear flat area ($A_{w,stud}$), PDC wear flat area ($A_{w,PDC}$), total wear flat area (A_w), cutter contact area ($A_{contact}$), the area in front of cutter face (A_v), and the area beneath the cutter face (A_h).

Two parameters, DOC and BG are needed to estimate the PDC bit rate of penetration. The DOC is increased from zero continuously, and the following sequences of calculations are performed until the weighted area beneath the cutter ($\mathcal{A}_2$) in Equation 3.5 becomes close enough or equal to the theoretically calculated area beneath the cutter ($\mathcal{A}_1$) in Equation 3.4. Each time the DOC in conjunction with BG is used to calculate the cutter contact area ($A_{contact}$) in Equation 3.1 or 3.3 (depending on BG), it gives the area beneath the cutter face (A_h) using Equation 3.10. The area beneath the cutter face (A_h) is used in conjunction with the weighted wear flat area (A_W') in Equation 3.6, to calculate the weighted area beneath the cutter ($\mathcal{A}_2$) using Equation 3.5. The depth of cut is accepted once the difference between $\mathcal{A}_2$ and $\mathcal{A}_1$ is achieved within a tolerance.

Once the DOC is achieved, the cutter contact area ($A_{contact}$) is calculated using Equation 3.1 or 3.3. The cutter contact area ($A_{contact}$) is turned into the area in front of cutter face (A_V) using Equation 3.11 theoretically.

$$A_v = A_{contact}.\,Cos(BR) \quad \ldots\ldots\ldots \text{Eq. } 3.11$$

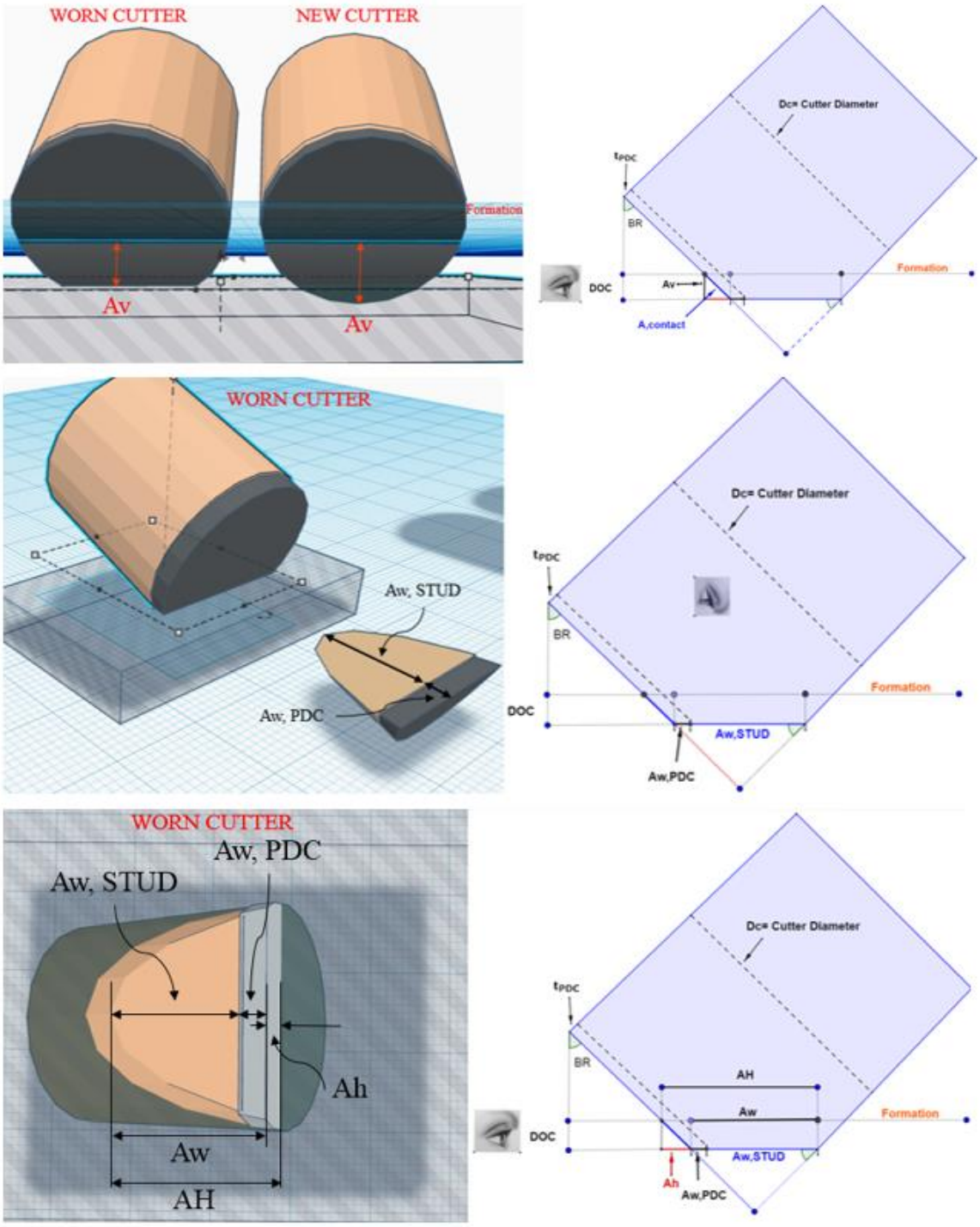

Figure 3.3. Schematic of different areas associated with the cutter penetration calculation

3.3 Interfacial friction angle (IFA) modeling

3.3.1 Single cutter IFA model

The interfacial friction coefficient can be recorded either by conducting direct shear tests (Smith, 1995; Smith et al., 2002) or single cutter tests in the lab (Richard, 1999). The direct shear test is one of the earliest and simple method for measuring the soil shear strength and shear strength between rock and contact surface (Smith et al., 2002). Although, the direct test device proved to be simple and rapid test device, it has all disadvantages of a direct shear tester apparatuses such as severe problems with controlling stress concentration on edges of the sample and potential for sample jamming and crushing within the carrier (Smith et al., 2002). The interfacial friction can be determined indirectly using single cutter tests in the lab maintaining constant PDC cutter depth of cut and velocity. To measure the interfacial friction angle (ψ or IFA) for a particular rock, the cutter axial and tangential forces are recorded while the cutter moves at a constant depth of cut and velocity on a sample of rock. The recorded cutter forces then can be used to calculate the interfacial friction angle using the Detournay and Defourny (1992) model. The Detournay and Defourny (1992) interfacial friction angle model is provided in Equation 3.12.

$$\psi = \mathrm{Tan}^{-1}\left(\frac{F_n}{F_t}\right) - BR \quad \ldots\ldots \text{Eq. } 3.12$$

Coudyzer and Richard in 2005 argued that the force angle cannot be viewed as a simple interfacial friction angle and more complex failure mechanisms (i.e. build-up edge of crushed material in cutting face) must be considered (Coudyzer and Richard, 2005). In this study, the single cutter data in conjunction with the Detournay and Defourny (1992) model (Equation 3.12) are used to estimate the IFA.

In 1987, Glowka conducted multiple single PDC cutter tests on different rock types including BSS, SWG, and TM. The single cutters with a constant velocity equal to 2.1 inches per second with different

diameters and wear flat areas were tested. Glowka (1987) applied a constant depth of cut and recorded the cutter normal and tangential (drag) forces. Hellvik et al. (2012) conducted tests on the PDC cutter with standard and variable chamfer (45 and 15-degree chamfer angle respectively) in the lab. They used a Vertical Turret Lathe (VTL) with a rock pie including Torrey buff sandstone, red sandstone, and TX pink granite. The VTL rotary speed was between 75 to 125 rpm, which gives a cutter velocity between 134 inches per second to 220 inches per second with an average speed equal to 177 inches per second. They reported the cutter forces for different BR angles and DOC for both standard and alternate cutters in TX pink granite.

The BSS and SWG (with unconfined compressive strength 7100 psi and 21500 psi respectively) from Glowka (1984) tests and the TX pink granite (with 19400 psi unconfined compressive strength) from Hellvik et al. (2012) were chosen to develop the single cutter IFA model. The potential parameters that affect the IFA are DOC, cutter diameter, cutter velocity, rock strength, mud type, cutter wear, and chamfer angle. In this study, the single cutter IFA model is developed by taking the cutter depth of cut, cutter velocity, and rock unconfined compressive strength into account. Akbrai et al. (2014) found that the PDC cutter diameter does not affect the frictional response considerable. The cutter velocity will affect the rock strain rate, and consequently the rock strength. In the single cutter IFA model, the UCS is representative of rock type and compressive strength. The single cutter IFA model has included the effect of strain rate, by taking simultaneously both UCS and cutter velocity into account.

The general shape of a single cutter IFA model is provided in Equations 3.13 through 3.20. The IFA model shape was selected considering the single cutter IFA behavior versus cutter depth of cut. It is observed that the IFA values begin with high values and it exponentially decreases versus depth of cut (phase I). After a threshold depth of cut, the IFA descending trend shifts from exponential to a smooth declining one (phase II). The selected IFA model can simulate both phases successfully.

Note that for soft rocks (i.e. BSS) the IFA model should be able to generate only a declining trend versus depth of cut (phase II). This is because of shearing mechanism comparing to the chipping one underneath the cutter. Depend on the rock UCS and cutter velocity, the IFA model can show phase II behavior for all depth of cuts as it is seen in the rocks like BSS. The normalized values are used in the model to avoid conflict of dimension between parameters. Based on the experimental data (Hellvik et al., 2012) the summation of IFA and BR is almost constant. Therefore, in the IFA model, the IFA value is summed up with the BR and both show up at the left side of Equation 3.13.

The a, b, and c are written with a similar shape as Equation 3.13. The reason for selecting a similar structure is that increasing the normalized cutter velocity and UCS should affect the IFA model behavior into some limits. In other words, increasing the cutter velocity or UCS, the Equation 3.17, 3.18, and 3.20 approach to a limit and because of that, the whole IFA model will be limited to boundaries that are determined using data.

In Equation 3.13, the $\psi_{\text{single cutter}}$ is single cutter interfacial friction angle, the δ_n is the normalized depth of cut (taking the cutter diameter into account, i.e. 0.5 inch), and a, b, and d are a function of normalized cutter velocity and normalized unconfined compressive strength.

$$\psi_{\text{single cutter}} + \text{BR} = a + \left(\frac{b}{{\delta_n}^c + d}\right) \ldots\ldots \text{Eq. 3.13}$$

$$\delta_n = \frac{\delta}{D_c} \ldots\ldots \text{Eq. 3.14}$$

$$V_n = \frac{V_c}{2.1} \ldots\ldots \text{Eq. 3.15}$$

$$\text{UCS}_n = \frac{\text{UCS}}{5000} \ldots\ldots \text{Eq. 3.16}$$

$$a = w_0 + \frac{w_1}{{V_n}^{w_2} + w_3} \ldots\ldots \text{Eq. } 3.17$$

$$b = w_4 + \frac{w_5}{{V_n}^{w_6} + w_7} \ldots\ldots \text{Eq. } 3.18$$

$$c = w_8 \ldots\ldots \text{Eq. } 3.19$$

$$d = w_9 + \frac{w_{10}}{{UCS_n}^{w_{11}} + w_{12}} \ldots\ldots \text{Eq. } 3.20$$

The a, b, c, and d are used to fit the single cutter IFA model (Equation 3.13) with the Glowka (1987) and Hellvik et al. (2012) data points for BSS, SWG and TX pink granite. The differential evolution algorithm (DEA) is applied to the set of data (Glowka 1984; Hellvik et al. 2012) to search the space of solutions and to find the best a, b, c, and d with their associated constants.

3.3.2 Full bit IFA model

A separate IFA model for full bit application is suggested to consider the effect of IFA on ROP performance. The full bit IFA model is similar to the single cutter IFA model (Equation 3.13 through 3.20) but has different constants. The reason for developing a separate full hole IFA model besides the single cutter IFA model is that the equivalent cutter concept introduced by Hareland and Rampersad (1994) is an approximation for simplification in the full hole model. The depth of cut of an individual cutter on bit face is a function of cutter distance from the bit center and the number of cutters. In essence, the number and arrangement of the cutter on the bit face affects the forces and DOCs of each individual cutter (see Appendix E). The cutter normal force is calculated by dividing the WOB to the number of cutters and is used for calculating the equivalent DOC and the final ROP. Therefore, calculating the IFA for the equivalent cutter on a bit face using the average WOC introduces potential errors to IFA estimations, and consequently, to the ROP estimations. The full bit IFA model set of equations are as follows.

$$\psi_{\text{full bit}} + BR = a + \left(\frac{b}{{\delta_n}^c + d}\right) \ldots\ldots \text{Eq. 3.21}$$

$$\delta_n = \frac{\delta}{D_c} \ldots\ldots \text{Eq. 3.22}$$

$$V_n = \frac{V_c}{2.1} \ldots\ldots \text{Eq. 3.23}$$

$$UCS_n = \frac{UCS}{5000} \ldots\ldots \text{Eq. 3.24}$$

$$a = w_0 + \frac{w_1}{{V_n}^{w_2} + w_3} \ldots\ldots \text{Eq. 3.25}$$

$$b = w_4 + \frac{w_5}{{V_n}^{w_6} + w_7} \ldots\ldots \text{Eq. 3.26}$$

$$c = w_8 \ldots\ldots \text{Eq. 3.27}$$

$$d = w_9 + \frac{w_{10}}{{UCS_n}^{w_{11}} + w_{12}} \ldots\ldots \text{Eq. 3.28}$$

3.4 Single cutter force model

3.4.1 Single cutter force model for sharp cutter

The sharp cutter normal and drag forces are calculated by multiplying the cutter projected contact area (Equation 3.1) on the X and Y axis with rock unconfined compressive strength (see Equation 3.29 and 3.30). Note that the cutter projected area is calculated by taking both the cutter BR and IFA into account.

$$F_n = \left(\left(\frac{D_c}{2}\right)^2 \times \text{Cos}^{-1}\left(\frac{\frac{D_c}{2} - \frac{DOC}{\text{Cos}(BR)}}{\frac{D_c}{2}}\right) - \left(\frac{D_c}{2} - \frac{DOC}{\text{Cos}(BR)}\right) \times \sqrt{D_c \times \frac{DOC}{\text{Cos}(BR)} - \left(\frac{DOC}{\text{Cos}(BR)}\right)^2}\right)$$

$$\times \text{Sin}(BR + \psi_{\text{single cutter}}) \times UCS \ \ldots\ldots \text{Eq. 3.29}$$

$$F_d = \left(\left(\frac{D_c}{2}\right)^2 \times \mathrm{Cos}^{-1}\left(\frac{\frac{D_c}{2} - \frac{DOC}{\mathrm{Cos}(BR)}}{\frac{D_c}{2}} \right) - \left(\frac{D_c}{2} - \frac{DOC}{\mathrm{Cos}(BR)}\right) \times \sqrt{D_c \times \frac{DOC}{\mathrm{Cos}(BR)} - \left(\frac{DOC}{\mathrm{Cos}(BR)}\right)^2} \right)$$

$$\times \mathrm{Cos}(BR + \psi_{\text{single cutter}}) \times UCS \quad \ldots\ldots \text{Eq. } 3.30$$

3.4.2 Single cutter force model for blunt cutter

The blunt cutter normal and drag forces are calculated using the following equations 3.31 and 3.32. The projection of cutter contact area on X and Y axis (for normal and drag forces respectively) are calculated by taking the cutter BR and IFA angles into account. The cutter wear flat area is multiplied with the UCS to achieve the additional normal force needed for cutter penetration (see Equation 3.31). The blunt cutter drag force model is provided in Equation 3.32. The additional normal force needed for the blunt cutter is calculated and multiplied with the rock internal friction coefficient to achieve the horizontal component. The cutter drag force is calculated by taking the additional horizontal force component into account (see Equation 3.32).

$$F_n$$

$$= \left(\left[\left(\frac{D_c}{2}\right)^2 . \mathrm{Cos}^{-1} \left(\frac{\frac{D_c}{2} - \left(\frac{\left(DOC + \frac{BG \times D_c \times \cos(BR)}{8}\right)}{\mathrm{Cos}(BR)} \right)}{\frac{D_c}{2}} \right) \right.$$

$$- \left(\frac{D_c}{2} \right.$$

$$\left. \left. - \left(\frac{\left(DOC + \frac{BG \times D_c \times \cos(BR)}{8}\right)}{\mathrm{Cos}(BR)} \right) \right) . \sqrt{2.\left(\frac{D_c}{2}\right).\left(\frac{\left(DOC + \frac{BG \times D_c \times \cos(BR)}{8}\right)}{\mathrm{Cos}(BR)} \right) - \left(\frac{\left(DOC + \frac{BG \times D_c \times \cos(BR)}{8}\right)}{\mathrm{Cos}(BR)} \right)^2} \right]$$

$$\left. - \left[\left(\frac{D_c}{2}\right)^2 . \mathrm{Cos}^{-1} \left(\frac{\frac{D_c}{2} - \left(\frac{BG.D_c}{8}\right)}{\frac{D_c}{2}} \right) - \left(\frac{D_c}{2} - \left(\frac{BG.D_c}{8}\right) \right) . \sqrt{2.\left(\frac{D_c}{2}\right).\left(\frac{BG.D_c}{8}\right) - \left(\frac{BG.D_c}{8}\right)^2} \right] \right) \times \mathrm{Sin}\left(BR + \psi_{\text{single cutter}}\right)$$

$$\times UCS + A_w \times UCS \quad \ldots\ldots\ldots \text{Eq. 3.31}$$

$$F_d = \left(\left[\left(\frac{D_c}{2}\right)^2 . \mathrm{Cos}^{-1} \left(\frac{\frac{D_c}{2} - \left(\frac{\left(\mathrm{DOC} + \frac{\mathrm{BG} \times D_c \times \cos(\mathrm{BR})}{8}\right)}{\mathrm{Cos(BR)}} \right)}{\frac{D_c}{2}} \right) \right.$$

$$- \left(\frac{D_c}{2} \right.$$

$$\left. \left. - \left(\frac{\left(\mathrm{DOC} + \frac{\mathrm{BG} \times D_c \times \cos(\mathrm{BR})}{8}\right)}{\mathrm{Cos(BR)}} \right) \right) . \sqrt{2.\left(\frac{D_c}{2}\right).\left(\frac{\left(\mathrm{DOC} + \frac{\mathrm{BG} \times D_c \times \cos(\mathrm{BR})}{8}\right)}{\mathrm{Cos(BR)}} \right) - \left(\frac{\left(\mathrm{DOC} + \frac{\mathrm{BG} \times D_c \times \cos(\mathrm{BR})}{8}\right)}{\mathrm{Cos(BR)}} \right)^2} \right]$$

$$\left. - \left[\left(\frac{D_c}{2}\right)^2 . \mathrm{Cos}^{-1} \left(\frac{\frac{D_c}{2} - \left(\frac{\mathrm{BG}.\, D_c}{8}\right)}{\frac{D_c}{2}} \right) - \left(\frac{D_c}{2} - \left(\frac{\mathrm{BG}.\, D_c}{8}\right) \right) . \sqrt{2.\left(\frac{D_c}{2}\right).\left(\frac{\mathrm{BG}.\, D_c}{8}\right) - \left(\frac{\mathrm{BG}.\, D_c}{8}\right)^2} \right] \right)$$

$$\times \mathrm{Cos}\left(\mathrm{BR} + \psi_{\text{single cutter}}\right) \times \mathrm{UCS} + \mu \times A_w \times \mathrm{UCS} \quad \ldots\ldots \text{Eq. } 3.32$$

In the previous set of equations, μ is rock internal friction coefficient and A_w is cutter wear flat area. Because of CP during the drilling, UCS in Equation 3.29 through 3.32 becomes CCS which is rock confined compressive strength.

3.5 New full bit PDC ROP model

The radius at which the bit areas are equal inside and outside the radius is called effective radius (R_e). The amount of rock volume that is cut by the bit inside and outside the effective radius is equal (Hareland and Rampersad, 1994). The equivalent bit radius concept is used in the new model to estimate the PDC bit ROP. Average BR and SR values are calculated from all the bit face cutters and assigned to a cutter traveling at the equivalent radius.

In the new ROP model, the volume of rock that is cut by the cutter at an effective radius is calculated theoretically. This volume is a direct function of the area in front of the cutter, which itself is a function

of the depth of cut. The area in front of the cutter (A_v) is multiplied by the effective radius and RPM to attain an estimation of cutting volume per minute. Two important assumptions when developing the ROP model include: The area in front of the cutter is constant for each rotation, and the geometric center of the cutter front area is fixed and rotates at a radius equal to the effective radius. The calculated cutting volume per minute is divided by the face area of the bit to achieve the ROP. The new model ROP is provided in Equation 3.33 and 3.34. In Equation 3.33, C_B is the number of blade normalized correlation coefficient, NOC is the number of cutters at bit face, RPM is the revolutions per minute, the R_e is equivalent radius in inches, A_v is the projected contact area in front of the cutter in a square inch, D_b is the bit diameter in inches and the ROP is in feet per hour.

$$ROP = C_B \times NOC \times \left(\frac{5 \times RPM \times \pi \times R_e \times A_v}{\frac{\pi}{4} {D_B}^2} \right) \quad \ldots\ldots\ldots \text{Eq. 3.33}$$

The cutter front area is a projection of cutter contact area (Equation 3.3) by taking the cutter BR, SR, IFA, and BG into accounts and is provided in Equation 3.34.

$$
\begin{aligned}
A_v = & \left[\left[\left(\frac{D_c}{2}\right)^2 . \mathrm{Cos}^{-1}\left(\frac{\frac{D_c}{2} - \left(\frac{\left(DOC + \frac{BG \times D_c \times \cos(BR)}{8}\right)}{\mathrm{Cos}(BR)}\right)}{\frac{D_c}{2}}\right)\right.\right. \\
& - \left(\frac{D_c}{2} - \left(\frac{\left(DOC + \frac{BG \times D_c \times \cos(BR)}{8}\right)}{\mathrm{Cos}(BR)}\right)\right) . \sqrt{2.\left(\frac{D_c}{2}\right).\left(\frac{\left(DOC + \frac{BG \times D_c \times \cos(BR)}{8}\right)}{\mathrm{Cos}(BR)}\right) - \left(\frac{\left(DOC + \frac{BG \times D_c \times \cos(BR)}{8}\right)}{\mathrm{Cos}(BR)}\right)^2} \Bigg] \\
& - \left[\left(\frac{D_c}{2}\right)^2 . \mathrm{Cos}^{-1}\left(\frac{\frac{D_c}{2} - \left(\frac{BG.D_c}{8}\right)}{\frac{D_c}{2}}\right) - \left(\frac{D_c}{2} - \left(\frac{BG.D_c}{8}\right)\right) . \sqrt{2.\left(\frac{D_c}{2}\right).\left(\frac{BG.D_c}{8}\right) - \left(\frac{BG.D_c}{8}\right)^2}\right] \Bigg] \times \mathrm{Cos}(BR + \psi_{\text{full bit}}) \\
& \times \mathrm{Cos}(SR) \ldots\ldots . . \mathrm{Eq.}\ 3.34
\end{aligned}
$$

3.6 New PDC bit wear model

Bit wear is one of the most important factors in ROP modeling. Bit wear gradually increases during drilling from zero BG (new bit) to 8 BG (completely worn out) based on the International Association of Drilling Contractor (IADC) system (Winters et al., 1987 a) and influences on the drilling performance. Therefore, having a well-developed bit wear estimation function is necessary for ROP modeling.

In general, the PDC cutter wear is divided into two categories. The abrasive wear, which is associated with the development of uniform wear flat and is a function of normal force on the cutter, cutter temperature, cutter velocity, formation properties (e.g. abrasiveness and lubricity) and cutter quality.

The second wear category is due to dynamic forces applied to the cutter. Chipped, broken and lost cutter typifies the wear caused by dynamic forces (Sinor and Warren, 1989). In this study, only abrasive wear is taken into account for developing a novel PDC bit wear model.

Cutter normal and drag forces influence the cutter during the cutting process and cause cutter abrasive wear. During the cutting process, the rock breaks and moves ahead and beneath the cutter face. The relational movement of cutting beneath the cutter face results in frictional force at cutter face, which is known as interfacial friction. The interfacial friction has a great influence on the cutter normal (F_n) and drag (F_d) force. Ignoring the interfacial friction phenomena results in under and overestimations for cutter normal and drag forces respectively. The physical work that is done by a single cutter is calculated by taking into account both cutter normal and drag forces. The amount of work that the cutter drag force does is proposed in Equation 3.33.

$$\frac{W_1}{\min} = 0.083 \times F_d \times \text{RPM} \times 2\pi R_e \ldots\ldots \text{Eq. 3.33}$$

The amount of work that is done by normal force at cutter is calculated in Equation 3.34.

$$\frac{W_2}{\min} = \frac{F_n \times \text{ROP}}{60} \ldots\ldots \text{Eq. 3.34}$$

The summation of these two works gives the total work that is done by cutter (Equation 3.35). In Equation 3.33 and 3.34, the F_n and F_d is cutter normal and drag forces (lb_f), RPM is revolution per minutes, R_e is effective radius (inch), ROP is in $\frac{ft}{hr}$, and the W_1, W_2 and W_T are works in $ft.lb_f$. The cutter normal and drag forces for sharp and blunt cutters (Equation 3.29 through 3.32) are developed using the single cutter data in chapter 4.

$$W_T = W_1 + W_2 \ldots\ldots \text{Eq. 3.35}$$

The wear constant (α) is the amount of work in ft. lb_f that should be done to wear off the unit volume of the cutter in cubic inches. The total work done by the cutter is turned into the worn volume V_{worn} in cubic inch, by taking the cutter wearing constant. The cutter is composed of PDC and stud material with different wear constants. Therefore, the total work should be turned into the cutter worn volume (V_{worn}) by taking an average of the PDC layer and stud wear constants (α_{PDC} and α_{stud}) into account. It is assumed that the PDC layer and stud volumes that are exposed to formation are proportional to their wear flat areas (thickness of the worn layer is very small at each revolution).

Figure 3.4 shows a schematic of a blunt cutter and its associated areas. The total area beneath the cutter (A_H) is composed of cutter wear flat area (A_w) and the area beneath the cutter face (A_h). In Figure 3.4, the A_w is cutter total wear flat area which is composed of PDC wear flat area ($A_{w,PDC}$), and stud wear flat area ($A_{w,STUD}$).

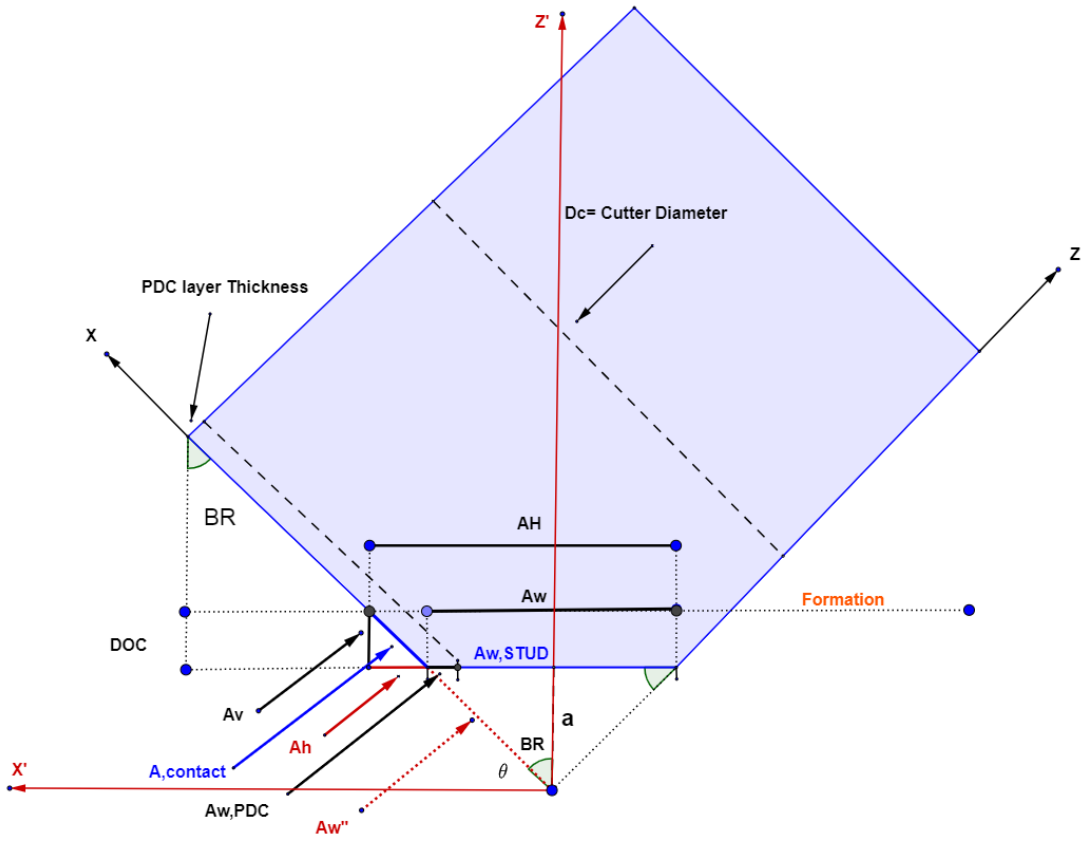

Figure 3.4. A schematic of a blunt PDC cutter and its associated areas

In Figure 3.5, a 3D representation of Figure 3.4 is provided. For a blunt cutter, the wear flat area can be assumed as a product of intersection between a tilted plane and a cylinder (A_w). In Figure 3.5, the θ and BR are complementary angles, the a is the depth of wear, and the intersection between the plane and cylinder is representative for the wear flat area (A_w)

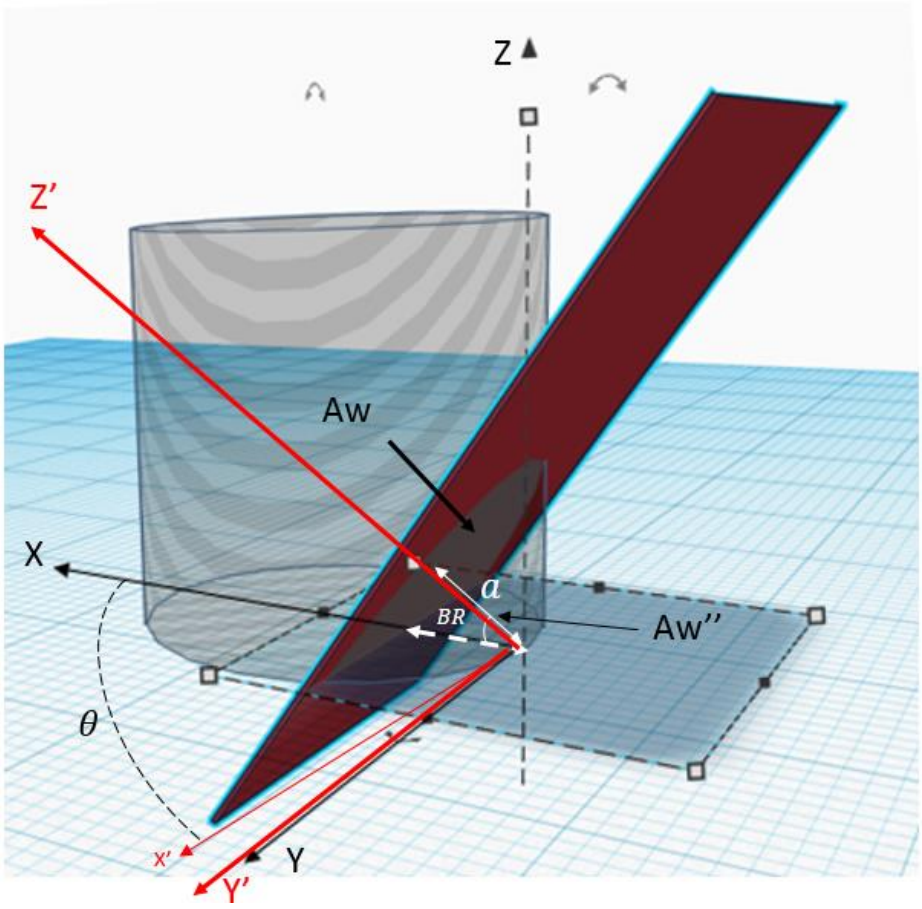

Figure 3.5 A 3D schematic of a PDC cutter and wear flat area from another perspective

The projection of cutter wear flat area (A''_w) is a sector of a circle on the X-Y plane. The A''_w can be found by taking the integral of an equation of a circle within the boundaries. The wear flat area detailed equations for both PDC ($A_{w,PDC}$) and stud ($A_{w,stud}$) are provided in Appendix B. The total cutter wear flat area (A_w) and PDC wear flat area ($A_{w,PDC}$) are calculated using Equation 3.7 and 3.8. The cutter stud wear flat area can be calculated by subtracting total wear flat area from PDC wear flat area in Equation 3.9.

In Equation 3.36, an average of the cutter wear coefficient is calculated by taking the volume fraction and wear coefficients of PDC and stud layer into account. In Equation 3.37, the cutter total work is divided into the average wear coefficient to achieve the cutter worn volume. Note that at the beginning of drilling, there is no wear flat area and the total work is turned into the cutter worn volume by taking only the PDC layer wear coefficient (α_{PDC}) into account.

$$\alpha_{ave} = \left(\left(\frac{A_{w,PDC}}{Aw}\right) \times \alpha_{PDC} + \left(\frac{A_{w,STUD}}{Aw}\right) \times \alpha_{stud}\right) \ldots\ldots\ldots \text{Eq. 3.36}$$

$$V_{worn} = \frac{W_T}{\alpha_{ave}} \ldots\ldots\ldots \text{Eq. 3.37}$$

The cutter total worn volume (cubic inch) geometrically is calculated using Equation 3.37. The cutter worn volume in Equation 3.38, gives the cutter worn volume (cubic inch) by taking the cutter diameter (inch) and BR for a given bit grade. The cutter BG is back-calculated by replacing the cutter worn volume from Equation 3.37 into Equation 3.38.

$$V_{total\ worn} = -\left[\frac{\left(\frac{D_c}{2}\right)^3}{\text{Tan(BR)}}\left[\left(\frac{\left(\frac{D_c}{2}\right)-\left(\frac{BG.D_c}{8}\right)}{\left(\frac{D_c}{2}\right)}\right) \times \arccos\left(\frac{\left(\frac{D_c}{2}\right)-\left(\frac{BG.D_c}{8}\right)}{\left(\frac{D_c}{2}\right)}\right) - \sqrt{1-\left(\frac{\left(\frac{D_c}{2}\right)-\left(\frac{BG.D_c}{8}\right)}{\left(\frac{D_c}{2}\right)}\right)^2}\right] + \frac{\left(\frac{D_c}{2}\right)^3}{3\,\text{Tan(BR)}}\left(\sqrt{1-\left(\frac{\left(\frac{BG.D_c}{8}\right)-\left(\frac{D_c}{2}\right)}{\left(\frac{D_c}{2}\right)}\right)^2}\right)^3\right] \ldots\ldots\ldots \text{Eq. 3.38}$$

In the above set of equations, the DOC is the depth of cut (inch), BG is bit grade, D_c is cutter diameter (inch), A_V is the area in front of cutter (square inch), D_b is bit diameter (square inch), and V_{worn} is worn volume in cubic inch. Figure 3.6 shows the schematic of the total worn-out section $V_{total\ worn}$ of a PDC cutter.

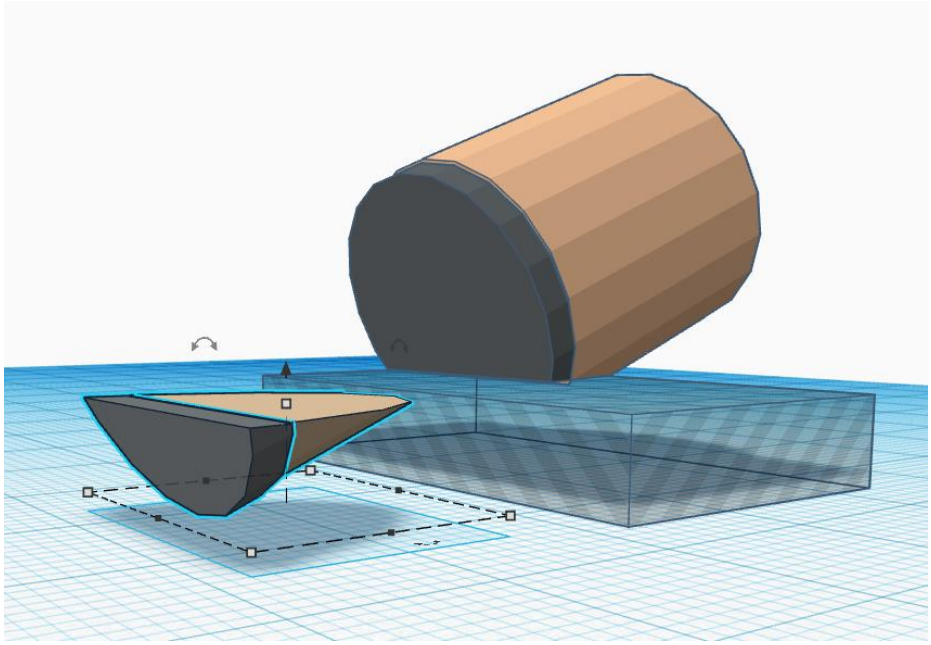

Figure 3.6. Schematic of a worn-out section of a PDC cutter

3.7 Metaheuristic Algorithms and Differential Evolution Algorithm (DEA)

Metaheuristic Algorithms (MAs) are procedures developed to find a sufficiently good solution to an optimization problem. The MAs create a set of feasible sample solutions for a problem and then try to increase the candidate's fitness iteratively. It is noticeable that using these methods to solve problems does not guarantee finding a global optimum answer. According to the search strategies classification, metaheuristics can be classified into local and global searches. The local search algorithms, such as hill-climbing, try to improve the fitness of an answer on a simple local domain and do not guarantee finding a global optimum answer.

The global search algorithms such as Ant Colony Optimization (ACO), Differential Evolutionary Algorithms (DEA) and Particles Swarm Optimization (PSO) were designed to achieve the global optimum answer. In another classification, the MAs can be divided into single-solution versus population-based searches. The single-solution algorithms, such as Simulated Annealing (SA), iterated local search, variable neighborhood search, and guided local search are used to improve the fitness of an individual in the population of candidates.

However, the population-based algorithms such as evolutionary computation, Genetic Algorithm (GA), and Particle Swarm Optimization (PSO) benefit from the population information to guide the algorithm toward the optimum solution (Bianchi et al., 2009 and Blum and Roli, 2003). In some applications, an algorithm (MAs) is combined with another one (so called-hybridization) to improve the searchability. The classification of MAs is shown in Figure 3.7.

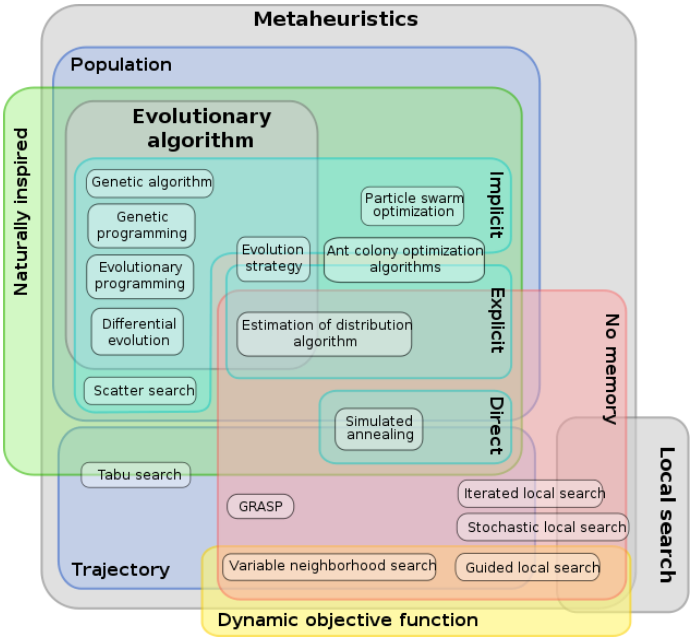

Figure 3.7. Different MAs classification (Dreo and Candan, 2017)

Storn and Price developed the Differential Evolution Algorithm (DE) in 1997 (Storn and Price, 1997). The DE algorithm is an iterative method that is used for optimization. The DE algorithm initiates by generating random candidates by taking the problem's assumptions, constraints, and limitations into account. In Figure 3.8, the candidates begin from random initial points and iteratively are guided toward the global optimum according to the DE algorithm formula. The algorithm flowchart is provided in Figure 3.9.

DE algorithm begins with a population of random candidate solutions and improves the fitness of population using its simple mathematical equation iteratively. As seen in Figure 3.9, the DE algorithm chooses a target vector (X_1) randomly, which is selected to be manipulated by the algorithm. The DE algorithm benefits from two weighting and crossover factors. The weighting factor, which is shown by

F, regulates the amplification of differential variation among candidates (Atashnezhad et al., 2017). The crossover factor determines the amount of recombination between two individual candidates.

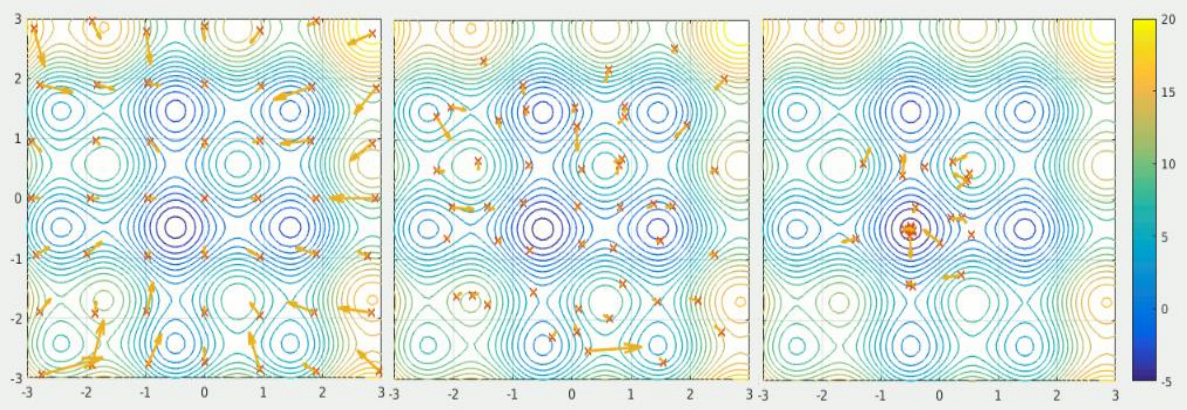

Figure 3.8 A contour of a 3D problem with PSO particles (Ephramac, 2017)

The algorithm selects two more vectors randomly (X_2, X_3) and calculates the difference ($X_3 - X_2$). The weighting factor is multiplied to the difference ($X_3 - X_2$) to achieve weighted difference vector $F \times (X_3 - X_2)$. The F value is primary within the range of 0.5 to 2 (Atashnezhad et al., 2017). A random vector (X_4), is chosen and added to the weighted difference vector to achieve the noisy random vector. In the end, a crossover is applied to the noisy random vector and target vector to achieve the trial vector. The fitness of the trial vector is compared to the target vector (X_1) and is replaced if it has higher fitness. This process can be repeated until a predetermined criterion, such as the number of iterations or fitness, is achieved.

In this study, the differential evolution algorithm (DEA) is applied to find the constants of single cutter and full bit interfacial friction models (Appendix F).

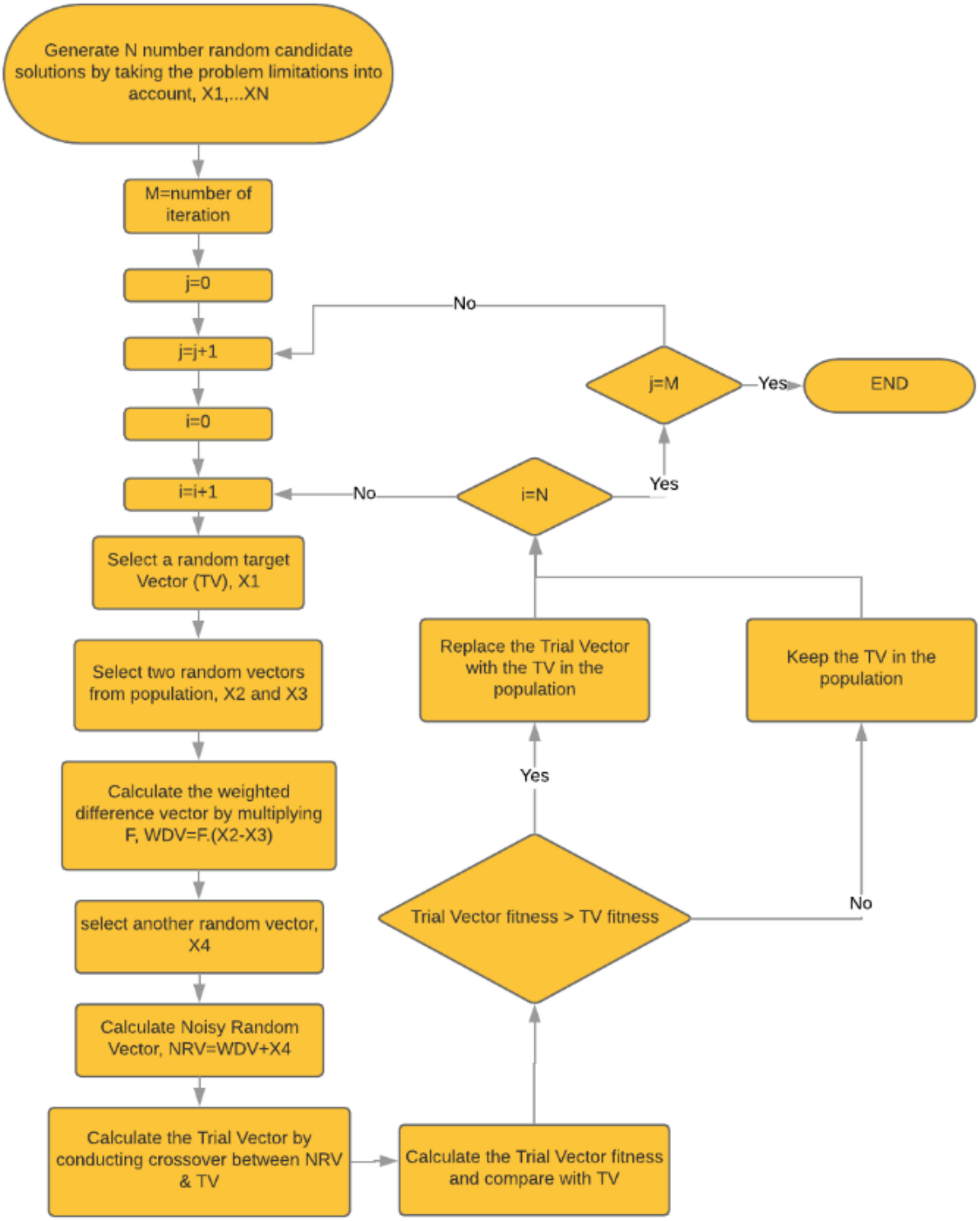

Figure 3.9. The differential algorithm flowchart

CHAPTER IV

RESULTS

This chapter shows the fitting results, verifications and application of the developed models including the single cutter model, the single cutter IFA model, full bit IFA model, and the newly developed full bit ROP model. The verification of the developed models is discussed utilizing sets of data for single cutter and full bit laboratory experiments. The sets of single cutter data are extracted from Glowka (1987) and Hellvik et al. (2012) single cutter experiments. The single cutter tests were conducted on cutters with different diameters, velocities and rock lithologies. The single cutter IFA model was fit on the single cutter data utilizing differential evolution algorithm (DEA) and the results was provided. A computer program was written in Python which solves the full bit IFA and the full bit ROP models simultaneously. The DEA used the computer program to develope the full bit IFA model using a set of full bit experiments data from Sandia National Lab (SNL) conducted in 2015, assuming zero CP and perfect drill bit hydraulic cleaning. Solving the developed full bit IFA model along with the PDC ROP model resulted in a very good estimation for ROP.

4.1 IFA model fitting results

The single cutter IFA model was developed using the Glowka (1987) and Hellvik et al. (2012) single cutter tests. The cutter details including BR angle, chamfer angle, diameter size, and cutter velocity are provided in table 4.1. The Detournay and Defourny (1992) model (DD model) (Equation 3.13) was applied to find the cutter IFA for each case in table 4.1 (see appendix G).

Table 4.1. Cutters details used for developing single cutter IFA model

Refrence	Cutter	Rock	UCS (psi)	Sharp or blunt	Cutter velocity	Dc (inch)	BR	Chamfer angle
Glowka (1987)	J	Berea sandstone	7100	Sharp	2.1	0.5	20	0
Glowka (1987)	K	Berea sandstone	7100	Sharp	2.1	0.75	20	0
Glowka (1987)	J	Sierra white granite	21500	Sharp	2.1	0.5	20	0
Glowka (1987)	D	Sierra white granite	21500	Blunt	2.1	0.5	20	0
Hellvik et al. (2012)	nan	TX pink granite	19400	Sharp	177	0.5	5	45
Hellvik et al. (2012)	nan	TX pink granite	19400	Sharp	177	0.5	10	45
Hellvik et al. (2012)	nan	TX pink granite	19400	Sharp	177	0.5	15	45
Hellvik et al. (2012)	nan	TX pink granite	19400	Sharp	177	0.5	20	45
Hellvik et al. (2012)	nan	TX pink granite	19400	Sharp	177	0.5	25	45
Hellvik et al. (2012)	nan	TX pink granite	19400	Sharp	177	0.5	30	45
Hellvik et al. (2012)	nan	TX pink granite	19400	Sharp	177	0.5	5	15
Hellvik et al. (2012)	nan	TX pink granite	19400	Sharp	177	0.5	10	15
Hellvik et al. (2012)	nan	TX pink granite	19400	Sharp	177	0.5	15	15
Hellvik et al. (2012)	nan	TX pink granite	19400	Sharp	177	0.5	20	15
Hellvik et al. (2012)	nan	TX pink granite	19400	Sharp	177	0.5	25	15
Hellvik et al. (2012)	nan	TX pink granite	19400	Sharp	177	0.5	30	15

The calculated IFA from the DD model hereafter is considered as IFA data. The single cutter IFA model (Equation 3.13 through 3.20) coefficients were found utilizing the differential evolution algorithm (DEA) and the sharp single cutter data (see table 4.1). The single cutter IFA model was used for the cutter normal and drag forces calculations, and to estimate the cutter interfacial friction angle (for data sets in table 4.1). An objective function was written in Python (see Appendix F) to perform the calculation for all cases in table 4.1 and to return the absolute difference between model and data points. The DEA algorithm was applied to the objective function to find the IFA model constants and reduce the absolute difference between data and model.

The single cutter IFA model and the coefficients are seen in Equation 4.1 through 4.4.

$$\psi_{\text{single cutter}} + \text{BR} = \text{a} + \left[\frac{\text{b}}{(\text{DOC}_\text{n})^{1.24} + \text{d}}\right] \ldots\ldots \text{Eq. 4.1}$$

$$\text{a} = \left(70.66 - \frac{130.09}{(\text{Vn})^{0.99} + 2.77}\right) \ldots\ldots \text{Eq. 4.2}$$

$$\text{b} = \left(0.49 + \frac{19.62}{(\text{Vn})^{1.15} + 40}\right) \ldots\ldots \text{Eq. 4.3}$$

$$\text{d} = \left(0.014 + \frac{0.99}{2.09 + (\text{UCSn})^{2.72}}\right) \ldots\ldots \text{Eq. 4.4}$$

Figures 4.1 through 4.8 compare the estimated IFA from the model (Equation 4.1 through 4.4) with the experimental data from all sharp cutter cases in table 4.1.

Figure 4.1 shows a comparison between the model-estimated IFA and the experimental data (achieved using DD model) for the cutter J in BSS (Glowka,1987).

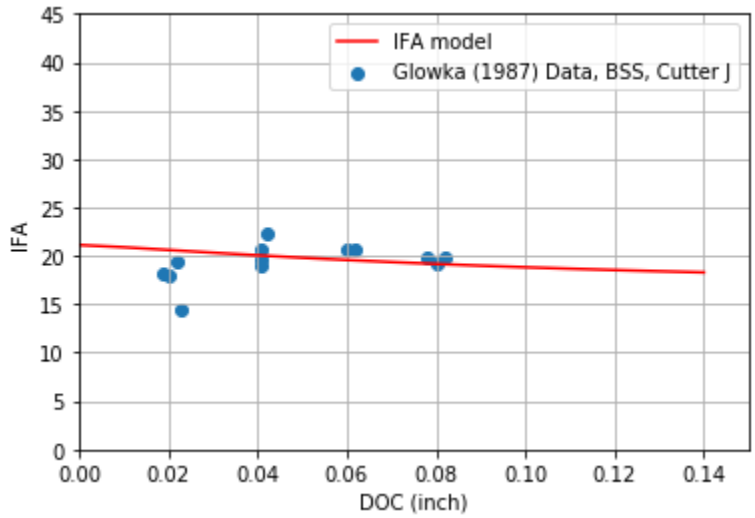

Figure 4.1. A comparison between model-estimated IFA and experimental data for cutter J in BSS

Figure 4.2 shows a comparison between the model-estimated IFA and the experimental data for the cutter K in BSS (Glowka,1987).

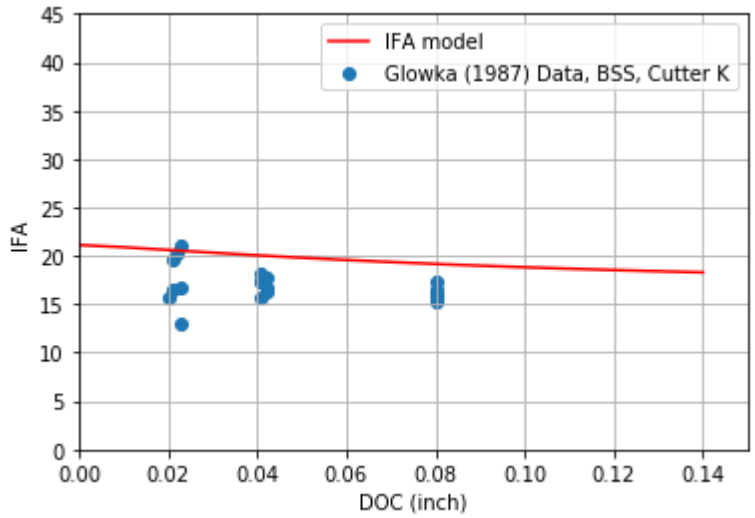

Figure 4.2. A comparison between model-estimated IFA and the experimental data for cutter K in BSS

Figure 4.3 shows a comparison between the model-estimated IFA and the experimental data for cutter J in SWG (Glowka,1987).

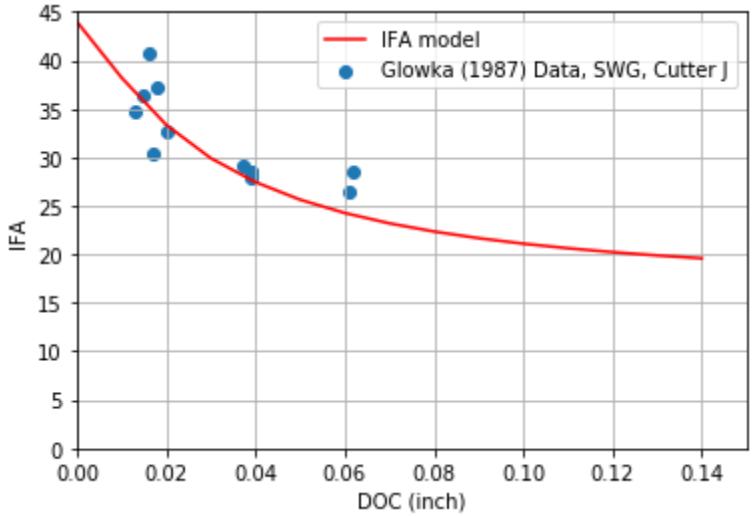

Figure 4.3. A comparison between model-estimated IFA and the experimental data for cutter J in SWG

Figures 4.4 and 4.5 show a comparison between the model-estimated IFA and the experimental data in TX pink granite with BR angles varying between 5º to 30º and chamfer angle 45º and 15º respectively.

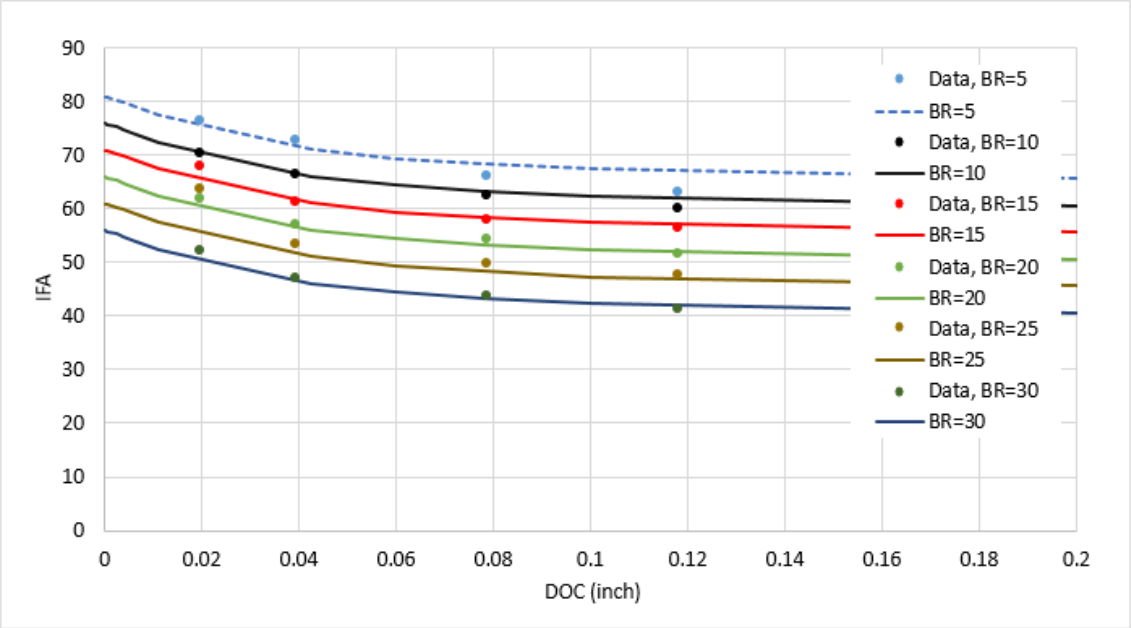

Figure 4.4. A comparison between model-estimated IFA and the experimental data for cutters (variable BR, chamfer =45), data from Hellvik et al. (2012)

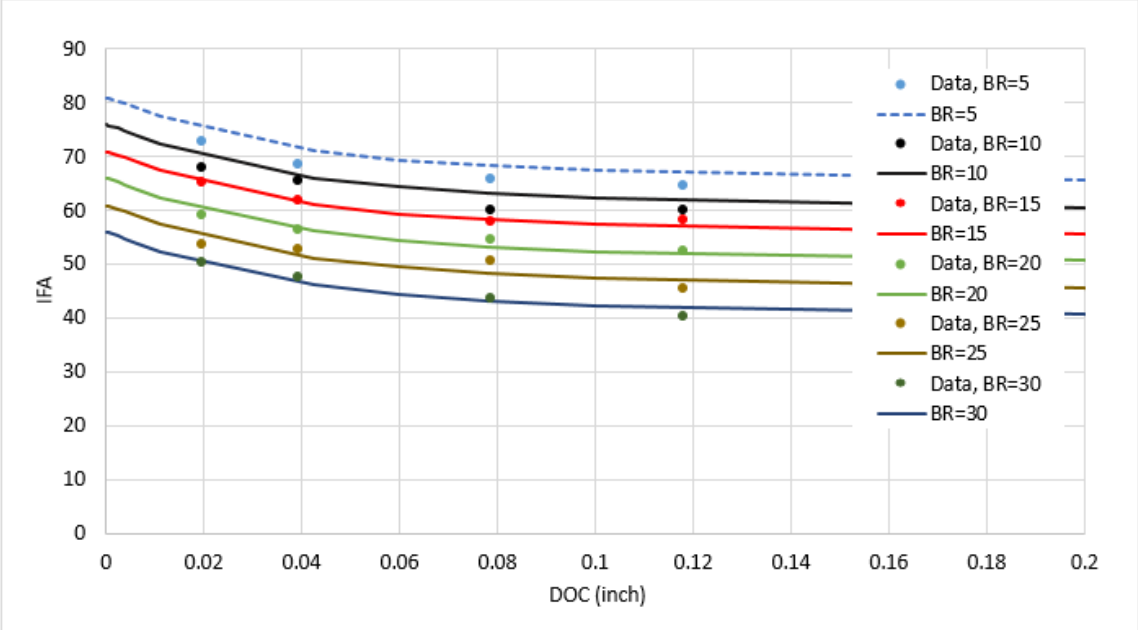

Figure 4.5. A comparison between model-estimated IFA and the experimental data for cutters (variable BR, chamfer =15), data from Hellvik et al. (2012)

Figures 4.6 and 4.7 show the sensitivity analysis of the IFA model for different unconfined compressive strengths and cutter velocities respectively for a specific drilling condition.

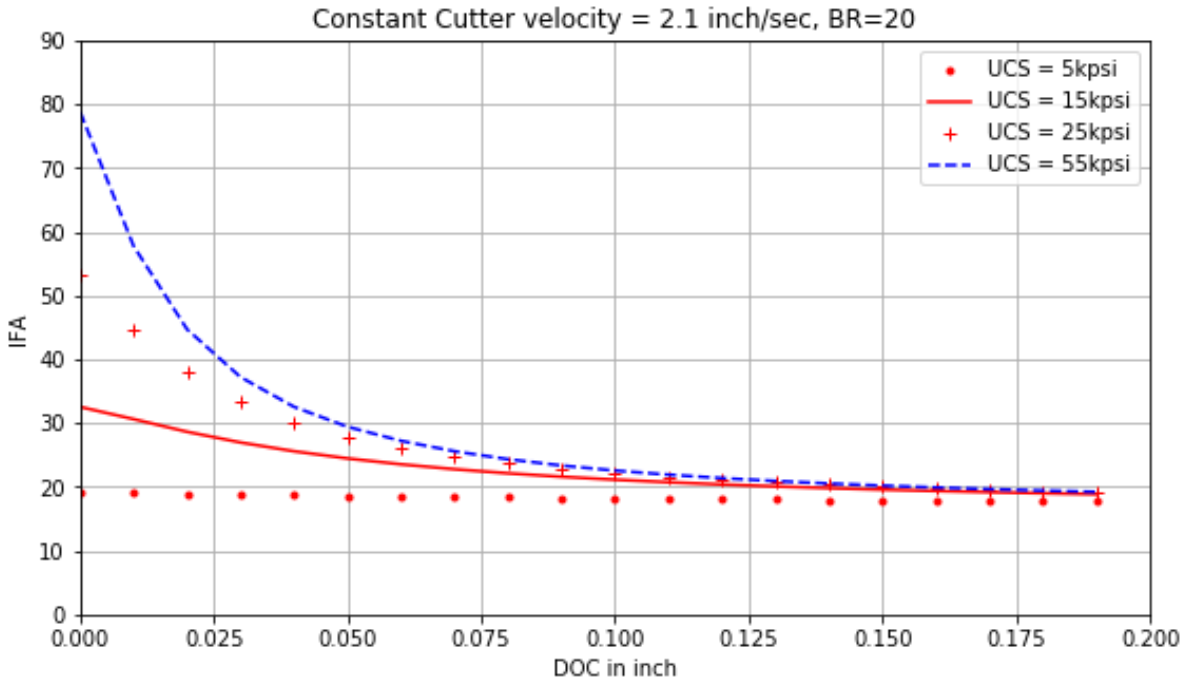

Figure 4.6. A sensitivity analysis on the IFA model for different rock UCSs at constant cutter velocity = 2.1 in/sec

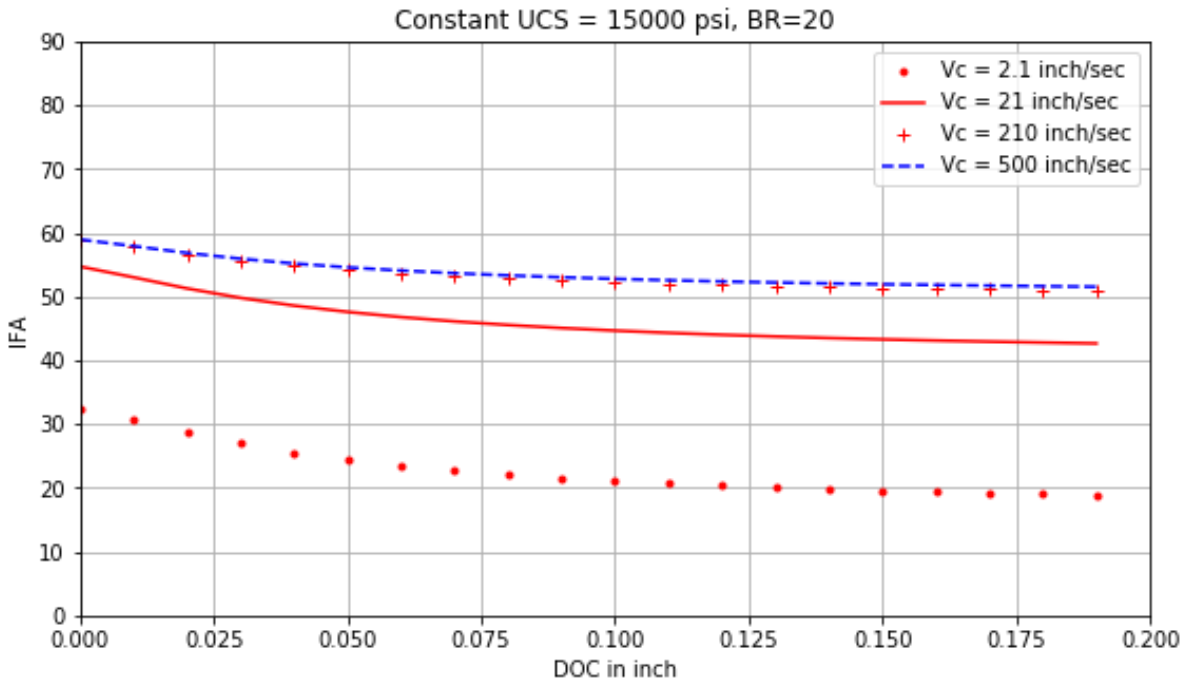

Figure 4.7. A sensitivity analysis on the IFA model for different cutter velocities at constant UCS = 15000 psi

4.2 PDC single cutter force model verification

Glowka, in 1987, conducted single cutter experiments and monitored the cutter axial and tangential forces. In this study, different cutters with different BG were dragged on SWG and BSS rock slabs at a constant depth of cut and velocity (2.1 inches/sec). For each cutter, the normal and drag forces were recorded. The results of single PDC cutter tests in SWG and BSS from Glowka (1987) were used for model fitting results.

Hellvik et al. (2012) conducted a series of tests on the chamfered cutters with a variety of BR angles ranging between 5º to 30º. A set of single cutter data from Hellvik et al. (2012) with a 15º chamfer angle were used for cutter normal and drag force estimation. The cutter depth of cut was used as an input variable and normal and drag forces were calculated based on the rock UCS. The cutter contact area for a sharp cutter at a constant depth of cut was calculated using Equation 3.1

For each test, the underneath and front area of the cutter were calculated based on the contact area and BR angle. The normal and drag forces were calculated by multiplying the underneath and front areas of the cutter by the rock UCS. The results would be the estimated normal and drag forces of the cutter without including the effect of interfacial friction.

In addition, the IFA model was applied to incorporate the effect of IFA in cutter forces estimation. The IFA model generates an estimation for interfacial friction angle by taking the cutter depth of cut, cutter velocity, and unconfined compressive strength into account (see Equation 4.1 through 4.4). The cutter contact area was turned into the cutter beneath and front areas by taking the summation of BR and IFA into account. Similarly, the normal and drag forces of a cutter were calculated by multiplying the cutter beneath and front areas with the rock UCS (Equations 3.29 and 3.30).

In the following pages, the DOC versus cutter normal and drag forces (Fn and Fd respectively) plots are presented before and after applying the single cutter IFA model. Note that, the IFA from data represent those values that were calculated using the DD model for all the cases in table 4.1.

4.2.1 Sharp cutter force model verification

Figures 4.8 to 4.16 show the estimated normal and drag forces versus the depth of cut for each cutter before and after applying the single cutter IFA model. The sets of tests from Glowka (1987) and Hellvik et al. (2012) were used to find the single cutter IFA model constants. Note that the cutters with 45º chamfer set data from Hellvik et al. (2012) were used.

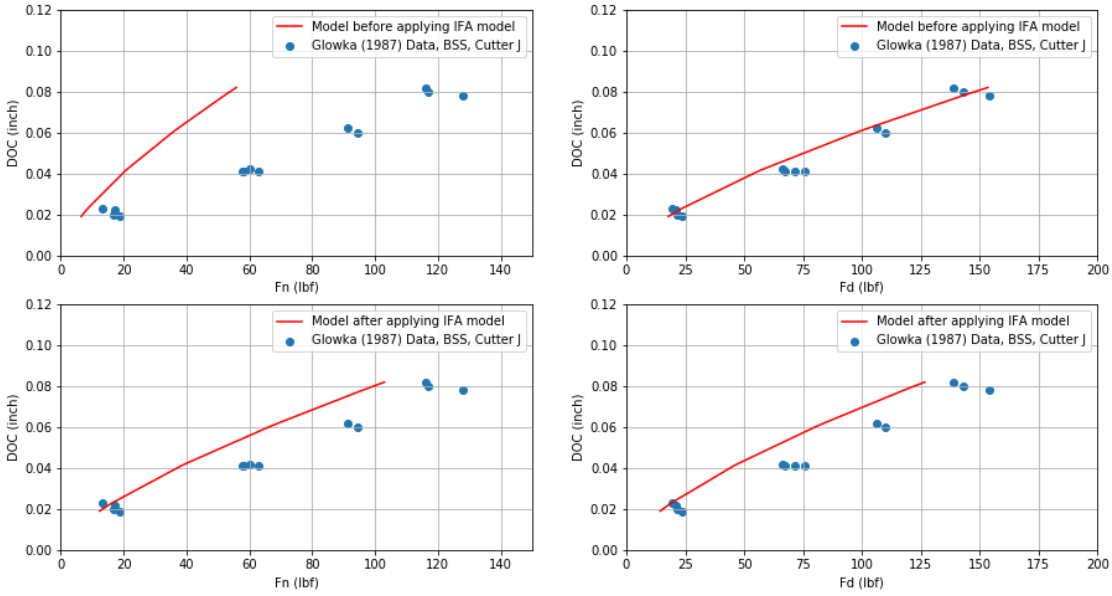

Figure 4.8. Normal and drag forces vs. DOC for sharp cutter J in BSS before and after applying the IFA model

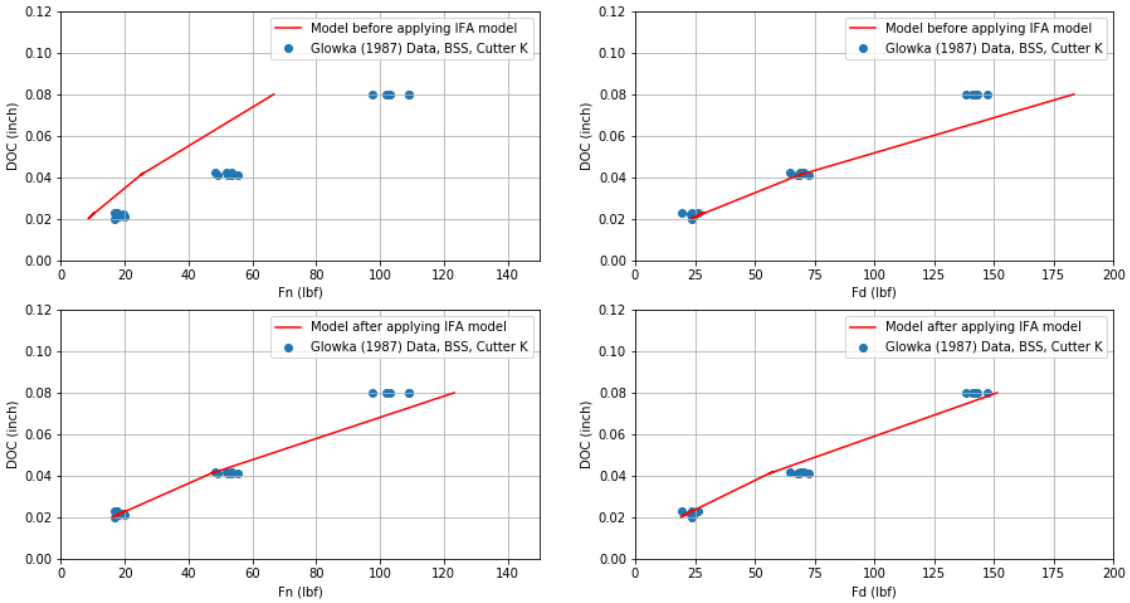

Figure 4.9. Normal and drag forces vs. DOC for sharp cutter K in BSS before and after applying the IFA model

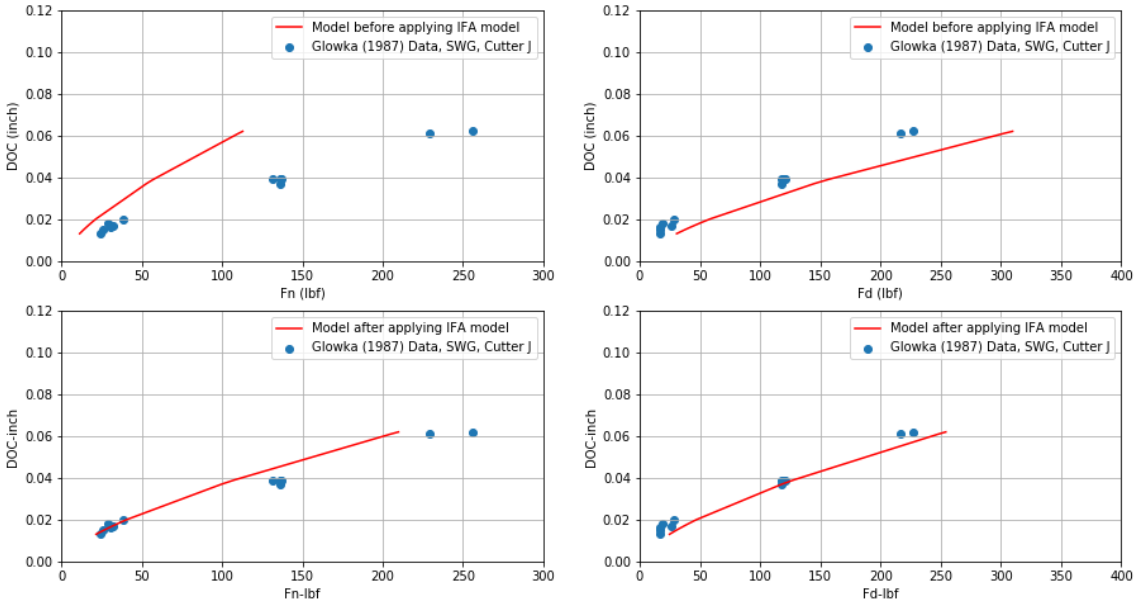

Figure 4.10. Normal and drag forces vs. DOC for sharp cutter J in SWG before and after applying the IFA model

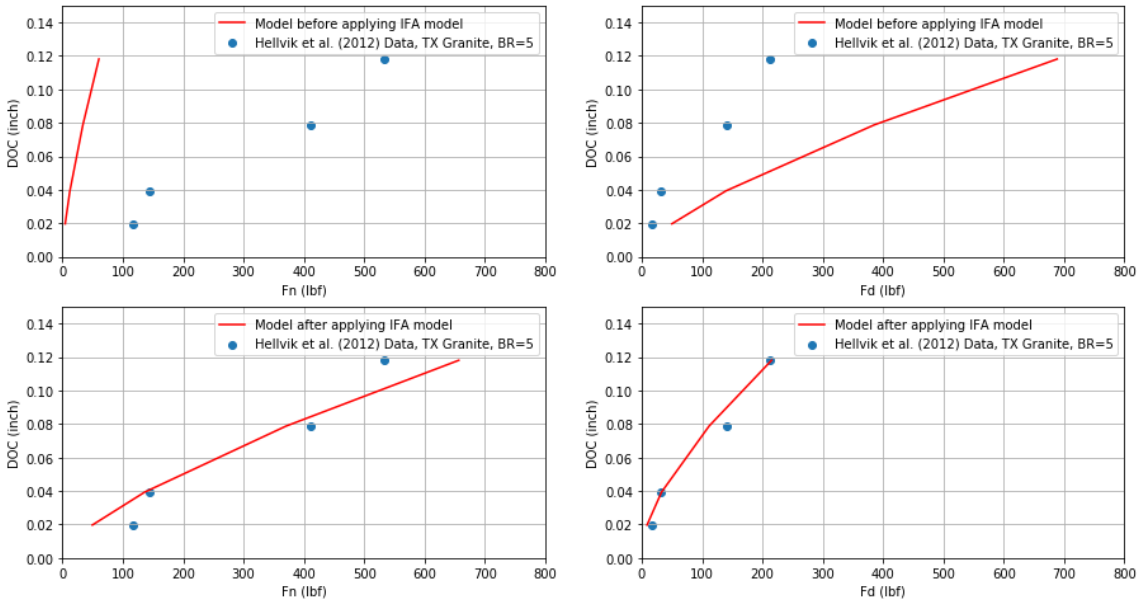

Figure 4.11. Normal and drag forces vs. DOC for sharp cutter with BR=5º in TX Granite (Hellvik et al., 2012)

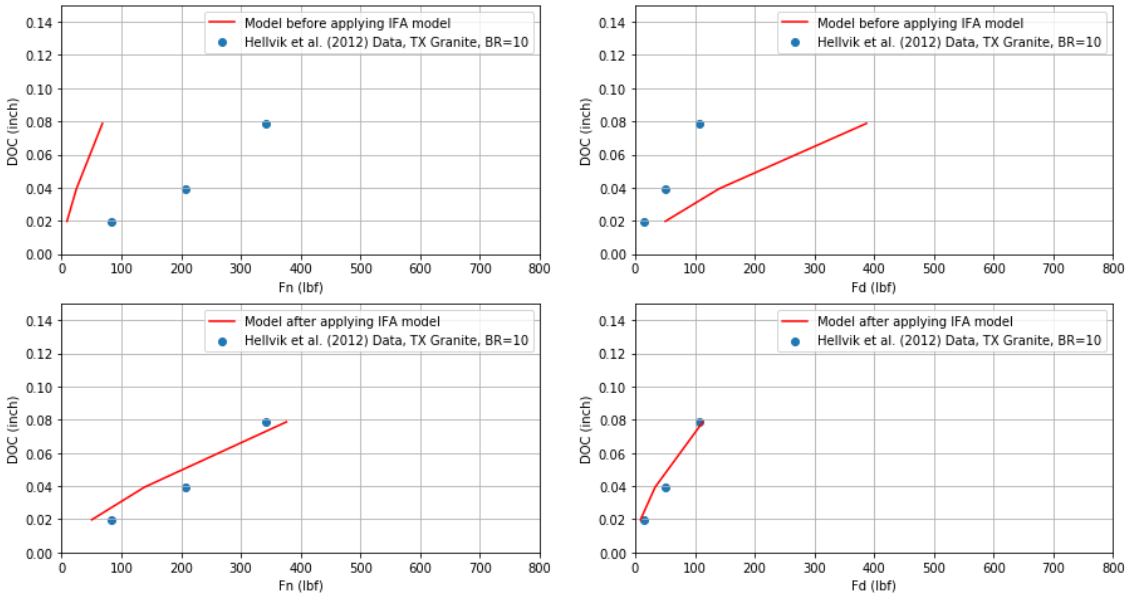

Figure 4.12. Normal and drag forces vs. DOC for sharp cutter with BR=10º in TX Granite (Hellvik et al., 2012)

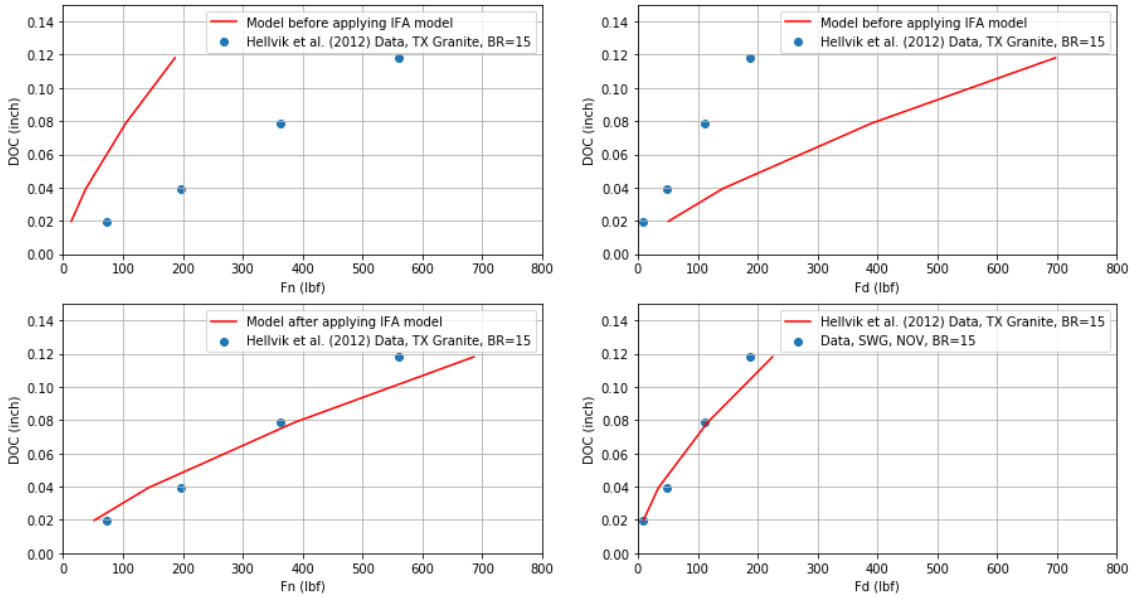

Figure 4.13. Normal and drag forces vs. DOC for sharp cutter with BR=15º in TX Granite (Hellvik et al., 2012)

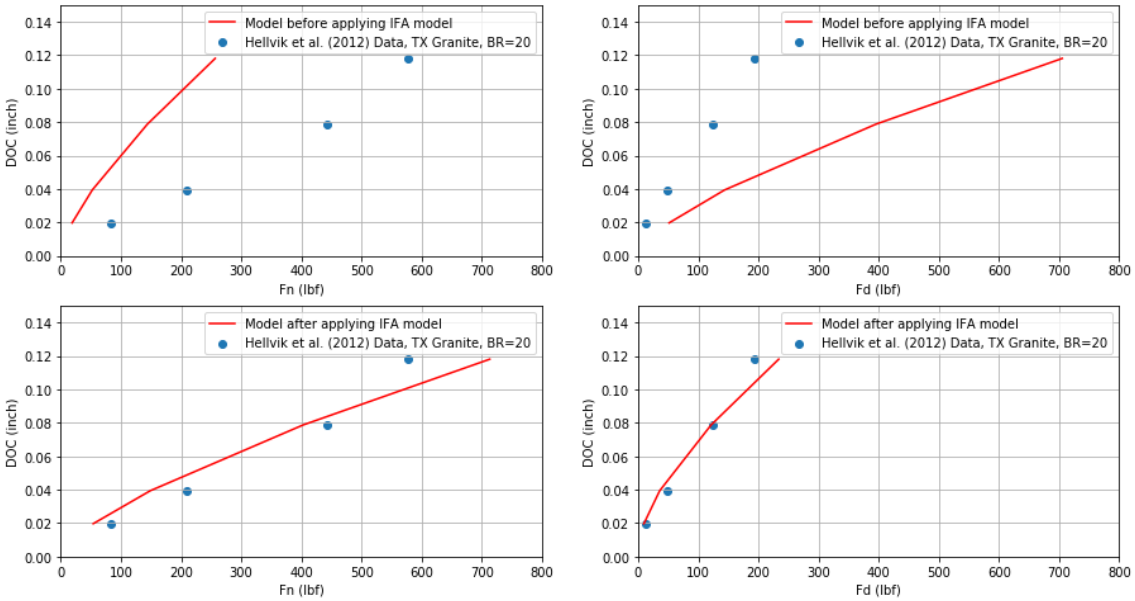

Figure 4.14. Normal and drag forces vs. DOC for sharp cutter with BR=20º in TX Granite (Hellvik et al., 2012)

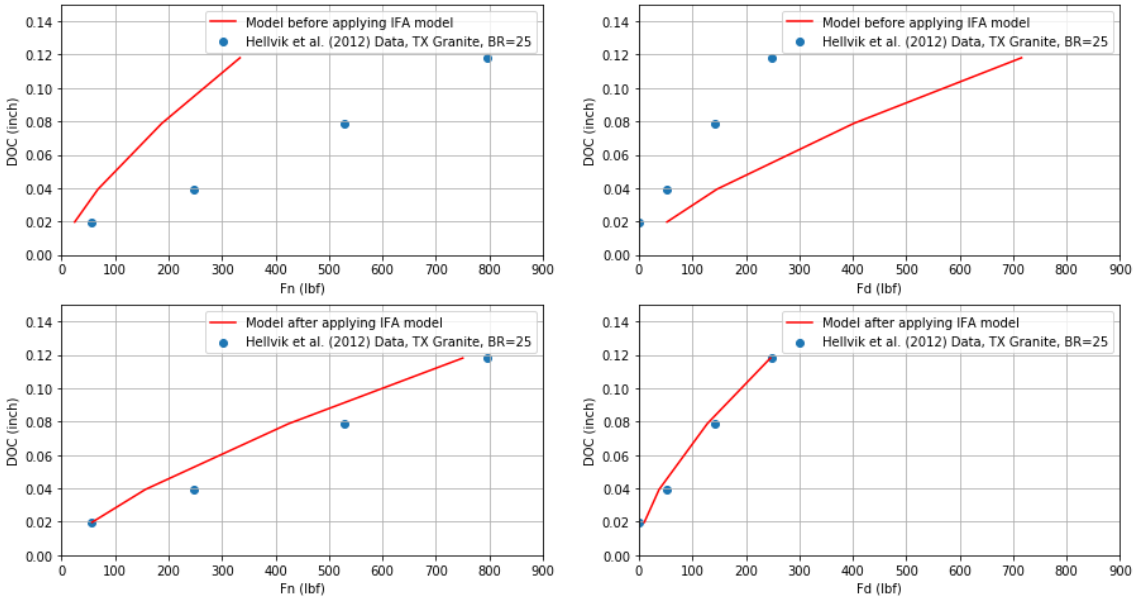

Figure 4.15. Normal and drag forces vs. DOC for sharp cutter with BR=25º in TX Granite (Hellvik et al., 2012)

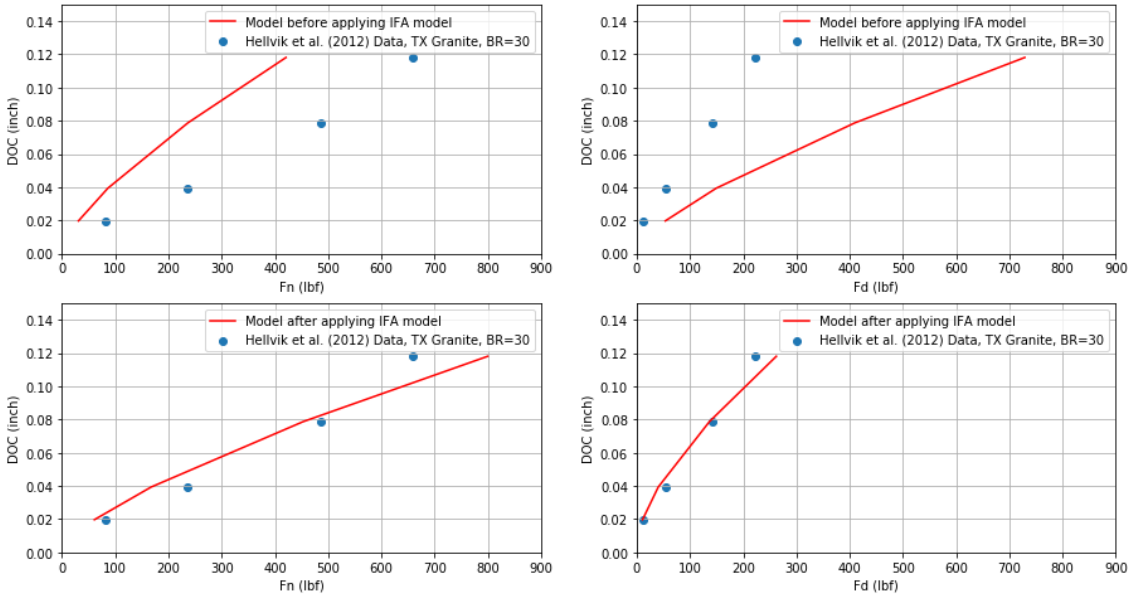

Figure 4.16. Normal and drag forces vs. DOC for sharp cutter with BR=30º in TX Granite (Hellvik et al., 2012)

As shown in Figure 4.8 to 4.16, the model underestimates and overestimates the cutter normal force and drag force respectively before applying the single cutter IFA model. The model provides an acceptable estimation for cutter forces after applying the single cutter IFA model. Theoretically, the cutter penetrates into the rock until the normal force over the area beneath the cutter becomes equal to

rock strength. For a fixed DOC, the ratio of the cutter front area to the underneath area with 20° BR is 2.74 ($\frac{1}{\tan(20)}$), however, this is true before the cutter begins cutting the rock. The interaction between the cutter face and rock results in interfacial friction. The direction of interfacial friction is upward and parallel to the cutter face. The interfacial friction can be translated to horizontal and vertical components as shown in Figure 4.17. The horizontal component of interfacial friction is in the same direction with theoretically calculated cutter drag force and therefore, it offsets a fraction of theoretically calculated cutter drag force. The normal component of interfacial friction is in the opposite direction of theoretically calculated cutter normal force and will be added to the cutter normal force (see Figure 4.17). Theoretically, it is expected that the BR angle governs the ratio of the cutter drag force to normal forces, while in practice, the ψ + BR appears as a governing angle. The ψ is called interfacial friction angle (IFA) and is calculated using the DD model. In Figure 4.17, the F_n and F_d are cutter normal and drag forces during the cutting process.

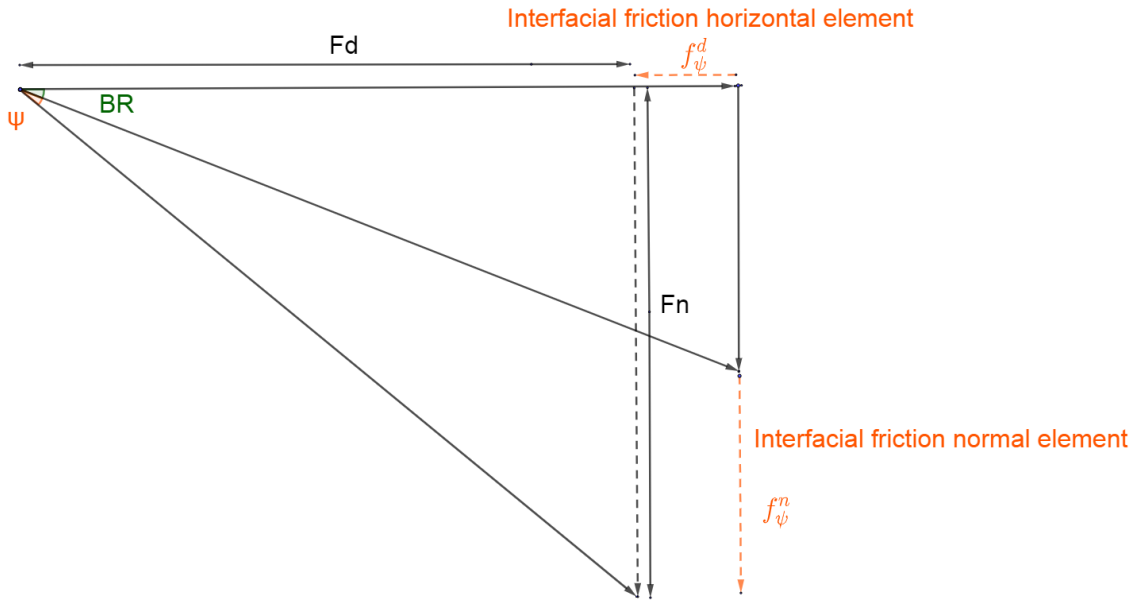

Figure 4.17. Schematic of cutter normal and drag forces and interfacial friction effect

4.2.2 Blunt cutter force model verification

Cutter D from Glowka (1987) single cutter tests (see table 4.1) was included in set of data as a representative for the blunt cutter for fitting the single cutter IFA model. The cutter D with a total wear flat area of 0.02 square inch and 20º BR angle was dragged on the SWG slab at a constant velocity of 2.1 inches per second. For a blunt cutter, the wear flat area affects the cutter forces beside the interfacial friction. In this case, the cutter forces are calculated before and after applying the IFA model as shown in Figure 4.18. The cutter wear flat area is multiplied with the rock UCS to calculate the additional normal penetration force needed for cutter D to achieve the DOC (Equation 3.31 and 3.32). The additional normal force is added to the calculated normal force (after applying single cutter IFA model) to incorporate the effect of the wear flat area.

Also, the additional normal force (wear flat area times UCS) is multiplied with the rock internal friction angle to achieve the frictional force (due to rock internal friction) at the wear flat area.

The friction coefficient at cutter wear flat– rock contact area is assumed equal to rock internal friction angle. This is due to adhesion of a thin layer of broken rock cuttings into the cutter wear flat area which was observed for carbonate rock by Dagrain and Richard in 2006 (Dagrain and Richard, 2006) and therefore, the interfacial friction is only function of rock and not wear flat area surface finish (Rahmani, 2013).

Detournay and Defourny in 1992 plotted the E-S diagram for BSS for Glowka single cutter tests. The plots give a straight line for BSS with slop equal to the friction coefficient at rock-wear flat contact area, which it is equal to 0.82 for BSS. They mentioned that this value (0.82) is close to rock internal friction coefficient and it is unusually high compared to reported values of the contact friction coefficient between tungsten carbide and sandstone.

Similar approach was used to calculate the SWG internal friction angle which is used in Equation 3.31 and 3.32 to calculate the cutter normal and drag forces. In Figure 4.18, the E-S diagram for cutter D

data from Glowka (1987) tests is shown. The slope of friction line is Figure 4.18 is close to 0.6 (0.5947) and it is used as SWG internal friction angle in single cutter model for blunt cutters (Equation 3.31 and 3.32) to calculate the cutter normal and drag forces.

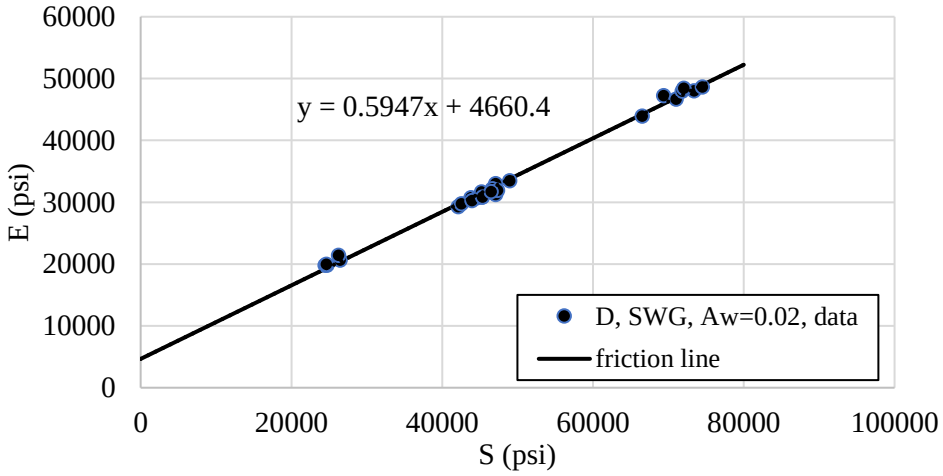

Figure 4.18. E-S diagram for blunt cutter D in SWG and friction line

The resultant frictional force at the cutter wear flat area is in the opposite direction of cutter movement and therefore is added to the cutter estimated drag force from the previous step (after applying the IFA model). The final estimation for cutter normal and drag forces are seen at the bottom of Figure 4.19.

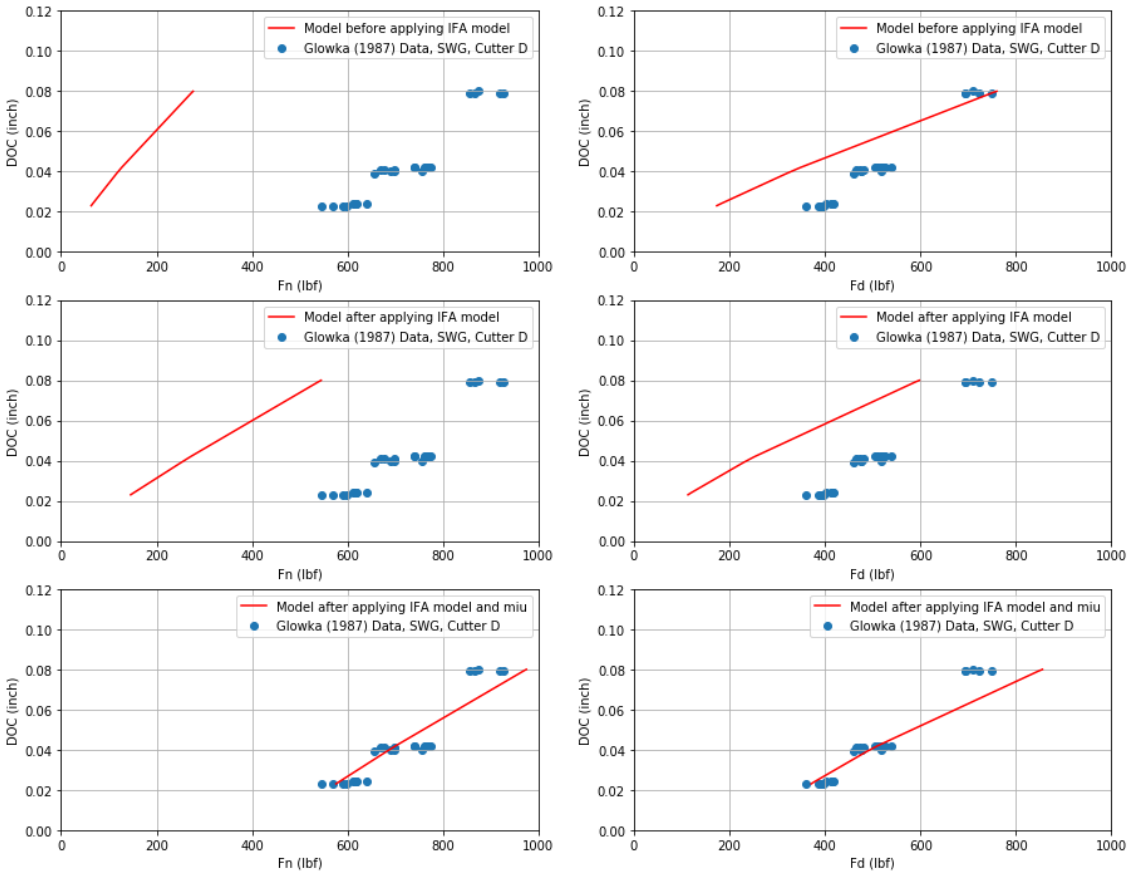

Figure 4.19. Comparison between model and data cutter normal and drag force for blunt cutter D in SWG before and after applying the IFA model and μ

4.3 New full bit ROP model fitting results

The full bit test data in SWG from Sandia National Lab was used for developing full bit IFA model (Raymond et al., 2015). Two Ulterra bit designs were tested, one with four and one with five blades with 3.75-inch diameter which had been used for testing at the Sandia National Laboratories (SNL) Hard Rock Drilling Facility (HRDF). Both PDC bits have twelve cutters at bit face and the equivalent cutters have an average of 20º BR and a 0.5-inch diameter. Figure 4.20 and 4.21, show the face view of the four and five-bladed PDC bits respectively.

Figure 4.20. Face view photograph of four-bladed PDC bit

Figure 4.21. Face view photograph of five-bladed PDC bit

The bit details including the number of cutters, cutters diameter, equivalent cutter BR angle, and rock types are shown in table 4.2 (see appendix G).

Table 4.2. Bits details used for developing full bit IFA model

	Number of blades	Number of cutters	Size (inch)	Equivalent cutter BR	RPM	Rock type
Bit # 1	4	12	3.75	20	100	SWG
Bit # 1	4	12	3.75	20	150	SWG
Bit # 1	4	12	3.75	20	200	SWG
Bit # 1	4	12	3.75	20	100	BSS
Bit # 1	4	12	3.75	20	150	BSS
Bit # 1	4	12	3.75	20	200	BSS
Bit # 2	5	12	3.75	20	100	SWG
Bit # 2	5	12	3.75	20	150	SWG
Bit # 2	5	12	3.75	20	200	SWG
Bit # 2	5	12	3.75	20	100	BSS
Bit # 2	5	12	3.75	20	150	BSS
Bit # 2	5	12	3.75	20	200	BSS

The differential evolution algorithm (DEA) was used to solve the full bit IFA model (Equation 3.21 through 3.28) and ROP models simultaneously. The goal is to find the constants of the full bit IFA model that will improve the model ROP estimation for all tests in table 4.2.

The following steps are taken to solve the ROP model (Equation 3.33) and the full bit IFA model (Equation 3.21 through 3.28) simultaneously.

The DEA generates a predetermined number of full bit IFA model constants (step 1 in Figure 4.22) in preset ranges which will be used to estimate the ROP for all cases in table 4.2 by the computer program (see Figure 4.22).

The computer program chose a full bit IFA model in step 1 and utilized the full bit data (data points) to calculate the fitness through step 2 and 3. In step 3, the computer program changed ψ_1, ranging between 0 to 70 (BR complementary angle) in 0.1 step intervals, and each time it calculated the absolute different between ψ_1 and ψ_2 (see Figure 4.22, step 3). The ψ_1 values were used to adjust the cutter front area (A_v), which is plugged into Equation 3.33 to calculate the ROP. The ROP value was divided by the RPM to obtain DOC, and the DOC was used along with the UCS and cutter velocity to calculate a new IFA (ψ_2) using a full bit IFA model selected in step 2.

The ψ_2 in step 3, is the full bit IFA model output which was selected in step 2. The ψ_1 that resulted in minimum absolute difference between ψ_1 and ψ_2 was selected as the best ψ value and was saved in the table in step 4 for each data point. The computer program used the next data point in step 2 and repeated the procedure in step 3 and 4 to find the best ψ value. The best ψ values were used to adjust the cutter front area and to calculate the PDC bit ROP. The summation of absolute difference between data and model ROP was calculated and reported as the full bit IFA model fitness. The procedure was written in Python and provided in Appendix F. The computer program took the same approach toward all full bit IFA models (step 1) and calculated a fitness value. The DEA used the full bit IFA model fitness and generated a new set of full bit IFA models which were later used for ROP calculation. Note that a condition should be applied to the program to make sure descending IFA values versus WOB are achieved. This is because the IFA decreases with an increase in cutter DOC as seen in the single cutter experiments.

The procedure was repeated until the algorithm received a maximum number of iterations, in this case 300. The full bit IFA model is provided in Equations 4.5 through 4.11.

$$\psi_{\text{full bit}} + \text{BR} = \text{a} + \left[\frac{\text{b}}{(\text{DOC}_\text{n})^{1.58} + \text{d}}\right] \ldots\ldots \text{Eq. 4.5}$$

$$\text{a} = \left(57.3 - \frac{96.44}{(\text{Vn})^{0.753} + 2.22}\right) \ldots\ldots \text{Eq. 4.9}$$

$$\text{b} = \left(1.886 + \frac{0.48}{(\text{Vn})^{1.6} + 0.79}\right) \ldots\ldots \text{Eq. 4.10}$$

$$\text{d} = \left(\frac{1.07}{(\text{UCSn})^{1.9} + 3}\right) \ldots\ldots \text{Eq. 4.11}$$

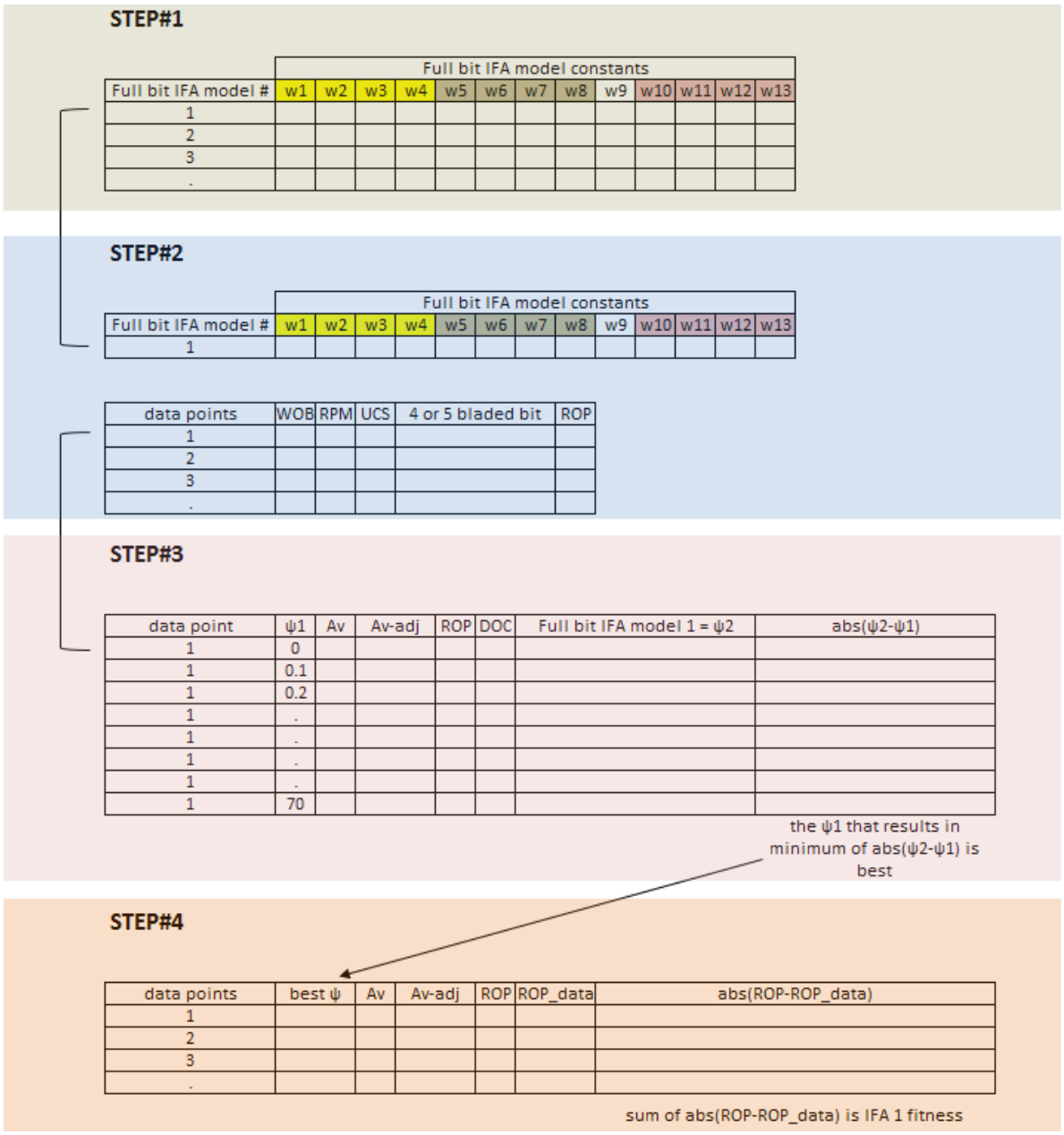

Figure 4.22. Developing full bit IFA model procedure

The blade coefficients of 0.9 and 1.07 were used to incorporate the blade effect in the ROP model for four and five bladed bits respectively. Figure 4.23 through 4.25 compares the ROP model estimation with reported ROP for four-bladed bits at different RPMs.

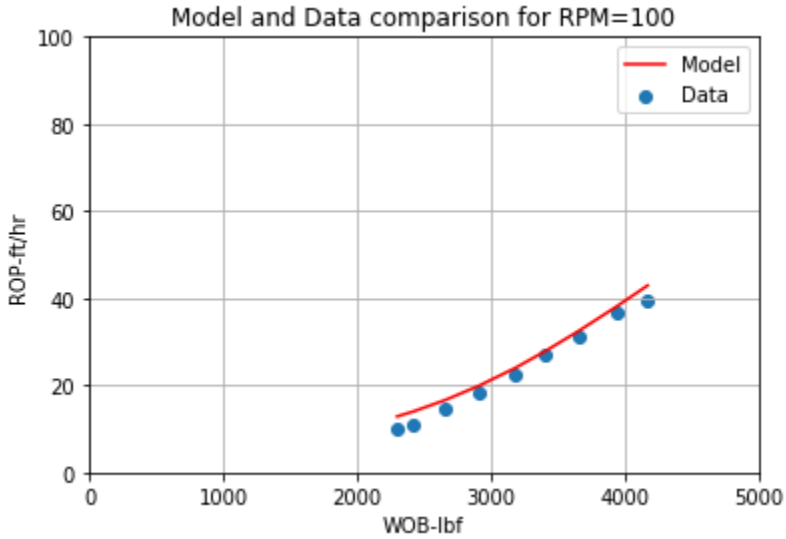

Figure 4.23. Comparison between the model and data ROP for four-bladed PDC bit at RPM=100 in SWG

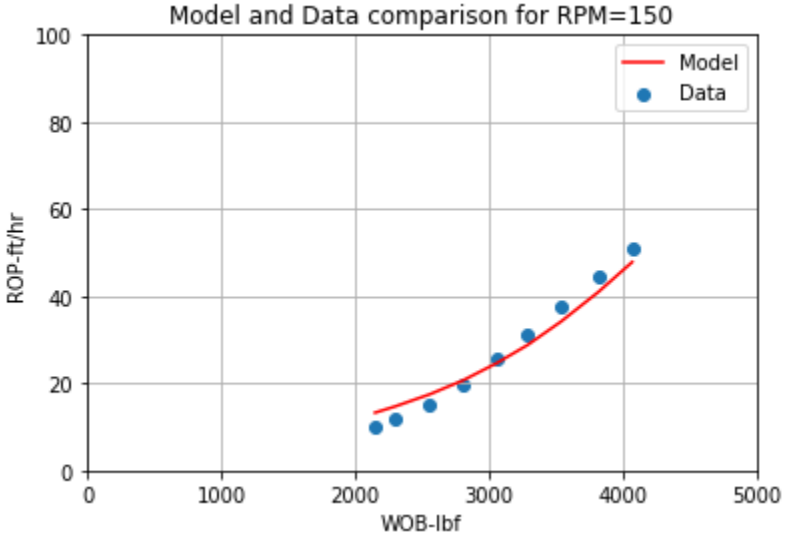

Figure 4.24. Comparison between the model and data ROP for four-bladed PDC bit at RPM=150 in SWG

Figure 4.25. Comparison between the model and data ROP for four-bladed PDC bit at RPM=200 in SWG

The comparison between the data and model are shown in Figure 4.26. In Figure 4.26, the red and black lines are representative for 10% up and down margin for a perfect match of the ROP values. It is observed that all model predictions are in the ± 10% margin of data points.

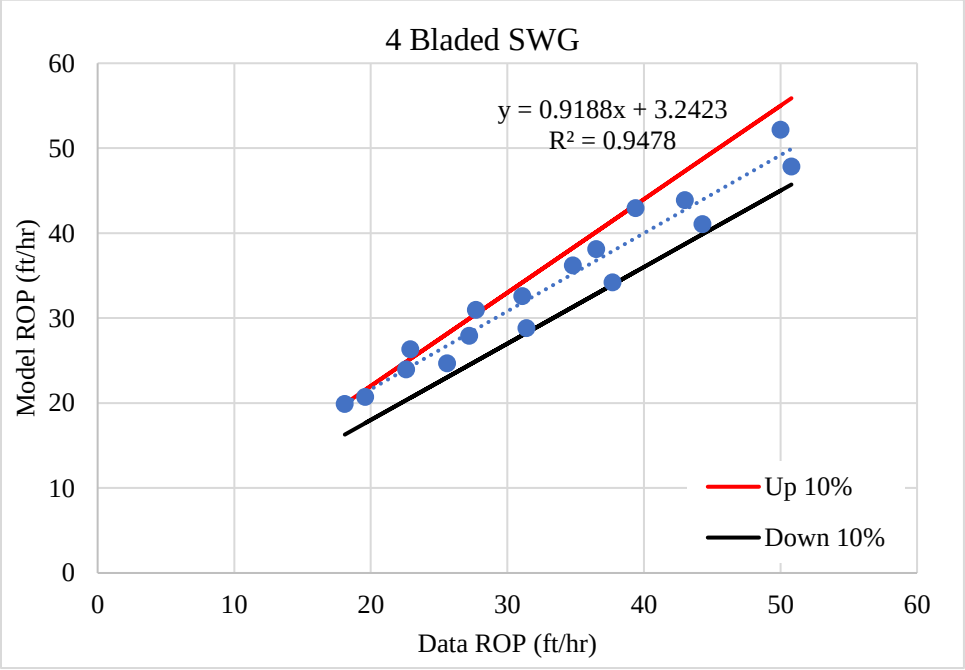

Figure 4.26. Comparison between the data and model for four bladed-bit in SWG

In Figure 4.27, three lines are fit on the model predictions (100 RPM, 150 RPM, and 200 RPM) for a four bladed bit in SWG and plotted along with the data points. It is observed that the lines intersect at a point (shown with yellow arrow) around 2420 lbf and two phases are recognized which are representative for the inefficient and efficient drilling process. Detournay et al. (2008) characterized the phase I by increasing the contact of wear flat area as the depth of cut slowly increases with the WOB (Spencer et al., 2017). The phase II begins once a threshold depth of cut has been achieved such that the rock cannot support the additional normal stress on cutter wear flat area. Therefore, applying additional normal stress results in driving the cutter further into the rock, which finally causes the bit to increase as if perfectly sharp (Spencer et al., 2017). The effective drilling occurs in phase II, and thus represents the target operating region.

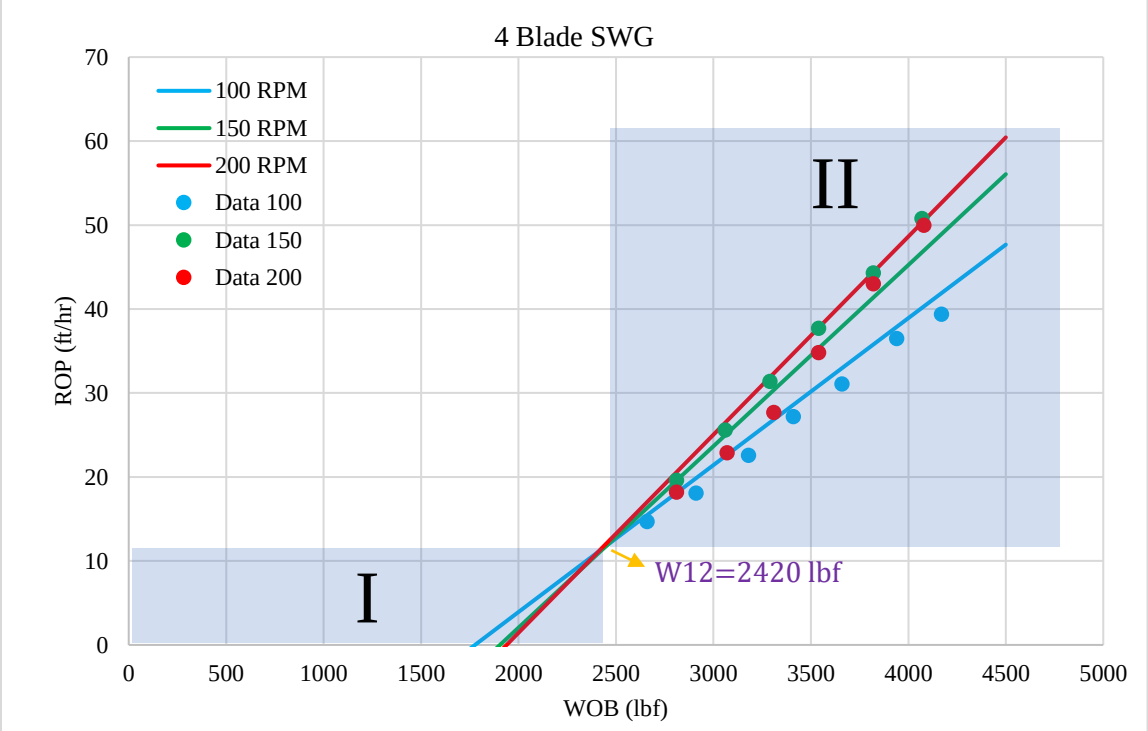

Figure 4.27. The cutting point and two cutting phases for a four-bladed bit in SWG

Figure 4.28 through 4.30 compare the ROP model estimation with reported ROP for a five-bladed bit at different RPMs in SWG.

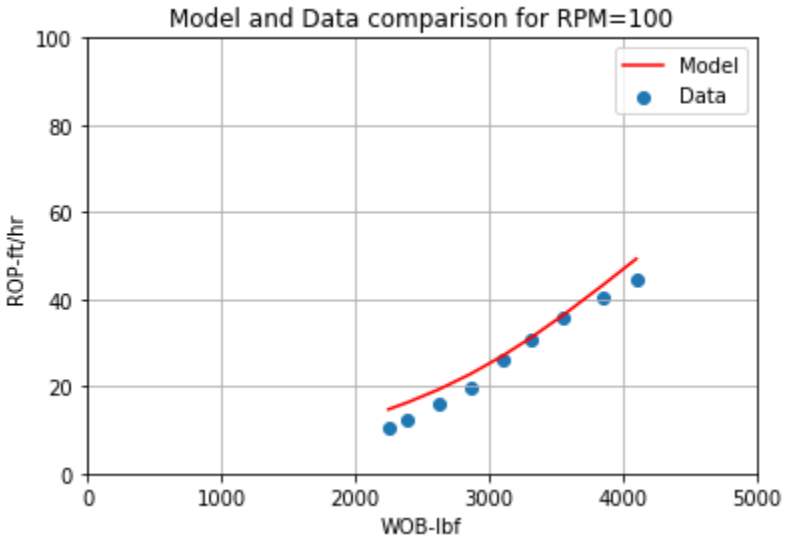

Figure 4.28. Comparison between the model and data ROP for five-bladed PDC bit at RPM=100 in SWG

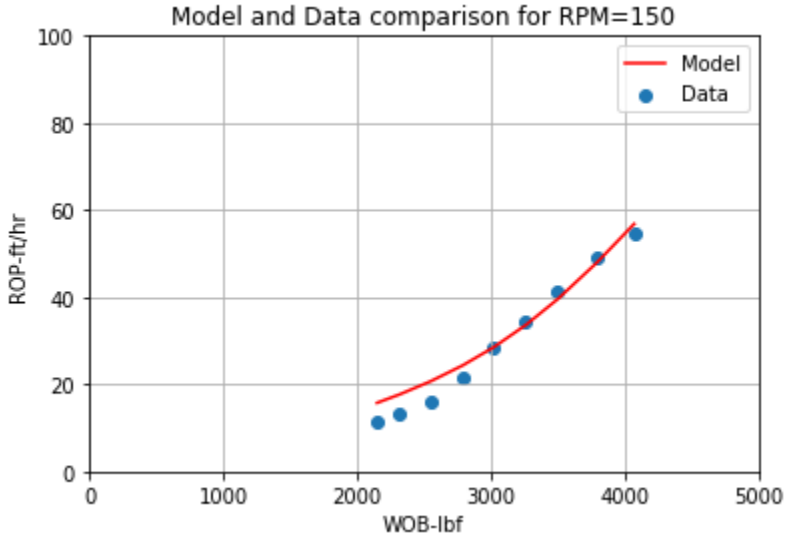

Figure 4.29. Comparison between the model and data ROP for five-bladed PDC bit at RPM=150 in SWG

Figure 4.30. Comparison between the model and data ROP for five-bladed PDC bit at RPM=200 in SWG

Similar to four bladed bits in SWG, it is observed that most model predictions are in the ± 10% margin of data points (see Figure 4.31).

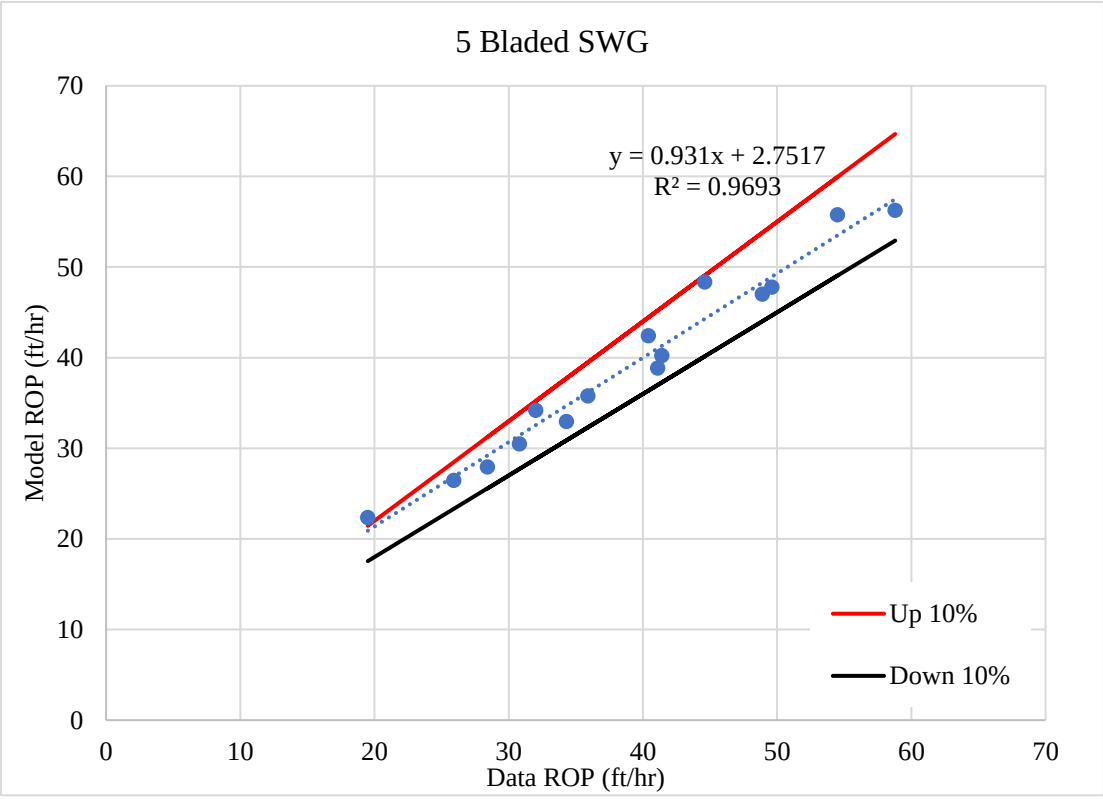

Figure 4.31. Comparison between the data and model for five bladed-bit in SWG

In Figure 4.32, three lines are fit on the model predictions (100 RPM, 150 RPM, and 200 RPM) for five bladed bit in SWG and plotted along with the data points.

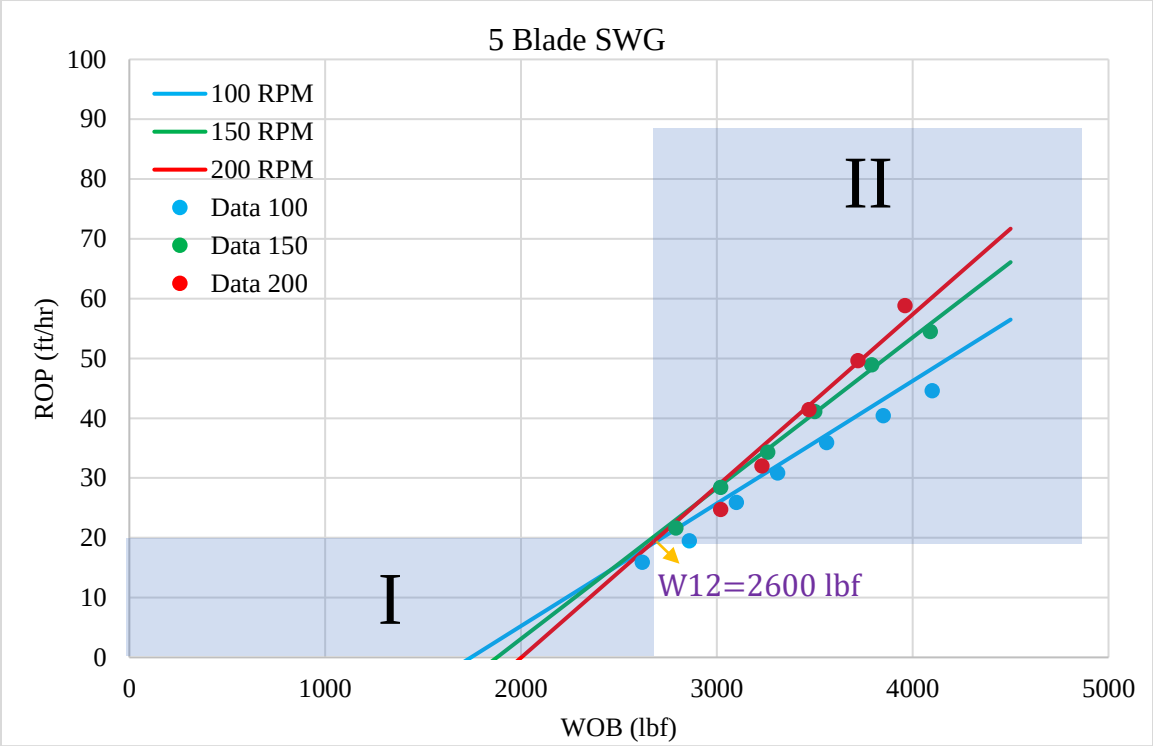

Figure 4.32. The cutting point and two cutting phases for a five-bladed bit in SWG

Figure 4.33 through 4.35 compare the ROP model estimation with reported ROP for a four-bladed bit at different RPMs in BSS.

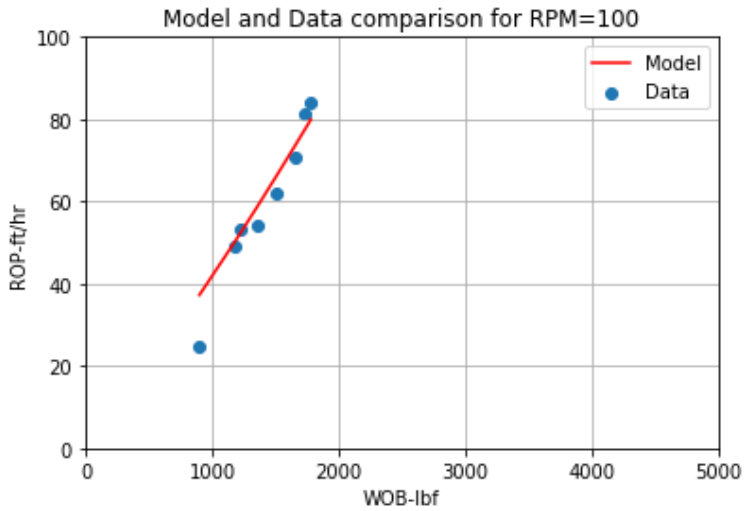

Figure 4.33. Comparison between the model and data ROP for four-bladed PDC bit at RPM=100 in BSS

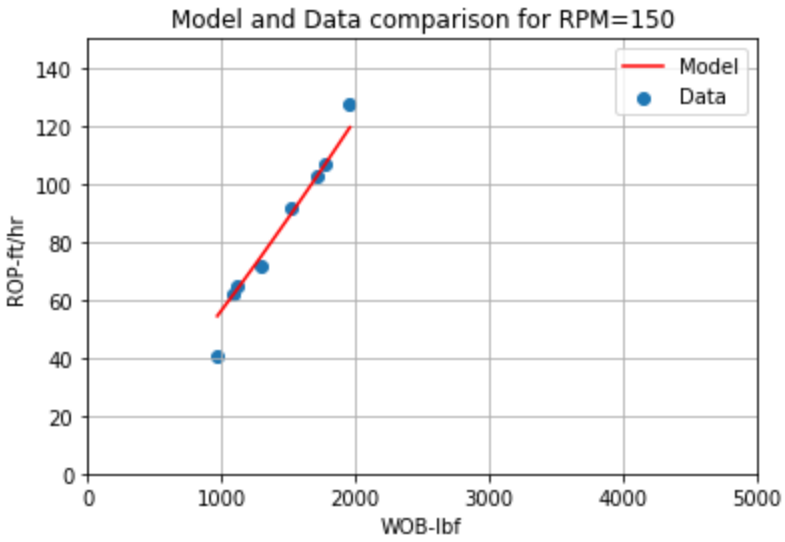

Figure 4.34. Comparison between the model and data ROP for four-bladed PDC bit at RPM=150 in BSS

Figure 4.35. Comparison between the model and data ROP for four-bladed PDC bit at RPM=200 in BSS

The model predictions are in the $\pm$ 10% margin of data points as is shown in the Figure 4.36.

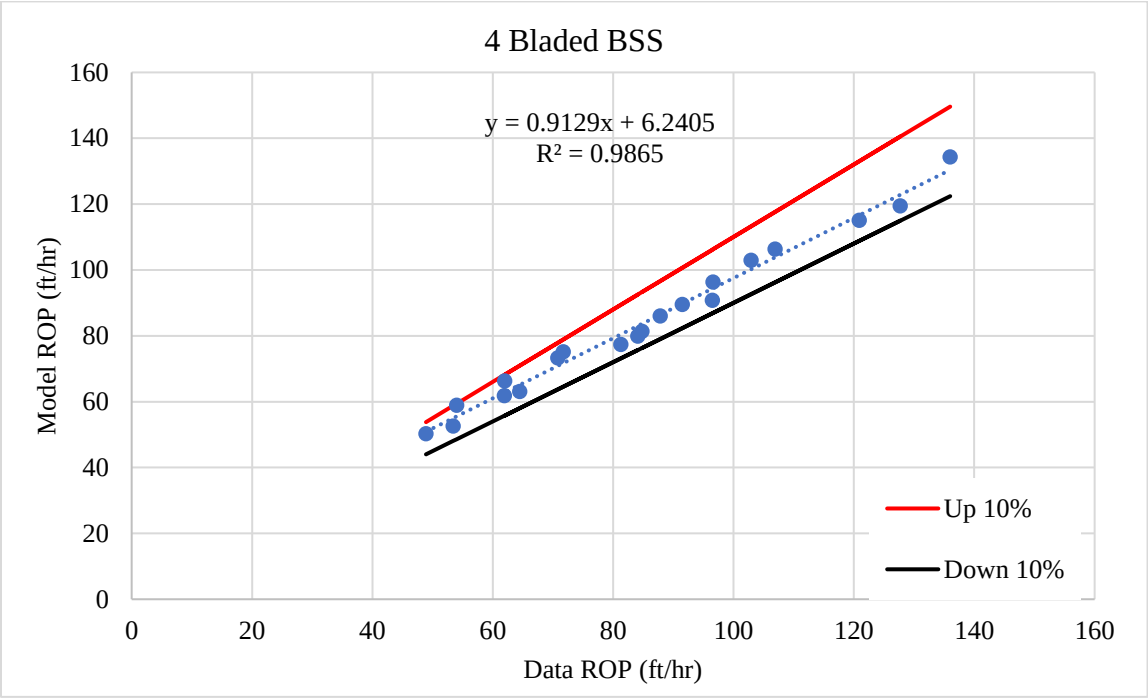

Figure 4.36. Comparison between the data and model for four bladed-bit in BSS

In Figure 4.37, three lines are fit with the model predictions (100 RPM, 150 RPM, and 200 RPM) for the four bladed bits in BSS and plotted along with the data points.

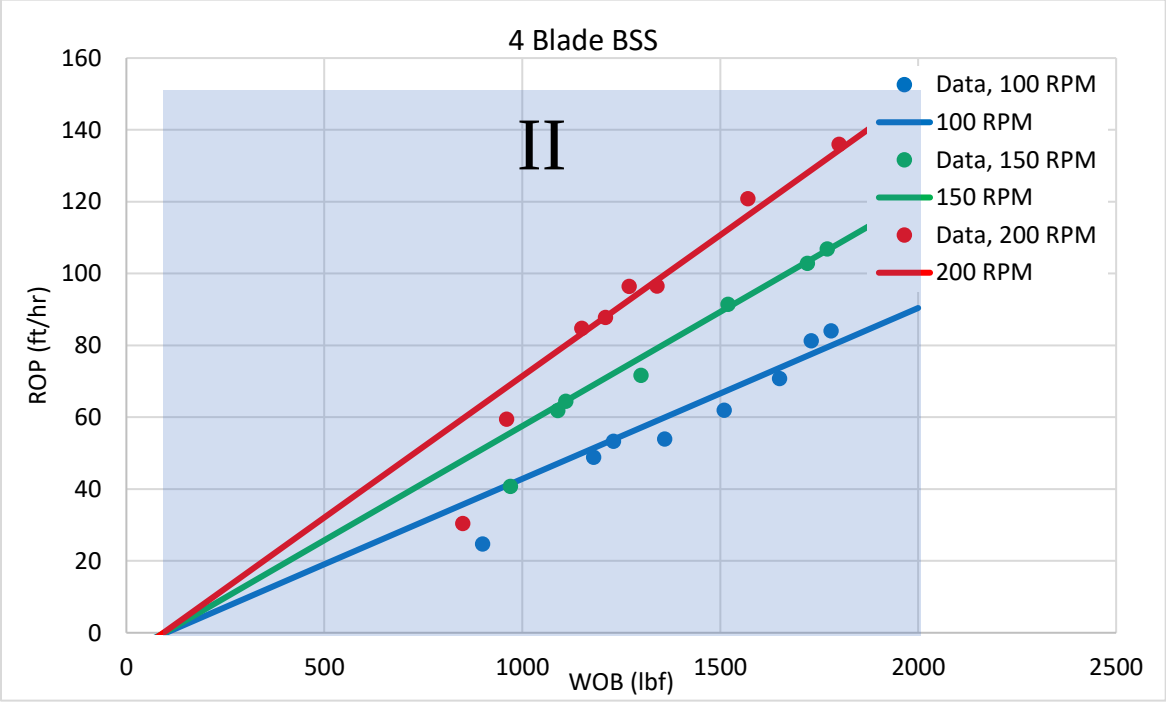

Figure 4.37. The cutting point and phase II for a four-bladed bit in BSS

Figure 4.38 through 4.40 compares the ROP model estimation with reported ROP for a five-bladed bit at different RPMs in BSS. The model provides a good estimation for data points (all estimations are in $\pm$ 10% margin) as is shown in the Figure 4.41.

Figure 4.38. Comparison between the model and data ROP for five-bladed PDC bit at RPM=100 in BSS

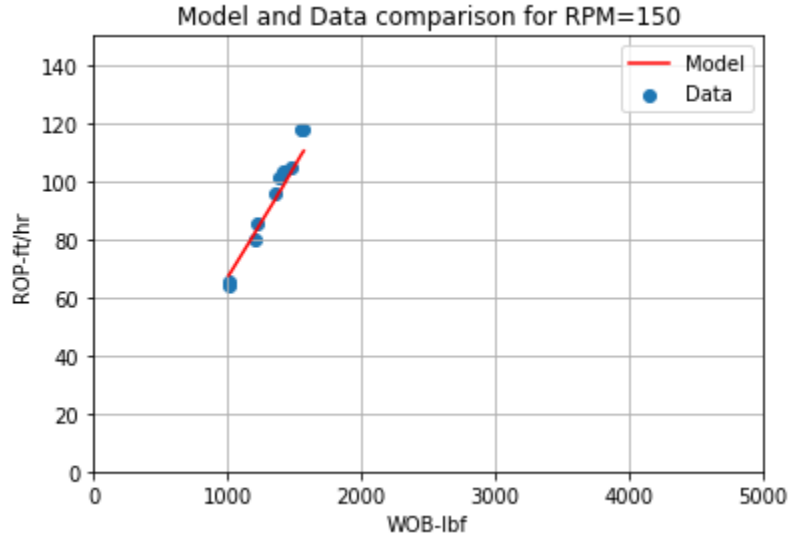

Figure 4.39. Comparison between the model and data ROP for five-bladed PDC bit at RPM=150 in BSS

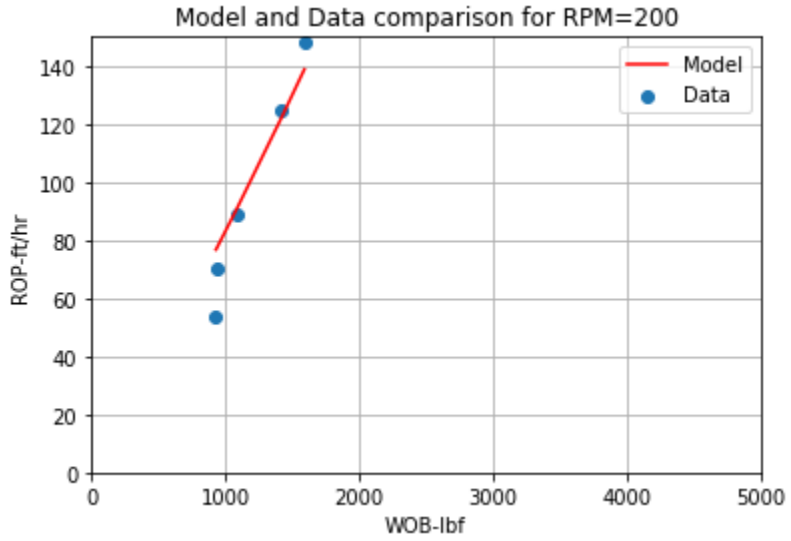

Figure 4.40. Comparison between the model and data ROP for five-bladed PDC bit at RPM=200 in BSS

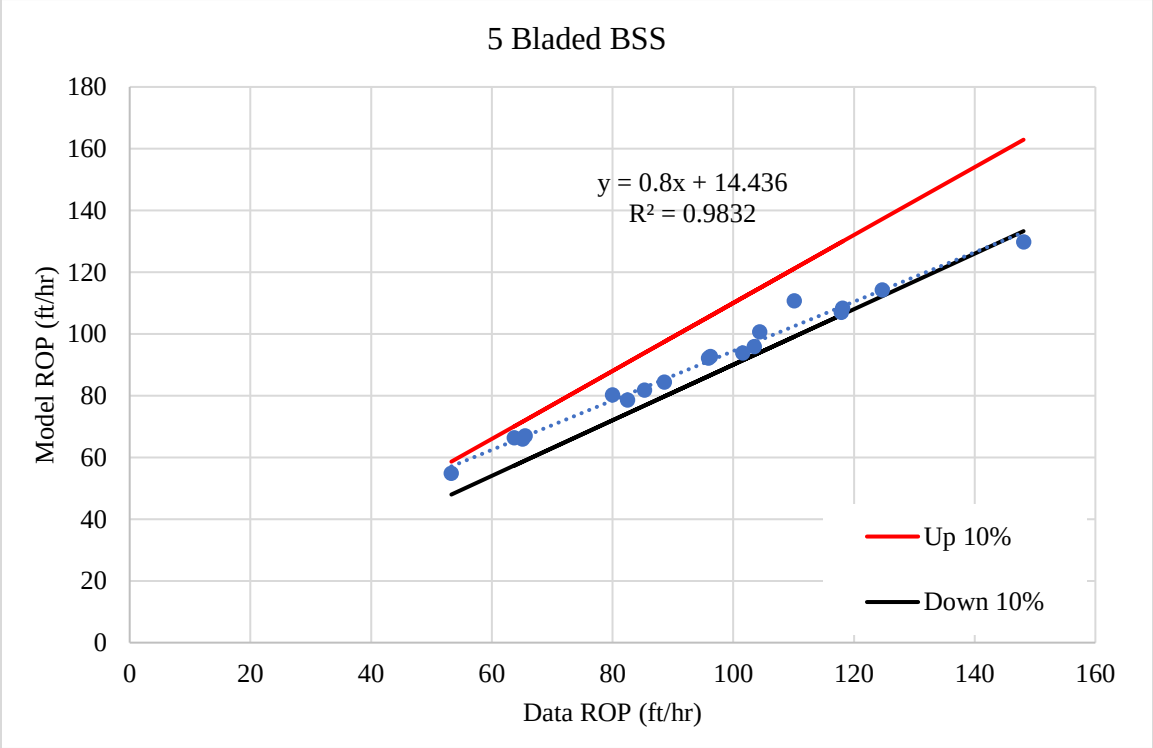

Figure 4.41. Comparison between the data and model ROP values for five bladed-bit in BSS

In Figure 4.42, three lines are fit on the model predictions (100 RPM, 150 RPM, and 200 RPM) for a five bladed bit in BSS and plotted along with the data points. As is expected for soft rocks, there is no phase I and a linear relation between WOB and ROP exists.

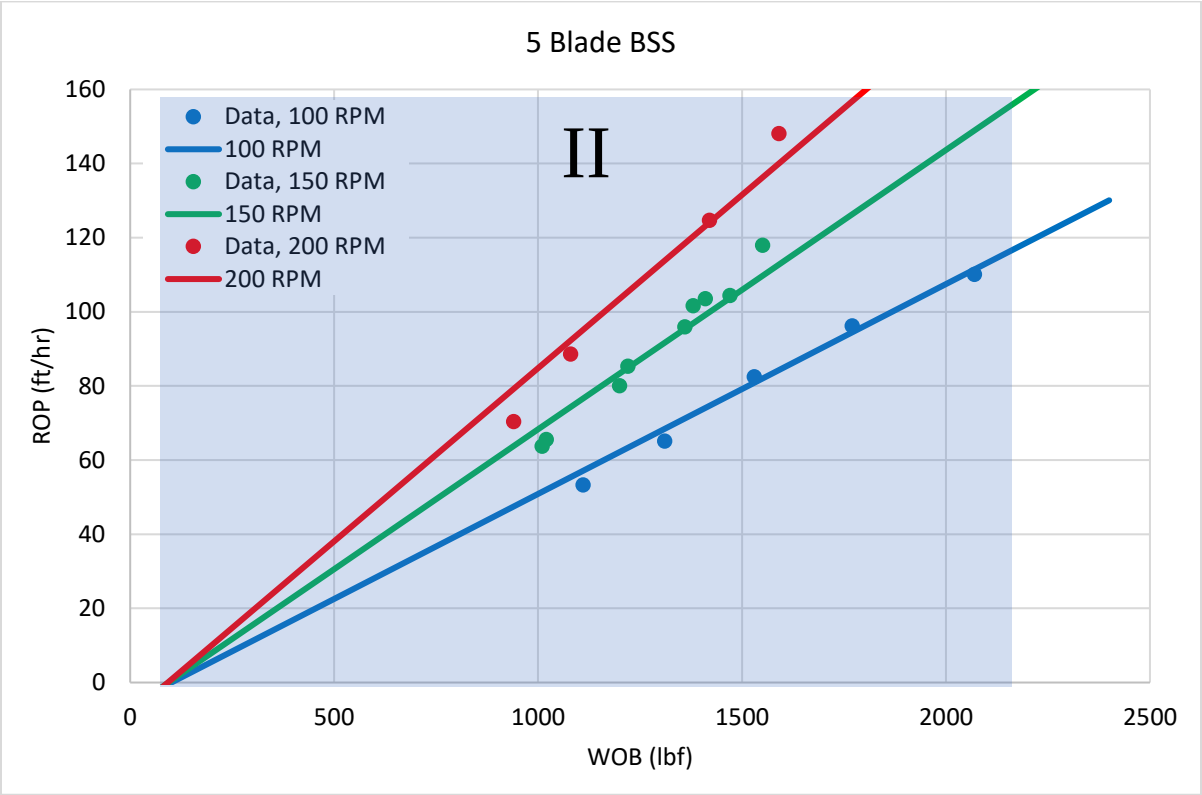

Figure 4.42. The cutting point and phase II for five-bladed bit in BSS

4.4 Sensitivity analysis of the newly developed PDC ROP model

A sensitivity analysis was performed on the newly developed PDC ROP model to investigate the effect of operational parameters (WOB and RPM) and bit design parameters. The analyzed parameters included WOB, RPM, bit diameter, and rock strength. The base cases for the aforementioned parameters were selected to run the analysis as shown in table 4.3.

Table 4.3. The base case numerical values used for full bit PDC ROP model sensitivity analysis

Parameters	base case numerical values
WOB (lbf)	8000
RPM	100
UCS (psi)	20000
Bit diameter (inch)	8.5
Number of cutters	30
ROP (ft/hr)	28.02

The drilling rate of penetration functionality also was plotted and displayed Figures 4.43 through 4.46.

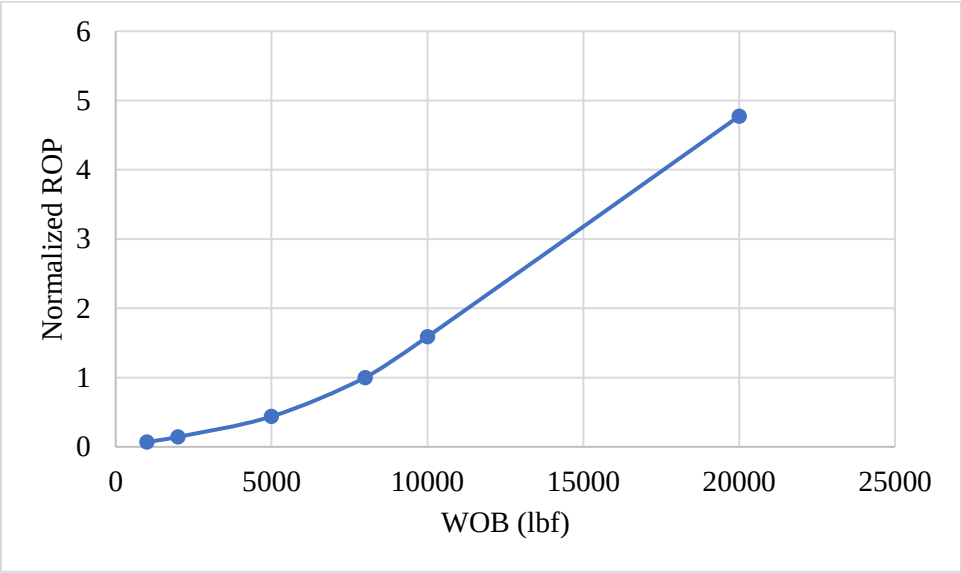

Figure 4.43. The drilling rate of penetration response to increase in WOB

The analysis of sensitivity of the rate of penetration on WOB shows that the drilling rate of penetration increases with an increase in WOB. The two drilling phases which are representative for inefficient and efficient drilling are detectable. The model was developed based on 100% efficient bottom hole cleaning and does not include the effect of hydraulics, yet. Therefore, the ROP model does not show decline in ROP curve once the flounder point is achieved.

The graph below (Figure 4.44) shows that the drilling rate of penetration increases versus RPM, however, the ROP-RPM trend is different for low and high RPM values. At lower RPM, the amount of the rock that is cut from the formation increases linearly with RPM which results in a linear trend for ROP versus RPM. At higher RPM values, the interfacial friction affects the cutter forces, which consequently reduces the bit equivalent DOC and ROP. The RPM nonlinearity can be due either to the interfacial friction angle or the change in rock strength (strain rate effect) as it was observed by Sano

et al. in 1981. In this study, it was assumed that the cutter velocity influenced the cutter interfacial friction angle, and therefore the cutter velocity was included in the IFA model.

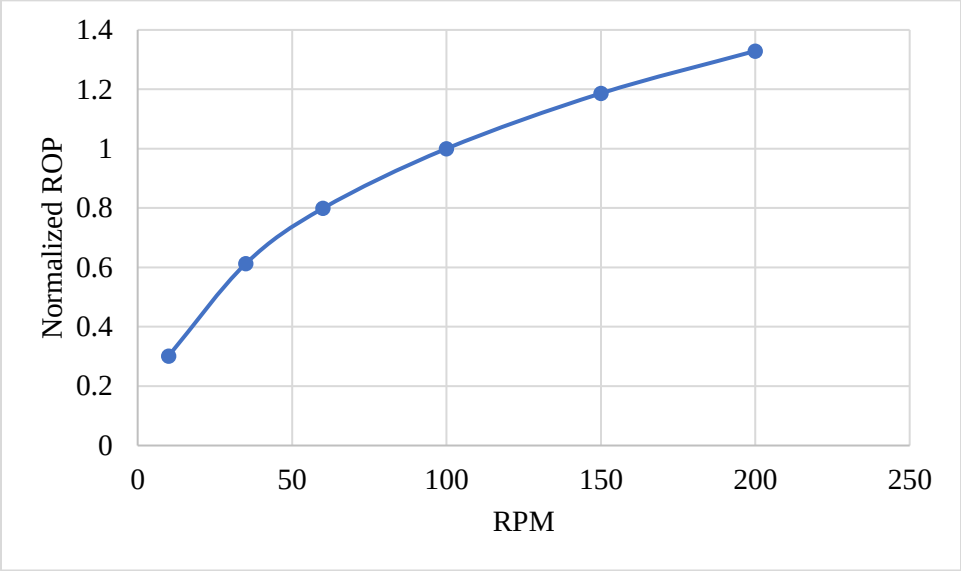

Figure 4.44. The drilling rate of penetration response to increase in RPM

Figure 4.45 shows the sensitivity analysis of bit diameter on PDC rate of penetration. Increase in bit diameter results in decrease in drilling rate of penetration as shown in the following graph. As the bit diameter increases at constant WOB, the larger volume is needed to be drilled by the bit per unit time, which consequently reduces the drilling rate.

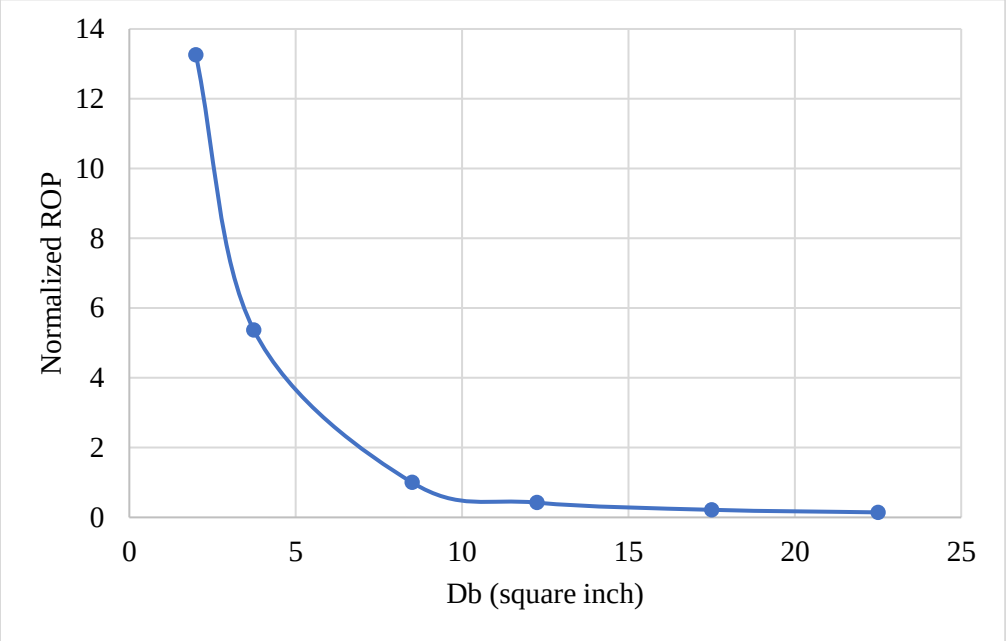

Figure 4.45. The drilling rate of penetration response to increase in bit diameter

Figure 4.46 shows the effect of rock compressive strength on PDC rate of penetration. As it is expected, the drilling rate of penetration decreases versus rock compressive strength. At constant WOB, the harder the rock (higher UCS values) is, the lower cutter DOC and ROP would be. In this case, it is observed that for UCS higher than 30,000 psi, zero drilling rate of penetration is achieved. For UCS values higher than 30,000 psi, the average stress on each PDC cutter (30 in this case) is so small that it results in small DOC values. The small DOC values result in higher interfacial friction angle (close to cutter complementary angle, i.e. 70º). The higher the IFA values are, the lower the adjusted cutter front area would be.

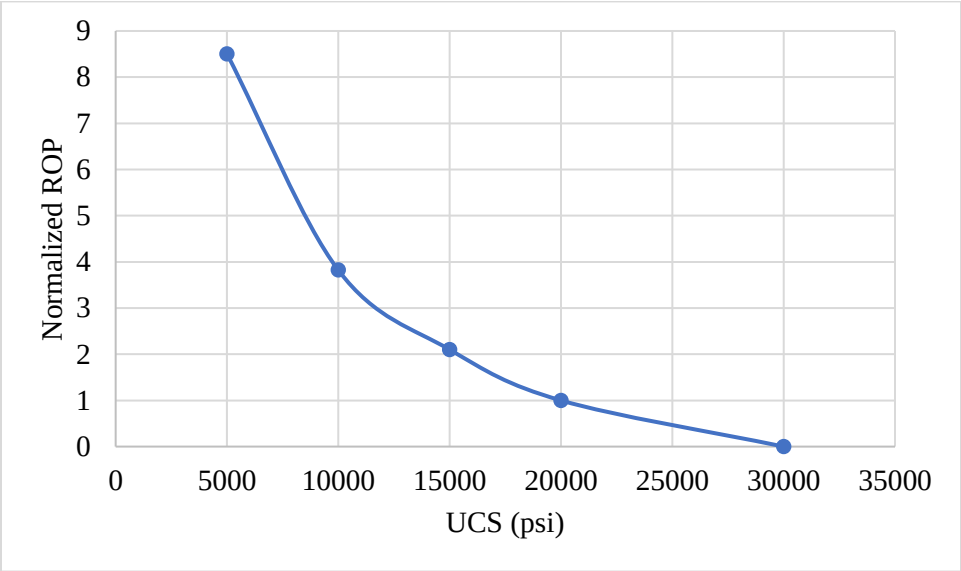

Figure 4.46. The drilling rate of penetration response to increase in UCS

The normalized sensitivity analysis of all above parameters are provided in the Figure 4.47.

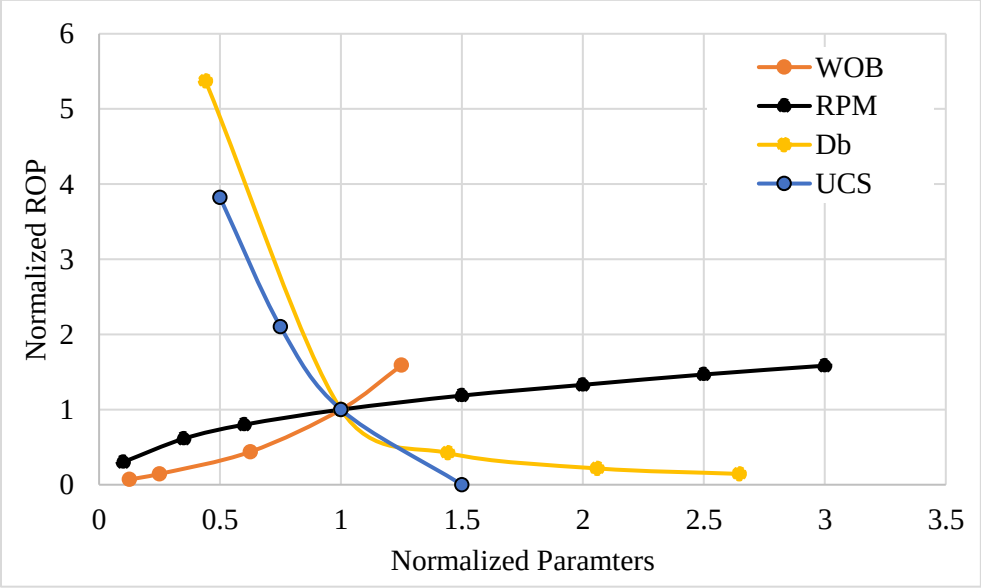

Figure 4.47. The PDC ROP model sensitivity analysis

4.5 PDC ROP model verification

At the following the PDC ROP model is verified for a bit with bigger diameter (8.5 inch) at several CCS, three RPM, and two equivalent BR angles. Warren and Armagost in 1988, evaluated the

performance of the 8.5-inch PDC bit in Carthage lime stone. The Winters et al. (1987 b) measured the rock compressive strength under different CP (see Figure 4.48).

The developed ROP Model in this study is applied along with the full bit IFA model for ROP estimation and the results are provided in the Figure 4.49 through 4.54. The Carthage limestone CCS was calculated taking the data from Winters et al. (1987 b) test data and CP into account. The CCS was used in the both ROP model and full bit IFA model models.

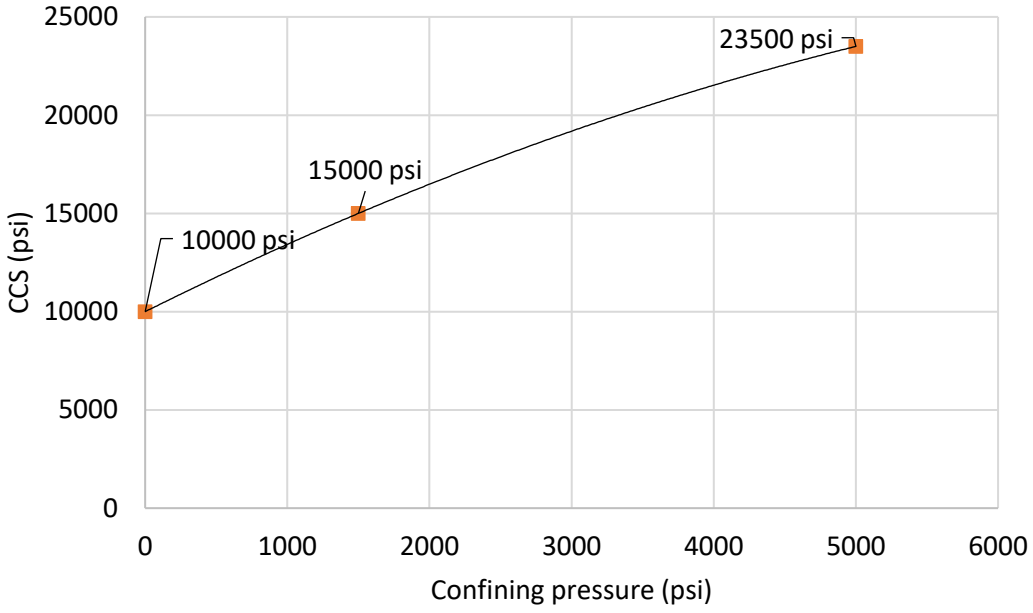

Figure 4.48. variation of Carthage lime CCS versus CP

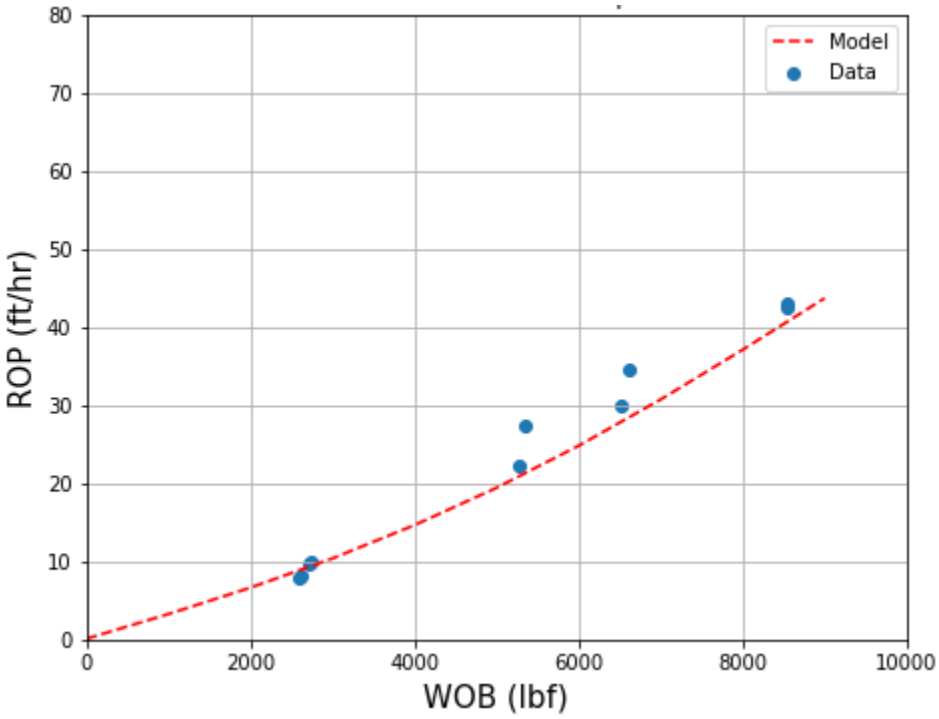

Figure 4.49. comparison between the model ROP and data for 8.5" PDC bit, RPM=120, UCS=10900 psi, CP=1400 psi, CCS=14654 psi, NOC=49, NOB=7, Dc=0.5 ", BR=20, ROP-constant=0.55

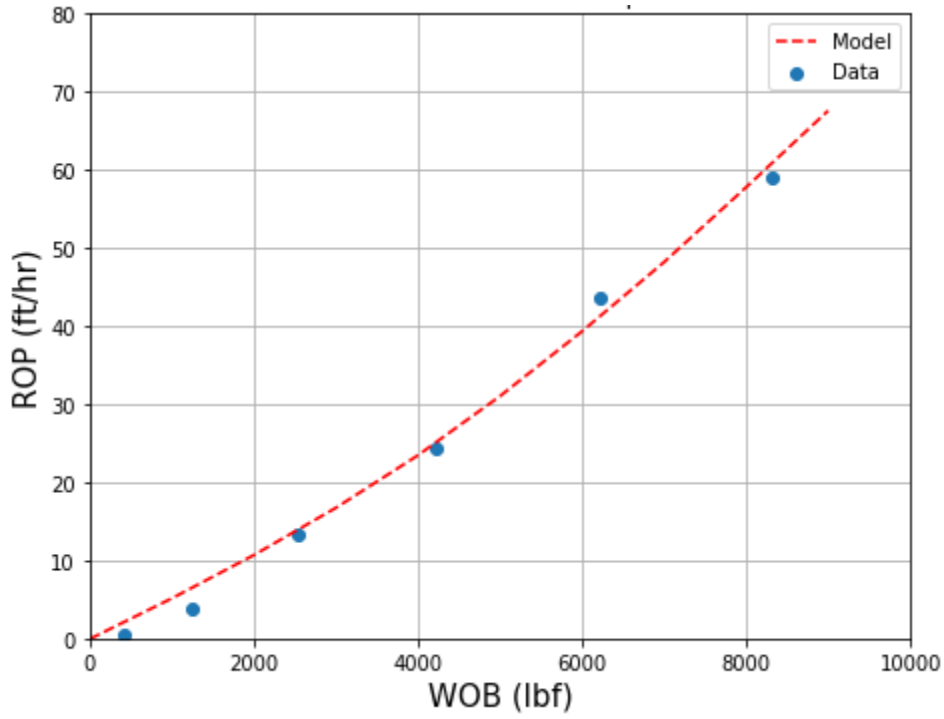

Figure 4.50. comparison between the model ROP and data for 8.5" PDC bit, RPM=170, UCS=10900 psi, CP=920 psi, CCS=103147 psi, NOC=49, NOB=7, Dc=0.5 ", BR=20, ROP-constant=0.55

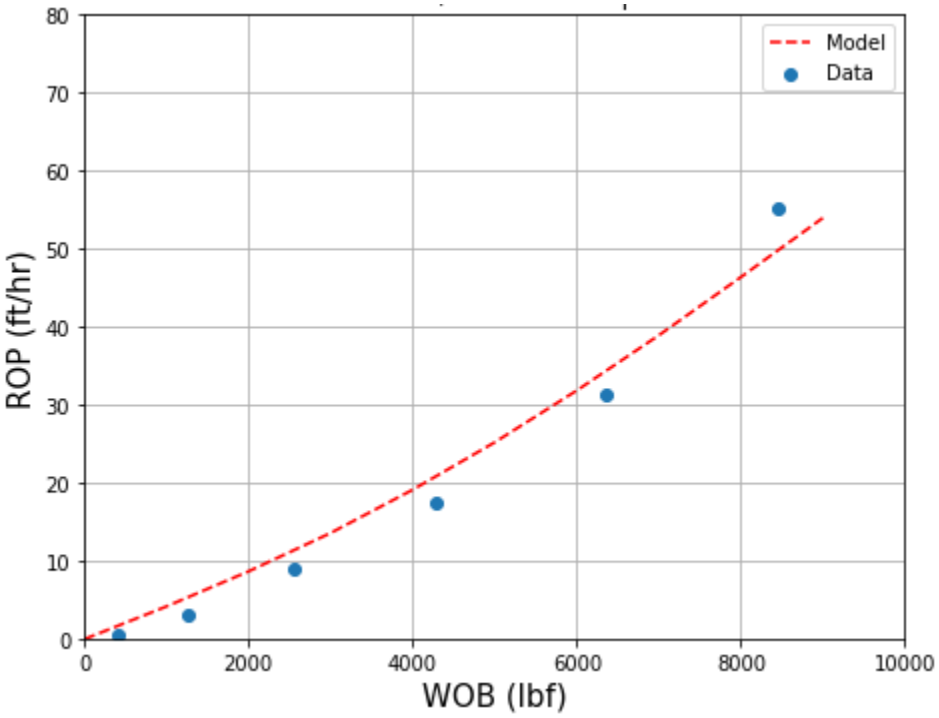

Figure 4.51. comparison between the model ROP and data for 8.5" PDC bit, RPM=120, UCS=10900 psi, CP=807 psi, CCS=12778 psi, NOC=49, NOB=7, Dc=0.5 ", BR=20, ROP-constant=0.55

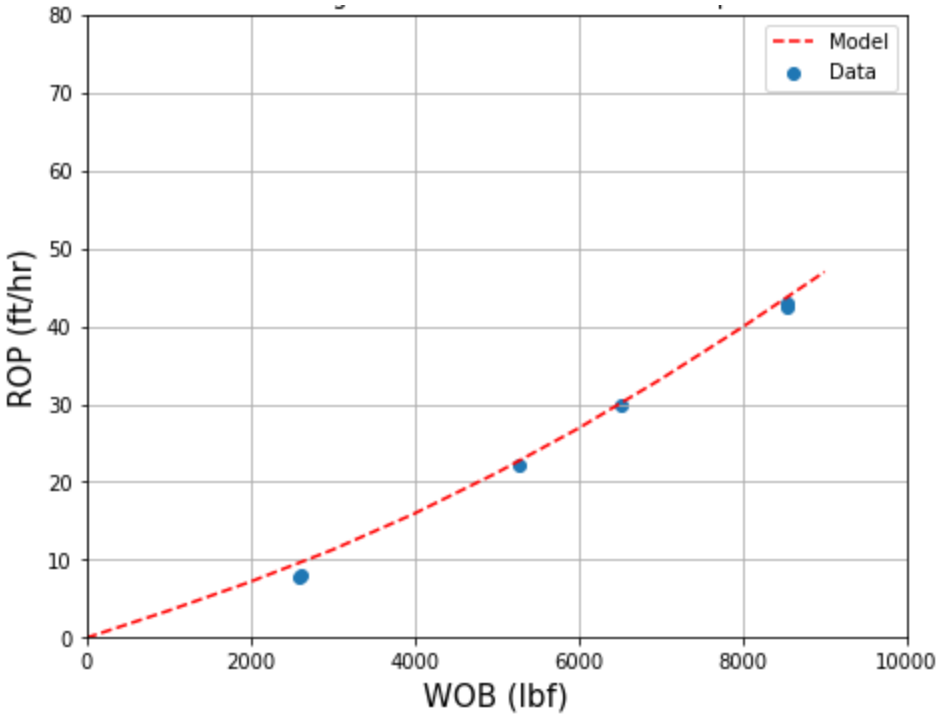

Figure 4.52. comparison between the model ROP and data for 8.5" PDC bit, RPM=120, UCS=10900 psi, CP=1200 psi, CCS=14037 psi, NOC=49, NOB=7, Dc=0.5 ", BR=13, ROP-constant=0.55

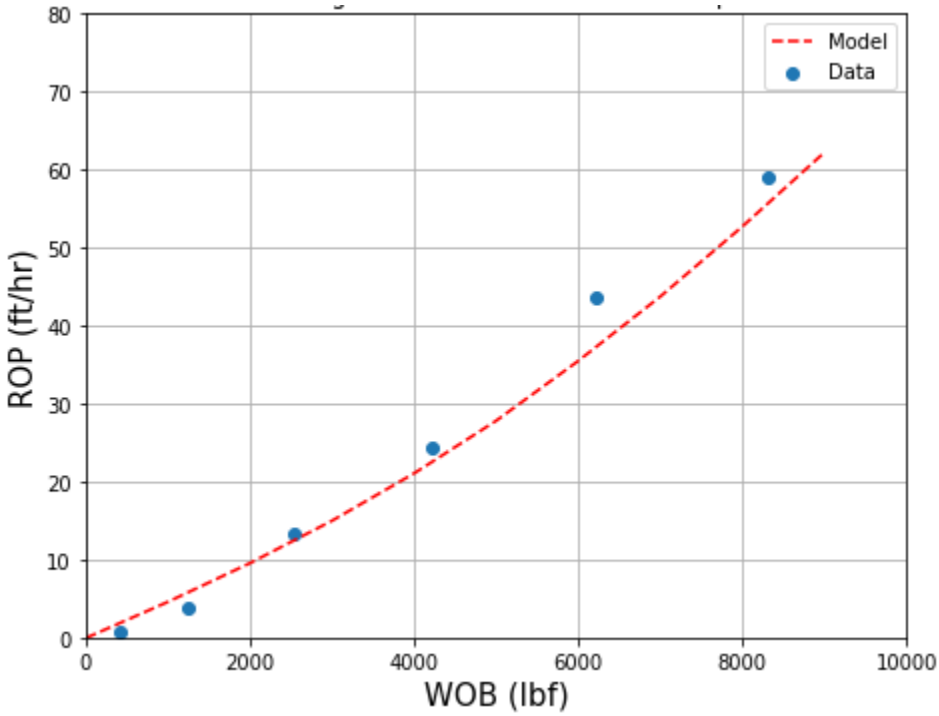

Figure 4.53. comparison between the model ROP and data for 8.5" PDC bit, RPM=175, UCS=10900 psi, CP=1200 psi, CCS=14037 psi, NOC=49, NOB=7, Dc=0.5 ", BR=13, ROP-constant=0.55

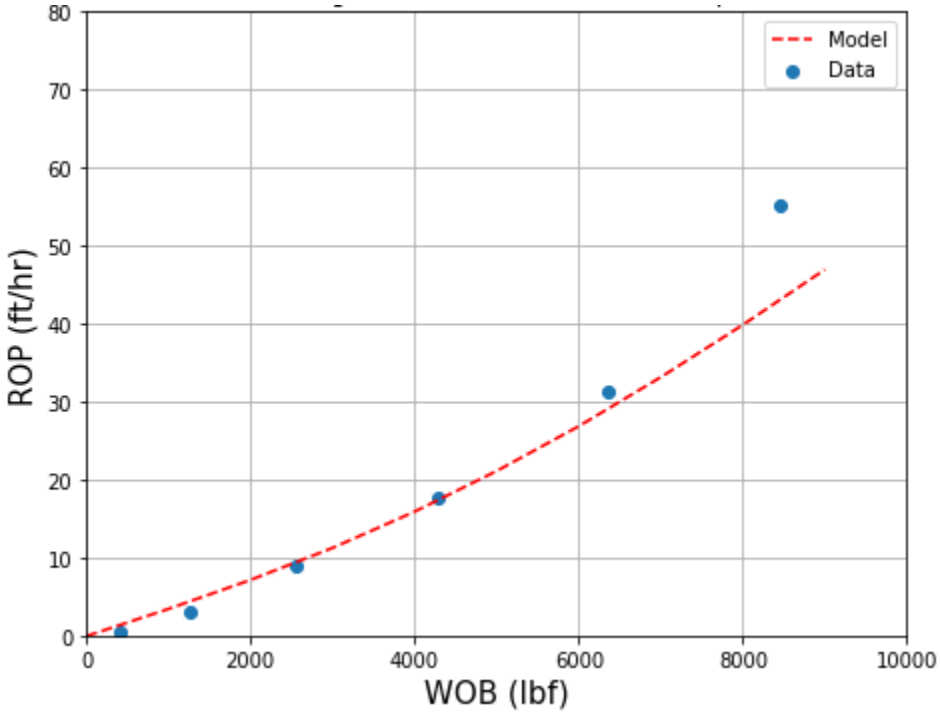

Figure 4.54. comparison between the model ROP and data for 8.5" PDC bit, RPM=120, UCS=10900 psi, CP=1200 psi, CCS=14037 psi, NOC=49, NOB=7, Dc=0.5 ", BR=13, ROP-constant=0.55

As it is seen in Figure 4.49 through 4.54 the model provides a good estimation for PDC ROP at different RPM, CCS, and BR values in Carthage limestone.

CHAPTER V

CONCLUSIONS AND FUTURE RECOMENDATION

CONCLUSIONS

The conclusions of this thesis are provided as follows.

- The flow of cut moving ahead and beneath the cutter results in a frictional force at the cutter face, known as interfacial friction. The interfacial friction plays an important role in the interaction between cutter and rock. Interfacial friction affects both cutters drag and normal forces considerably. The interfacial friction shows up as an angle known as the interfacial friction angle (IFA), and is calculated using the DD model (Equation 3.12) for a sharp cutters. In this study, a single cutter IFA model was developed for sharp cutters using the data from literature. The single cutter IFA model takes the cutter velocity, cutter depth of cut, and velocity into account. The cutter IFA model is used cooperatively with the single cutter force models to estimate the cutter drag and normal force, which has potential application for simulating cutter wear (real-time bit wear model).
- The single cutter tests show that the cutter chamfer does not have a great effect on the IFA.
- A single cutter analytical force model was developed for sharp and blunt cutters that generate promising estimation for cutter normal and drag forces in BSS, SWG, and TX pink granite lithologies.

- The single cutter model was scaled up and used for developing a full PDC bit ROP model. A full bit IFA model was developed and used to adjust the effect of friction on cutter depth of cut and to improve the PDC ROP model estimations. The new PDC ROP model is solved with the full bit IFA model, and therefore, it has included the effect of interfacial friction force. In the new full bit ROP model, the effect of the number of blades is shown in a constant, C_B , which was found equal to 0.9 and 1.07 respectively for the four and five bladed bits.
- The developed full bit model along with developed full bit IFA model were verified for new bits at three RPM, two equivalent BR angles, and four CPs with 100% perfect bit cleaning.
- The effect of RPM on the ROP model was incorporated in the new full bit model. Increasing RPM will increase the volume of cut per unit time and consequently result in higher ROP values. However, the higher RPM will result in higher cutter velocities, which increases the cutter IFA, and decreases the cutter depth of cut and ROP.
- The new model can be used for detecting phase II in drilling, which is representative for efficient drilling. In this case, the ROP model should be solved at two different RPMs to achieve the intersect WOB. The WOBs less than intersection WOB happen in phase I while the WOBs over intersection point are in phase II.
- The differential evolution algorithm (DEA) was applied to develop two IFA models for single cutter and full bit. The DEA was written in Python notebook and provided in Appendix F. The python is an open-source, integrated high level, general-purpose programing language.

FUTURE RECOMMENDATIONS

- In the new PDC ROP model the effect of cutter arrangement, interaction, and exposure were ignored. These factors can be integrated into future models to improve ROP simulation accuracy.
- The efficiency of PDC and stud wear flat areas is not equal, due to having different material and quality. An attempt should be made to consider the effect of wear flat area efficacy on cutter depth of cut, and consequently the ROP.
- The CP is an important parameter which affects the cutter forces tremendously during drilling. The effect of CP on single cutter forces should be studied for different rock hardness and lithologies which later can be used for improving single cutter and full bit IFA models.
- An attempt should be made to find a relationship between the single cutter and full bit IFA models. The potential implication of a single cutter IFA model placed directly into the ROP model can be studied. It is suggested to modify the equivalent cutter definition based on Appendix E and use it for estimating the accurate equivalent normal force and depth of cut.
- The effect of drilling fluid, cutter surface finish, chamfer angle, and cutter balling should be studied for single and full bit IFA models. It is expected that mentioned parameters affect the IFA model, which is a key element for estimating the ROP accurately.
- The blade effect was incorporated into ROP by multiplying constant C_B into the model. An attempt should be made to investigate the effect of the number of blades on PDC bit performance.
- The model should be verified for bits with different diameters.
- The IFA model was developed based on DOC, UCS, and cutter velocity. It is noteworthy to mention that in the IFA model, the UCS was replaced with CCS because of the having

CP. However, the potential of including the CP effect into the IFA model as a separate parameter should be investigated in the future works. It is expected that the frictional behavior of soft rock under CP be different than those rocks with higher UCS. In other words, two rocks with same CCS and different UCS (under two different CP) can behave differently just because of their lithologies. Having separate UCS and CP in the IFA model will give model more room for simulating more sophisticated behaviors.

REFERENCES

Amer, M.M., Dahab, A.S. & El-Sayed, A.A.H., (2017). "An ROP predictive model in nile delta area using artificial neural networks". In SPE Kingdom of Saudi Arabia Annual Technical Symposium and Exhibition, 24-27 April, Dammam, Saudi Arabia

Akbari, B., S. Z. Miska, M. Yu, & R. Rahmani (2014). "The effects of size, chamfer geometry, and back rake angle on frictional response of PDC cutters". In 48th U.S. Rock Mechanics/Geomechanics Symposium, 1-4 June, Minneapolis, Minnesota

Arehart, R. A. (1989). "Drill Bit Diagnosis Using Neural Network". In SPE 19558, Proc. the SPE Annual Technical Conference and Exhibition, San Antonio, TX, pp. 24-28. 1989.

Ashrafi, S. B., Anemangely, M., Sabah, M., & Ameri, M. J. (2018). "Application of hybrid artificial neural networks for predicting rate of penetration (ROP): A case study from Marun oil field". Journal of Petroleum Science and Engineering 175, 604-623.

Atashnezhad, A., Wood, D.A., Fereidounpour, A., & Khosravanian, R. (2014). "Designing and optimizing deviated wellbore trajectories using novel particle swarm algorithms". Journal of Natural Gas Science and Engineering 21, 1184-1204.

Atashnezhad, A., Cedola, A. E., & Hareland, G. (2017). "An Empirical Model to Estimate a Critical Stimulation Design Parameter Using Drilling Data". SPE Western Regional Meeting, 23-27 April, Bakersfield, California.

Bourgoyne A, T., & F. S. Young Jr. (1974). "A multiple regression approach to optimal drilling and abnormal pressure detection". Society of Petroleum Engineers Journal 14, no. 04, 371-384.

Bianchi, L., Dorigo, M., Gambardella, L. M., & Gutjahr, W. J. (2009). "A survey on metaheuristics for stochastic combinatorial optimization". Natural Computing, 8(2), 239-287.

Bilgesu, H. I., Tetrick, L. T., Altmis, U., Mohaghegh, S. & Ameri, S. (1997). "A new approach for the prediction of rate of penetration (ROP) values". In SPE Eastern Regional Meeting, 22-24 October, Lexington, Kentucky.

Bingham, G. (1965). "A new approach to interpreting rock drillability". Technical Manual Reprint, Oil and Gas Journal, 93 P.

Blum, C., & Roli, A. (2003). “Metaheuristics in combinatorial optimization: Overview and conceptual comparison”. ACM computing surveys (CSUR) 35, no. 3, 268-308.

Carrapatoso, C.M., Lautenschläger, C.E.R., Righetto, G.L., da Fontoura, S.A.B. & Inoue, N. (2016). “Rock Cutting Analysis Employing Finite and Discrete Element Methods”. Journal of Mechanics Engineering and Automation 6 (2016) 100-108 doi: 10.17265/2159-5275/2016.02.006

Cheng, Z., Li, G., Huang, Z., Sheng, M., Wu, X. & Yang, J., (2019). “Analytical modelling of rock cutting force and failure surface in linear cutting test by single PDC cutter”. Journal of Petroleum Science and Engineering.

Chen, C. Y., & Ye, F. (2012). “Particle swarm optimization algorithm and its application to clustering analysis”. In Electrical Power Distribution Networks (EPDC), Proceedings of 17th Conference on (pp. 789-794). IEEE.

Chen, K. H., Wang, K. J., Tsai, M. L., Wang, K. M., Adrian, A. M., Cheng, W. C., & Chang, K. S. (2014). “Gene selection for cancer identification: a decision tree model empowered by particle swarm optimization algorithm”. BMC bioinformatics, 15(1), 49.

Coudyzer, C. & Richard, T. (2005). “Influence of the back and side rake angles in rock cutting”. In AADE 2005 National Technical Conference and Exhibition, Wyndam Greenspoint, Houston, TX, April, pp. 5-7.

Dagrain, F., & T. Richard (2006). “On the influence of PDC wear and rock type on friction coefficient and cutting efficiency”. In EUROROCK: Multiphysics coupling and long term behaviour in rock mechanics.

Dashevskiy, D., Dubinsky, V. & Macpherson, J.D. (1999). “Application of neural networks for predictive control in drilling dynamics”. In SPE Annual Technical Conference and Exhibition, 3-6 October, Houston, Texas.

Detournay, E. & Drescher, A. (1992). “Plastic flow regimes for a tool cutting a cohesive-frictional material”. In Proceeding 4Th Int. Symp. On Numerical Methods in Geomechanics (NUMOG IV). Balkema: Rotterdam.

Detournay, E. & Defourny, P. (1992). “A phenomenological model for the drilling action of drag bits”. In International journal of rock mechanics and mining sciences & geomechanics abstracts, vol. 29, no. 1, pp. 13-23. Pergamon.

Detournay, E., Richard, T. & Shepherd, M. (2008). “Drilling response of drag bits: theory and experiment”. International Journal of Rock Mechanics and Mining Sciences45, no. 8 : 1347-1360.

Dreo, J., & Candan, C. (2017), “Different classification of metaheuristics”, Retrieved from https://en.wikipedia.org/wiki/File:Metaheuristics_classification.svg

Dupriest, F.E. & Koederitz, W.L. (2005). “Maximizing drill rates with real-time surveillance of mechanical specific energy”. In SPE/IADC Drilling Conference, 23-25 February, Amsterdam, Netherlands

EIA, (2016). “Trends in US Oil and Natural Gas Upstream Costs”. US Energy Information Administration Report, March, Retrieved from https://www.eia.gov/analysis/studies/drilling/pdf/upstream.pdf.

Elkatatny, S.M., Tariq, Z., Mahmoud, M.A. & Al-AbdulJabbar, A. (2017). “Optimization of rate of penetration using artificial intelligent techniques”. In 51st U.S. Rock Mechanics/Geomechanics Symposium, 25-28 June, San Francisco, California, USA

Ephramac, (2017). “2D-partikelschwarm sucht globales minimum”, Available at https://commons.wikimedia.org/wiki/File:ParticleSwarmArrowsAnimation.gif.

Erdeljan, A., Capko, D., Vukmirovic, S., Bojanic, D., & Congradac, V. (2014). “Distributed PSO algorithm for data model partitioning in power distribution systems”. Journal of applied research and technology, 12(5), 947-957.

Eren, T., & Ozbayoglu, M. E. (2010). “Real time optimization of drilling parameters during drilling operations”. SPE Oil and Gas India Conference and Exhibition, 20-22 January, Mumbai, India.

Ernst, H. & Merchant, M.E. (1941). “Chip formation, friction and finish”. Publisher: Cincinnati milling machine Company.

Fruhwirth, R.K., Thonhauser, G. & Mathis, W. (2006). “Hybrid simulation using neural networks to predict drilling hydraulics in real time”. In SPE Annual Technical Conference and Exhibition, 24-27 September, San Antonio, Texas.

Galle, E. M., & Woods, H. B. (1963). “Best constant weight and rotary speed for rotary rock bits”. Drilling and Production Practice, 1 January, New York, New York.

Gaur, S., Ch, S., Graillot, D., Chahar, B. R., & Kumar, D. N. (2013). “Application of artificial neural networks and particle swarm optimization for the management of groundwater resources”. Water resources management, 27(3), 927-941.

Gerbaud, L., Menand, S. & Sellami, H. (2006). “PDC bits: all comes from the cutter rock interaction”. In IADC/SPE Drilling Conference held in Miami, Florida, USA, 21-23 Fabruary.

Gidh, Y.K., Purwanto, A. & Ibrahim, H (2012). “Artificial neural network drilling parameter optimization system improves ROP by predicting/managing bit wear”. In SPE Intelligent Energy International, 27-29 March, Utrecht, the Netherlands.

Glowka, D. A. (1987). “Development of a method for predicting the performance and wear of PDC drill bits”. Sandia National Laboratories. Page 19.

Glowka, D. A. (1985). “Implications of thermal wear phenomena for PDC bit design and operation”. SPE Annual Technical Conference and Exhibition, 22-26 September, Las Vegas, Nevada.

Glowka, D. A., & Stone, C. (1985). “Thermal response of polycrystalline diamond compact cutters under simulated downhole conditions”. Society of Petroleum Engineers Journal, 25(02), 143-156, April, Pages 143-156.

Graham, J. W., & Muench, N. L. (1959, January). “Analytical determination of optimum bit weight and rotary speed combinations”. In Fall Meeting of the Society of Petroleum Engineers of AIME. Society of Petroleum Engineers.

Hamrick, T. R. (2011). “Optimization of Operating Parameters for Minimum Mechanical Specific Energy in Drilling”. Doctoral dissertation, West Virginia University.

Hanson, J.M. & Hansen, W.R. (1995). “Dynamics modeling of PDC bits”. SPE/IADC Drilling Conference, 28 February-2 March, Amsterdam, Netherlands.

Hareland, G., & Rampersad, P. R. (1994). “Drag-bit model including wear”. SPE Latin America/Caribbean Petroleum Engineering Conference, 27-29 April, Buenos Aires, Argentina.

Hareland, G., Nygaard, R., & Virginillo, B. K. (2007). “Drilling simulation versus actual performance in Western Canada”. Rocky Mountain Oil & Gas Technology Symposium, 16-18 April, Denver, Colorado, U.S.A.

Hareland, G., Olea Uribe, I. V., Shirkavand, F., & Teichrob, R. R. (2008). “Advanced Drilling Simulation Proves Managed-Pressure Drilling (MPD) Economical in Gas field Developments in Western Canada”. CIPC/SPE Gas Technology Symposium Joint Conference, 16-19 June, Calgary, Alberta, Canada. (a)

Hareland, G., Motahhari, H. R., Hayes, J. P., & Qureshi, A. (2008). “Increased Drilling Efficiency of Gas Storage Wells Proven Using Drilling Simulator”. CIPC/SPE Gas Technology Symposium Joint Conference, 16-19 June, Calgary, Alberta, Canada. (b)

Hegde, C., Daigle, H., Millwater, H. & Gray, K., (2017). “Analysis of rate of penetration (ROP) prediction in drilling using physics-based and data-driven models”. Journal of Petroleum Science and Engineering, 159, pp.295-306.

Hegde, C. & Gray, K., (2018). “Evaluation of coupled machine learning models for drilling optimization”. Journal of Natural Gas Science and Engineering, 56, pp.397-407.

Hellvik, S., Nygaard, R., Hoel, E., Andersen, M.A. & Francis, M. (2012). “PDC cutter and bit development for challenging conglomerate drilling in the Luno field-offshore Norway”. In IADC/SPE Drilling Conference and Exhibition, 6-8 March, San Diego, California, USA

Rampersad, P. R., Hareland, G., & Boonyapaluk, P. (1994). “Drilling optimization using drilling data and available technology”. SPE Latin America/Caribbean Petroleum Engineering Conference. 27-29 April, Buenos Aires, Argentina

Rahmani, R. (2013). “Analytical Modeling and Diagnosis of Penetration Rate Performance of PDC Bits”. Doctoral dissertation, Louisiana State University and Agricultural and Mechanical College.

Reed, R. L. (1972). “A Monte Carlo Approach to Optimal Drilling”. Society of Petroleum Engineers Journal, 12(05), 423-438.

Richard, T. (1999). “Determination of rock strength from cutting tests”. PhD dissertation, University of Minnesota.

Russell, S. J., & Norvig, P. (2016). “Artificial intelligence: a modern approach”. Malaysia; Pearson Education Limited

Russell, S., & Norvig, P. (2003). “Artificial intelligence: a modern approach”.

Rommetveit, R., Bjørkevoll, K.S., Halsey, G.W., Larsen, H.F., Merlo, A., Nossaman, L.N., Sweep, M.N., Silseth, K.M. & Ødegaard, S.I. (2004). “Drilltronics: an integrated system for real-time optimization of the drilling process”. In IADC/SPE Drilling Conference. Society of Petroleum Engineers.

Karri, V. (1999). “RBF neural network for thrust and torque predictions in drilling operations”. In Proceedings Third International Conference on Computational Intelligence and Multimedia Applications. ICCIMA'99 (Cat. No. PR00300), pp. 55-59. IEEE.

Kerkar, P. B., Hareland, G., Fonseca, E. R., & Hackbarth, C. J. (2014). “Estimation of rock compressive strength using downhole weight-on-bit and drilling models”. International Petroleum Technology Conference, 19 January.

Lummus, James L. (1970). “Drilling optimization”. Journal of Petroleum Technology 22, no. 11, 1-379.

Maidla, E.E. and Ohara, S. (1991). “Field verification of drilling models and computerized selection of drill bit, WOB, and drillstring rotation”. SPE Drilling Engineering 6, no. 03 : 189-195.

Malik, A. J., Shahzad, W., & Khan, F. A. (2011). “Binary PSO and random forests algorithm for PROBE attacks detection in a network”. In Evolutionary Computation (CEC), IEEE Congress on (pp. 662-668).

Marana, A.N., Papa, J.P., Ferreira, M.V., Miura, K. & Torres, F.A.C. (2010). “An intelligent system to detect drilling problems through drilled-cuttings-return analysis”. In IADC/SPE Drilling Conference and Exhibition, 2-4 February, New Orleans, Louisiana, USA.

Maurer, W. C. (1962). “The "perfect-cleaning" theory of rotary drilling”. Journal of Petroleum Technology, 14(11), 1-270.

Merchant, M. E. (1944). “Basic mechanics of the metal-cutting process”. ASME J. of Applied Mechanics 11 : A168.

Merchant, M. E. (1940). “The mechanism of static friction”. Journal of Applied Physics 11, no. 3 : 230-230.

Mohaghegh, S., Arefi, R., Ameri, S. & Rose, D. (1995). “Design and development of an artificial neural network for estimation of formation permeability”. Paper (SPE 28237) first presented at the SPE Petroleum Computer Conference held in Dallas. July 31-Aug. 3.

Motahhari, H. R., Hareland, G., & James, J. A. (2010). “Improved drilling efficiency technique using integrated PDM and PDC bit parameters”. Journal of Canadian Petroleum Technology, 49(10), 45-52.

Nishimatsu, Y (1972). “The mechanics of rock cutting”. In International Journal of Rock Mechanics and Mining Sciences & Geomechanics Abstracts, vol. 9, no. 2, pp. 261-270. Pergamon.

Omran, M. G., Engelbrecht, A. P., & Salman, A. (2006). “Particle swarm optimization for pattern recognition and image processing”. In Swarm intelligence in data mining (pp. 125-151). Springer, Berlin, Heidelberg.

Sano, O., Ito, I. and Terada, M., (1981). “Influence of strain rate on dilatancy and strength of Oshima granite under uniaxial compression”. Journal of Geophysical Research: Solid Earth 86, no. B10 : 9299-9311.

Soares, C. & Gray, K., (2019). “Real-time predictive capabilities of analytical and machine learning rate of penetration (ROP) models”. Journal of Petroleum Science and Engineering, 172, pp.934-959.

Pandey, S., Wu, L., Guru, S. M., & Buyya, R. (2010). “A particle swarm optimization-based heuristic for scheduling workflow applications in cloud computing environments”. In Advanced information networking and applications (AINA), 24th IEEE international conference on (pp. 400-407). IEEE.

Price, K. V. (1996). “Differential evolution: a fast and simple numerical optimizer”. In Fuzzy Information Processing Society, NAFIPS., Biennial Conference of the North American (pp. 524-527). IEEE.

Self, R. (2016). “Use of Particle Swarm Optimization Algorithm to Reduce Drilling Costs by Finding Optimal Operational Parameters”. Master of science thesis, Oklahoma State University.

Self, R,. Atashnezhad, A,. & Hareland, G, (2017). “Field Application of a Particle Swarm Optimization (PSO) and a Rate of Penetration (ROP) Model Routine to Reduce Overal Drilling Cost by Finding Optimal Bits, Pull Depth and Operating Parameters”, AADE-17-NTCE-123, Houston, Texas, April 11-12.

Shen, H., Zhu, Y., Liu, T., & Jin, L. (2009). “Particle swarm optimization in solving vehicle routing problem”. In Intelligent Computation Technology and Automation,. ICICTA'09. Second International Conference on (Vol. 1, pp. 287-291). IEEE.

Sinor, L. A., Powers, J. R., & Warren, T. M. (1998). “The effect of PDC cutter density, back rake, size, and speed on performance”. IADC/SPE Drilling Conference, 3-6 March, Dallas, Texas.

Sinor, A., & Warren, T. M. (1989). “Drag Bit Wear Model”. Society of Petroleum Engineers. Page 128-136, doi:10.2118/16699-PA,

Smith, J.R. (1998). “Diagnosis of Poor PDC Bit Performance in Deep Shales”. Doctoral dissertation, Louisiana State University and Agricultural and Mechanical College.

Soares, C., Daigle, H., & Gray, K. (2016). “Evaluation of PDC bit ROP models and the effect of rock strength on model coefficients”. Journal of Natural Gas Science and Engineering, 34, 1225-1236.

Speer, J. W. (1958). “A method for determining optimum drilling techniques”. Drilling and Production Practice, 1 January, New York, New York. Pages 130-147.

Spencer, S.J., Mazumdar, A., Su, J.C., Foris, A. & Buerger, S.P., (2017). “Estimation and control for efficient autonomous drilling through layered materials”. In American Control Conference (ACC) (pp. 176-182). IEEE.

Storn, R., & Price, K. (1997). “Differential evolution–a simple and efficient heuristic for global optimization over continuous spaces”. Journal of global optimization, 11(4), 341-359.

Teale, R. (1965). “The concept of specific energy in rock drilling”. In International Journal of Rock Mechanics and Mining Sciences & Geomechanics Abstracts, vol. 2, no. 1, pp. 57-73. Pergamon.

Urade, H. S., & Patel, R. (2012). “Dynamic particle swarm optimization to solve multi-objective optimization problem”. Procedia Technology, 6, 283-290.

Walker, B. H., Black, A. D., Klauber, W. P., Little, T., & Khodaverdian, M. (1986). “Roller-bit penetration rate response as a function of rock properties and well depth”. SPE Annual Technical Conference and Exhibition, 5-8 October, New Orleans, Louisiana.

Warren, T. M. (1987). “Penetration rate performance of roller cone bits”. SPE Drilling Engineering, 2(01), 9-18.

Warren, T.M. & Armagost, W.K., (1988). “Laboratory drilling performance of PDC bits”. SPE drilling engineering, 3(02), pp.125-135. Publisher: Society of Petroleum Engineers, Issue02, Publication Date June.

Winters, W. J., & Doiron, H. H. (1987). “The 1987 IADC fixed cutter bit classification system”. SPE/IADC Drilling Conference, 15-18 March, New Orleans, Louisiana. (a)

Winters, W.J., Warren, T.M. & Onyia, E.C., (1987). “Roller bit model with rock ductility and cone offset”. In SPE Annual Technical Conference and Exhibition. Society of Petroleum Engineers. SPE Annual Technical Conference and Exhibition, 27-30 September, Dallas, Texas (b)

Yan, Wenzhuo (1997). “Single PDC cutter force modeling for hard rock cutting”. PhD diss., New Mexico Institute of Mining and Technology.

Zhang, Y., Xie, X., & Cheng, T. (2010). “Application of PSO and SVM in image classification”. In Computer Science and Information Technology (ICCSIT), 3rd IEEE International Conference on (Vol. 6, pp. 629-631). IEEE.

APPENDIX A

Cutter contact area calculation

A.1 Approach 1

A schematic of a cutter face (sharp) is seen in Figure A.1. In Figure A.1, the r is cutter radius (half of the cutter diameter-D_c), θ is half of triangle vertex angle (is seen in green), Z is the height of the triangle, L is the projection of cutter depth of cut (DOC) on cutter face, X is the base of triangle, and the Z' is the projection of Z by taking the cutter BR angle into account.

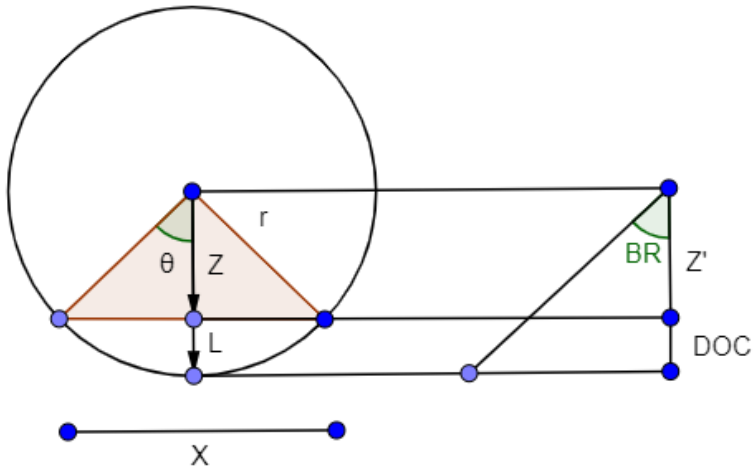

Figure A.1. The schematic of a sharp cutter front face (left) and side view (right)

The area of a circle sector and the triangle in Figure A.1 are calculated using Equations A.1 and A.2.

$$A_{sector} = \frac{2\theta}{360}\pi r^2 \ldots\ldots\ldots \text{Eq. A. 1}$$

$$A_{triangle} = \frac{ZX}{2} \ldots\ldots\ldots \text{Eq. A. 2}$$

The depth when the cutter penetrates half the cutter diameter of the cutter is the threshold depth of cut (DOC_T).The threshold depth of cut is defined in the Equation A.3 and is seen in Figure A.2.

$$DOC_T = \frac{D_c}{2}\mathrm{Cos}(BR) \ldots\ldots \text{Eq. A. 3}$$

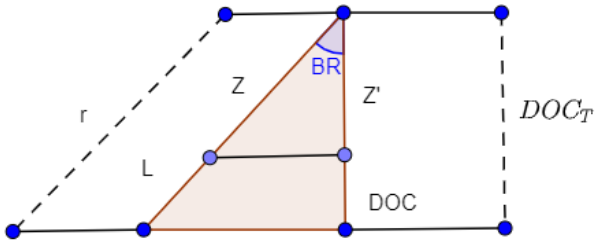

Figure A.2. The schematic of the depth of cut and threshold depth of cut

The triangle in Figure A.1 is seen in Figure A.3. Using Pythagorean Theorem (see Figure A.3):

$$r^2 = Z^2 + \frac{X^2}{4} \ldots\ldots \text{Eq. A. 4}$$

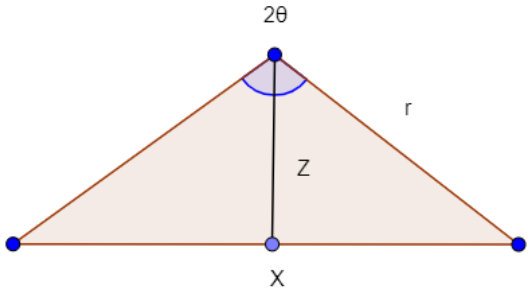

Figure A.3. A schematic of a triangle

A.1.1 Cutter Contact area calculation for sharp cutter

A.1.1.1 Calculations for Z when the $DOC < DOC_T$

The Z in Figure A.1 is equal to the difference between the cutter radius (r) and L (see Equation A.5).

$$Z = r - L \ldots\ldots \text{Eq. A. 5}$$

Replacing the r and L will give Equation A.6.

$$Z = \frac{D_c}{2} - \frac{DOC}{\mathrm{Cos}(BR)} \ldots\ldots \text{Eq. A. 6}$$

A.1.1.2 Calculations for X when the $DOC < DOC_T$

Using Pythagorean Theorem (see Equation A.4 and Figure A.2), the Equation A.7 is achieved.

$$\frac{X^2}{4} = r^2 - Z^2 \ldots\ldots \text{Eq. A. 7}$$

Rearranging Equation A.7, the Equation A.8 is achieved.

$$X = 2\sqrt{r^2 - Z^2} \ldots\ldots \text{Eq. A. 8}$$

Replacing r with half of the cutter diameter, and Z from Equation A.6 into Equation A.8 the X is calculated using Equation A.9.

$$X = 2\sqrt{\frac{{D_c}^2}{4} - (\frac{D_c}{2} - \frac{DOC}{Cos(BR)})^2} \ldots\ldots \text{Eq. A. 9}$$

A.1.1.3 Calculations for θ when the $DOC < DOC_T$

The θ is calculated using Equations A.10 (see Figure A.1).

$$Tan(\theta) = \frac{\frac{X}{2}}{Z} \ldots\ldots \text{Eq. A. 10}$$

Rearranging Equation A.10 will result in Equation A.11.

$$\theta = Tan^{-1}\left(\frac{X}{2.Z}\right) \ldots\ldots \text{Eq. A. 11}$$

Replacing the X and Z into the Equation A.11, the θ is calculated for the $DOC<DOC_T$

$$\theta = Tan^{-1}\left(\frac{\sqrt{\frac{{D_c}^2}{4} - \left(\frac{D_c}{2} - \frac{DOC}{Cos(BR)}\right)^2}}{\frac{D_c}{2} - \frac{DOC}{Cos(BR)}}\right) \ldots\ldots \text{Eq. A. 15}$$

A.1.1.4 Calculations cutter contact area when $DOC < DOC_T$

The cutter contact area is calculated using Equation A.16.

$$A_{contact} = A_{Sector} - A_{Triangle} \ldots\ldots \text{Eq. A. 16}$$

The cutter sector area and triangle area were calculated in Equation A.1 and A.2. The triangle area (Equation A.2) is turned into Equation A.17 by replacing the Z and X (see Equations A.6 and A.9).

$$A_{triangle} = \left(\frac{\left(\frac{D_c}{2} - \frac{DOC}{Cos(BR)}\right) \cdot \left(2\sqrt{\frac{{D_c}^2}{4} - (\frac{D_c}{2} - \frac{DOC}{Cos(BR)})^2}\right)}{2} \right) \ldots\ldots \text{Eq. A. 17}$$

The cutter contact area is calculated using Equation A.18.

$$A_{contact} = \left(\frac{\left(Tan^{-1}\left(\frac{\sqrt{\frac{{D_c}^2}{4} - \left(\frac{D_c}{2} - \frac{DOC}{Cos(BR)}\right)^2}}{\frac{D_c}{2} - \frac{DOC}{Cos(BR)}} \right)\right) \pi {D_c}^2}{720} \right) - \left(\frac{\left(\frac{D_c}{2} - \frac{DOC}{Cos(BR)}\right) \times \left(2\sqrt{\frac{{D_c}^2}{4} - (\frac{D_c}{2} - \frac{DOC}{Cos(BR)})^2}\right)}{2} \right) \ldots\ldots \text{Eq. A. 18}$$

A.1.1.5 Calculations cutter contact area when $DOC = DOC_T$

When the $DOC = DOC_T$, the cutter penetrated by half and, therefore the cutter contact area would be half of total cutter face area and it is seen in Equation A.19.

$$A_{contact} = \pi \frac{{D_c}^2}{8} \quad \ldots\ldots \text{Eq. A. 19}$$

A.1.1.6 Calculations for Z when the $DOC > DOC_T$

A schematic of a cutter when the DOC is greater than the threshold DOC is seen in Figure A.4.

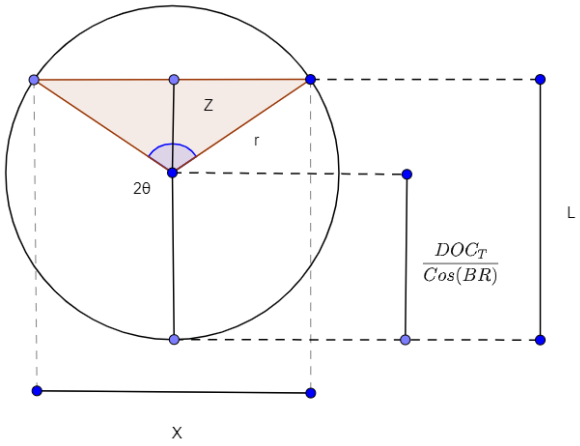

Figure A.4. A schematic of a cutter face area when the cutter depth of cut is greater than the threshold depth of cut

When the DOC is greater than the threshold depth of cut, the Z is calculated using Equation A.20.

$$Z = -r + L \ldots\ldots \text{Eq. A. 20}$$

Replacing the r and L will give Equation A.21.

$$Z = -\frac{D_c}{2} + \frac{DOC}{Cos(BR)} \ldots\ldots \text{Eq. A. 21}$$

A.1.1.7 Calculations for X when the $DOC > DOC_T$

Using Pythagorean Theorem (see Equation A.4 and Figure A.2), the Equation A.7 was achieved (see Equation A.7). Rearranging Equation A.7, the Equation A.8 is achieved (see Equation A.8). Replacing the r with half of the cutter diameter, and Z from Equation A.21 into Equation A.8 the X is calculated in Equation A.22.

$$X = 2\sqrt{\frac{{D_c}^2}{4} - (-\frac{D_c}{2} + \frac{DOC}{Cos(BR)})^2} \ldots\ldots \text{Eq. A. 22}$$

A.1.1.8 Calculations for θ when the $DOC > DOC_T$

The θ is calculated using Equations A.10 (see Figure A.1). Rearranging Equation A.10 will result in Equation A.11 (see Equation A.11). Replacing the X (Equation A.22), and Z (Equation A.21) into the Equation A.11, the θ is calculated in Equation A.23.

$$\theta = \mathrm{Tan}^{-1}\left(\frac{\sqrt{\frac{D_c{}^2}{4} - \left(-\frac{D_c}{2} + \frac{DOC}{\mathrm{Cos}(BR)}\right)^2}}{-\frac{D_c}{2} + \frac{DOC}{\mathrm{Cos}(BR)}}\right) \ldots\ldots \text{Eq. A. 23}$$

A.1.1.9 Calculations cutter contact area when $DOC > DOC_T$

The cutter contact area is calculated using Equation A.24.

$$A_{contact} = A_{Sector} + A_{Triangle} \ \ldots\ldots \text{Eq. A. 24}$$

The cutter sector area is calculated in the Equation A.25.

$$A_{Sector} = \pi r^2 - \frac{2\theta}{360}\pi r^2 \ \ldots\ldots \text{Eq. A. 25}$$

The triangle area is calculated in Equation A.26. The Equation A.2 is turned into Equation A.26 by replacing the Z and X (see Equations A.21 and A.22).

$$A_{triangle} = \left(\frac{\left(-\frac{D_c}{2} + \frac{DOC}{\mathrm{Cos}(BR)}\right) \times \left(2\sqrt{-\frac{D_c{}^2}{4} + (\frac{D_c}{2} - \frac{DOC}{\mathrm{Cos}(BR)})^2}\right)}{2}\right) \ldots\ldots \text{Eq. A. 26}$$

The cutter contact area is calculated using Equation A.27.

$$A_{contact} = \left(\pi\left(\frac{D_c}{2}\right)^2 - \frac{2\left(\mathrm{Tan}^{-1}\left(\frac{\sqrt{-\frac{{D_c}^2}{4} + \left(\frac{D_c}{2} - \frac{DOC}{\mathrm{Cos}(BR)}\right)^2}}{-\frac{D_c}{2} + \frac{DOC}{\mathrm{Cos}(BR)}}\right)\right)}{360}\pi\left(\frac{D_c}{2}\right)^2 \right) + \left(\frac{\left(-\frac{D_c}{2} + \frac{DOC}{\mathrm{Cos}(BR)}\right) \times \left(2\sqrt{-\frac{{D_c}^2}{4} + (\frac{D_c}{2} - \frac{DOC}{\mathrm{Cos}(BR)})^2}\right)}{2} \right) \ldots\ldots\ldots \text{Eq. A. 27}$$

A.1.2 Cutter worn area calculation for a blunt cutter

A.1.2.1 Calculations for Z when the BG < 4

A schematic of a cutter face (blunt) is seen in Figure A.5. In Figure A.5, the r is cutter radius (half of the cutter diameter-D_c), θ is half of triangle vertex angle (is seen in green), Z is the height of the triangle, the $h_w$is the cutter wear length, the h_w' is the projection of h_w on the vertical axis, the X is the base of the triangle, and the Z' is the projection of Z by taking the cutter BR angle into account.

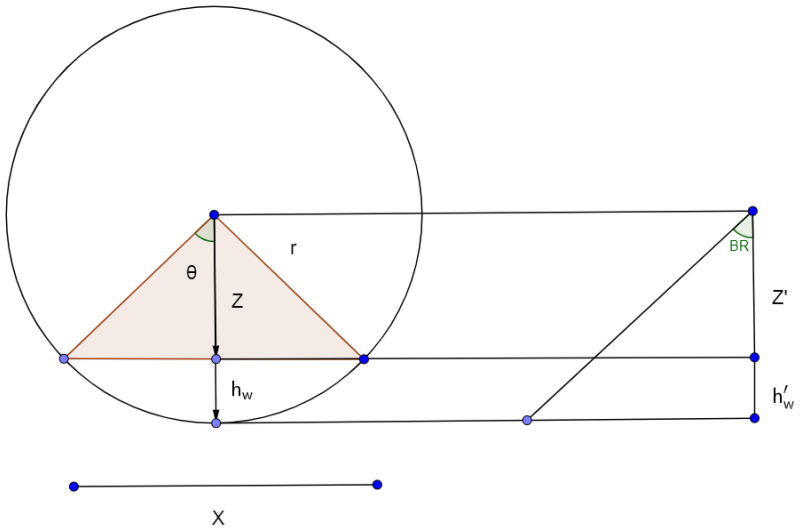

Figure A.5. A schematic of a blunt cutter front face view (left) and side view (right)

The area of a circle sector and the triangle in Figure A.5 are calculated using Equations A.1 and A.2.

The Z in Figure A.5 is equal to the difference between cutter radius (r), and length of wear (see Equation A.28).

$$Z = r - h_w \quad \ldots\ldots \text{Eq. A. 28}$$

The h_w is equal to bit grade times cutter diameter divided by 8. Replacing the h_w in Equation A.28 will results in Equation A.29.

$$Z = r - \frac{BG.D_c}{8} \quad \ldots\ldots \text{Eq. A. 29}$$

Replacing the r with half of the cutter diameter will result in Equation A.30.

$$Z = \frac{D_c}{2} - \frac{BG.D_c}{8} \quad \ldots\ldots \text{Eq. A. 30}$$

A.1.2.2 Calculations for X when the $BG < 4$

Using Pythagorean Theorem (see Equation A.4 and Figure A.2), the Equation A.7 is achieved. Rearranging Equation A.7, the Equation A.8 is achieved. Replacing the r with half of the cutter diameter, and Z from Equation A.30 into Equation A.8 the X is calculated using Equation A.31.

$$X = 2\sqrt{\frac{{D_c}^2}{4} - \left(\frac{D_c}{2} - \frac{\left(\frac{BG.D_c}{8}\right)}{\cos(BR)}\right)^2} \quad \ldots\ldots \text{Eq. A. 31}$$

A.1.2.3 Calculations for θ when the $BG < 4$

The θ is calculated using Equations A.10 (see Figure A.1). Rearranging Equation A.10 will result in Equation A.11. Replacing the Z and X from Equation A.30 and A.31 into the Equation A.11, the θ is calculated for $BG < 4$.

$$\theta = \tan^{-1}\left(\frac{\sqrt{\frac{{D_c}^2}{4} - \left(\frac{D_c}{2} - \frac{\left(\frac{BG.D_c}{8}\right)}{\cos(BR)}\right)^2}}{\frac{D_c}{2} - \frac{BG.D_c}{8}}\right) \quad \ldots\ldots \text{Eq. A. 32}$$

A.1.2.4 Calculations cutter worn area when $BG < 4$

The cutter worn area is calculated by subtracting the circle sector area from triangle as seen in Figure A.5. The cutter sector area and triangle area were calculated in Equation A.1 and A.2. The

triangle area (Equation A.2) is turned into Equation A.33 by replacing the Z and X (see Equations A.30 and A.31).

$$A_{triangle} = \left(\frac{\left(\frac{D_c}{2} - \frac{BG.D_c}{8}\right).\left(2\sqrt{\frac{{D_c}^2}{4} - (\frac{D_c}{2} - \frac{\left(\frac{BG.D_c}{8}\right)}{Cos(BR)})^2}\right)}{2} \right) \ldots\ldots \text{Eq. A. 33}$$

The Equation A.32 is replaced into Equation A.1, and using Equation A.33 and A.16, the cutter worn area is achieved (see Equation A.34).

$$A_{worn} = \left(\frac{\left(Tan^{-1}\left(\frac{\sqrt{\frac{{D_c}^2}{4} - \left(\frac{D_c}{2} - \frac{BG.D_c}{8}\right)^2}}{\frac{D_c}{2} - \frac{BG.D_c}{8}}\right)\right)\pi {D_c}^2}{720} \right) - \left(\frac{\left(\frac{D_c}{2} - \frac{BG.D_c}{8}\right) \times \left(2\sqrt{{D_c}^2/4 - (\frac{D_c}{2} - \frac{BG.D_c}{8})^2}\right)}{2} \right) \ldots\ldots \text{Eq. A. 34}$$

A.1.2.5 Calculations cutter worn area when $BG = 4$

When the $BG = 4$, the cutter is half worn therefore the cutter worn area would be half of total cutter face area and it is seen in Equation A.35.

$$A_{worn} = \pi \frac{{D_c}^2}{8} \quad \ldots\ldots \text{Eq. A. 35}$$

A.1.2.6 Calculations for Z when the $BG > 4$

A schematic of a cutter when the BG is greater than 4 is seen in Figure A.6.

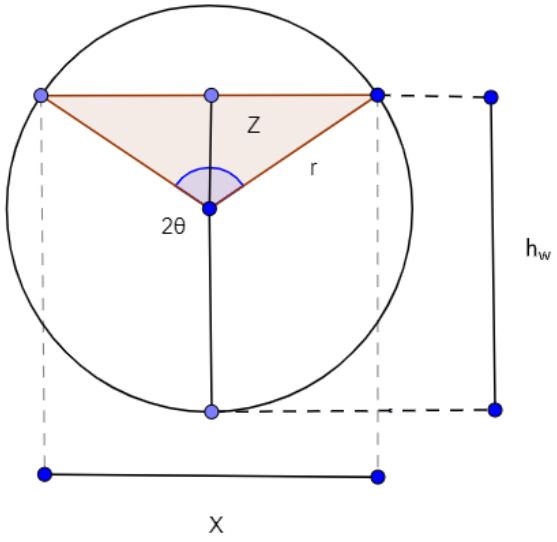

Figure A.6. A schematic of a cutter face area when the BG > 4

When the BG $>$ 4, the Z is calculated using Equation A.36.

$$Z = -r + h_w \ldots\ldots \text{Eq. A. 36}$$

Replacing h_w in Equation, A.36 will give Equation A.37.

$$Z = -r + \frac{BG.D_c}{8} \ldots\ldots \text{Eq. A. 37}$$

Replacing the r with half of the cutter diameter will result in Equation A.38.

$$Z = -\frac{D_c}{2} + \frac{BG.D_c}{8} \ldots\ldots \text{Eq. A. 38}$$

A.1.2.7 Calculations for X when the BG $>$ 4

Using Pythagorean Theorem (see Equation A.4 and Figure A.2), the Equation A.7 is achieved. Rearranging Equation A.7, the Equation A.8 is achieved. Replacing the r with half of the cutter diameter, and Z from Equation A.38 into Equation A.8 the X is calculated using Equation A.39.

$$X = 2\sqrt{\frac{{D_c}^2}{4} - \left(-\frac{D_c}{2} + \frac{BG.D_c}{8}\right)^2} \ldots\ldots \text{Eq. A. 39}$$

A.1.1.8 Calculations for θ when the BG $>$ 4

The θ is calculated using Equations A.10 (see Figure A.1). Rearranging Equation A.10 will result in Equation A.11 (see Equation A.11). Replacing the X (Equation A.39), and Z (Equation A.38) into the Equation A.11, the θ is calculated in Equation A.40.

$$\theta = \mathrm{Tan}^{-1}\left(\frac{\sqrt{\frac{D_c{}^2}{4} - \left(-\frac{D_c}{2} + \frac{BG.D_c}{8}\right)^2}}{-\frac{D_c}{2} + \frac{BG.D_c}{8}}\right) \ldots\ldots \text{Eq. A. 40}$$

A.1.2.9 Calculations for cutter worn area when $BG > 4$

The cutter worn area is calculated using Equation A.41.

$$A_{contact} = A_{Sector} + A_{Triangle} \ \ldots\ldots \text{Eq. A. 41}$$

The cutter sector area is calculated in the Equation A.25. The triangle area is calculated in Equation A.26. The Equation A.2 is turned into Equation A.42 by replacing the Z and X (see Equations A.38 and A.39).

$$A_{triangle} = \left(\frac{\left(-\frac{D_c}{2} + \frac{BG.D_c}{8}\right) \times \left(2\sqrt{-\frac{D_c{}^2}{4} + \left(\frac{D_c}{2} - \frac{BG.D_c}{8}\right)^2}\right)}{2}\right) \ldots\ldots \text{Eq. A. 42}$$

The Equation A.40 is replaced into Equation A.1, and using Equation A.42 and A.25, the cutter worn area is achieved (see Equation A.43).

$$A_{worn} = \left(\pi\left(\frac{D_c}{2}\right)^2 - \frac{2\left(\mathrm{Tan}^{-1}\left(\frac{\sqrt{-\frac{D_c{}^2}{4} + \left(\frac{D_c}{2} - \frac{BG.D_c}{8}\right)^2}}{-\frac{D_c}{2} + \frac{BG.D_c}{8}}\right)\right)}{360}\pi\left(\frac{D_c}{2}\right)^2\right) + \left(\frac{\left(-\frac{D_c}{2} + \frac{BG.D_c}{8}\right) \times \left(2\sqrt{-\frac{D_c{}^2}{4} + \left(\frac{D_c}{2} - \frac{BG.D_c}{8}\right)^2}\right)}{2}\right) \ldots\ldots \text{Eq. A. 43}$$

A.1.3 Cutter contact area calculation

A sharp cutter contact area is calculated using Equations A.27. Figure A.7 shows a schematic of a blunt cutter. A blunt cutter contact area (BC) is calculated by subtracting the contact area of a sharp

cutter (BD) with a depth of cut equal to DOC_2 from the cutter worn area (CD) of a blunt cutter with a depth of cut equal to DOC and reported BG (see Figure A.7). The DOC_2 equation is provided in Equation A.44.

$$DOC_2 = DOC + \frac{BG \times D_c \times \cos(BR)}{8} \quad \ldots\ldots\ldots \text{Eq. A. 44}$$

Therefore, to calculate the contact area of a blunt cutter (BC) with a depth of cut equal to DOC, and wear equal to BG the following steps should be taken.

1) The contact area of a sharp cutter with a depth of cut equal to DOC_2 (BD) is calculated using Equation A.18 or A.27 (check the condition, whether the DOC is less or greater than threshold DOC).
2) The worn area of a blunt cutter (CD) with reported BG is calculated using Equation A. 34 or A.43 (check the condition, whether the BG is less or greater than 4).
3) The area from step 1 is subtracted from the area in step 2 to achieve the blunt cutter contact area (BC).

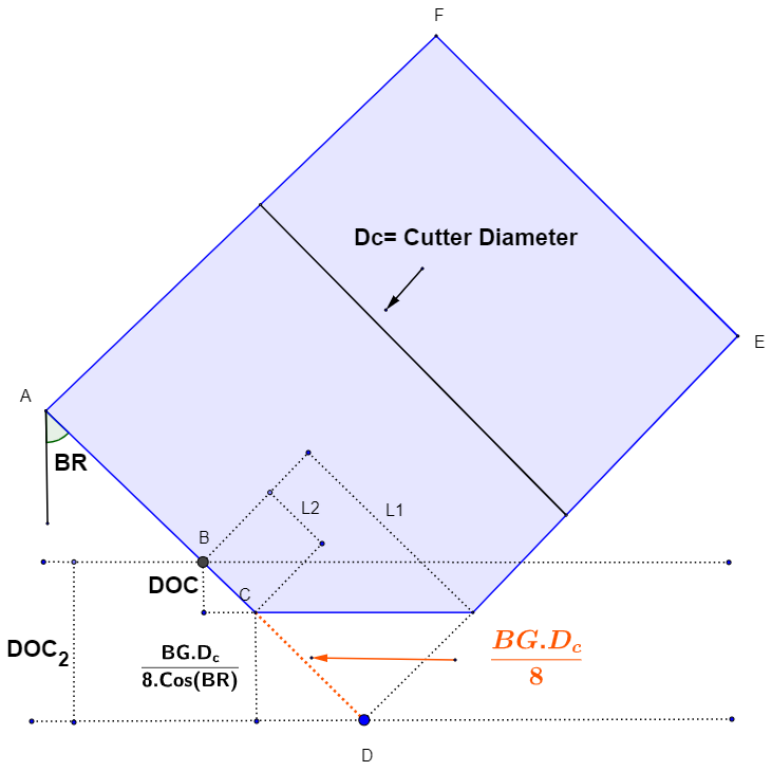

Figure A.7. A schematic of a blunt cutter

A.2 Approach # 2

The circle segment area is calculated as a function of cutter depth of cut and cutter BG. In the following the circle segment area calculations are provided. Circle segment calculations reference: http://mathworld.wolfram.com/CircularSegment.html

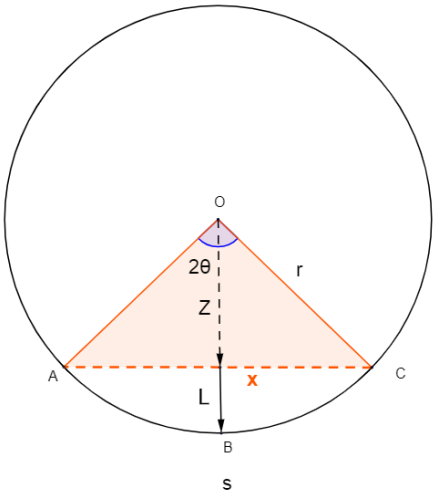

Figure A.8. A schematic of the circle segment area (ABCA)

The cutter radius is provided in the Equation A.45.

$$r = L + Z \ldots\ldots \text{Eq. A. 45}$$

The circle arc is achieved using Equation A.46.

$$s = r(2\theta) \ldots\ldots \text{Eq. A. 46}$$

Base on trigonometry, the Equations A.47 and A.48 are achieved.

$$Z = r.\cos(\theta) \ldots\ldots \text{Eq. A. 47}$$

$$Z = \frac{1}{2}.X.\cot(\theta) \ldots\ldots \text{Eq. A. 48}$$

Taking the triangle in Figure A.8 into account, the Equation A.49 is achieved.

$$Z = \frac{1}{2}\sqrt{4r^2 - X^2} \ldots\ldots \text{Eq. A. 49}$$

Moreover, the length of the chord (see the triangle AOC in Figure A.8) can be written in the form of Equations A.50 to A. 53.

$$X = 2r.\sin(\theta) \ldots\ldots \text{Eq. A. 50}$$

$$X = 2Z.\tan(\theta) \ldots\ldots \text{Eq. A. 51}$$

$$X = 2\sqrt{r^2 - Z^2} \ldots\ldots \text{Eq. A. 52}$$

$$X = 2\sqrt{L(2r - L)} \ldots\ldots \text{Eq. A. 53}$$

From elementary trigonometry, the angle θ obeys the following relationships provided in Equations A.54 to A.57.

$$2\theta = \frac{s}{r} \dots\dots\dots \text{Eq. A. 54}$$

$$2\theta = 2\cos^{-1}\left(\frac{Z}{r}\right) \dots\dots\dots \text{Eq. A. 55}$$

$$2\theta = 2\tan^{-1}\left(\frac{X}{2Z}\right) \dots\dots\dots \text{Eq. A. 56}$$

$$2\theta = 2\sin^{-1}\left(\frac{X}{2r}\right) \dots\dots\dots \text{Eq. A. 57}$$

The area of the segment (ABCA) is then simply given by the area of the circular sector (the entire wedge -ABCOA) minus the area of the bottom triangular portion (ACOA).

$$A_{segment} = A_{Sector} - A_{triangle} \dots\dots\dots \text{Eq. A. 58}$$

Replacing in the sector and triangle areas into the Equation A.58 will result in Equation A.59.

$$A_{segment} = \frac{1}{2}r^2(2\theta - \sin 2\theta) \dots\dots\dots \text{Eq. A. 59}$$

Note that the angle θ is in radian and should be turned into a degree. Expanding the Equation A.59, and replacing 2θ from Equation A.46 into the first section and replacing the second part will result in Equation A.60.

$$A_{segment} = \frac{1}{2}(rs - XZ) \dots\dots\dots \text{Eq. A. 60}$$

Replacing s, Z, and X from Equations A.46, A.49, A.53, and A.55 into Equation A.60 will result in Equation A.61.

$$A_{segment} = r^2\cos^{-1}\left(\frac{Z}{r}\right) - Z\sqrt{r^2 - Z^2} \dots\dots\dots \text{Eq. A. 61}$$

Replace Z from Equation A.45 into Equation A.61 will result in Equation A.62.

$$A_{segment} = r^2\cos^{-1}\left(\frac{r - L}{r}\right) - (r - L)\sqrt{2rL - L^2} \dots\dots\dots \text{Eq. A. 62}$$

Replace the circle radius with cutter diameter will results in Equation A.63 (Note that the segment area is equal to cutter contact area).

$$A_{contact} = \left(\frac{D_c}{2}\right)^2 . \text{Cos}^{-1}\left(\frac{\frac{D_c}{2} - L}{\frac{D_c}{2}}\right) - \left(\frac{D_c}{2} - L\right) . \sqrt{2.\left(\frac{D_c}{2}\right).L - (L)^2} \dots\dots\dots \text{Eq. A. 63}$$

A.2.1 Cutter Contact area calculation for a sharp cutter

For a sharp cutter, the L (see Figure A.8) in Equation A.63 is equal to L1 (see Figure A.9). The L1 is calculated in Equation A.64.

$$L1 = \frac{DOC}{Cos(BR)} \ldots\ldots\ldots \text{Eq. A. 64}$$

Replacing L1 (see Equation A.64) into L (see Equation A.63) will result in Equation A.65. The Equation A.65 is used to calculate the cutter contact area for a sharp cutter when the DOC,D_c, and BR are known.

$$A_{contact} = \left(\frac{D_c}{2}\right)^2 \times Cos^{-1}\left(\frac{\frac{D_c}{2} - \frac{DOC}{Cos(BR)}}{\frac{D_c}{2}}\right) - \left(\frac{D_c}{2} - \frac{DOC}{Cos(BR)}\right) \times \sqrt{D_c \times \frac{DOC}{Cos(BR)} - \left(\frac{DOC}{Cos(BR)}\right)^2} \ldots\ldots\ldots \text{Eq. A. 65}$$

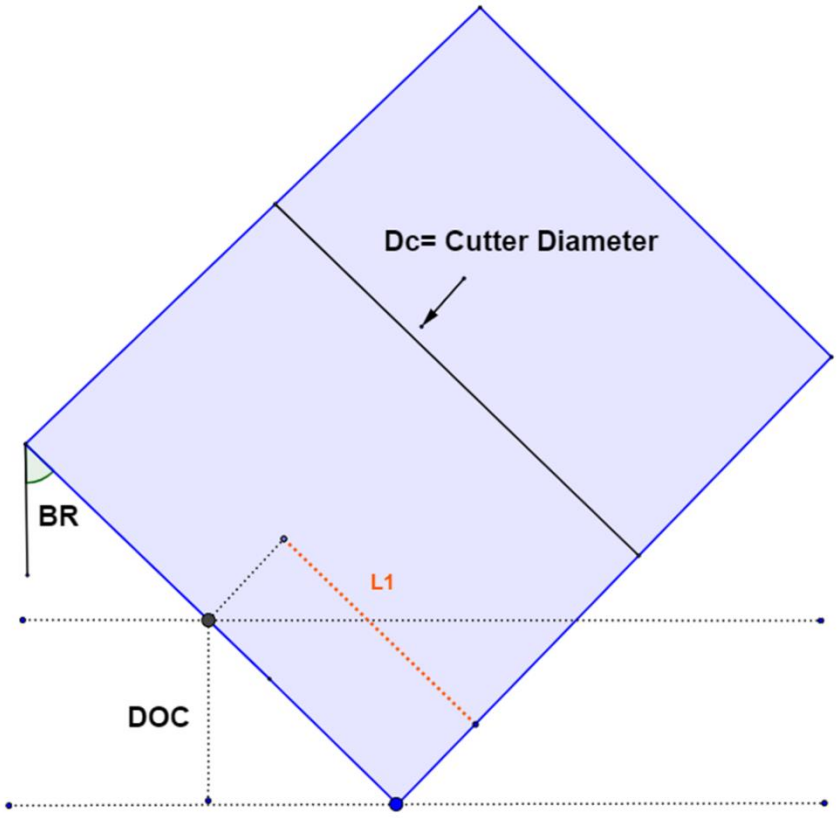

Figure A.9. A schematic of a sharp cutter

A.2.2 Cutter Contact area calculation for a blunt cutter

For a blunt cutter, similar to section A.3, (see Figure A.7), a blunt cutter contact area (BC) is calculated by subtracting the contact area of a sharp cutter (BD) with a depth of cut equal to DOC_2 from the cutter worn area (CD) of a blunt cutter with reported BG (see Figure A.7). The DOC_2 equation is provided in Equation A.44.

$$A_{contact} = \left[\left(\frac{D_c}{2}\right)^2 . \cos^{-1}\left(\frac{\frac{D_c}{2} - \left(\frac{DOC_2}{\cos(BR)}\right)}{\frac{D_c}{2}}\right) - \left(\frac{D_c}{2} - \left(\frac{DOC_2}{\cos(BR)}\right)\right) . \sqrt{2.\left(\frac{D_c}{2}\right).\left(\frac{DOC_2}{\cos(BR)}\right) - \left(\frac{DOC_2}{\cos(BR)}\right)^2}\right] - \left[\left(\frac{D_c}{2}\right)^2 . \cos^{-1}\left(\frac{\frac{D_c}{2} - \left(\frac{BG.D_c}{8}\right)}{\frac{D_c}{2}}\right) - \left(\frac{D_c}{2} - \left(\frac{BG.D_c}{8}\right)\right) . \sqrt{2.\left(\frac{D_c}{2}\right).\left(\frac{BG.D_c}{8}\right) - \left(\frac{BG.D_c}{8}\right)^2}\right] \dots\dots\dots \text{Eq. A. 66}$$

Replacing the DOC_2 using Equation A.44 in Equation A.66 will result in Equation A.67.

$$A_{contact} = \left[\left(\frac{D_c}{2}\right)^2 . \cos^{-1}\left(\frac{\frac{D_c}{2} - \left(\frac{\left(DOC + \frac{BG \times D_c \times \cos(BR)}{8}\right)}{\cos(BR)}\right)}{\frac{D_c}{2}}\right) - \left(\frac{D_c}{2} - \left(\frac{\left(DOC + \frac{BG \times D_c \times \cos(BR)}{8}\right)}{\cos(BR)}\right)\right) . \sqrt{2.\left(\frac{D_c}{2}\right).\left(\frac{\left(DOC + \frac{BG \times D_c \times \cos(BR)}{8}\right)}{\cos(BR)}\right) - \left(\frac{\left(DOC + \frac{BG \times D_c \times \cos(BR)}{8}\right)}{\cos(BR)}\right)^2}\right] - \left[\left(\frac{D_c}{2}\right)^2 . \cos^{-1}\left(\frac{\frac{D_c}{2} - \left(\frac{BG.D_c}{8}\right)}{\frac{D_c}{2}}\right) - \left(\frac{D_c}{2} - \left(\frac{BG.D_c}{8}\right)\right) . \sqrt{2.\left(\frac{D_c}{2}\right).\left(\frac{BG.D_c}{8}\right) - \left(\frac{BG.D_c}{8}\right)^2}\right] \dots\dots\dots \text{Eq. A. 67}$$

APPENDIX B

Wear Flat Area Calculations

B.1 Approach 1

In Figure B.1, a plane and a cylinder are shown. The plane intersected with the bottom side of the cylinder on the X-Y-Z coordinate. In Figure B.1, the A_w is the cutter wear flat area and the A_w' is the projection of cutter wear flat area on the X-Y plane. Note that the Y and Y' are laid on each other and X'-Y'-Z' can rotate around its fixed Y' axis.

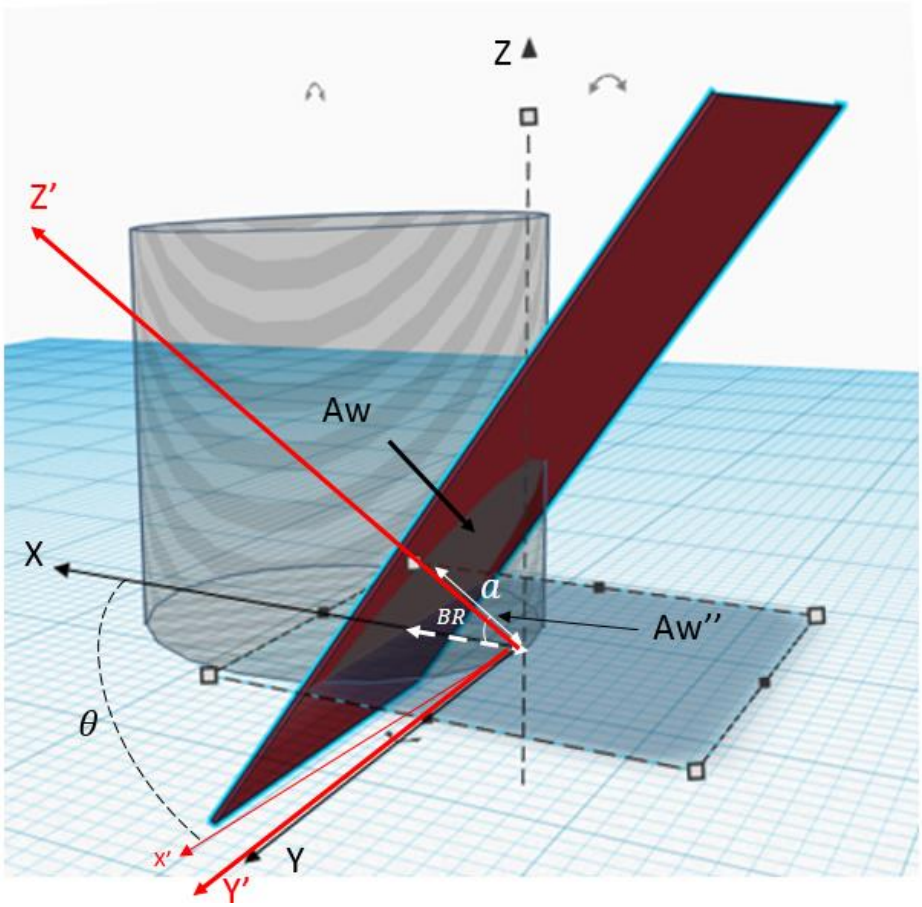

Figure B.1. A 3D schematic of a cylinder and a plane intersection and details areas

In the following equations, the L is the height of cutter (cylinder), the r is cutter radius, "a" is the depth of worn, and the θ is the rotation degree between the two X'-Y'-Z' and X-Y-Z coordinates. The plane is in the X'-Y'-Z' coordinate and its equation is provided at the Equation B.1.

$$Z' = a \dots\dots \text{Eq. B. 1}$$

The X'-Y'-Z' coordinate rotates θ degree counter-clockwise to match with the X-Y-Z coordinate. The new equation of the plane in the new coordinate is calculated at the following.

$$\begin{bmatrix} \text{Cos}\theta & \text{Sin}\theta \\ -\text{Sin}\theta & \text{Cos}\theta \end{bmatrix} \begin{bmatrix} X' & Z' \\ 1 & 0 \\ 0 & 1 \end{bmatrix} = \begin{bmatrix} X & Z \\ \text{Cos}\theta & -\text{Sin}\theta \\ \text{Sin}\theta & \text{Cos}\theta \end{bmatrix} \dots\dots \text{Eq. B. 2}$$

Thus

$$X = X'.\text{Cos}\theta + Z'.\text{Sin}\theta \dots\dots \text{Eq. B. 3}$$

$$Z = -X'.\text{Sin}\theta + Z'.\text{Cos}\theta \dots\dots \text{Eq. B. 4}$$

Multiplying Equation B.3 & B.4 by Sin (θ) and Cos (θ) respectively

$$X.\text{Sin}\theta = X'.\text{Cos}\theta.\text{Sin}\theta + Z'.\text{Sin}\theta^2 \dots\dots \text{Eq. B. 5}$$

$$Z.\text{Cos}\theta = -X'.\text{Sin}\theta.\text{Cos}\theta + Z'.\text{Cos}\theta^2 \dots\dots \text{Eq. B. 6}$$

Adding up Equation B.5 and B.6

$$Z' = X.\text{Sin}\theta + Z.\text{Cos}\theta \dots\dots \text{Eq. B. 7}$$

Plugging the Equation B.1 into the Equation B.7, the plane equation in X-Y-Z coordinate would be:

$$a = X.\text{Sin}\theta + Z.\text{Cos}\theta \dots\dots \text{Eq. B. 8}$$

The cylinder is perpendicular to the plane X-Y-Z. The image of intersection between the plane and cylinder in the X-Y-Z coordinate is provided at Figure B.2. In Figure B.2, the AE is representative of the bottom intersection between the plane and the X-Y, and the BD is the projection of the plane intersected with the top of the cylinder on X-Y.

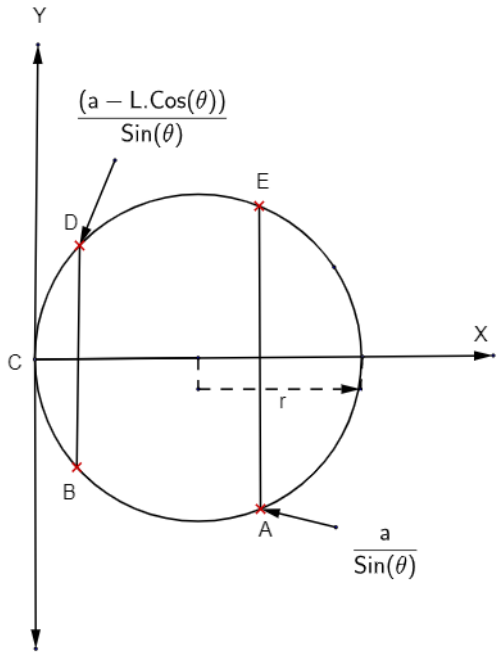

Figure B.2. The intersection between the plane and the top and bottom of a cylinder on the X-Y coordinate (top side view)

The two vertical lines show the intersection between the bottom and the top of the cylinder on the X-Y plane. The intersection points are calculated using the following equations. The bottom and top intersection are calculated using Equation B.8 when the Z=0 and L respectively.

$$\text{at } Z = 0 \text{ then } X = \frac{a}{Sin\theta} \dots\dots \text{Eq. B. 9}$$

$$\text{at } Z = L \text{ then } X = \frac{a - L.Cos\theta}{Sin\theta} \dots\dots \text{Eq. B. 10}$$

The conditions are:

$$0 < \frac{a - L.Cos\theta}{Sin\theta} < \frac{a}{Sin\theta} < D_c \dots\dots \text{Eq. B. 11}$$

In the above equations, the Dc is cylinder diameter (cutter). The area of the intersection (representation of cutter wear flat area) between the plane and cylinder in the X-Y-Z coordinate can be calculated by taking integral between the boundaries (Equation B.9 and B.10) and circle equation in the X-Y plane (Equation B.12). The circle equation is provided in the following.

$$(X - r)^2 + Y^2 = r^2 \dots\dots \text{Eq. B. 12}$$

To find the ABDEA surface area in Figure B.2 (which is representative of projected wear flat area), the Equation B.13 is used which is representative of the DE curve derived from Equation B.12.

$$Y = \sqrt{-X^2 + 2rX} \dots\dots \text{Eq. B. 13}$$

The Wear flat area is calculated using Equation B.14. The area between Equation B.13 and the X-axis is calculated by taking the integral of Equation B.13 with specified boundaries (see Equation B.11) and then it is doubled and is divided by the Cos (θ) to come up with the wear flat area (A_w). The θ is both the cutter BR complementary angle and the rotation angle between two X-Y-Z and X'-Y'-Z' coordinates (see Figure B.1).

$$A_w = \frac{2}{Cos(\theta)} \int_{\frac{a-L.Cos\theta}{Sin\theta}}^{\frac{a}{Sin\theta}} \sqrt{-X^2 + 2rX}\, dx \dots\dots \text{Eq. B. 14}$$

Solving integral:

$$\int \sqrt{-X^2 + 2rX}\, dx \dots\dots \text{Eq. B. 15}$$

Rewrite Equation B.15.

$$2rX - X^2 = -(X^2 - 2rX + r^2) + r^2 \dots\dots \text{Eq. B. 16}$$

Rewrite Equation B.16 to Equation B.17 (similar to Pythagorean theorem).

$$= r^2 - (X - r)^2 \dots\dots \text{Eq. B. 17}$$

Change the parameter X to θ.

$$X - r = r.Sin\theta \dots\dots \text{Eq. B. 18}$$

Take derivation from both sides of Equation B.18.

$$dX = r.Cos(\theta).d\theta \dots\dots \text{Eq. B. 19}$$

Rearrange Equation B.18 and rewrite it in Equation B.20.

$$Sin\theta = \frac{X - r}{r} \dots\dots \text{Eq. B. 20}$$

Plugging the Equation B.17, B.18 and B.19 into Equation B.15 will result in Equation B.21.

$$= \int \sqrt{r^2 - r^2.Sin^2\theta}\,.r.Cos\theta\, d\theta \dots\dots \text{Eq. B. 21}$$

Rewrite Equation B.21 into Equation B.22

$$= \int r^2.Cos^2\theta\, d\theta \dots\dots \text{Eq. B. 22}$$

Rewrite the Cos in Equation B.22 using trigonometry rules.

$$= \int r^2 . \frac{1 + \text{Cos}2\theta}{2} \, d\theta \; \ldots\ldots \text{Eq. B. 23}$$

Solve the integral in Equation B.23.

$$= \frac{r^2}{2} (\theta + \frac{\text{Sin}2\theta}{2}) \ldots\ldots \text{Eq. B. 24}$$

Open the Equation B.24 using trigonometry rules.

$$= \frac{r^2}{2} (\theta + \text{Sin}\theta . \text{Cos}\theta) \ldots\ldots \text{Eq. B. 25}$$

Replace the θ in Equation B.25 using Equation B.18 and the Pythagorean theorem.

$$= \frac{r^2}{2} (\text{Sin}^{-1}(\frac{X - r}{r}) + \frac{X - r}{r} . \frac{\sqrt{2rX - X^2}}{r}) \ldots\ldots \text{Eq. B. 26}$$

Introduce the integral boundaries into the Equation B.27.

$$= \frac{r^2}{2} \left(\text{Sin}^{-1}(\frac{X - r}{r}) + \frac{(X - r)\sqrt{2rX - X^2}}{r^2} \right) \Bigg[\begin{matrix} \frac{a}{\text{Sin}\theta} \\ \frac{a - L.\text{Cos}\theta}{\text{Sin}\theta} \end{matrix} \ldots\ldots \text{Eq. B. 27}$$

Replacing the boundaries and assuming the lower bound is zero and doubling the surface area and returning the surface area to the original one (by multiplying with $\frac{1}{\text{Cos}\theta}$) then:

$$A_w = \left(\left(\frac{r^2}{2} \left(\text{Sin}^{-1}(\frac{(\frac{a}{\text{Sin}\theta}) - r}{r}) + \frac{(\frac{a}{\text{Sin}\theta} - r)\sqrt{2r(\frac{a}{\text{Sin}\theta}) - (\frac{a}{\text{Sin}\theta})^2}}{r^2} \right) \right) - \left(\frac{r^2}{2} \left(\text{Sin}^{-1}(\frac{(\frac{a - L.\text{Cos}\theta}{\text{Sin}\theta}) - r}{r}) + \frac{(\frac{a - L.\text{Cos}\theta}{\text{Sin}\theta} - r)\sqrt{2r(\frac{a - L.\text{Cos}\theta}{\text{Sin}\theta}) - (\frac{a - L.\text{Cos}\theta}{\text{Sin}\theta})^2}}{r^2} \right) \right) \right) \times \frac{2}{\text{Cos}\theta} \ldots\ldots \text{Eq. B. 28}$$

The r is equal to half of the cutter diameter then,

$$A_w = \left(\left(\frac{\left(\frac{Dc}{2}\right)^2}{2} \left(\sin^{-1}\left(\frac{\left(\frac{a}{\sin\theta}\right) - \frac{Dc}{2}}{\frac{Dc}{2}}\right) + \frac{\left(\frac{a}{\sin\theta} - \frac{Dc}{2}\right)\sqrt{2\left(\frac{Dc}{2}\right)\left(\frac{a}{\sin\theta}\right) - \left(\frac{a}{\sin\theta}\right)^2}}{\left(\frac{Dc}{2}\right)^2} \right) \right) \right.$$

$$\left. - \left(\frac{\left(\frac{Dc}{2}\right)^2}{2} \left(\sin^{-1}\left(\frac{\left(\frac{a - L.\cos\theta}{\sin\theta}\right) - \frac{Dc}{2}}{\frac{Dc}{2}}\right) \right. \right. \right.$$

$$\left. \left. \left. + \frac{\left(\frac{a - L.\cos\theta}{\sin\theta} - \frac{Dc}{2}\right)\sqrt{2\left(\frac{Dc}{2}\right)\left(\frac{a - L.\cos\theta}{\sin\theta}\right) - \left(\frac{a - L.\cos\theta}{\sin\theta}\right)^2}}{\left(\frac{Dc}{2}\right)^2} \right) \right) \right)$$

$$\times \frac{2}{\cos\theta} \quad \ldots\ldots \text{Eq. B. 29}$$

$$a = \left(\frac{BG.\, D_c.\cos(BR)}{8}\right) \ldots\ldots \text{Eq. B. 30}$$

Replacing the θ with (90-BR) and depth of wear (a) using Equation B.30 will result in Equation 31.

$$A_w = \left(\left(\frac{\left(\frac{Dc}{2}\right)^2}{2}\left(\mathrm{Sin}^{-1}\left(\frac{\left(\frac{\left(\frac{BG.D_c.\mathrm{Cos}(BR)}{8}\right)}{\mathrm{Sin}(90-BR)}\right)-\frac{Dc}{2}}{\left(\frac{Dc}{2}\right)}\right)+\frac{\left(\frac{\left(\frac{BG.D_c.\mathrm{Cos}(BR)}{8}\right)}{\mathrm{Sin}(90-BR)}-\frac{Dc}{2}\right)\sqrt{2\left(\frac{Dc}{2}\right)\left(\frac{\left(\frac{BG.D_c.\mathrm{Cos}(BR)}{8}\right)}{\mathrm{Sin}(90-BR)}\right)-\left(\frac{\left(\frac{BG.D_c.\mathrm{Cos}(BR)}{8}\right)}{\mathrm{Sin}(90-BR)}\right)^2}}{\left(\frac{Dc}{2}\right)^2}\right)\right)\right) - \left(\frac{\left(\frac{Dc}{2}\right)^2}{2}\left(\mathrm{Sin}^{-1}\left(\frac{\left(\frac{\left(\frac{BG.D_c.\mathrm{Cos}(BR)}{8}\right)-L.\mathrm{Cos}(90-BR)}{\mathrm{Sin}(90-BR)}\right)-\frac{Dc}{2}}{\left(\frac{Dc}{2}\right)}\right)+\frac{\left(\frac{\left(\frac{BG.D_c.\mathrm{Cos}(BR)}{8}\right)-L.\mathrm{Cos}(90-BR)}{\mathrm{Sin}(90-BR)}-\frac{Dc}{2}\right)\sqrt{2\left(\frac{Dc}{2}\right)\left(\frac{\left(\frac{BG.D_c.\mathrm{Cos}(BR)}{8}\right)-L.\mathrm{Cos}(90-BR)}{\mathrm{Sin}(90-BR)}\right)-\left(\frac{\left(\frac{BG.D_c.\mathrm{Cos}(BR)}{8}\right)-L.\mathrm{Cos}(90-BR)}{\mathrm{Sin}(90-BR)}\right)^2}}{\left(\frac{Dc}{2}\right)^2}\right)\right)\right) \times \frac{2}{\mathrm{Cos}(90-BR)} \quad \ldots\ldots\ldots \text{Eq. B. 31}$$

Conditions are:

$$\text{The integral upper boundary is } \frac{a}{\mathrm{Sin}\theta} < Dc$$

$$\text{Integral lower boundary is } \frac{a - L.\mathrm{Cos}\theta}{\mathrm{Sin}\theta} > 0$$

If the $\frac{a-L.\cos\theta}{\sin\theta} = 0$ then the cutter wear flat area is calculated using Equation B.32.

$$A_w = \left(\frac{\left(\frac{Dc}{2}\right)^2}{2} \left(\sin^{-1} \left(\frac{\left(\frac{\left(\frac{BG.\,D_c.\,\cos(BR)}{8}\right)}{\sin(90-BR)} \right) - \frac{Dc}{2}}{\left(\frac{Dc}{2}\right)} \right) + \frac{\left(\frac{\left(\frac{BG.\,D_c.\,\cos(BR)}{8}\right)}{\sin(90-BR)} - \frac{Dc}{2} \right) \sqrt{2\left(\frac{Dc}{2}\right)\left(\frac{\left(\frac{BG.\,D_c.\,\cos(BR)}{8}\right)}{\sin(90-BR)} \right) - \left(\frac{\left(\frac{BG.\,D_c.\,\cos(BR)}{8}\right)}{\sin(90-BR)} \right)^2}}{\left(\frac{Dc}{2}\right)^2} \right) \right) \times \frac{2}{\cos(90-BR)} \quad \ldots\ldots\ldots \text{Eq. B. 32}$$

Conditions are:

$$\text{The integral upper boundary is } \frac{a}{\sin\theta} < Dc$$

$$\text{The integral lower boundary is } 0$$

If the length of the cylinder (L) assume equal to PDC thickness length then the PDC wear flat area is calculated by replacing the PDC thickness (t_{PDC}) with L in the Equation B.31 and it is seen in the Equation B.33.

$$
\begin{aligned}
A_{w,PDC} &= \left(\left(\frac{\left(\frac{Dc}{2}\right)^2}{2}\left(\mathrm{Sin}^{-1}\left(\frac{\left(\frac{\left(\frac{BG.\,D_c.\,Cos(BR)}{8}\right)}{Sin(90-BR)}\right)-\frac{Dc}{2}}{\left(\frac{Dc}{2}\right)}\right)+\frac{\left(\frac{\left(\frac{BG.\,D_c.\,Cos(BR)}{8}\right)}{Sin(90-BR)}-\frac{Dc}{2}\right)\sqrt{2\left(\frac{Dc}{2}\right)\left(\frac{\left(\frac{BG.\,D_c.\,Cos(BR)}{8}\right)}{Sin(90-BR)}\right)-\left(\frac{\left(\frac{BG.\,D_c.\,Cos(BR)}{8}\right)}{Sin(90-BR)}\right)^2}}{\left(\frac{Dc}{2}\right)^2}\right)\right)\right.\\
&\left.-\left(\frac{\left(\frac{Dc}{2}\right)^2}{2}\left(\mathrm{Sin}^{-1}\left(\frac{\left(\frac{\left(\frac{BG.\,D_c.\,Cos(BR)}{8}\right)-t_{PDC}.\,Cos(90-BR)}{Sin\theta}\right)-\frac{Dc}{2}}{\left(\frac{Dc}{2}\right)}\right)\right.\right.\\
&\left.\left.+\frac{\left(\frac{\left(\frac{BG.\,D_c.\,Cos(BR)}{8}\right)-t_{PDC}.\,Cos(90-BR)}{Sin(90-BR)}-\frac{Dc}{2}\right)\sqrt{2\left(\frac{Dc}{2}\right)\left(\frac{\left(\frac{BG.\,D_c.\,Cos(BR)}{8}\right)-t_{PDC}.\,Cos(90-BR)}{Sin(90-BR)}\right)-\left(\frac{\left(\frac{BG.\,D_c.\,Cos(BR)}{8}\right)-t_{PDC}.\,Cos(90-BR)}{Sin(90-BR)}\right)^2}}{\left(\frac{Dc}{2}\right)^2}\right)\right)\right)\\
&\times\frac{2}{Cos(90-BR)} \quad \ldots\ldots\ldots \mathrm{Eq.\,B.33}
\end{aligned}
$$

The wear flat area beneath the cutter stud is calculated by subtracting the total wear flat area (Equation B.32) from PDC wear flat area (Equation B.33).

$$A_{w,Stud} = A_w - A_{w,PDC} \quad \ldots\ldots\ldots \mathrm{Eq.\,B.34}$$

B.2 Approach 2

The total wear flat area projection on the X-Y-Z plane is a segment of a circle. The circle segment area was calculated in Equation A.63. The Equation A.63 can be applied to calculate the segment area of a circle in Figure B.2. Once the circle segment was calculated, it can be projected by taking the cutter (θ) into account to achieve the cutter wear flat area.

APPENDIX C

Cutter Worn Volume Calculations

The goal of this section is to find the volume of the worn-out section of a cutter. The worn-out section for a cutter is seen (assigned number 1) in Figure C.1.

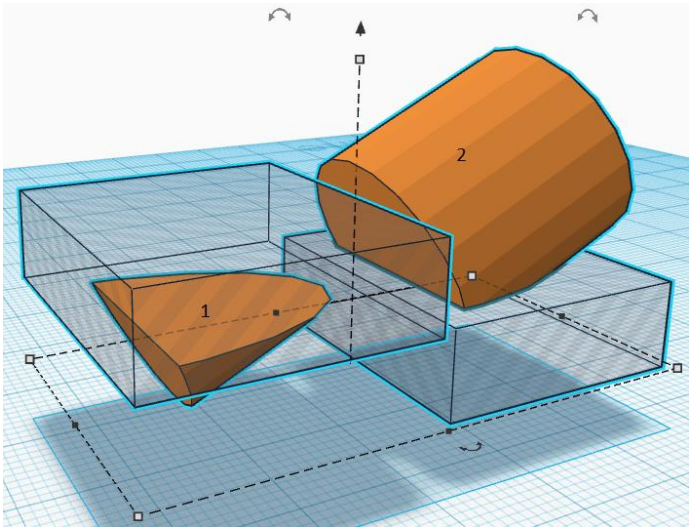

Figure C.1. A 3D schematic of a blunt cutter (assigned number 2) and the worn section (assigned number 1)

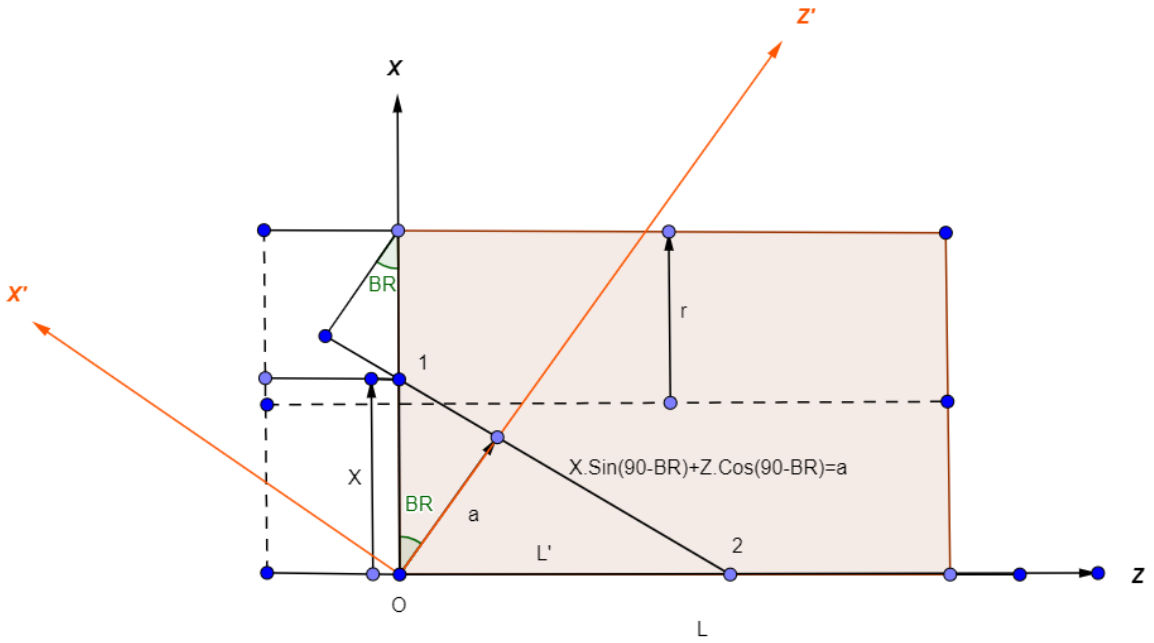

Figure C.2. A side view schematic of a cutter

Figure C.2 shows a cylinder (cutter) laid down on Z-axis. The face of the cylinder is on the X –Y and is shown in Figure C.3. The Y-axis is perpendicular to X and Z plane and it comes out of X-Z origin (point O). In Figure C.2, the line that connects point 1 to point 2 is a 2D representation of a plane in the X'-Z' coordinate. In Figure C.2, the L is the length of the cylinder. The L' is the length of the line between O and point 2. The goal is to calculate the volume of a worn wedge (assigned 1 in Figure C.1) that is seen as a 2D triangle between point O and points 1 and 2 in Figure C.2. The circle segment area can be calculated using Equation C.1 (see appendix A.2).

$$A_{segment} = \left(\frac{D_c}{2}\right)^2 . Cos^{-1}\left(\frac{\frac{D_c}{2} - X}{\frac{D_c}{2}}\right) - \left(\frac{D_c}{2} - X\right) . \sqrt{2.\left(\frac{D_c}{2}\right).X - (X)^2} \ldots\ldots \text{Eq. C. 1}$$

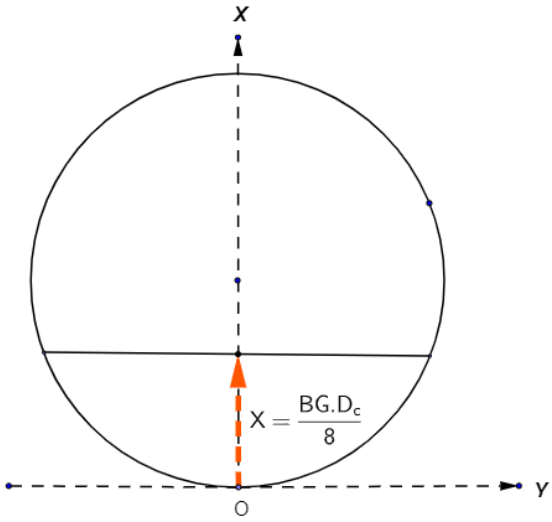

Figure C.3. Cutter front face on X-Y coordinate (front side view)

The area of the circle segment in Figure C.3 is a function of X (see Equation C.1). The variable X in the circle can be written as a function of Z (see Equation C.7). The cutter worn volume can be found by taking an integral of circle segment area (Equation C.1) and between Z=0 and Z=b (point 1 and 2 in Figure C.2). For the above integral, the lower boundary is calculated by X=0 in-plane Equation (Equation C.2). The Equation C.2 is achieved by replacing θ with the 90-BR in Equation B.8 (see appendix B).

$$a = X.\mathrm{Sin}(90 - BR) + Z.\mathrm{Cos}(90 - BR) \ldots\ldots\ldots \mathrm{Eq.\,C.\,2}$$

The L' is calculated using Equation C.3 (see Figure C.2).

$$L' = \frac{a}{\mathrm{Cos}(90 - BR)} \ldots\ldots\ldots \mathrm{Eq.\,C.\,3}$$

In the Equation C.3, the a is the depth of worn and it is calculated in Equation C.4.

$$a = \left(\frac{BG.D_c}{8}\right).\mathrm{Cos}(BR) \ldots\ldots\ldots \mathrm{Eq.\,C.\,4}$$

Replacing a from Equation C.4 into Equation C.3 will result in Equation C.5.

$$L' = \frac{\left(\frac{BG.D_c}{8}\right).Cos(BR)}{Cos(90-BR)} = \frac{\left(\frac{BG.D_c}{8}\right).Cos(BR)}{Sin(BR)} = Cot(BR).\left(\frac{BG.D_c}{8}\right) \ldots\ldots\ldots Eq.C.5$$

The X in Equation C.1 is provided in the following.

$$X = f(z) \ldots\ldots\ldots Eq.C.6$$

Replacing a line equation into Equation C.6 will results in Equation C.7.

$$X = A.Z + B \ldots\ldots\ldots Eq.C.7$$

To achieve the coefficients of the line in Equation C.7, two points are needed.

C.1 Cutter worn volume calculation (including PDC and STUD)

In this case, the point 2 intersection is less than cylinder length and then

$$\text{Condition: } L' < L$$

Intersection points (point 1 and 2 in Figure C.2) are:

$$\begin{pmatrix}\text{intersection points}\\ \text{point1} =\\ \text{point2} =\end{pmatrix}\begin{pmatrix} X & Z \\ \frac{BG.D_c}{8} & 0 \\ 0 & L' = Cot(BR).\left(\frac{BG.D_c}{8}\right)\end{pmatrix}$$

The A and B are found by taking the above intersection points and Equation C.7 into account (see Equations C.8 and C.9).

$$A = -Tan(BR) \ldots\ldots\ldots Eq.C.8$$

$$B = \left(\frac{BG.D_c}{8}\right) \ldots\ldots\ldots Eq.C.9$$

Equation C.7 is turned into Equation C.10 using Equation C.8 and C.9.

$$X = -Tan(BR).Z + \left(\frac{BG.D_c}{8}\right) \ldots\ldots\ldots Eq.C.10$$

Replacing X from Equation C.10 into Equation C.1 will result in Equation C.11.

$$A_{segment} = \left(\frac{D_c}{2}\right)^2 . \arccos\left(\frac{\frac{D_c}{2} - \left(-\mathrm{Tan}(BR).Z + \left(\frac{BG.D_c}{8}\right)\right)}{\frac{D_c}{2}}\right) - \left(\frac{D_c}{2} - (-\mathrm{Tan}(BR).Z + \left(\frac{BG.D_c}{8}\right)\right). \sqrt{2.\left(\frac{D_c}{2}\right).\left(-\mathrm{Tan}(BR).Z + \left(\frac{BG.D_c}{8}\right)\right) - \left(-\mathrm{Tan}(BR).Z + \left(\frac{BG.D_c}{8}\right)\right)^2} \dots\dots.. \mathrm{Eq.\ C.11}$$

The cutter worn volume then is calculates by taking an integral from Equation C.11 between boundaries. The integral boundaries are seen in Equation C.12.

$$\int_0^{\mathrm{Cot}(BR).\left(\frac{BG.D_c}{8}\right)} A(Z)dZ \dots\dots.. \mathrm{Eq.\ C.12}$$

The above integral is simplified by separating and defining new variables at the following. The parameters A, D, C and X are defined in Equation C.13.

$$A = \left(\frac{D_c}{2}\right), D = -\mathrm{Tan}(BR), C = \left(\frac{BG.D_c}{8}\right), X = Z \dots\dots.. \mathrm{Eq.\ C.13}$$

Replace the A, D, C, and X into the Equation C.13 will result in Equation C.14.

$$I = \int A^2 \arccos\left(\frac{A - (DX + C)}{A}\right) dX - \int (A - (DX + C)). \sqrt{2A(DX + C) - (DX + C)^2} dX \dots\dots.. \mathrm{Eq.\ C.14}$$

The above integral is composed of two separate integrals and it is shown in Equation C.15.

$$I = I_1 - I_2 \dots\dots.. \mathrm{Eq.\ C.15}$$

Integral I_1 is seen Equation C.16.

$$I_1 = \int A^2 \arccos\left(\frac{A-(DX+C)}{A}\right) dX \dots\dots \text{Eq. C. 16}$$

The base integral for Equation C.16 is Equation C.17. Therefore, the Equation C.17 is solved at the following.

$$I = \int \arccos(\theta) d\theta \dots\dots \text{Eq. C. 17}$$

Assume u as follow

$$u = \arccos(\theta) \dots\dots \text{Eq. C. 18}$$

Take derivation from u in Equation C.18 will results in Equation C.19.

$$du = \frac{-d\theta}{\sqrt{1-\theta^2}} \dots\dots \text{Eq. C. 19}$$

Change the parameters

$$dv = d\theta \rightarrow v = \theta \dots\dots \text{Eq. C. 20}$$

Note that: $\int udv = uv - \int vdu$

Rewrite the integral

$$I = \theta.\arccos(\theta) + \int \frac{\theta.d\theta}{\sqrt{1-\theta^2}} \dots\dots \text{Eq. C. 21}$$

Change the parameters (introduce t) and take derivation

$$t = 1-\theta^2; dt = -2\theta d\theta \dots\dots \text{Eq. C. 22}$$

Replace t into Equation C.22

$$= \theta.\arccos(\theta) - \frac{1}{2}\int \frac{dt}{\sqrt{t}} \dots\dots \text{Eq. C. 23}$$

Rewrite the Equation C.23

$$= \theta.\arccos(\theta) - \frac{1}{2}\int t^{\frac{-1}{2}} dt \dots\dots.. \text{Eq. C. 24}$$

Solve and rewrite Equation C.24

$$= \theta.\arccos(\theta) - \frac{1}{2}.\frac{t^{\frac{1}{2}}}{\frac{1}{2}} \dots\dots.. \text{Eq. C. 25}$$

Replace t with θ in Equation C.25 (see Equation C.22).

$$I = \theta.\arccos(\theta) - \sqrt{1-\theta^2} \dots\dots.. \text{Eq. C. 26}$$

Therefore, the integral (see Equation C.17) solution would be

$$\int \arccos(\theta) d\theta = \theta.\arccos(\theta) - \sqrt{1-\theta^2} \dots\dots.. \text{Eq. C. 27}$$

Replace the parameters into integral C.17

$$I_1 = \int A^2 \arccos(\frac{A-C}{A} - \frac{DX}{A}) dX \dots\dots.. \text{Eq. C. 28}$$

Taking the A^2 out of integral

$$I_1 = A^2 \int \arccos(\frac{A-C}{A} - \frac{DX}{A}) dX \dots\dots.. \text{Eq. C. 29}$$

In Equation C.29, the X coefficient $(\frac{D}{A})$ in arccos comes out of integral and will be multiplied with A^2 as it is shown in the Equation C.30.

The solution of integral I_1 is provided at the following

$$I_1 = \frac{-A^3}{D}\left(\left(\frac{A-(DX+C)}{A}\right).\arccos\left(\frac{A-(DX+C)}{A}\right) - \sqrt{1-(\frac{A-(DX+C)}{A})^2}\right) \dots\dots.. \text{Eq. C. 30}$$

The second part of the integral I (Equation C.14) is seen in the Equation C.31. The following steps should be taken to solve Equation C.31.

$$I_2 = \int (A - (DX + C)).\sqrt{2A(DX + C) - (DX + C)^2}dX \dots\dots.. Eq.\,C.\,31$$

Change the parameter as it is provided in the Equation C.32

$$y = DX + C \dots\dots.. Eq.\,C.\,32$$

Take derivation from Equation C.32

$$dy = DdX \dots\dots.. Eq.\,C.\,33$$

Replace the Equations C.32 and C.33 into Equation C.34

$$I_2 = \frac{1}{D}\int (A - y).\sqrt{2Ay - y^2}dy \dots\dots.. Eq.\,C.\,34$$

Rewrite the Equation C.34

$$I_2 = \frac{1}{D}\int (A - y).\sqrt{A^2 - (y - A)^2}dy \dots\dots.. Eq.\,C.\,35$$

Change the parameters using Equation C.36 (similar to Pythagorean theorem).

$$y - A = A.\,Sin(\theta) \dots\dots.. Eq.\,C.\,36$$

Take derivation from Equation C.36

$$dy = A.\,Cos(\theta) \dots\dots.. Eq.\,C.\,37$$

Replace the Equation C.36 and C.37 into Equation C.35

$$I_2 = \frac{1}{D}\int A.\,Sin(\theta).\sqrt{A^2 - A^2.\,Sin(\theta)^2}\,.\,A.\,Cos(\theta)d\theta \dots\dots.. Eq.\,C.\,38$$

Taking the constant out of integral

$$I_2 = \frac{A^3}{D}\int \mathrm{Sin}(\theta).\mathrm{Cos}^2(\theta)d\theta \dots\dots.. \mathrm{Eq.\ C.\ 39}$$

Change the parameters and define u as following

$$u = \mathrm{Cos}(\theta) \dots\dots.. \mathrm{Eq.\ C.\ 40}$$

Take integral from Equation C.40

$$du = -\mathrm{Sin}(\theta).d\theta \dots\dots.. \mathrm{Eq.\ C.\ 41}$$

Replace the Equation C.40 and C.41 into Equation C.39

$$= -\frac{A^3}{D}\int u^2 du \dots\dots.. \mathrm{Eq.\ C.\ 42}$$

Solve the Integral in Equation C.42 and replace the u

$$\frac{A^3}{D}.\frac{u^3}{3} = \frac{A^3}{D}.\frac{\mathrm{Cos}^3(\theta)}{3} \dots\dots.. \mathrm{Eq.\ C.\ 43}$$

Rewrite and replace the θ (see Equation C.36) as it is provided at the following

$$= -\frac{A^3}{3D}(\sqrt{1-\mathrm{Sin}^2(\theta)})^3 = \frac{A^3}{3D}(\sqrt{1-(\frac{y-A}{A})^2})^3 \dots\dots.. \mathrm{Eq.\ C.\ 44}$$

Replace the y (see Equation C.32) and rewrite the Equation C.44

$$I_2 = -\frac{A^3}{3D}\left(\sqrt{1-(\frac{DX+C-A}{A})^2}\right)^3 \dots\dots.. \mathrm{Eq.\ C.\ 45}$$

The integral I answer is provided in Equation C.46.

$$I = \frac{-A^3}{D}\left(\left(\frac{A-(DX+C)}{A}\right).\arccos\left(\frac{A-(DX+C)}{A}\right) - \sqrt{1-(\frac{A-(DX+C)}{A})^2}\right) + \frac{A^3}{3D}\left(\sqrt{1-(\frac{DX+C-A}{A})^2)}\right)^3 \quad \ldots\ldots\ldots \text{Eq. C. 46}$$

Replacing A, D, C, and X (from Equation C.13) into Equation C.46 will result in Equation C.47. Note the boundaries should replace the Z to achieve the final answer (note boundaries in Equation C.47).

V_c = Cutter Volume

$$= \left\{\frac{-\left(\frac{D_c}{2}\right)^3}{-\operatorname{Tan}(BR)}\left[\left(\frac{\left(\frac{D_c}{2}\right)-\left(-\operatorname{Tan}(BR)\,Z+\left(\frac{BG.D_c}{8}\right)\right)}{\left(\frac{D_c}{2}\right)}\right).\arccos\left(\frac{\left(\frac{D_c}{2}\right)-\left(-\operatorname{Tan}(BR)\,Z+\left(\frac{BG.D_c}{8}\right)\right)}{\left(\frac{D_c}{2}\right)}\right) - \sqrt{1-\left(\frac{\left(\frac{D_c}{2}\right)-\left(-\operatorname{Tan}(BR)\,Z+\left(\frac{BG.D_c}{8}\right)\right)}{\left(\frac{D_c}{2}\right)}\right)^2}\right] + \frac{\left(\frac{D_c}{2}\right)^3}{-3\operatorname{Tan}(BR)}\left(\sqrt{1-(\frac{-\operatorname{Tan}(BR)\,Z+\left(\frac{BG.D_c}{8}\right)-\left(\frac{D_c}{2}\right)}{\left(\frac{D_c}{2}\right)})^2)}\right)^3\right\}\Bigg[_0^{\operatorname{Cot}(BR).\left(\frac{BG.D_c}{8}\right)} \quad \ldots\ldots\ldots \text{Eq. C. 47}$$

Replace the boundaries into Equation C.47 will result in Equation C.48.

V_c = Cutter Volume

$$= \frac{-\left(\frac{D_c}{2}\right)^3}{-\operatorname{Tan}(BR)}\left[\left(\frac{\left(\frac{D_c}{2}\right)-\left(-\operatorname{Tan}(BR).\operatorname{Cot}(BR).\left(\frac{BG.D_c}{8}\right)+\left(\frac{BG.D_c}{8}\right)\right)}{\left(\frac{D_c}{2}\right)}\right).\arccos\left(\frac{\left(\frac{D_c}{2}\right)-\left(-\operatorname{Tan}(BR).\operatorname{Cot}(BR).\left(\frac{BG.D_c}{8}\right)+\left(\frac{BG.D_c}{8}\right)\right)}{\left(\frac{D_c}{2}\right)}\right)$$

$$-\sqrt{1-\left(\frac{\left(\frac{D_c}{2}\right)-\left(-\operatorname{Tan}(BR).\operatorname{Cot}(BR).\left(\frac{BG.D_c}{8}\right)+\left(\frac{BG.D_c}{8}\right)\right)}{\left(\frac{D_c}{2}\right)}\right)^2}\Bigg]$$

$$+\frac{\left(\frac{D_c}{2}\right)^3}{-3\operatorname{Tan}(BR)}\left(\sqrt{1-\left(\frac{-\operatorname{Tan}(BR).\operatorname{Cot}(BR).\left(\frac{BG.D_c}{8}\right)+\left(\frac{BG.D_c}{8}\right)-\left(\frac{D_c}{2}\right)}{\left(\frac{D_c}{2}\right)}\right)^2}\right)^3$$

$$-\left[\frac{-\left(\frac{D_c}{2}\right)^3}{-\operatorname{Tan}(BR)}\left[\left(\frac{\left(\frac{D_c}{2}\right)-\left(\left(\frac{BG.D_c}{8}\right)\right)}{\left(\frac{D_c}{2}\right)}\right).\arccos\left(\frac{\left(\frac{D_c}{2}\right)-\left(\left(\frac{BG.D_c}{8}\right)\right)}{\left(\frac{D_c}{2}\right)}\right)-\sqrt{1-\left(\frac{\left(\frac{D_c}{2}\right)-\left(\left(\frac{BG.D_c}{8}\right)\right)}{\left(\frac{D_c}{2}\right)}\right)^2}\right]\right.$$

$$\left.+\frac{\left(\frac{D_c}{2}\right)^3}{-3\operatorname{Tan}(BR)}\left(\sqrt{1-\left(\frac{\left(\frac{BG.D_c}{8}\right)-\left(\frac{D_c}{2}\right)}{\left(\frac{D_c}{2}\right)}\right)^2}\right)^3\right] \ldots\ldots\ldots \text{Eq. C. 48}$$

The cutter volume Equation is provided in the Equation C.49.

$$V_c = \text{Cutter Volume}$$

$$= -\left[\frac{\left(\frac{D_c}{2}\right)^3}{\text{Tan}(BR)}\left[\left(\frac{\left(\frac{D_c}{2}\right)-\left(\frac{BG.D_c}{8}\right)}{\left(\frac{D_c}{2}\right)}\right).\arccos\left(\frac{\left(\frac{D_c}{2}\right)-\left(\frac{BG.D_c}{8}\right)}{\left(\frac{D_c}{2}\right)}\right) - \sqrt{1-\left(\frac{\left(\frac{D_c}{2}\right)-\left(\frac{BG.D_c}{8}\right)}{\left(\frac{D_c}{2}\right)}\right)^2}\right]\right.$$

$$\left. - \frac{\left(\frac{D_c}{2}\right)^3}{3\,\text{Tan}(BR)}\left(\sqrt{1-\left(\frac{\left(\frac{BG.D_c}{8}\right)-\left(\frac{D_c}{2}\right)}{\left(\frac{D_c}{2}\right)}\right)^2}\right)^3\right] \ldots\ldots \text{Eq. C. 49}$$

C.2 PDC worn volume calculation

In this case, the point 2 intersection is greater than cylinder length and then

$$\text{Condition: } L' > L$$

Writing the X as a function of Z.

$$X = f(z) \ldots\ldots \text{Eq. C. 50}$$

Replacing line Equation into Equation C.50.

$$X = A'.Z + B' \ldots\ldots \text{Eq. C. 51}$$

Intersection points are:

$$\begin{pmatrix}\text{intersection points}\\ \text{point1}\\ \text{point2}\end{pmatrix}\begin{pmatrix} X & Z \\ \frac{BG.D_c}{8} & 0 \\ \left(\frac{a - L.\cos(90-BR)}{\sin(90-BR)}\right) & L\end{pmatrix} \ldots\ldots \text{Eq. C. 52}$$

Replacing the a from Equation C.4 into Equation C.52.

$$\begin{pmatrix}\text{intersection points}\\ \text{point1}\\ \text{point2}\end{pmatrix}\begin{pmatrix} X & Z \\ \frac{BG.D_c}{8} & 0 \\ \left(\frac{\left(\frac{BG.D_c}{8}\right).\text{Cos}(BR)-L.\cos(90-BR)}{\sin(90-BR)}\right) & L \end{pmatrix} \dots\dots\text{Eq. C. 53}$$

The slope of the line in Equation C.51 is achieved by taking the intersection points (see Equation C.53) into account.

$$A' = \frac{\text{point2(X)} - \text{point1(X)}}{\text{point2(Z)} - \text{point1(Z)}} \dots\dots\text{Eq. C. 54}$$

The Y-intercept of Equation C.51 is provided in Equation C.55.

$$B' = \text{point1(X)} \dots\dots\text{Eq. C. 55}$$

Replacing point 1 and point 2 values into Equation C.54 and C.55 will result in Equation C.56 and C.57.

$$A' = \frac{\left(\frac{\left(\frac{BG.D_c}{8}\right).\text{Cos}(BR)-L.\cos(90-BR)}{\sin(90-BR)}\right)-\frac{BG.D_c}{8}}{L} \dots\dots\text{Eq. C. 56}$$

$$B' = \frac{BG.D_c}{8} \dots\dots\text{Eq. C. 57}$$

Therefore, the Equation C.51 can be written in the following Equation.

$$X = \left(\frac{\left(\frac{\left(\frac{BG.D_c}{8}\right).\text{Cos}(BR)-L.\cos(90-BR)}{\sin(90-BR)}\right)-\frac{BG.D_c}{8}}{L}\right).Z + \left(\frac{BG.D_c}{8}\right) \dots\dots\text{Eq. C. 58}$$

Replacing X (Equation C.51) into Equation C.1, results in Equation C.59.

$$A_{Segment} = \left(\frac{D_c}{2}\right)^2 . \arccos\left(\frac{\frac{D_c}{2} - (A'.Z+B')}{\frac{D_c}{2}}\right) - \left(\frac{D_c}{2} - (A'.Z+B')\right). \sqrt{2.\left(\frac{D_c}{2}\right).(A'.Z+B') - (A'.Z + B')^2} \quad \ldots\ldots \text{Eq. C. 59}$$

Renaming variables and replacing into Equation C.59 using Equation C.60, would result in Equation C.61.

$$A = \left(\frac{D_c}{2}\right), D = A', C=B', X = Z \ldots\ldots \text{Eq. C. 60}$$

$$I = \int A^2 \arccos\left(\frac{A - (DX + C)}{A}\right) dX + \int (A - (DX + C)). \sqrt{2A(DX + C) - (DX + C)^2} dX \ldots\ldots \text{Eq. C. 61}$$

Solving the above integral results in Equation C.62.

$$I = \frac{-A^3}{D}\left(\left(\frac{A - (DX + C)}{A}\right). \arccos\left(\frac{A - (DX + C)}{A}\right) - \sqrt{1 - \left(\frac{A - (DX + C)}{A}\right)^2}\right) - \frac{A^3}{3D}\left(\sqrt{1 - \left(\frac{DX + C - A}{A}\right)^2}\right)^3 \quad \ldots\ldots \text{Eq. C. 62}$$

Replacing variables, A, D, C, and X (check out Equation C.60) into Equation C.62 results in Equation C.63.

Replacing the integral boundaries into the Equation C.63 will result in Equation C.64. The Equation C.64 can be used to find the volume of PDC by replacing the L with the PDC thickness.

V_c = Cutter Volume

$$= \left\{ \frac{-\left(\frac{D_c}{2}\right)^3}{D} \left[\left(\frac{\left(\frac{D_c}{2}\right) - \left(\left(\left(\frac{\left(\frac{BG.D_c}{8}\right).\mathrm{Cos}(BR) - L.\cos(90-BR)}{\sin(90-BR)} \right) - \frac{BG.D_c}{8} \right) \frac{}{L} .Z + \left(\frac{BG.D_c}{8}\right) \right)}{\left(\frac{D_c}{2}\right)} \right) \times \arccos \left(\frac{\left(\frac{D_c}{2}\right) - \left(\left(\left(\frac{\left(\frac{BG.D_c}{8}\right).\mathrm{Cos}(BR) - L.\cos(90-BR)}{\sin(90-BR)} \right) - \frac{BG.D_c}{8} \right) \frac{}{L} .Z + \left(\frac{BG.D_c}{8}\right) \right)}{\left(\frac{D_c}{2}\right)} \right) - \sqrt{1 - \left(\frac{\left(\frac{D_c}{2}\right) - \left(\left(\left(\frac{\left(\frac{BG.D_c}{8}\right).\mathrm{Cos}(BR) - L.\cos(90-BR)}{\sin(90-BR)} \right) - \frac{BG.D_c}{8} \right) \frac{}{L} .Z + \left(\frac{BG.D_c}{8}\right) \right)}{\left(\frac{D_c}{2}\right)} \right)^2} \right] \right\}$$

$$-\frac{\left(\frac{D_c}{2}\right)^3}{3D}\left(\sqrt{1-\left(\frac{\left(\frac{\left(\frac{BG.D_c}{8}\right).\cos(BR)-L.\cos(90-BR)}{\sin(90-BR)}\right)-\frac{BG.D_c}{8}}{L}.Z+\left(\frac{BG.D_c}{8}\right)-\left(\frac{D_c}{2}\right)}{\left(\frac{D_c}{2}\right)}\right)^2}\right)^3\Bigg\}\Big[_0^L \quad \ldots\ldots\ldots \text{Eq. C. 63}$$

$$V_c = \text{Cutter Volume} = \left[\frac{-\left(\frac{D_c}{2}\right)^3}{D} \left[\left(\frac{\left(\frac{D_c}{2}\right) - \left(\left(\left(\frac{\left(\frac{BG.D_c}{8}\right).\text{Cos}(BR) - L.\cos(90-BR)}{\sin(90-BR)} \right) - \frac{BG.D_c}{8} \right) / L \right).L + \left(\frac{BG.D_c}{8}\right) \right)}{\left(\frac{D_c}{2}\right)} \right) \times \arccos \left(\frac{\left(\frac{D_c}{2}\right) - \left(\left(\left(\frac{\left(\frac{BG.D_c}{8}\right).\text{Cos}(BR) - L.\cos(90-BR)}{\sin(90-BR)} \right) - \frac{BG.D_c}{8} \right) / L \right).L + \left(\frac{BG.D_c}{8}\right) \right)}{\left(\frac{D_c}{2}\right)} \right) - \sqrt{1 - \left(\frac{\left(\frac{D_c}{2}\right) - \left(\left(\left(\frac{\left(\frac{BG.D_c}{8}\right).\text{Cos}(BR) - L.\cos(90-BR)}{\sin(90-BR)} \right) - \frac{BG.D_c}{8} \right) / L \right).L + \left(\frac{BG.D_c}{8}\right) \right)}{\left(\frac{D_c}{2}\right)} \right)^2} \right] \right]$$

$$-\frac{\left(\frac{D_c}{2}\right)^2}{-3D}\left(\sqrt{1-\left(\frac{\left(\left(\frac{\left(\frac{BG.D_c}{8}\right).\mathrm{Cos}(BR)-L.\cos(90-BR)}{\sin(90-BR)}\right)-\frac{BG.D_c}{8}}{L}\right).L+\left(\frac{BG.D_c}{8}\right)-\left(\frac{D_c}{2}\right)}{\left(\frac{D_c}{2}\right)}\right)^2}\right)^3$$

$$-\left[\frac{-\left(\frac{D_c}{2}\right)^3}{-\tan(BR)}\left[\times \arccos\left(\frac{\left(\frac{D_c}{2}\right)-\left(\left(\frac{BG.D_c}{8}\right)\right)}{\left(\frac{D_c}{2}\right)}\right)\right.\right.$$
$$\left.\left.-\sqrt{1-\left(\frac{\left(\frac{D_c}{2}\right)-\left(\left(\frac{BG.D_c}{8}\right)\right)}{\left(\frac{D_c}{2}\right)}\right)^2}\right]$$
$$\left.-\frac{\left(\frac{D_c}{2}\right)^3}{-3\tan(BR)}\left(\sqrt{1-\left(\frac{\left(\frac{BG.D_c}{8}\right)-\left(\frac{D_c}{2}\right)}{\left(\frac{D_c}{2}\right)}\right)^2}\right)^3\right] \ldots\ldots\ldots \text{Eq. C. 64.}$$

APPENDIX D

Cutter Wear Flat Area Length and Width

The goal of this section is to find the wear flat area length (L) and width (W).

D.1 Wear Flat Area Width Calculations

Assume Figure D.1. shows a schematic of a PDC cutter in X-Y coordinate and point C is the center of the circle. The circle equation in the Cartesian coordination is expressed as Equation D.1

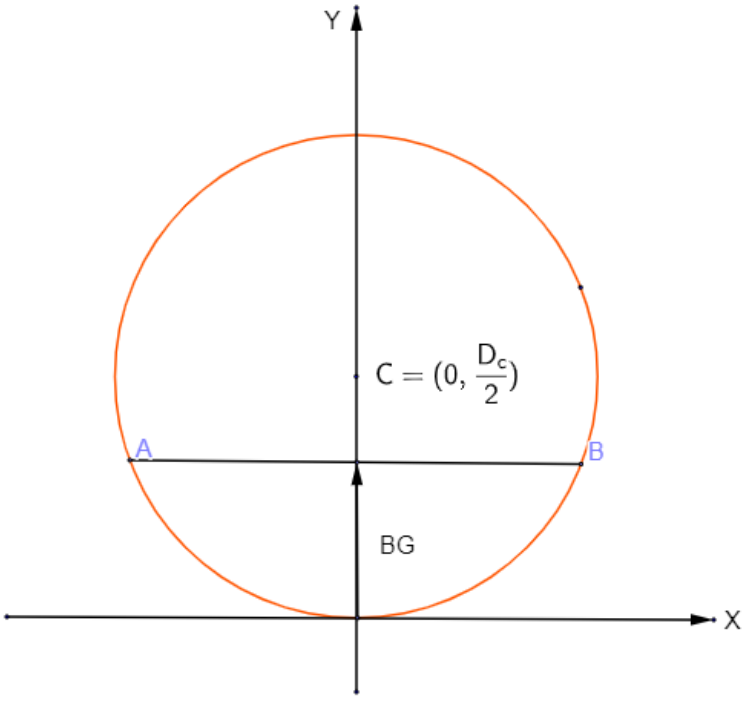

Figure D.1. A schematic of a cutter in X-Y coordinate

$$X^2 + \left(Y - \left(\frac{D_c}{2}\right)\right)^2 = \left(\frac{D_c}{2}\right)^2 \ldots\ldots Eq.D.1$$

In Figure D.1, the BG (bit grade) is representative of cutter worn length section on the cutter face, the AB is the cutter wear flat area width (W). The cutter wear flat area width (AB) is calculated as follows.

Rearrange Y in the Equation D.1.

$$X^2 = \left(\frac{D_c}{2}\right)^2 - \left(Y - \left(\frac{D_c}{2}\right)\right)^2 \ldots\ldots Eq.D.2$$

Rewrite the Equation D.2.

$$X^2 = -Y^2 + 2 \times (Y)\left(\left(\frac{D_c}{2}\right)\right) \ldots\ldots Eq.D.3$$

Replace Y using Equation D.4 into Equation D.3.

$$Y = \left(\frac{BG \times D_c}{8}\right) \ldots\ldots Eq.D.4$$

$$X^2 = -\left(\frac{BG \times D_c}{8}\right)^2 + 2 \times \left(\left(\frac{BG \times D_c}{8}\right)\right)\left(\left(\frac{D_c}{2}\right)\right) \ldots\ldots Eq.D.5$$

Therefore, X is calculated using Equation D.6. The Equation D.6 gives the X coordinate of points A and B with negative and positive signs respectively.

$$X = \pm\sqrt{\left(-\left(\frac{BG \times D_c}{8}\right)^2 + 2 \times \left(\left(\frac{BG \times D_c}{8}\right)\right)\left(\left(\frac{D_c}{2}\right)\right)\right)} \ldots\ldots Eq.D.6$$

The wear flat area width then is calculated using Equation D.7.

$$W = 2 \times \sqrt{\left(-\left(\frac{BG \times D_c}{8}\right)^2 + 2 \times \left(\left(\frac{BG \times D_c}{8}\right)\right)\left(\left(\frac{D_c}{2}\right)\right)\right)} \ldots\ldots Eq.D.7$$

The Equation D.7 was applied to a cutter with the 0.52-inch diameter and the results are shown in Figure D.2.

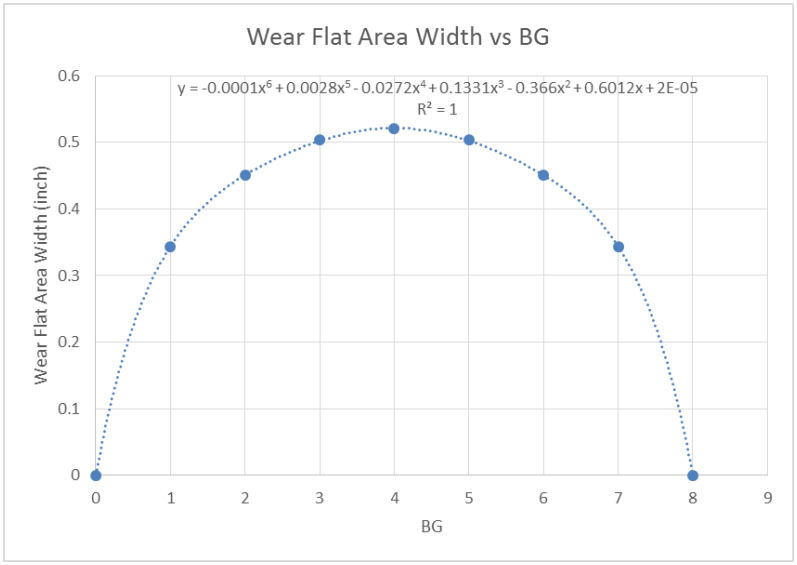

Figure D.2. Wear Flat Area width versus bit grade for a cutter with a 0.52-inch diameter

D.2 Wear Flat Area Length Calculations

In Figure D.3, a cutter wear flat area is shown from the bottom side perspective. The cutter wear flat area length is seen with a red arrow in Figure D.3.

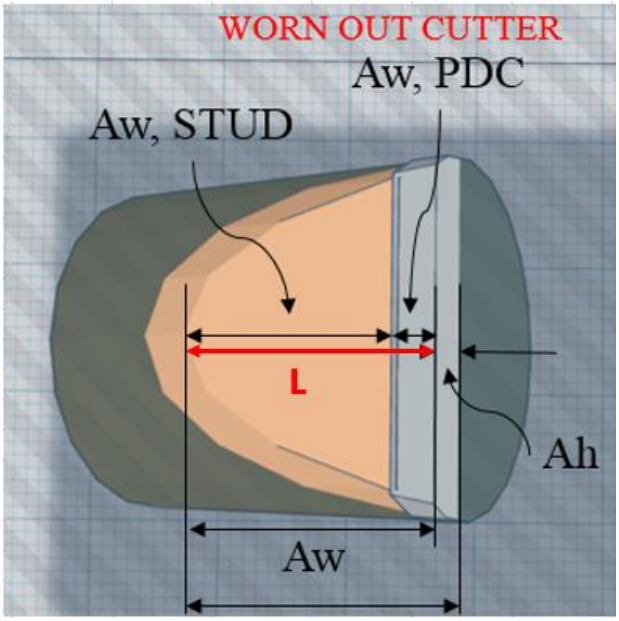

Figure D.3. A schematic of a cutter wear flat area and its length (red arrow)

In a 3D perspective, Figure D.4 shows the wear flat area (A_w), the L (BC) is wear flat area length, α is cutter BR complementary angle, and the OB is the length of wear on cutter face. The BG is turned into OB length using Equation D.8.

$$OB = \left(\frac{BG \times D_c}{8}\right) \ldots\ldots Eq.D.8$$

The OB is turned into the L (BC) by taking the cutter complementary angle (α), using Equation D.9.

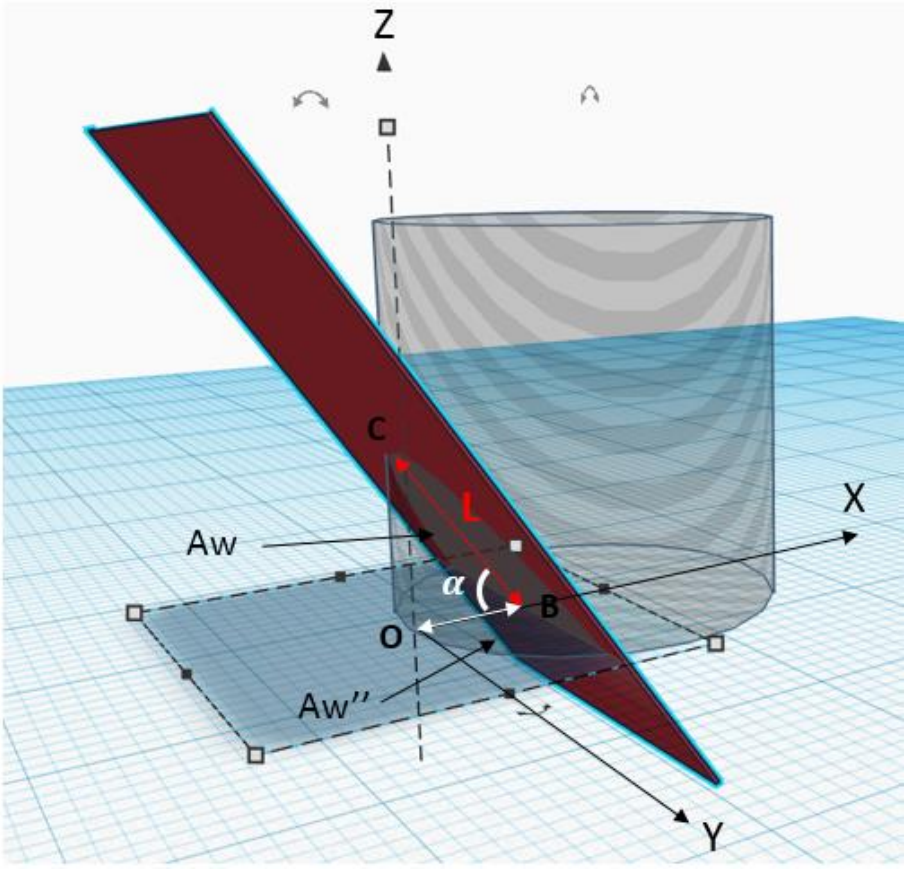

Figure D.4. A 3D schematic of a cutter wear flat area

The cutter wear flat area length is calculated using Equations D.8 and D.9.

$$L = \frac{OB}{cos(\alpha)} \ldots\ldots Eq.D.9$$

In case that the cutter wear flat area is known, the Equation A.63 can be used to back-calculate the BC (cutter wear flat area length). In this case, the cutter wear flat area first should be turned into the A_w'' by taking the α into account. The A_w'' then is used in conjunction with the Equation A.63 to back-calculated the OB length. The OB length is turned into the BC by taking the α into account (see Equation D.9).

APPENDIX E

The PDC cutters are assumed to penetrate with the same rate as the bit into the formation. The rate of penetration is used to show that the cutters depth of cut is function of the number of cutters and arrangement on the bit face. Assume a theoretical flat face PDC bit in Figure E.1, with 2 cutters and 4 cutters mounted to a maximum radius R1 and R2 respectively. In Figure E.1, R_{1C} and R_{2C} are the distance between the bit axis and cutter centers mounted at R1 and R2 respectively.

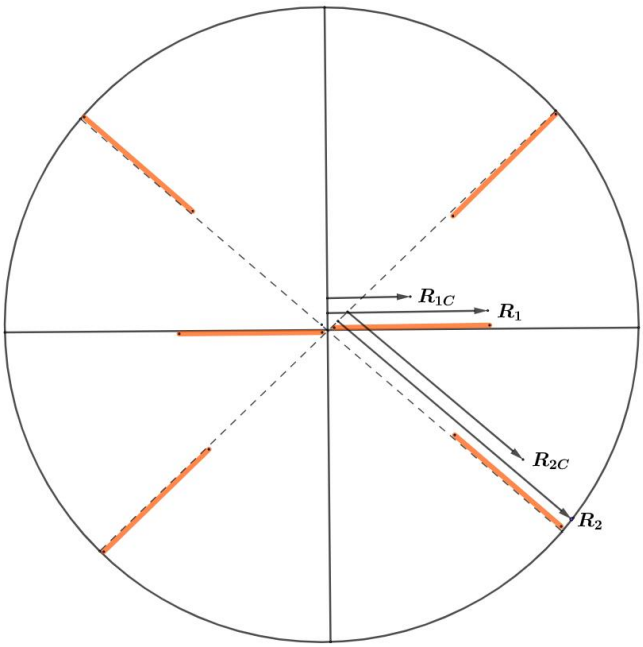

Figure E.1. A theoretical flat face bit with 2 and 4 cutters mounted at R_{1C} and R_{2C} respectively

The rate of penetration (ROP) for all of these cutters arrangement at radius equal to R1 and R2 are equal and it is proposed in Equation E.1.

$$\mathrm{ROP} = \frac{5 \times \mathrm{RPM} \times (\mathrm{NOC} \times \mathrm{A_V} \times 2\pi \times \mathrm{R_e})}{\pi \times (\mathrm{R^2})} \ldots\ldots \mathrm{Eq.\,E.\,1.}$$

In Equation E.1, the R is bit radius, R_e is equivalent radius, A_V is equivalent cutter front area, RPM is revolution per minute, and NOC a is the number of cutters.

The two cutters close to the bit center axis are drilled the cylindrical core (labeled A) as it is depicted in Figure E.2. The rest of cutters (four cutters) drill the hollow cylindrical shape core (labeled B) numbers 2 in Figure E.2.

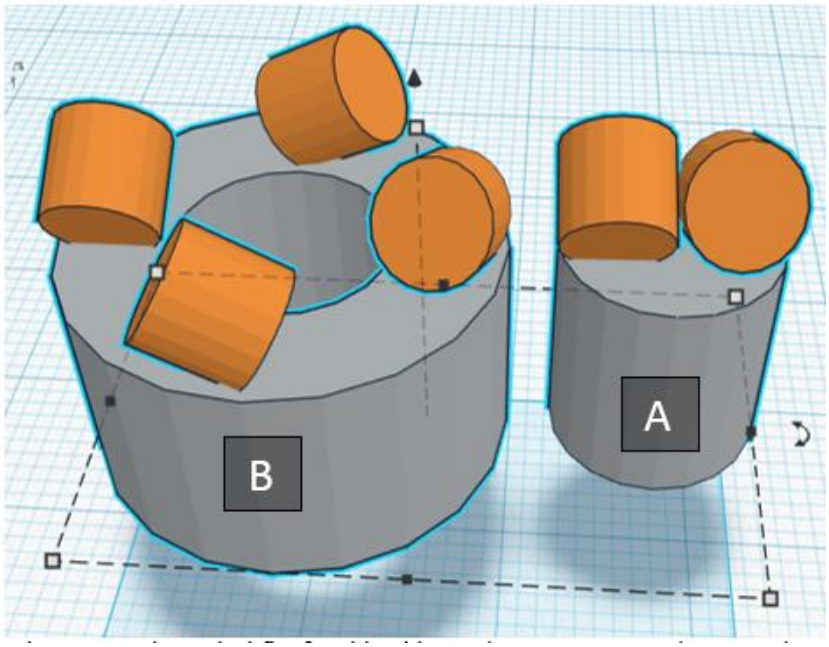

Figure E.2. A theoretical flat face bit with 2 and 4 cutters mounted at R1 and R2

The cutters drill cylindrical shapes (A is a solid cylinder and B is a hollow cylinder in Figure E.2) simultaneously and therefore the rate of penetration for cutters mounted at the radius R_{1C} is the same as R_{2C}. Assuming the volume of A=B, Equation E.2 can be derived.

$$\frac{5 \times \mathrm{RPM} \times (\mathrm{NOC_{R1}} \times \mathrm{A_{V1}} \times 2\pi \times \mathrm{R_{1C}})}{\pi \times \mathrm{R_1^2}} = \frac{5 \times \mathrm{RPM} \times (\mathrm{NOC_{R2}} \times \mathrm{A_{V2}} \times 2\pi \times \mathrm{R_{2C}})}{\pi \times (\mathrm{R_2^2} - \mathrm{R_1^2})} \ldots\ldots \mathrm{Eq.\,E.\,2.}$$

In Equation E.2, $\mathrm{NOC_{R1}}$ and $\mathrm{NOC_{R2}}$ are number of cutters at the radius equal to $\mathrm{R_1}$ and $\mathrm{R_2}$ respectively. The $\mathrm{R_{1C}}$ and $\mathrm{R_{2C}}$ equations are provided at the following.

$$\mathrm{R_{1C}} = \frac{\mathrm{R_1}}{2} \ldots\ldots \mathrm{Eq.\,E.\,3.}$$

$$R_{2C} = R_1 + \left(\frac{R_2 - R_1}{2}\right) \ldots\ldots \text{Eq. E. 4.}$$

For cutters mounted at radius J the R_{jC} is defined as

$$R_{jC} = R_{j-1} + \left(\frac{R_j - R_{j-1}}{2}\right) \ldots\ldots \text{Eq. E. E. 5.}$$

Simplifying Equation E.2

$$\frac{(NOC_{R1} \times A_{V1} \times R_{1C})}{R_1^2} = \frac{(NOC_{R2} \times A_{V2} \times R_{2C})}{(R_2^2 - R_1^2)} \ldots\ldots \text{Eq. E. 6.}$$

Replacing Equations E.3 and E.4 in Equation E.7

$$\frac{\left(NOC_{R1} \times A_{V1} \times \left(\frac{R_1}{2}\right)\right)}{R_1^2} = \frac{\left(NOC_{R2} \times A_{V2} \times \left(R_1 + \left(\frac{R_2 - R_1}{2}\right)\right)\right)}{(R_2^2 - R_1^2)} \ldots\ldots \text{Eq. E. 7.}$$

Rearranging Equation E.7

$$\frac{A_{V1}}{A_{V2}} = \frac{NOC_{R2} \times \left(R_1 + \left(\frac{R_2 - R_1}{2}\right)\right) \times R_1^2}{NOC_{R1} \times \left(\frac{R_1}{2}\right) \times (R_2^2 - R_1^2)} \ldots\ldots \text{Eq. E. 8.}$$

Using the same assumption and expanding to more than two radiuses (R_1,R_2, ... R_j), the Equation E.8 is turned into Equation E.9.

$$\frac{A_{V1}}{A_{Vj}} = \frac{NOC_{Rj} \times \left(R_{j-1} + \left(\frac{R_j - R_{j-1}}{2}\right)\right) \times R_1^2}{NOC_{R1} \times \left(\frac{R_1}{2}\right) \times \left(R_j^2 - R_{j-1}^2\right)} \ldots\ldots \text{Eq. E. 8.}$$

The area in front of cutters at the radius equal to R1 is related to the other cutters through Equation E.9.

$$A_{Vj} = \left(\frac{NOC_{R1} \times \left(\frac{R_1}{2}\right) \times \left(R_j^2 - R_{j-1}^2\right)}{NOC_{Rj} \times \left(R_{j-1} + \left(\frac{R_j - R_{j-1}}{2}\right)\right) \times R_1^2} \right) \times A_{V1} \ldots\ldots \text{Eq. E. 9.}$$

The area beneath all cutters can be calculated using Equation E.10.

$$NOC_{R1} \times A_{B1} + NOC_{R2} \times A_{B2} + \cdots + NOC_{Rj} \times A_{Bj} = \frac{WOB}{CCS} \ldots\ldots \text{Eq. E. 10.}$$

When the depth of cut is known, the area in front of the cutter can be achieved using Equation E.11.

$$\tan(BR) = \frac{A_B}{A_F} \ldots\ldots \text{Eq. E. 11.}$$

Following set of equations can be driven to achieve the area in front of cutter at radius R1 (Equation E.18). The Equation E.10 and Equation E.11 result in Equation E12.

$$NOC_{R1} \times A_{V1} + NOC_{R2} \times A_{V2} + \cdots + NOC_{Rj} \times A_{Vj} = \frac{WOB}{CCS \times \tan(BR)} \ldots\ldots \text{Eq. E. 12.}$$

Simplifying Equation E.12 into Equation E.13.

$$NOC_{R1} \times A_{V1} + \sum_{j=2}^{n} NOC_{Rj} \times A_{Vj} = \frac{WOB}{CCS \times \tan(BR)} \ldots\ldots \text{Eq. E. 13.}$$

Rearranging Equation E.13 into Equation E.14.

$$NOC_{R1} \times A_{V1} + \sum_{j=2}^{n} NOC_{Rj} \times \left(\left(\frac{NOC_{R1} \times \left(\frac{R_1}{2}\right) \times \left(R_j^2 - R_{j-1}^2\right)}{NOC_{Rj} \times \left(R_{j-1} + \left(\frac{R_j - R_{j-1}}{2}\right)\right) \times R_1^2} \right) \times A_{V1} \right) = \frac{WOB}{CCS \times \tan(BR)} \ldots\ldots \text{Eq. E. 14.}$$

The NOC_{Rj} is goes away with NOC_{Rj} at denominator results in Equation E.15.

$$NOC_{R1} \times A_{V1} + \sum_{j=2}^{n} \left(\left(\frac{NOC_{R1} \times \left(\frac{R_1}{2}\right) \times \left(R_j^2 - R_{j-1}^2\right)}{\left(R_{j-1} + \left(\frac{R_j - R_{j-1}}{2}\right)\right) \times R_1^2} \right) \times A_{V1} \right) = \frac{WOB}{CCS \times \tan(BR)} \ldots\ldots \text{Eq. E. 15.}$$

Rearranging Equation E.15 to Equation E.16.

$$NOC_{R1} \times A_{V1} + (NOC_{R1} \times A_{V1}) \sum_{j=2}^{n} \left(\left(\frac{\left(\frac{R_1}{2}\right) \times \left(R_j^2 - R_{j-1}^2\right)}{\left(R_{j-1} + \left(\frac{R_j - R_{j-1}}{2}\right)\right) \times R_1^2} \right) \right) = \frac{WOB}{CCS \times \tan(BR)} \ldots\ldots \text{Eq. E. 16.}$$

Rearranging Equation E.16 to Equation E.17.

$$NOC_{R1} \times A_{V1} \times \left(1 + \sum_{j=2}^{n} \left(\left(\frac{\left(\frac{R_1}{2}\right) \times \left(R_j^2 - R_{j-1}^2\right)}{\left(R_{j-1} + \left(\frac{R_j - R_{j-1}}{2}\right)\right) \times R_1^2} \right) \right) \right) = \frac{WOB}{CCS \times \tan(BR)} \ldots\ldots \text{Eq. E. 17.}$$

Rearranging Equation E.17 to Equation E.18.

$$A_{V1} \times = \frac{\left(\frac{WOB}{CCS \times \tan(BR)}\right)}{NOC_{R1} \times \left(1 + \sum_{j=2}^{n} \left(\left(\frac{\left(\frac{R_1}{2}\right) \times \left(R_j^2 - R_{j-1}^2\right)}{\left(R_{j-1} + \left(\frac{R_j - R_{j-1}}{2}\right)\right) \times R_1^2} \right) \right) \right)} \ldots\ldots \text{Eq. E. 18.}$$

The cutter depth of cut relates to cutter beneath and front area. The cutter front area is related to other cutters number and arrangement (see Equation E.18).

- Note that the above equations was developed using the following assumptions. There is not interaction between cutters at different radiuses.
- There is zero exposure between cutters at the same radius.

APPENDIX F

The codes are provided at

https://github.com/Atashnezhad/OOP/blob/master/curvefit-gh-allcases-dea-oop.ipynb.

docker pull atashnezhad/developeifa:latest

In [1]:
```
import math
import time
import numpy as np
import pandas as pd
import matplotlib.pyplot as plt
import concurrent.futures
```

In [2]:
```
from platform import python_version
print(python_version())
```

```
3.7.1
```

In [3]:
```
class cutter:

    def __init__(self, BR, Vc, UCS, Dc, Aw, cutter_DOC_data_list, cutter_IFA_data_list, cutter_Fn_data, cutter_Fd_data):
        self.BR = BR # cutter back rake angle
        self.Vc = Vc # cutter velocity
        self.DOC_data = cutter_DOC_data_list # list of cutter depth of cut (data)
        self.IFA_data = cutter_IFA_data_list # list of cutter IFA values (data)
        self.VN = Vc / 2.1 # normalized cutter velocity
        self.UCS = UCS # rock unconfined compressive strength
        self.UCSN = UCS / 5000 # normalized rock unconfined compressive strength
        self.Dc = Dc # cutter diameter
        self.Rc = Dc/2 # cutter radius
        self.Aw = Aw # wearflat area sq-inch
        self.Fn_data = cutter_Fn_data # cutter normal force. for blunt cutter case.
        self.Fd_data = cutter_Fd_data # cutter drag force. for blunt cutter case.

    def Model_IFA(self, DOC,w):
        ''' A model for IFA calculation. it takes DOC,
        normalized cutter velocity, normalized rock
        UCS and cutter back rake and returns the IFA.'''
        DOCn = DOC / self.Dc # normalize DOC
        C1 = w[0] + (w[1])/((self.VN)**w[2] + w[3])
        C2 = w[4] + (w[5])/((self.VN)**w[6]+ w[7])
        C_P = w[8]
        C3 = w[9] + w[10]/((self.UCSN**w[11])+w[12])
        return (C1+C2/((DOCn**C_P)+C3))-self.BR

    def Find_L(self):
        '''A function that search for L on cutter face.
        Applicable to blunt cutter.'''
        diff = 10
        L = 0
        while diff > 0.0001:
            L += 0.00001
            A_segment_esti = ((self.Rc)**2*math.acos((self.Rc-L)/self.Rc)\
```

```
        L = 0
        while diff > 0.0001:
            L += 0.00001
            A_segment_esti = ((self.Rc)**2*math.acos((self.Rc-L)/self.Rc)\
                        -(self.Rc-L)*((self.Dc*L-(L)**2)**0.5))
            diff = abs(self.Aw_on_cutter_face-A_segment_esti)
        return L

    def Calculate_fitness(self, w):

        if self.Aw == 0:

            self.IFA_using_Model = [self.Model_IFA(DOC,w) for DOC in self.DOC_data]
            self.ABS_Error = sum([abs((i-j)/i) for i,j in zip(self.IFA_data,self.IFA_using_Model)])/len(self.DOC_data)

        else:

            self.Fn_Fd_list = [i / j for i, j in zip(self.Fn_data, self.Fd_data)] # cutter normal to drag force ratio
            self.IFA_list_DD_Model = [((math.atan(Fn_Fd)*180)/math.pi-self.BR) for Fn_Fd in self.Fn_Fd_list] # calculated IFA li
st
            self.IFA_list_with_Model = [self.Model_IFA(DOC,w) for DOC in self.DOC_data]
            self.Aw_on_cutter_face = self.Aw*math.cos(math.radians((90-self.BR)))
            self.L_list = [(DOC/math.cos(math.radians(self.BR))) for DOC in self.DOC_data] # DOC projected length on cutter face
            self.L_worn = self.Find_L() # single value
            self.Total_L = [(self.L_worn + L) for L in self.L_list] # total L, summation
            self.A_total_segment = [((self.Rc)**2*math.acos((self.Rc-L)/self.Rc)-(self.Rc-L)*((self.Dc*L-(L)**2)**0.5)) for L in
self.Total_L]
            self.A_real_contact_list = [(a-self.Aw_on_cutter_face) for a in self.A_total_segment]
            #=============================================================================
            self.A_F_list_without_IFA = [(A_contact*math.cos(math.radians(self.BR))) for A_contact in self.A_real_contact_list]
            self.F_d_without_IFA = [A_F * self.UCS for A_F in self.A_F_list_without_IFA]
            self.A_F_list_with_IFA = [(A_contact*math.cos(math.radians(IFA+self.BR))) for IFA, A_contact in zip(self.IFA_list_wi
th_Model, self.A_real_contact_list)]
            self.F_d_with_IFA = [A_F * self.UCS for A_F in self.A_F_list_with_IFA]
            self.A_B_list_without_IFA = [(A_contact*math.sin(math.radians(self.BR))) for A_contact in self.A_real_contact_list]
            self.F_n_without_IFA = [A_B * self.UCS for A_B in self.A_B_list_without_IFA]
            self.A_B_list_with_IFA = [(A_contact*math.sin(math.radians(IFA+self.BR))) for IFA, A_contact in zip(self.IFA_list_wi
th_Model, self.A_real_contact_list)]
            self.F_n_with_IFA = [A_B * self.UCS for A_B in self.A_B_list_with_IFA]
            #=============================================================================
            miu = 0.6 # internal friction coefficient for SWG
            self.F_n_with_IFA_miu = [Fn + self.Aw*self.UCS for Fn in self.F_n_with_IFA]
            self.F_d_with_IFA_miu = [Fd+(self.Aw*self.UCS*miu) for Fd in self.F_d_with_IFA]
            #=============================================================================
            self.ABS_Error_Fn = sum([abs((i-j)/j) for i,j in zip(self.F_n_with_IFA_miu, self.Fn_data)])/len(self.DOC_data)
            self.ABS_Error_Fd = sum([abs((i-j)/j) for i,j in zip(self.F_d_with_IFA_miu, self.Fd_data)])/len(self.DOC_data)
            self.ABS_Error = self.ABS_Error_Fn + self.ABS_Error_Fd
        return (self.ABS_Error)
```

Data for Case1: UCS = 3000 psi, Vc = 2.1 in/sec, BR = 20, Dc = 0.5"

In [4]:
```
case1_DOC_data = [0.001,0.005,0.01,0.015,0.02,0.025,0.03,0.035,0.04,0.045,0.05,0.055\
                ,0.06,0.065,0.07,0.075,0.08,0.085,0.09,0.095,0.1,0.105,0.11,0.115,0.12]
case1_IFA_data = [10,10,10,10,10,10,10,10,10,10,10,10,10,\
                        10,10,10,10,10,10,10,10,10,10,10,10]
case1_Fn_data = 0
case1_Fd_data = 0

#'(BR, Vc, UCS, Dc, Aw, cutter_DOC_data_list, cutter_IFA_data_list, cutter_Fn_data, cutter_Fd_data)'
case1 = cutter(20, 2.1, 3000, 0.5, 0, case1_DOC_data, case1_IFA_data, case1_Fn_data, case1_Fd_data)
#print('Case1 details',case1.__dict__)
```

Data for Case2: UCS = 7100 psi, Vc = 2.1 in/sec, BR = 20, Dc = 0.5"

In [5]:
```
case2_DOC_data = [0.001,0.005,0.01,0.015,0.02,0.025,0.03,0.035,0.04,0.045,0.05,0.055\
                ,0.06,0.065,0.07,0.075,0.08,0.085,0.09,0.095,0.1,0.105,0.11,0.115,0.12]
case2_IFA_data = [20,20,20,20,20,20,20,20,20,20,20,20,20,\
                        20,20,20,20,20,20,20,20,20,20,20]
case2_Fn_data = 0
case2_Fd_data = 0

#'(BR, Vc, UCS, Dc, Aw, cutter_DOC_data_list, cutter_IFA_data_list, cutter_Fn_data, cutter_Fd_data)'
case2 = cutter(20, 2.1, 7100, 0.5, 0, case2_DOC_data, case2_IFA_data, case2_Fn_data, case2_Fd_data)
#print('Case2 details',case2.__dict__)
```

Data for Case3: UCS = 21500 psi, Vc = 2.1 in/sec, BR = 20, Dc = 0.5"

In [6]:
```
case3_DOC_data = [0.001,0.005,0.01,0.015,0.02,0.025,0.03,0.035,0.04,0.045,0.05,0.055\
                ,0.06,0.065,0.07,0.075,0.08,0.085,0.09,0.095,0.1,0.105,0.11,0.115,0.12]
case3_IFA_data = [62.49,44.78,38.80,35.67,33.61,32.09,30.90,29.93,29.12,28.42,27.80,\
                        27.26,26.77,26.33,25.93,25.57,25.23,24.91,24.62,24.34,24.09,23.85,\
                        23.62,23.40,23.20]
case3_Fn_data = 0
case3_Fd_data = 0

#'(BR, Vc, UCS, Dc, Aw, cutter_DOC_data_list, cutter_IFA_data_list, cutter_Fn_data, cutter_Fd_data)'
case3 = cutter(20, 2.1, 21500, 0.5, 0, case3_DOC_data, case3_IFA_data, case3_Fn_data, case3_Fd_data)
#print('Case3 details',case3.__dict__)
```

Data for Case4: UCS = 19400 psi, Vc = 177 in/sec, BR = 5, Dc = 0.5"

In [7]:
```
case4_DOC_data = [0.001,0.005,0.01,0.015,0.02,0.025,0.03,0.035,0.04,0.045,0.05,0.055\
                 ,0.06,0.065,0.07,0.075,0.08,0.085,0.09,0.095,0.1,0.105,0.11,0.115,0.12]
case4_IFA_data = [107.23,89.83,83.24,79.61,77.13,75.26,73.76,72.52,71.47,70.55,\
                          69.73,69.01,68.35,67.75,67.20,66.69,66.22,65.78,65.37,\
                          64.98,64.61,64.27,63.94,63.63,63.33]
case4_Fn_data = 0
case4_Fd_data = 0

#'(BR, Vc, UCS, Dc, Aw, cutter_DOC_data_list, cutter_IFA_data_list, cutter_Fn_data, cutter_Fd_data)'
case4 = cutter(20, 177, 19400, 0.5, 0, case4_DOC_data, case4_IFA_data, case4_Fn_data, case4_Fd_data)
#print('Case4 details',case4.__dict__)
```

Data for Case5: UCS = 19400 psi, Vc = 177 in/sec, BR = 10, Dc = 0.5"

In [8]:
```
case5_DOC_data = [0.001,0.005,0.01,0.015,0.02,0.025,0.03,0.035,0.04,0.045,0.05,0.055\
                 ,0.06,0.065,0.07,0.075,0.08,0.085,0.09,0.095,0.1,0.105,0.11,0.115,0.12]
case5_IFA_data = [91.54,79.45,74.75,72.13,70.33,68.96,67.86,66.95,\
                          66.16,65.48,64.88,64.34,63.84,63.40,62.98,62.60,\
                          62.25,61.92,61.61,61.31,61.04,60.78,60.53,60.29,60.07]
case5_Fn_data = 0
case5_Fd_data = 0

#'(BR, Vc, UCS, Dc, Aw, cutter_DOC_data_list, cutter_IFA_data_list, cutter_Fn_data, cutter_Fd_data)'
case5 = cutter(10, 177, 19400, 0.5, 0, case5_DOC_data, case5_IFA_data, case5_Fn_data, case5_Fd_data)
#print('Case5 details',case5.__dict__)
```

Data for Case6: UCS = 19400 psi, Vc = 177 in/sec, BR = 15, Dc = 0.5"

In [9]:
```
case6_DOC_data = [0.001,0.005,0.01,0.015,0.02,0.025,0.03,0.035,0.04,0.045,0.05,0.055\
                 ,0.06,0.065,0.07,0.075,0.08,0.085,0.09,0.095,0.1,0.105,0.11,0.115,0.12]
case6_IFA_data = [91.14,77.21,71.89,68.95,66.94,65.42,64.20,63.19,\
                          62.33,61.58,60.91,60.32,59.78,59.29,58.84,58.42,\
                          58.03,57.67,57.33,57.01,56.71,56.43,56.16,55.90,55.66]
case6_Fn_data = 0
case6_Fd_data = 0

#'(BR, Vc, UCS, Dc, Aw, cutter_DOC_data_list, cutter_IFA_data_list, cutter_Fn_data, cutter_Fd_data)'
case6 = cutter(15, 177, 19400, 0.5, 0, case6_DOC_data, case6_IFA_data, case6_Fn_data, case6_Fd_data)
#print('Case6 details',case6.__dict__)
```

Data for Case7: UCS = 19400 psi, Vc = 177 in/sec, BR = 20, Dc = 0.5"

In [10]:
```
case7_DOC_data = [0.001,0.005,0.01,0.015,0.02,0.025,0.03,0.035,0.04,0.045,0.05,0.055\
                 ,0.06,0.065,0.07,0.075,0.08,0.085,0.09,0.095,0.1,0.105,0.11,0.115,0.12]
case7_IFA_data = [82.65,70.59,65.96,63.39,61.63,60.29,59.22,58.34,\
                          57.58,56.92,56.33,55.81,55.34,54.90,54.51,54.14,\
                          53.80,53.48,53.18,52.90,52.63,52.38,52.14,51.92,51.70]
case7_Fn_data = 0
case7_Fd_data = 0

#'(BR, Vc, UCS, Dc, Aw, cutter_DOC_data_list, cutter_IFA_data_list, cutter_Fn_data, cutter_Fd_data)'
case7 = cutter(20, 177, 19400, 0.5, 0, case7_DOC_data, case7_IFA_data, case7_Fn_data, case7_Fd_data)
#print('Case7 details',case7.__dict__)
```

Data for Case8: UCS = 19400 psi, Vc = 177 in/sec, BR = 25, Dc = 0.5"

In [11]:
```
case8_DOC_data = [0.001,0.005,0.01,0.015,0.02,0.025,0.03,0.035,0.04,0.045,0.05,0.055\
                 ,0.06,0.065,0.07,0.075,0.08,0.085,0.09,0.095,0.1,0.105,0.11,0.115,0.12]
case8_IFA_data = [99.48,77.14,69.14,64.85,61.97,59.82,58.12,56.72,\
                          55.54,54.51,53.61,52.81,52.09,51.44,50.84,50.29,\
                          49.78,49.30,48.86,48.44,48.05,47.68,47.33,47.00,46.69]
case8_Fn_data = 0
case8_Fd_data = 0

#'(BR, Vc, UCS, Dc, Aw, cutter_DOC_data_list, cutter_IFA_data_list, cutter_Fn_data, cutter_Fd_data)'
case8 = cutter(25, 177, 19400, 0.5, 0, case8_DOC_data, case8_IFA_data, case8_Fn_data, case8_Fd_data)
#print('Case8 details',case8.__dict__)
```

Data for Case9: UCS = 19400 psi, Vc = 177 in/sec, BR = 30, Dc = 0.5"

In [12]:
```
case9_DOC_data = [0.001,0.005,0.01,0.015,0.02,0.025,0.03,0.035,0.04,0.045,0.05,0.055\
                 ,0.06,0.065,0.07,0.075,0.08,0.085,0.09,0.095,0.1,0.105,0.11,0.115,0.12]
case9_IFA_data = [76.83,62.32,56.95,54.03,52.04,50.56,49.37,48.39,\
                          47.56,46.84,46.20,45.63,45.12,44.65,44.22,43.83,\
                          43.46,43.12,42.80,42.50,42.22,41.95,41.70,41.46,41.23]
case9_Fn_data = 0
case9_Fd_data = 0

#'(BR, Vc, UCS, Dc, Aw, cutter_DOC_data_list, cutter_IFA_data_list, cutter_Fn_data, cutter_Fd_data)'
case9 = cutter(30, 177, 19400, 0.5, 0, case9_DOC_data, case9_IFA_data, case9_Fn_data, case9_Fd_data)
#print('Case9 details',case9.__dict__)
```

Data for Case10: UCS = 21500 psi, Vc = 2.1 in/sec, BR = 20 , Dc = 0.75", Aw = 0.02 sq-inch

In [13]:
```
case10_DOC_data = [0.023,0.023,0.023,0.023,0.024,0.024,0.024,0.024,0.039,0.04,\
                   0.04,0.04,0.041,0.041,0.041,0.042,0.042,0.042,0.042,0.042,\
                   0.042,0.042,0.079,0.079,0.079,0.079,0.08]
case10_IFA_data = 0
case10_Fn_data = [545,568,599,590,610,617,640,619,657,689,699,756,669,676,698,\
                  770,770,739,763,741,774,760,855,865,926,918,875]
case10_Fd_data = [360,387,392,396,401,412,418,416,461,475,476,517,466,473,481,\
                  511,540,518,526,504,522,519,694,694,722,750,710]

#'(BR, Vc, UCS, Dc, Aw, cutter_DOC_data_list, cutter_IFA_data_list, cutter_Fn_data, cutter_Fd_data)'
case10 = cutter(20, 2.1, 21500, 0.75, 0.02, case10_DOC_data, case10_IFA_data, case10_Fn_data, case10_Fd_data)
#print('Case10 details',case10.__dict__)
```

In [14]:
```
class Full_bit:

    def __init__(self, ROP_constant, Data_WOB, Data_ROP, Db, RPM, UCS, NOC, BR, Dc):
        self.ROPcons = ROP_constant
        self.Data_WOB = Data_WOB
        self.Data_ROP = Data_ROP
        self.Db = Db
        self.RPM = RPM
        self.UCS = UCS
        self.NOC = NOC
        self.BR = BR
        self.Dc = Dc

        self.Ac = math.pi*self.Dc**2 / 4 # cutter face area sq-inch
        self.Re = self.Db/(2*(2**0.5)) # calculate the equivalent radius
        self.Number_of_DataPoints = len(self.Data_WOB)
        self.WOC = [self.Data_WOB[i]/self.NOC for i in range(0,self.Number_of_DataPoints)] # calculate the weight on cutter
        self.A_bit = (math.pi*(self.Db**2))/4 # bit area
        self.AB = [WOC/self.UCS for WOC in self.WOC ] # calculate the cutter beanth area
        self.AB = [(self.Ac*math.sin(self.BR)) if x > (self.Ac*math.sin(self.BR)) else x for x in self.AB] # filter those values
that are greater than availabe cutter beanth area
        self.UCSN = self.UCS/5000 # calculate the normalized UCS
        self.V_Cutter_Equivalent = 2*math.pi*self.Re*self.RPM/60 # calculate equivalent velocity
        self.VN = self.V_Cutter_Equivalent/2.1 # normalize the equivalent velocity


    def A_Front(self, AB, IFA):
        '''A function that takes the cutter beneath area,
        back rake and IFA and returns the cutter front area.'''
        return AB/math.tan(math.radians(self.BR+IFA))
```

```
    def ROP_model(self, AF):
        '''A ROP model (function). A function that takes number of cutters (NOC),
        bit equivalent radius (Re), cutter front area (AF), cutter back rake (BR),
        interfacial friction angle (IFA), revolutions per minute (RPM), and bit area (A_bit).'''
        return ((2*self.NOC*math.pi*self.Re*AF*self.RPM)/(self.A_bit))*5


    def Model_IFA(self, DOC, w):
        #A model for IFA calculation. it takes DOC,
        #normalized cutter velocity, normalized rock
        #UCS and cutter back rake and returns the IFA.

        DOCn = DOC / self.Dc # normalize DOC
        C1 = w[0] + (w[1])/((self.VN)**w[2] + w[3])
        C2 = w[4] + (w[5])/((self.VN)**w[6]+ w[7])
        C_P = w[8]
        C3 = w[9]+w[10]/((self.UCSN**w[11])+w[12])

        return (C1+C2/((DOCn**C_P)+C3))-self.BR



    def Find_IFA(self, AB, maxvalue, w):
        #A function that finds the best IFA value that satisfy
        #both the ROP DOC and developed Model-IFA
        diff1 = 1000000000000000 # initite it with a big value
        Number_of_random_attempts = 10000
        IFA_search = 0

        while diff1 > 0.0001 and IFA_search < maxvalue:

            IFA_search = IFA_search + 0.1
            AF = self.A_Front(AB,IFA_search) #calculate the cutter front area
            ROP = self.ROP_model(AF) # calculate the ROP
            DOC = ROP/(self.RPM*5) # calculate the depth of cut
            IFA = self.Model_IFA(DOC, w)

            diff2 = abs(IFA_search - IFA)

            if diff2 < diff1:
                diff1 = diff2
                self.Best_IFA = IFA_search

        return self.Best_IFA, diff1
```

```
    def Calculate_ROP(self, AB, maxvalue, w):
        ''' A function that takes the cutter beneath
        area and returns the ROP estimated'''
        IFA, diff = self.Find_IFA(AB, maxvalue, w)
        AF = self.A_Front(AB,IFA)
        Estimated_ROP = self.ROPcons * self.ROP_model(AF)
        return Estimated_ROP, IFA, diff

    def Calculate_fitness(self, w):

        #=============================================================================================================
        #ROP calculation
        self.ROP_Model_esti_list = []
        self.IFAlist = []
        self.difflist = []
        self.maxvalue = 90 - self.BR

        for i in range(0,self.Number_of_DataPoints):
            self.ROP_Model_esti, IFA, diff = self.Calculate_ROP(self.AB[i], self.maxvalue, w)
            self.ROP_Model_esti_list.append(self.ROP_Model_esti)
            self.difflist.append(diff)
            self.maxvalue = IFA # make sure descending trend for IFA vs DOC
            self.IFAlist.append(IFA)
        #=============================================================================================================
        self.error_ROP_list = [abs((ROP_Model - Data_ROP)/Data_ROP) for ROP_Model, Data_ROP in zip(self.ROP_Model_esti_list,sel
f.Data_ROP)]
        self.error_ROP = sum(self.error_ROP_list)/len(self.Data_WOB)
        return self.error_ROP
```

Data for case1_FullBit = error function_SWG_4B_100

In [15]:
```
Data_WOB = [2300,2420,2660,2910,3180,3410,3660,3940,4170] # insert the WOB data into the list
Data_ROP = [9.9,11,14.7,18.1,22.6,27.2,31.1,36.5,39.4] # insert the ROP data into the list

#'(ROP_constant, Data_WOB, Data_ROP, Db, RPM, UCS, NOC, BR, Dc)'
case1_FullBit = Full_bit(0.9, Data_WOB, Data_ROP, 3.75, 100, 21500, 12, 20, 0.5)
#case1_FullBit.Calculate_fitness(w)
```

Data for case2_FullBit = error function_SWG_4B_150

In [16]:
```
Data_WOB = [2150,2300,2560,2810,3060,3290,3540,3820,4070] # insert the WOB data into the list
Data_ROP = [10.2,11.9,15.1,19.6,25.6,31.4,37.7,44.3,50.8] # insert the ROP data into the list

#'(ROP_constant, Data_WOB, Data_ROP, Db, RPM, UCS, NOC, BR, Dc)'
case2_FullBit = Full_bit(0.9, Data_WOB, Data_ROP, 3.75, 150, 21500, 12, 20, 0.5)
#case2_FullBit.Calculate_fitness(w)
```

Data for case3_FullBit = error function_SWG_4B_200

In [17]:
```
Data_WOB = [2280,2380,2570,2810,3070,3310,3540,3820,4080] # insert the WOB data into the list
Data_ROP = [11.4,12.5,14.9,18.2,22.9,27.7,34.8,43,50] # insert the ROP data into the list

#'(ROP_constant, Data_WOB, Data_ROP, Db, RPM, UCS, NOC, BR, Dc)'
case3_FullBit = Full_bit(0.9, Data_WOB, Data_ROP, 3.75, 200, 21500, 12, 20, 0.5)
#case3_FullBit.Calculate_fitness(w)
```

Data for case4_FullBit = error function_BSS_4B_100

In [18]:
```
Data_WOB = [900,1180,1230,1360,1510,1650,1730,1780] # insert the WOB data into the list
Data_ROP = [24.8,48.9,53.4,54,62,70.8,81.3,84.1] # insert the ROP data into the list

#'(ROP_constant, Data_WOB, Data_ROP, Db, RPM, UCS, NOC, BR, Dc)'
case4_FullBit = Full_bit(0.9, Data_WOB, Data_ROP, 3.75, 100, 7100, 12, 20, 0.5)
#case4_FullBit.Calculate_fitness(w)
```

Data for case5_FullBit = error function_BSS_4B_150

In [19]:
```
Data_WOB = [970,1090,1110,1300,1520,1720,1770,1960] # insert the WOB data into the list
Data_ROP = [40.8,61.9,64.5,71.7,91.5,102.9,106.9,127.7] # insert the ROP data into the list

#'(ROP_constant, Data_WOB, Data_ROP, Db, RPM, UCS, NOC, BR, Dc)'
case5_FullBit = Full_bit(0.9, Data_WOB, Data_ROP, 3.75, 150, 7100, 12, 20, 0.5)
#case5_FullBit.Calculate_fitness(w)
```

Data for case6_FullBit = error function_BSS_4B_200

In [20]:
```
Data_WOB = [850,960,1150,1210,1270,1340,1570,1800] # insert the WOB data into the list
Data_ROP = [30.5,59.5,84.8,87.8,96.5,96.6,120.9,136] # insert the ROP data into the list

#'(ROP_constant, Data_WOB, Data_ROP, Db, RPM, UCS, NOC, BR, Dc)'
case6_FullBit = Full_bit(0.9, Data_WOB, Data_ROP, 3.75, 200, 7100, 12, 20, 0.5)
#case6_FullBit.Calculate_fitness(w)
```

DEA

In [21]:
```
def de(fobj, bounds, mut=0.8, crossp=0.7, popsize=100, its=10):
    dimensions = len(bounds)
    pop = np.random.rand(popsize, dimensions)
    min_b, max_b = np.asarray(bounds).T
    diff = np.fabs(min_b - max_b)
    pop_denorm = min_b + pop * diff
    fitness = np.asarray([fobj(ind) for ind in pop_denorm])
    best_idx = np.argmin(fitness)
    best = pop_denorm[best_idx]
    for i in range(its):
        for j in range(popsize):
            idxs = [idx for idx in range(popsize) if idx != j]
            a, b, c = pop[np.random.choice(idxs, 3, replace = False)]
            mutant = np.clip(a + mut * (b - c), 0, 1)
            cross_points = np.random.rand(dimensions) < crossp
            if not np.any(cross_points):
                cross_points[np.random.randint(0, dimensions)] = True
            trial = np.where(cross_points, mutant, pop[j])
            trial_denorm = min_b + trial * diff
            f = fobj(trial_denorm)
            if f < fitness[j]:
                fitness[j] = f
                pop[j] = trial
                if f < fitness[best_idx]:
                    best_idx = j
                    best = trial_denorm
        print("Iteration number= %s" % (i))
        print("Best Fitness= %s" % (fitness[best_idx]))
        #print("Best values= %s" % (best))
        yield best, fitness[best_idx]
```

In [22]:
```
#Define objective function-min sq
def ERROR(w):
    #============================
    w = w.tolist()
    #============================
    ERROR_value1 =\
    case1_FullBit.Calculate_fitness(w)+\
    case2_FullBit.Calculate_fitness(w)+\
    case3_FullBit.Calculate_fitness(w)
    case4_FullBit.Calculate_fitness(w)+\
    case5_FullBit.Calculate_fitness(w)+\
    case6_FullBit.Calculate_fitness(w)
    #============================
    ERROR_value2 =\
    case1.Calculate_fitness(w)+\
    case2.Calculate_fitness(w)+\
    case3.Calculate_fitness(w)+\
    case4.Calculate_fitness(w)+\
    case5.Calculate_fitness(w)+\
    case6.Calculate_fitness(w)+\
    case7.Calculate_fitness(w)+\
    case8.Calculate_fitness(w)+\
    case9.Calculate_fitness(w)+\
    case10.Calculate_fitness(w)

    #============================
    ERROR_value = (ERROR_value1/3 + ERROR_value2/8)/2
    #============================
    return (ERROR_value)
```

In [23]:
```
start_time = time.time()
#Apply the DE algorithm to the function + boundries and number of iterations
result = list(de(ERROR, [(0, 100),(-150, 0),(1, 2.5),(0, 3),\
                         (0, 20),(0, 0),(1, 2.5),(0, 100),\
                         (0, 2.5),\
                         (0, 20),(-100, 100),(0, 2.5),(0, 100)], mut=0.8, crossp=0.7, popsize=15, its=10))
df = pd.DataFrame(result)
print("--- %s seconds ---" % (time.time() - start_time))
```

```
Iteration number= 0
Best Fitness= 0.3436644439721298
Iteration number= 1
Best Fitness= 0.2802018008802526
Iteration number= 2
Best Fitness= 0.2802018008802526
Iteration number= 3
Best Fitness= 0.2802018008802526
```

In [24]:
```
print(df.tail(1))
```

```
                                                   0         1
9  [77.31284117723584, -122.51631289414792, 1.362...  0.273926
```

In [25]:
```
df['w1'], df['w2'],df['w3'], df['w4'], df['w5'],\
df['w6'], df['w7'],df['w8'], df['w9'], df['w10'],\
df['w11'], df['w12'], df['w13']= zip(*df[0])
cols = [0]
df.drop(df.columns[cols],axis=1,inplace=True)
df.columns.values[0] = "Fitness"
best_coff = list(zip(df.iloc[len(df)-1,1:]))
print(best_coff)
```

```
[(77.31284117723584,), (-122.51631289414792,), (1.3623245570255147,), (1.7254435491948101,), (20.0,), (0.0,), (1.0,), (100.0,),
(0.8548920238842506,), (5.9639378864442225,), (71.68459515568935,), (1.0684216643078899,), (44.022800732416805,)]
```

In [26]:
```
data_ncol=len(df.columns)
#Plot fitness versus iteration
fig = plt.figure(figsize=(21,24))
for i in range(1,(data_ncol+1)):
    if i<data_ncol:
        plt.subplot(5, 3, i)
        plt.plot(df['w{}'.format(i)],'bo', markersize=4)
        plt.xlabel('Iteration')
        plt.ylabel('w{}'.format(i))
        plt.grid(True)
    else:
        plt.subplot(5, 3, data_ncol)
        plt.plot(df['Fitness'],'red', markersize=4)
        plt.xlabel('Iteration')
        plt.ylabel('Fitness')
        plt.grid(True)
plt.show()
```

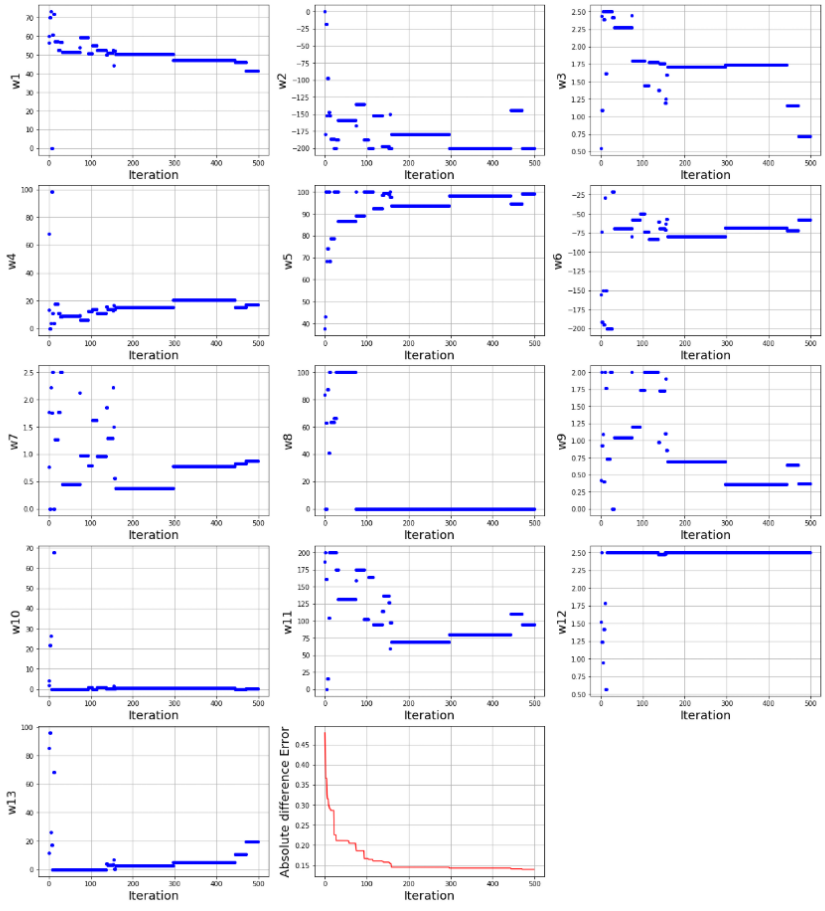

APPENDIX G

The full bit data and single cutter data used in this study are provided at the following tables.

Table G.1 Four-Blade bit results in SWG at 100 rpm (Raymond et al., 2015)

Data Pt. #	Penetration Interval [in]	R.O.P [ft/hr]	Depth of Cut [in/rev]	Weight on Bit [lbf]	Torque [ft×lb]	Rotary Speed [rpm]	Torsional Power [hp]
1	7.0- 7.8	9.9	.020	2300	166	102.	3.9
2	8.1 - 9.1	11.0	.022	2420	176	101.	4.1
3	10.2 - 11.4	14.7	.029	2660	197	102.	4.6
4	12.2 - 13.7	18.1	.036	2910	217	101.	4.9
5	14.5 - 16.4	22.6	.045	3180	241	101.	5.4
6	17.2 - 19.4	27.2	.054	3410	264	102.	5.8
7	19.9 - 22.5	31.1	.061	3660	285	102.	6.2
8	23.7 - 26.7	36.5	.072	3940	313	101.	6.7
9	28.0 - 31.3	39.4	.077	4170	342	103.	7.4

Table G.2 Four-Blade bit results in SWG at 150 rpm (Raymond et al., 2015)

Data Pt. #	Penetration Interval [in]	R.O.P [ft/hr]	Depth of Cut [in/rev]	Weight on Bit [lbf]	Torque [ft×lb]	Rotary Speed [rpm]	Torsional Power [hp]
1	6.8 - 7.5	10.2	.013	2150	146	152.	5.3
2	7.7 - 8.5	11.9	.016	2300	158	151.	5.6
3	8.9 - 9.9	15.1	.020	2560	176	151.	6.1
4	10.3 -11.6	19.6	.026	2810	198	151.	6.8
5	12.3 – 14.0	25.6	.034	3060	223	151.	7.5
6	14.6 - 16.7	31.4	.041	3290	245	152.	8.1
7	17.1 - 19.6	37.7	.050	3540	267	152.	8.8
8	21.0 – 24.0	44.3	.058	3820	290	152.	9.5
9	25.6 – 29.0	50.8	.067	4070	312	152.	10.1

Table G.3 Four-Blade bit results in SWG at 200 rpm (Raymond et al., 2015)

Data Pt. #	Penetration Interval [in]	R.O.P [ft/hr]	Depth of Cut [in/rev]	Weight on Bit [lbf]	Torque [ft×lb]	Rotary Speed [rpm]	Torsional Power [hp]
1	7.1 - 7.6	11.4	.011	2280	139	202.	6.8
2	8.0 - 8.6	12.5	.012	2380	146	202.	7.1
3	9.2 - 9.9	14.9	.015	2570	158	202.	7.5
4	10.4 - 11.3	18.2	.018	2810	174	202.	8.1
5	12.1 - 13.3	22.9	.023	3070	192	201.	8.8
6	14.4 - 15.8	27.7	.028	3310	209	202.	9.5
7	16.8 - 18.5	34.8	.035	3540	228	201.	10.2
8	21.6 - 23.8	43.0	.043	3820	250	201.	11.0
9	26.0 - 28.5	50.0	.050	4080	271	199.	11.7

Table G.4 Five-Blade bit results in SWG at 100 rpm (Raymond et al., 2015)

Data Pt. #	Penetration Interval [in]	R.O.P [ft/hr]	Depth of Cut [in/rev]	Weight on Bit [lbf]	Torque [ft×lb]	Rotary Speed [rpm]	Torsional Power [hp]
1	7.1 - 7.8	10.5	.020	2250	177	106.	4.3
2	8.0 - 8.8	12.3	.023	2390	192	107.	4.6
3	9.1 - 10.2	15.9	.030	2620	205	106.	4.9
4	10.5 - 11.8	19.5	.037	2860	220	106.	5.2
5	12.7 - 14.4	25.9	.049	3100	248	107.	5.8
6	15.0 - 17.6	30.8	.058	3310	270	107.	6.3
7	17.7 - 20.1	35.9	.067	3560	297	107.	6.8
8	21.4 - 24.1	40.4	.075	3850	317	108.	7.3
9	25.2 - 28.2	44.6	.083	4100	337	108.	7.7

Table G.5 Five-Blade bit results in SWG at 150 rpm (Raymond et al., 2015)

Data Pt. #	Penetration Interval [in]	R.O.P [ft/hr]	Depth of Cut [in/rev]	Weight on Bit [lbf]	Torque [ft×lb]	Rotary Speed [rpm]	Torsional Power [hp]
1	7.2 - 7.7	11.5	.015	2150	140	150.	5.1
2	8.0 - 8.7	13.4	.018	2320	151	150.	5.4
3	9.4 - 10.3	16.2	.022	2550	161	150.	5.7
4	10.6 - 11.7	21.6	.029	2790	183	150.	6.3
5	12.5 - 13.9	28.4	.038	3020	204	151.	6.9
6	14.7 - 16.4	34.3	.046	3260	226	151.	7.6
7	18.0 - 20.1	41.1	.054	3500	248	152.	8.3
8	21.6 - 24.1	48.9	.064	3790	276	152.	9.0
9	26.6 - 29.4	54.5	.071	4090	296	153.	9.7

Table G.6 Five-Blade bit results in SWG at 200 rpm (Raymond et al., 2015)

Data Pt. #	Penetration Interval [in]	R.O.P [ft/hr]	Depth of Cut [in/rev]	Weight on Bit [lbf]	Torque [ft×lb]	Rotary Speed [rpm]	Torsional Power [hp]
1	6.8 - 7.6	11.3	.012	2080	119	196.	5.9
2	8.0 - 8.8	11.4	.012	2260	219	196.	6.2
3	9.2 - 10.2	14.6	.015	2510	137	196.	6.4
4	10.7 - 11.9	18.4	.019	2760	149	195.	6.9
5	12.3 - 13.9	24.7	.025	3020	170	194.	7.7
6	14.4 - 16.5	32.0	.033	3230	190	195.	8.4
7	17.6 - 20.3	41.4	.043	3470	214	195.	9.3
8	21.4 - 24.7	49.6	.051	3720	236	195.	10.2
9	25.8 - 29.7	58.8	.061	3960	262	193.	11.0

Table G.7 Four-Blade bit results in BSS at 100 rpm (Raymond et al., 2015)

Data Pt. #	Penetration Interval [in]	R.O.P [ft/hr]	Depth of Cut [in/rev]	Weight on Bit [lbf]	Torque [ft×lb]	Rotary Speed [rpm]	Torsional Power [hp]
1	6.5 - 8.3	24.8	.051	900	68	97.	1.9
2	9.1 – 13.0	48.9	.100	1180	104	97.	2.6
3	13.9 - 18.9	53.4	.110	1230	105	97.	2.6
4	15.4 - 18.3	54.0	.111	1360	118	97.	2.9
5	19.0 - 21.7	62.0	.127	1510	129	98.	3.1
6	20.3 - 24.1	70.8	.146	1650	143	98.	3.3
7	22.8 - 25.5	81.3	.168	1730	156	98.	3.5
8	27.0 - 29.7	84.1	.174	1780	156	98.	3.5

Table G.8 Four-Blade bit results in BSS at 150 rpm (Raymond et al., 2015)

Data Pt. #	Penetration Interval [in]	R.O.P [ft/hr]	Depth of Cut [in/rev]	Weight on Bit [lbf]	Torque [ft×lb]	Rotary Speed [rpm]	Torsional Power [hp]
1	7.2 - 9.9	40.8	.056	970	75	146.	3.2
2	9.8 - 10.8	61.9	.083	1090	88	146.	3.6
3	10.3 - 12.3	64.5	.087	1110	91	146.	3.7
4	13.6 – 16.0	71.7	.099	1300	105	146.	4.0
5	15.8 - 19.2	91.5	.123	1520	124	148.	4.6
6	16.8 - 20.4	102.9	.141	1720	141	149.	5.0
7	20.2 - 24.0	106.9	.146	1770	148	149.	5.2
8	21.1 - 24.5	127.7	.173	1960	162	149.	5.7

Table G.9 Four-Blade bit results in BSS at 200 rpm (Raymond et al., 2015)

Data Pt. #	Penetration Interval [in]	R.O.P [ft/hr]	Depth of Cut [in/rev]	Weight on Bit [lbf]	Torque [ft×lb]	Rotary Speed [rpm]	Torsional Power [hp]
1	6.5- 7.2	30.5	.031	850	57	195.	3.8
2	7.8 - 9.7	59.5	.060	960	77	195.	4.3
3	8.9 - 10.9	84.8	.087	1150	95	196.	5.2
4	10.2 - 12.5	87.8	.090	1210	105	197.	5.6
5	12.4 - 14.7	96.5	.097	1270	113	198.	5.7
6	13.1 - 17.0	96.6	.098	1340	123	198.	6.1
7	16.6 - 19.8	120.9	.124	1570	135	198.	6.7
8	19.4 - 21.4	136.0	.138	1800	161	199.	7.5

Table G.10 Five-Blade bit results in BSS at 100 rpm (Raymond et al., 2015)

Data Pt. #	Penetration Interval [in]	R.O.P [ft/hr]	Depth of Cut [in/rev]	Weight on Bit [lbf]	Torque [ft×lb]	Rotary Speed [rpm]	Torsional Power [hp]
1	7.5 – 10.0	53.3	.104	1110	101	102.	2.8
2	10.2 - 14.3	65.1	.127	1310	118	102.	3.1
3	15.1 - 20.3	82.5	.161	1530	138	103.	3.5
4	26.8 - 25.7	96.2	.189	1770	160	103.	3.9
5	31.0- 31.6	110.1	.217	2070	187	103.	4.4

Table G.11 Five-Blade bit results in BSS at 150 rpm (Raymond et al., 2015)

Data Pt. #	Penetration Interval [in]	R.O.P [ft/hr]	Depth of Cut [in/rev]	Weight on Bit [lbf]	Torque [ft×lb]	Rotary Speed [rpm]	Torsional Power [hp]
1	7.3 - 9.7	63.7	.083	1010	85	152.	3.9
2	8.3 - 11.3	65.5	.085	1020	87	152.	4.0
3	11.0 - 12.6	80.0	.105	1200	99	152.	4.3
4	11.7 - 13.4	85.3	.112	1220	101	152.	4.3
5	13.1 - 16.3	95.9	.126	1360	110	153.	4.6
6	13.6 - 18.7	101.6	.133	1380	113	153.	4.6
7	17.0 – 20.0	103.5	.135	1410	115	153.	4.7
8	19.3 - 22.5	104.4	.138	1470	121	153.	4.9
9	20.2 - 22.8	117.9	.155	1550	125	154.	5.0
10	23.2 - 27.8	118.1	.155	1570	128	154.	5.0

Table G.12 Five-Blade bit results in BSS at 200 rpm (Raymond et al., 2015)

Data Pt. #	Penetration Interval [in]	R.O.P [ft/hr]	Depth of Cut [in/rev]	Weight on Bit [lbf]	Torque [ft×lb]	Rotary Speed [rpm]	Torsional Power [hp]
1	6.8 - 7.5	53.7	.054	930	79	196.	4.6
2	7.7 - 9.4	70.4	.071	940	86	197.	4.9
3	10.4 - 13.3	88.6	.090	1080	94	198.	5.2
4	13.9 - 18.1	124.7	.127	1420	124	198.	6.3
5	19.8 - 22.3	148.1	.151	1590	144	198.	7.0

Table G.13 Description of cutters used in the laboratory tests (Glowka, 1987)

CUTTER	A_w (in^2)	w (in)	L (in)	COMPACT DIAMETER (in)	WEARFLAT TYPE *
A	0.016	0.220	0.090	0.50	F
B	0.017	0.240	0.070	0.50	F
C	0.017	0.340	0.050	0.50	F
D	0.020	0.320	0.100	0.75	L
E	0.022	0.220	0.140	0.50	F,L
F	0.030-0.040	0.300-0.320	0.140-0.180	0.50	M,L
G	0.032	0.360	0.130	0.75	L
H**	0.029	0.340	0.120	0.75	L
I	0.040	0.320	0.180	0.50	M
J	0.000	0.000	0.000	0.50	S
K	0.000	0.00	0.00	0.75	S

* F = field-worn; L = laboratory-worn; M = machine ground; S = sharp.
** Cutter H used in waterjet-assisted cuts.
All cutters had a backrake angle of 20^o.

Table G.14 Dry, non-interacting cut test data for BSS (Glowka, 1987)

CUTTER	A_w (in^2)	w (in)	L (in)	δ (in)	F (lb)	F_d (lb)	F/A_w (psi)	F_d /F
J	0.000	0.000	0.000	0.023	13.3	19.4	---	1.46
J	0.000	0.000	0.000	0.020	16.9	21.7	---	1.28
J	0.000	0.000	0.000	0.022	17.3	21.0	---	1.21
J	0.000	0.000	0.000	0.019	18.6	23.6	---	1.27
J	0.000	0.000	0.000	0.042	60.1	66.0	---	1.10
J	0.000	0.000	0.000	0.041	62.8	75.6	---	1.20
J	0.000	0.000	0.000	0.041	58.1	71.7	---	1.23
J	0.000	0.000	0.000	0.041	57.9	67.5	---	1.17
J	0.000	0.000	0.000	0.080	117.0	143.0	---	1.22
J	0.000	0.000	0.000	0.082	116.0	139.0	---	1.20
J	0.000	0.000	0.000	0.078	128.0	154.0	---	1.20
J	0.000	0.000	0.000	0.060	94.5	110.0	---	1.16
J	0.000	0.000	0.000	0.062	91.3	106.0	---	1.16
K	0.000	0.000	0.000	0.021	18.0	24.3	---	1.35
K	0.000	0.000	0.000	0.023	17.0	26.1	---	1.54
K	0.000	0.000	0.000	0.023	16.7	19.2	---	1.15
K	0.000	0.000	0.000	0.020	16.9	23.5	---	1.39
K	0.000	0.000	0.000	0.022	19.6	23.1	---	1.18
K	0.000	0.000	0.000	0.023	17.7	23.7	---	1.34
K	0.000	0.000	0.000	0.021	19.8	24.0	---	1.21
K	0.000	0.000	0.000	0.041	55.5	72.5	---	1.31
K	0.000	0.000	0.000	0.042	51.8	70.5	---	1.36
K	0.000	0.000	0.000	0.042	53.5	69.0	---	1.29
K	0.000	0.000	0.000	0.042	48.2	64.5	---	1.34
K	0.000	0.000	0.000	0.041	53.5	68.0	---	1.27
K	0.000	0.000	0.000	0.041	49.2	68.3	---	1.39
K	0.000	0.000	0.000	0.041	52.1	68.2	---	1.31
K	0.000	0.000	0.000	0.080	109.0	147.0	---	1.35
K	0.000	0.000	0.000	0.080	102.0	142.0	---	1.39
K	0.000	0.000	0.000	0.080	109.0	143.0	---	1.31
K	0.000	0.000	0.000	0.080	97.5	138.0	---	1.42
K	0.000	0.000	0.000	0.080	103.0	141.0	---	1.37

Table G.15 Dry, non-interacting cut test data for SWG (Glowka, 1987)

CUTTER	A_w (in^2)	w (in)	L (in)	δ (in)	F (lb)	F_d (lb)	F/A_w (psi)	F_d /F
J	0.000	0.000	0.000	0.017	31.7	26.3	---	0.83
J	0.000	0.000	0.000	0.015	25.3	16.8	---	0.66
J	0.000	0.000	0.000	0.016	30.4	17.0	---	0.56
J	0.000	0.000	0.000	0.018	29.2	18.8	---	0.64
J	0.000	0.000	0.000	0.013	23.9	16.9	---	0.71
J	0.000	0.000	0.000	0.020	38.0	28.9	---	0.76
J	0.000	0.000	0.000	0.039	131.0	118.0	---	0.90
J	0.000	0.000	0.000	0.039	136.0	120.0	---	0.88
J	0.000	0.000	0.000	0.039	137.0	121.0	---	0.88
J	0.000	0.000	0.000	0.037	136.0	118.0	---	0.87
J	0.000	0.000	0.000	0.061	229.0	217.0	---	0.95
J	0.000	0.000	0.000	0.062	256.0	227.0	---	0.89
D	0.020	0.320	0.100	0.023	545.0	360.0	27250.	0.66
D	0.020	0.320	0.100	0.023	568.0	387.0	28400.	0.68
D	0.020	0.320	0.100	0.023	599.0	392.0	29950.	0.65
D	0.020	0.320	0.100	0.023	590.0	396.0	29500.	0.67
D	0.020	0.320	0.100	0.024	610.0	401.0	30500.	0.66
D	0.020	0.320	0.100	0.024	617.0	412.0	30850.	0.67
D	0.020	0.320	0.100	0.024	640.0	418.0	32000.	0.65
D	0.020	0.320	0.100	0.024	619.0	416.0	30950.	0.67
D	0.020	0.320	0.100	0.039	657.0	461.0	32850.	0.70
D	0.020	0.320	0.100	0.040	689.0	475.0	34450.	0.69
D	0.020	0.320	0.100	0.041	669.0	466.0	33450.	0.70
D	0.020	0.320	0.100	0.041	676.0	473.0	33800.	0.70
D	0.020	0.320	0.100	0.041	698.0	481.0	34900.	0.69
D	0.020	0.320	0.100	0.040	699.0	476.0	34950.	0.68
D	0.020	0.320	0.100	0.040	756.0	517.0	37800.	0.68
D	0.020	0.320	0.100	0.042	770.0	511.0	38500.	0.66
D	0.020	0.320	0.100	0.042	770.0	540.0	38500.	0.70
D	0.020	0.320	0.100	0.042	739.0	518.0	36950.	0.70
D	0.020	0.320	0.100	0.042	763.0	526.0	38150.	0.69
D	0.020	0.320	0.100	0.042	741.0	504.0	37050.	0.68
D	0.020	0.320	0.100	0.042	774.0	522.0	38700.	0.67
D	0.020	0.320	0.100	0.042	760.0	519.0	38000.	0.68
D	0.020	0.320	0.100	0.079	855.0	694.0	42750.	0.81
D	0.020	0.320	0.100	0.080	875.0	710.0	43750.	0.81
D	0.020	0.320	0.100	0.079	865.0	694.0	43250.	0.80
D	0.020	0.320	0.100	0.079	926.0	722.0	46300.	0.78
D	0.020	0.320	0.100	0.079	918.0	750.0	45900.	0.82

Table G.16 Averaged forces with varying BR, chamfer angles and depth of cut (standard chamfer geometry and alternative chamfer geometry, chamfer angle forty five and fifteen degree respectively), (Hellvik et al., 2012)

STANDARD CHAMFER GEOMETRY RESULTS

MEAN FORCE, X-direction (tangential)					MEAN FORCE, Y-direction (radial)				MEAN FORCE, Z-direction (WOB)			
Std	DOC, mm				DOC, mm				DOC, mm			
Rake	0.5	1	2	3	0.5	1	2	3	0.5	1	2	3
5	-0.2	-0.2	-0.7	-1.0	0.1	0.1	0.6	0.9	0.5	0.6	1.8	2.4
10	-0.1	-0.4	-0.7		0.1	0.2	0.5		0.4	0.9	1.5	
15	-0.2	-0.4	-0.8	-1.2	0.0	0.2	0.5	0.8	0.3	0.9	1.6	2.5
20	-0.1	-0.4	-0.9	-1.4	0.1	0.2	0.6	0.9	0.4	0.9	2.0	2.6
25	-0.1	-0.4	-1.0	-1.7	0.0	0.2	0.6	1.1	0.3	1.1	2.3	3.5
30	-0.2	-0.4	-1.0	-1.5	0.0	0.2	0.6	1.0	0.4	1.0	2.2	2.9
	RMS FORCE, X-direction				RMS FORCE, Y-direction				RMS FORCE, Z-direction			
Std	DOC, mm				DOC, mm				DOC, mm			
Rake	0.5	1	2	3	0.5	1	2	3	0.5	1	2	3
5	0.2	0.3	0.9	1.2	0.1	0.2	0.7	1.1	0.6	0.9	2.2	2.8
10	0.2	0.5	0.9		0.1	0.3	0.6		0.5	1.2	2.0	
15	0.2	0.5	1.0	1.4	0.1	0.3	0.6	1.0	0.5	1.1	2.0	3.0
20	0.2	0.5	1.1	1.6	0.1	0.3	0.7	1.0	0.5	1.2	2.4	3.0
25	0.2	0.5	1.2	1.9	0.0	0.3	0.8	1.3	0.4	1.4	2.9	4.2
30	0.2	0.5	1.2	1.7	0.1	0.3	0.8	1.2	0.5	1.3	2.7	3.6

ALTERNATIVE CHAMFER GEOMETRY RESULTS

MEAN FORCE, X-direction					MEAN FORCE, Y-direction				MEAN FORCE, Z-direction			
Alt	DOC, mm				DOC, mm				DOC, mm			
Rake	0.5	1	2	3	0.5	1	2	3	0.5	1	2	3
5	-0.1	-0.2	-0.5	-0.7	0.1	0.2	0.5	0.6	0.3	0.6	1.3	1.7
10	-0.1	-0.3	-0.6	-0.8	0.0	0.2	0.5	0.5	0.3	0.7	1.4	1.5
15	-0.1	-0.2	-0.6	-0.7	0.0	0.1	0.4	0.4	0.2	0.4	1.2	1.3
20	-0.1	-0.2	-0.6	-0.9	0.0	0.1	0.3	0.5	0.2	0.5	1.1	1.4
25	-0.1	-0.3	-0.7	-1.2	0.0	0.1	0.3	0.8	0.3	0.7	1.2	2.0
30	-0.1	-0.3	-0.7	-0.9	0.0	0.1	0.4	0.6	0.3	0.7	1.2	1.4
	RMS FORCE, X-direction				RMS FORCE, Y-direction				RMS FORCE, Z-direction			
Alt	DOC, mm				DOC, mm				DOC, mm			
Rake	0.5	1	2	3	0.5	1	2	3	0.5	1	2	3
5	0.1	0.3	0.6	0.9	0.1	0.2	0.5	0.7	0.4	0.8	1.6	2.0
10	0.2	0.3	0.7	1.0	0.1	0.2	0.6	0.7	0.4	0.8	1.7	1.9
15	0.1	0.2	0.7	0.9	0.1	0.1	0.5	0.5	0.3	0.6	1.5	1.7
20	0.1	0.3	0.8	1.2	0.1	0.1	0.4	0.6	0.3	0.6	1.4	1.9
25	0.2	0.4	0.9	1.6	0.1	0.2	0.4	0.9	0.4	0.9	1.6	2.6
30	0.2	0.3	0.8	1.1	0.1	0.2	0.4	0.7	0.4	0.8	1.5	1.9

VITA

AMIN ATASHNEZHAD

Candidate for the Degree of

Doctor of Philosophy

Dissertation: INCORPORATING THE INTERFACIAL FRICTION ANGLE CONCEPT INTO THE PDC SINGLE CUTTER AND FULL BIT MODELING

Major Field: Chemical Engineering

Biographical:

Education:

Completed the requirements for the Doctor of Philosophy in Chemical Engineering at Oklahoma State University, Stillwater, Oklahoma in December 2019.

Completed the requirements for the Master of Science in Petroleum Engineering at Amirkabir University of Technology, Tehran in 2011.

Completed the requirements for the Bachelor of Science in Petroleum Engineering at Azad University branch of Omidiyeh in 2008.

Professional Memberships: SPE, AADE